3rd Annual Workshop Proceedings
7th EC FP – SKIN
AMPHOS21 – Barcelona – Spain
21st – 22th November 2013

Deliverable D6.14

SLOW PROCESSES IN CLOSE-TO-EQUILIBRIUM CONDITIONS FOR RADIONUCLIDES IN WATER/SOLID SYSTEMS OF RELEVANCE TO NUCLEAR WASTE MANAGEMENT
SKIN

COLLABORATIVE PROJECT (CP)

Grant agreement N°.: FP7-269688

Submitting organizations: AMPHOS, ARMINES
Actual submission: Project Month 38

Start date of the project: 01 January 2011
Duration: 36 months

FOREWORD

The present document is the proceedings of the last 3rd Annual Workshop of the Euratom FP7 Collaborative Project SKIN (Slow processes in close-to-equilibrium conditions for radionuclides in water/solid systems of relevance to nuclear waste management). The project started in January 2011 and had three years duration. The final workshop was hosted by AMPHOS 21 and held in Barcelona (Spain) 21st – 22th November 2013. Annual workshops bring together, partners, associated group and external interested groups.

The proceedings aim to be available to a broad scientific community on the outcome of the SKIN project through the scientific-technical contributions. The proceedings give information about the project structure and the different activities around the project with the scientific and technical documentations of each partner on the latest progress of the work. Exhaustive information about the project can be found under *http://www.emn.fr/z-subatech/skin/index.php/Main_Page*.

All the scientific-technical papers submitted have been reviewed for the proceeding by the End-User Group (EUG) the work progress and dissemination strategies in the light of the needs of the IGD-TP strategic research agenda as well as of their national programmes for implementation of geological disposal. EUG is a specific group including members of the *IGD-TP platform*, of waste management and regulators TSO organizations.

Thanks are due to all the authors of the submitted Scientific and Technical papers for review and to the workpackage leaders who provided an overview of the workpackage for the proceedings. We would like to acknowledge especially the reviewers, members of the EUG, who provided comments and recommendations for the papers and for the proceeding. Their active participation throughout the 3-years project allows to ensure its progress.

TABLE OF CONTENT

THE PROJECT

SKIN (01/01/2011 – 31/12/2013 - 3 years) is a European Project accepted within the 7th Framework Programme of the European Atomic Energy Community (FP7 Euratom) for nuclear research and training activities. It is a collaborative project including 9 partners from 6 European countries and 1 Asian partner: ARMINES/SUBATECH (France), Karlsruhe Institute of Technology (Germany), Forschungszentrum Jülich (Germany), Svensk Kärnbränslehantering AB (Sweden), AMPHOS 21 (Spain), Chalmers University of Technology (Sweden), Stockholm University (Sweden), Paul Scherrer Institute (Switzerland), Loughborough University (United Kingdom) and Peking University (China).

The objective of SKIN is to assess the relevant individual processes in the near-field and far-field to allow the development of robust methodologies for performance and safety assessment. In fact, due to the slow groundwater movement in confined deep geological formations, the system "radionuclides – minerals – engineered barrier materials – water" will be close to chemical equilibrium. These systems, controlling radionuclide mobility, have been studied for many years, but only a little attention has been given to the fact that, due to the long disposal time, individual very slow processes can have a significant impact on the mobility of radionuclides, despite local equilibrium states being achieved. The results would integrate and complete the FP7 Euratom Programme for the implementation of geological disposal of radioactive waste.

The work program is structured along 4 RTD work packages (WP2-5). They cover near-field and far-field aspects to assess the slow processes close-to-equilibrium which results will be implemented in Performance Assessment/Safety Case. Experimental programs are performed in WP2 and WP3: WP2 focuses on the formation and on slow processes close-to-equilibrium of solid solutions in aqueous environments under waste repository near-field and far-field aspects as well as cement-related systems; WP3 focuses on the understanding of the kinetics of alteration of oxides form primary solids, as well as the secondary solid phases expected to form under repository conditions after the eventual release of the radionuclides present in the different waste. WP4 assesses the experimental results by geochemical thermodynamic modeling and its new partial-equilibrium approach and by the affinity law and its validity close to equilibrium. WP5 performs a synthesis of results of experimental, modeling and safety assessment approaches in the context of a full assessment of the literature, and inclusion of literature data. Specific work packages on knowledge management, education and training (WP6) and administrative management issues (WP1) are also included in the project.

The present proceedings document the outcome of the 3rd Annual Project Workshop and give an overview of the outcome of the three years project.

THE THIRD ANNUAL WORKSHOP

OBJECTIVES

The Workshop combines different activities and meetings with the following objectives:

- Informing about the scientific progress
- Informing about the administrative status
- Discussing various topics of interest
- Informing/agreeing upon the last reporting

Emphasis was on scientific-technical topics with administrative issues kept to the minimum necessary.

RTD SESSIONS

Two days of plenary sessions was programmed where the results from the different work packages were presented. For the last final workshop, two lecturers have been invited:

- Prof. Dr. Andreas Lüttge from the University of Bremen (Germany)
- Dr. Claire Corkhill from the University of Sheffield (UK)

WP2: Experimental Programme 1: Study of solid-solution formation for selected host solids (carbonates, sulfates, silicates, cements) and radionuclides of interest in the near/far field of a radioactive waste repository

1. J. Hincliff, M. Felipe-Sotelo, N. Evans (LU): *Radionuclide in binding systems*
2. M. Klinkenberg, F. Brandt, U. Breuer, D. Bosbach (FZJ): *Uptake of Radium by barite under repository relevant conditons*
3. F. Heberling, V. Metz, S. Hofmann (KIT):
   a. *Work Package 2, Task 2.2: Sequestration of Eu(III), Se(IV,VI), and Np(V) by Carbonate minerals: Calcite / Aragonite*
   b. *Work Package 2, Task 2.1 (KIT contribution): Ra uptake by barite,$^{226}Ra^2$ - $^{133}Ba^{2+}$ "cocktail" experiments*
4. T. Suzuki-Muresan, K. David, S. Ribet, B. Grambow (SUBATECH/Armines): *Silicates*

WP3: Experimental Programme 2: Assessment of the kinetics of dissolution of tetravalent oxides under quasi-equilibrium conditions, and the impact of major factors on the rate of retention and release of radionuclides

1. T. Suzuki-Muresan J. Vandenborre, B. Grambow (SUBATECH/Armines): *Thorium oxide solubility behavior vs. the surface crystalline state*
2. M. Grivé, E. Colàs and L. Duro (Amphos 21): *Interaction between Uranium and Iron (III) oxides*

3. D. Cui, K. Spahiu (SU, SKB): *The influence of clay slurry invasion on the dissolution of spent nuclear fuel under reductive repository environments*

WP4: Modeling and Theory: Development of a new partial equilibrium approach to geochemical modeling of the slow uptake of radionuclides in host solid solutions, applied to the experimental and literature data

4. B. Thien, D. Kulik (PSI): *Adding uptake kinetics and surface entrapment to geochemical models: Simulations of uptake of cations and anions (SeIV) in calcite*
5. D. Kulik, B. Thien (PSI): *Thermodynamic/kinetic modeling of trace element uptake into solid solutions: GEM code extensions and test results*
6. E. Curti (PSI): *Modelling Ra uptake by barite*

Invited lecture:

1. Prof. Dr. Andreas Lüttge (University of Bremen): *Mineral and Glass Dissolution: New Thoughts on an Old Problem*
2. Dr. Claire Corkhill (University of Sheffield): *Immobilisation Science Laboratory, Dept. Of Materials Science & Engineering*

WP5: Synthesis and Safety Assessment: Overall synthesis of the project results together with previous studies and its impact on the uncertainties for safety assessment

B. Grambow, F. Brandt, L. Duro, D. Kulik (SUBATECH/Armines, FZJ, Amphos 21, PSI): *overall synthesis*

STRUCTURE OF THE PROCEEDINGS

The proceedings present individual scientific and technical contributions.

WP OVERVIEW

OVERVIEW WP2: CALCITE, BARITE, CLAYS, CEMENT

D. Bosbach

Forschungszentrum Jülich (FZJ)

d.bosbach@fz-juelich.de

Objectives of this WP

WP2 addresses the uptake of radionuclides for selected solid solutions which occur in the near field, and the far field including cement related systems. The following tasks were studied in detail:

- The applicability of $Ra_xBa_{1-x}SO_4$ solid solution - aqueous solution thermodynamics to a specific repository relevant scenario: Radium exchange with barite
- Sequestration of Eu(III), Se(IV,VI), and Np(V) by calcite
- Identification of radionuclide binding in complex cement related systems
- The reversibility of solid/solution interaction with clays

Five different partners work together within this working package: Karlsruhe Institute of Technology (KIT) works on carbonates. Forschungszentrum Jülich (FZJ), KIT and Chalmers University of Technology (CHT) together work on sulfates. ARMINES works on clays and Loughborough University (LU) on cements.

Summary of reported work

Carbonates (WP2-1):

- Frank Heberling and Sascha Hofmann (KIT) *Sequestration of Eu(III), Se(IV,VI), and Np(V) by calcite* – Aragonite to calcite recrystallization experiments were carried out to investigate the uptake of Eu(III) and Np(V) into the calcite structure under close-to-equilibrium conditions. The results presented here focus on the uptake of Eu(III).

Experiments confirm the very high affinity of Eu^{3+} towards incorporation into $CaCO_3$ minerals aragonite and calcite. Sorption onto aragonite proceeds, depending which mechanism is assumed, with an adsorption KD = 200 L/m^2 or a solid solution partition coefficient, D = 1350. On Eu-reacted aragonite only incorporation species are detected by TRLFS. At high solid to liquid ratio, Eu^{3+} incorporation into calcite has no significant impact on the calcite growth / aragonite dissolution rate.

TRLFS indicates that coupled substitution corresponding to the formation of a $Na_xEu_xCa_{(2-2x)}(CO_3)_2$ solid solution between $NaEu(CO_3)_2$ and $Ca_2(CO_3)_2$ endmembers, is the most relevant incorporation mechanism for Eu^{3+} in calcite involved in experiments in this study. Comparison to previous studies shows that this is not generally the case. In previous

studies other mechanisms were identified to be most likely, or the Na, Eu incorporation species was accompanied by significant amounts of other species. At low solid to liquid ratio a meta-stable situation can be achieved and calcite formation is inhibited. This phenomenon may only be explained for a solubility of the virtual $NaEu(CO_3)_2$ endmember of $\log_{10}(K_{SP}(NaEu(CO_3)_2:virtual)) \leq -21.3$.

Sulfates (WP2-2):

- Klinkenberg et al. (FZJ) *Uptake of Radium under Repository relevant conditions* – ^{226}Radium uptake by barite was monitored in batch experiments at close-to-equilibrium conditions. Two different types of barite were used. Detailed SEM and ToF-SIMS investigations were conducted in order to investigate the recrystallization mechanism and the evolution of the morphology. SEM investigations clearly show an additional coarsening effect due to the presence of Radium for one barite sample and a change of morphology for the other barite powder.

TOF-SIMS indicates a structural uptake of Radium and the transformation of pure barite to a $Ba_xRa_{1-x}SO_4$ solid solution. A Ba/Ra ratio was calculated from several TOF-SIMS measurements. The resulting TOF-SIMS Ra/Ba intensity distribution has its maximum between 2 and 4×10^{-3}, corresponding well with estimations from the macroscopic results, assuming full recrystallization.

In conclusion, the addition of Ra to a barite at close-to-equilibrium conditions has a major impact on the system leading to a fast re-equilibration to a $Ba_{1-x}Ra_xSO_4$ solid solution and visible effects on the particle size distribution, even at room temperature.

Silicates (WP2-3):

- Suzuki-Muresan et al. (Armines) *Determination of Dissolution and Precipitation Rates of Clayey Materials by* $^{29}Si/^{28}Si$ *isotopic exchange. Effect of temperature* – Surface studies on illite, illite/smectite and Callovo-Oxfordian argillite clay mineral phases were performed at close-to-equilibrium conditions for three temperatures (35, 50 and 90 °C) in 0.01 mol/L NaCl solution. Prior the experiments, the clays were purified by elutriation to remove the quartz phase. Characterization of the solids was done by SEM, XRD and XPS. Concentrations of Si, Fe and Al were measured in solution by Q-ICP-MS. Maximum concentrationa of Si were determined for each solid in contact with the solution and a pseudo-equilibrium was reached after 50 days of contact time. These values ($\sim 10^{-5} - \sim 10^{-4}$ mol/L) under the solubility of quartz values correspond to the solubility values of the clays. The Fe concentration in solution was 2.5×10^{-6} mol/L whereas Al was 3×10^{-6} mol/L in solution. After 326 to 483 days of alteration, a ^{29}Si spike was added to each system studied. The results obtained for the illite/smectite system indicate that at close-to-equilibrium conditions a dynamic exchange of ^{29}Si and ^{28}Si occurs at the interface solid/solution. The isotopic exchange was performed

during 100 days with a dissolution rate of $\sim 7 \times 10^{-15}$ mol Si/m²/s and a precipitation rate of $\sim 4 \times 10^{-15}$ mol Si/m²/s. The XPS and XRD analyses indicate no modification for both initial and altered illite/smectite after 538 days of alteration. XRD analyses for illite and Callovo-Oxfordian argillite showed no structural modifications after 640 days of experiments.

Cement (WP2-4):

- Hinchliff et al. (LU): *Diffusion and advection in cementitious media* – Within this WP, experimental methods were developed for the investigation of diffusive and advective transport of radioactive isotopes through cementitious media. A series of radial diffusion and advection experiments have been undertaken and examples are presented where significant results have been obtained. In the diffusion experiments the effects of high ionic strength and cellulose degradation products (CDP) on the mobility of strontium are described at both tracer and tracer plus carrier concentrations. Ca migration in the same radial configuration has been observed using autoradiography. The advection experiments required the development and manufacture of a purpose designed cell, the new cell is described and the results for ^{90}Sr and ^{45}Ca are presented. All experiments have been undertaken on intact samples of the cementitious medium.

OVERVIEW WP3: OXIDES

Lara Duro

AMPHOS 21 (Spain)

lara.duro@amphos21

Objectives of this WP

The global objective of this WP is the assessment of the dissolution processes of oxides of relevance for the safety assessment of the repository in close-to-equilibrium conditions. To this aim, the following specific investigations were defined from the onset of the projet:

- Study of the nature and long term kinetics of the interaction between actinides and major near field components, linking short-term sorption and long-term coprecipitation processes and their study through specific solid spectroscopy.

- Study of the kinetics of dissolution of tetravalent oxides under conditions close to equilibrium, with special focus on the study of the solid-liquid interface, including monitoring of the composition of the surface through isotopic exchange techniques.

- Study of the effect of near field materials on the kinetics of dissolution of tetravalent oxides and the potential of bentonite colloids as drivers for dissolution enhancement.

6 Different partners work within this workpackage: ARMINES, Loughborough University (LU) Stockholm University (SU) and SKB work on the study of the dissolution of tetravalent actinides under quasi equilibrium conditions. To this aim, ARMINES works with ThO_2, LU works with TcO_2, and SU and SKB work with UO_2 and with ThO_2 as a proxy for UO_2 in order to avoid unwanted oxidation of UO_2 to U(VI). Amphos 21, SU and the University of Beijing (PKU) work on the influence of major systems present in the repository on the rate of dissolution of matrix-related material and the retention/release of radionuclides.

In this third annual workshop proceedings, most partners of WP3 have presented a Scientific and Technical contribution showing some of the advances in the results. A summary of the work presented in the workshop follows.

Summary of reported work

WP3.1. *Study the interaction between U and Fe oxides (Amphos 21)*

In previous workshops, the effect of uranium in the aging process of ferrihydrite and the effect of this aging on the mobility of Uranium was presented, supported by results from XRD, μ-XRF and EXAFS Fe K-edge and U LIII-edge. In this last workshop, the information was complemented by the report on the experiments of release of uranium from coprecipitates in the presence of carbonates. The experiments, conducted in a flow-through fashion,

permitted the derivation of release rates of uranium from the coprecipitates. The results indicated the non-congruency of the dissolution of uranium and iron, showing a preferential release of uranium versus iron. The comparison of the dissolution of uranium from the coprecipitates and that from schoepite showed a retarding effect of the coprecipitate on the dissolution of uranium. In the light of the rate laws derived, it was proposed that the dissolution of uranium is governed by the formation of a surface complex between uranium and carbonate that can also involve iron. The results are reported in more detail in one contribution of these proceedings.

WP3.2. *Solubility and dissolution of ThO_2 (ARMINES)*

The study of ARMINES was focused on the dissolution behaviour of ThO_2 and the influence of the surface. In previous workshops, the method for synthesis of different crystallinity ThO_2 solids was presented, characterisation of the samples, surface area and dissolution data were presented. In this last workshop, the results presented focused on the isotopic exchange between Th232 and Th229 at the solid surface, as an indication of the dissolution mechanism. From the results, it was concluded that the grain boundaries presented a large influence on the extent of isotopic exchange. In this way, the solids presenting low crystallinity or a large amount of grain boundaries showed higher isotopic exchange than solids of high crystallinity (synthesised at 1500 °C and with low grain boundary densities. The results are reported in more detail in one contribution in these proceedings.

WP3.3. *Solubility and dissolution of TcO_2 (Loughborough University)*

The study of the dissolution and solubility of TcO_2 involved the synthesis of the solid phase and its characterisation. Experiments to study its dissolution were set up at different pH and different ionic strengths. Results after contact times until 10,000 hours indicated a stronger effect of pH than of ionic strength over the final "steady state" concentration of technetium in solution. The substitution of the solution after 10,000 hours by fresh solutions produced concentrations of Tc in solution statistically different from those obtained in the previous experiments. These experiments are reported in more detail in two contributions in these proceedings.

WP3.4. *UO_2 dissolution (Studsvik and SKB)*

WP3.4 studied two different issues i) the dissolution process of UO_2 and the isotopic exchange at the surface and ii) the effect of bentonite slurries on the dissolution of UO_2. In this last workshop the work presented was on the effect of bentonite (montmorillonite) on UO_2 dissolution, and it is reported in more detail in one contribution in these proceedings. In order to avoid oxidation problems, ThO_2 was used as a proxy for UO_2 in the experiments. The

results show that the process of sorption of Th on the surface of montmorillonite is much faster that the dissolution of ThO_2 and, therefore, much lower concentrations are measured in the case of having the clay present in the system.

WP3.5. *Decomposition of U(VI)-Arsenazo III complex by Fenton reaction induced by Gamma irradiation (Beijing University)*

The contribution of the university of Beijing was not presented in this workshop, but can be found in the proceedings of the second annual workshop.

OVERVIEW WP4: THEORY AND MODELLING

Dmitrii A. Kulik

Paul Scherrer Institut (Switzerland)

dmitrii.kulik@psi.ch

Task objectives to date:

4.1. To review existing models of time-dependent trace element uptake in host minerals; To find a generalized approach suitable for implementation in geochemical modelling codes; To perform initial tests of routines implementing this approach in the GEM-Selektor code.

4.2. To collaborate with partners involved in WP2 Task 2.1, in order to interpret experimental data on barite recrystallization kinetics and on the uptake of radium in the barite structure.

4.3. To review the literature data for some typical mineral rates expressed as function of the chemical affinity.

Summary of reported work:

4.1. Thermodynamics alone is usually not sufficient to predict growth-rate dependencies of trace element uptake in host mineral solid solutions. In this study, two uptake kinetic models were analyzed and found to be promising in terms of mechanistic understanding and potential for implementation in geochemical modeling codes. The Growth Surface Entrapment Model (Watson, 2004) and the Surface Reaction Kinetic Model (DePaolo, 2011) were shown to be complementary, and under certain assumptions merged into a single analytical expression. This Unified Uptake Kinetics Model was implemented in GEMS3K and GEM-Selektor codes (http://gems.web.psi.ch), a Gibbs energy minimization package for geochemical modelling. In turn, this extends the applicability of UUKM to accounting for the non-trivial factors influencing the trace element partitioning into solid solutions, such as changes in aqueous solution composition and speciation, or depletion effects in closed geochemical systems.

This UUKM implementation *(Deliverable 4.2 Report)* has been tested on the literature data on trace cation uptake kinetics in calcite, as well as against the new experimental data for selenite incorporation during fast co-precipitation with calcite (F. Heberling, WP2). The UUKM variant with an extremely high enrichment factor and rather low sub-surface diffusivity parameter was found to be consistent with this data representing an extreme case of the growth surface entrapment. More experiments at much lower calcite growth rates are needed to verify the UUKM-predicted trend for this system.

4.2. Kinetic/thermodynamic modelling of experimental data produced at FZJ on Ra uptake during the recrystallization of two commercial barites (Sachtleben and Aldrich) was updated and now includes the data extending up to 658 days reaction time. After a first slow kinetic

step lasting up to 120-180 days, the growth rate suddenly increases to values of up to 400 $\mu mol\ m^{-2}d^{-1}$, suggesting nucleation of a new $(Ba,Ra)SO_4$ phase from supersaturation with the ideal or even negative interaction parameter ($a_0 \leq 0$). After this fast nucleation step, Ra concentrations in the aqueous solution slowly increase, approaching the equilibrium line of a regular $(Ba,Ra)SO_4$ solid solution with interaction parameter $a_0 = 1.0$, in agreement with theoretical predictions based on atomistic simulations. These trends may suggest Ra entrapment during the fast precipitation event, followed by some release due to slow recrystallization towards the "true" aqueous - solid solution equilibrium.

The Ra uptake experiments carried out at CHALMERS and KIT-INE involved low (picomolar to nanomolar) total Ra concentrations; the [133]Ba tracer was added simultaneously to the Ra tracer, allowing the independent determination of $(Ra,Ba)SO_4$ recrystallization rates. The Ba tracer data indicate for both sets of experiments recrystallization rates and a_0-values comparable to those inferred from earlier published experiments conducted in a similar range of total Ra concentration. However, the results of the KIT-INE experiments fail to be interpreted in terms of classical heterogeneous and homogeneous recrystallization models, but can be successfully described with a new "continuous recrystallization model" assuming the repeated dissolution-precipitation of previously formed Ra-barite monolayers.

One conclusion drawn from modelling of three experimental data sets is that the interaction parameter a_0 for the $(Ba,Ra)SO_4$ solid solution is confined between 0.0 and ~ 1.0. The latter value seems to reflect thermodynamic equilibrium, in agreement with theoretical predictions from atomistic simulations (Vinograd et al., 2013). This finding has a direct relevance for the safety assessment of radioactive waste repository sites, as it may reduce the safety margins for the mobility of radium in such environments.

4.3. In this study, a review of literature data concerning the dissolution or precipitation kinetic properties of selected minerals (oxides, hydroxides or aluminosilicates) as function of the chemical affinity (deviation from equilibrium) has been performed. Considered studies combine the Transition State Theory and the Surface Complexation Modeling concept for expressing a rate law as function of solution composition and chemical affinity. It is shown that different classes of rate models exist, but in most cases, no single generalized rate equation can be used to model mineral dissolution over the full range of geochemical conditions; a sequence of different rate laws with parameters of little to no physical meaning must be used so far. For several minerals, it seems to be premature to test the affinity law close to equilibrium because of the lack of coherent and precise experimental data.

S+T CONTRIBUTIONS

RADIONUCLIDE BINDING IN CEMENT SYSTEMS

John Hinchliff*, Nick Evans, Monica Felipe Sotelo

Loughborough University (UK)

* Corresponding author: cmjh5@lboro.ac.uk

Abstract

A series of radial diffusion and advection experiments have been undertaken and examples are presented where significant results have been obtained. In the diffusion experiments the effects of high ionic strength and cellulose degradation products (CDP) on the mobility of strontium are described at both tracer and tracer plus carrier concentrations. Ca migration in the same radial configuration has been observed using autoradiography. The advection experiments required the development and manufacture of a purpose designed cell, the new cell is described and the results for ^{90}Sr and ^{45}Ca are presented. All experiments have been undertaken on intact samples of the cementitious medium.

Introduction

This paper describes examples from a series of diffusion and advection experiments. These dynamic experiments aim to understand the interaction between cementitious media and radionuclides relevant to the geological disposal of radioactive waste.

The cementitious media being studied are NRVB (Nirex Reference Vault Backfill) and a waste packaging grout containing PFA (pulverised fuel ash). The experiments on the PFA grout have not yielded any evidence of diffusion and it has been assumed that precipitation has occurred due to very low solubility. Consequently, the discussion here concentrates on the NRVB experiments. The radionuclides being studied are ^{90}Sr, ^{45}Ca, ^{241}Am, ^{152}Eu and ^{75}Se. Migration of ^{90}Sr and ^{45}Ca has been observed in the diffusion and advection experiments but there is currently no evidence of migration of ^{241}Am and ^{152}Eu. The ^{90}Sr experiments ran smoothly with manageable durations (stabilising at < 200 days) and as a consequence it was also possible to undertake experiments demonstrating the effects of high ionic strength and the presence of CDP on Sr mobility. The ^{75}Se diffusion experiments have been running for six months and migration has not been observed.

Diffusion Experiments

The radial diffusion experimental technique uses small pre-cast cylinders of the cementitious matrix under investigation, in this case, NRVB. The appropriate concentration of radionuclide tracer and carrier (if required) is introduced into a cavity in the centre of the cylinder which is then sealed and placed in a solution previously equilibrated with the solid matrix. The increase in concentration of the isotope in the external solution is then determined at defined time intervals.

90Sr Diffusion

Tracer only (13.5 kBq of ^{90}Sr) and tracer with carrier (13.5 kBq of ^{90}Sr with 21.8 mg Sr as Sr(NO$_3$)$_2$; equivalent to ~10^{-3} mol dm^{-3} if fully equilibrated with the receiving solution) radial diffusion experiments on NRVB were undertaken using ^{90}Sr in the presence and absence of CDP. Two similar tracer only experiments were undertaken where the ionic strength of the solution was increased. In the first of these experiments sufficient Na/KCl was added to produce a 0.1 mol dm^{-3} solution. In the second experiment the same mass of Na/KCl was added to the central core with the tracer, the purpose was to create a high ionic strength gradient that would equilibrate to 0.1 mol·dm^{-3} as the experiment progressed. These experiments were originally devised because the ionic strength of the CDP solutions was noted to be higher (most likely due to the 80 °C production temperature) than the NRVB equilibrated water.

The ^{90}Sr diffusion experiments proceeded fast enough to be monitored via the increase of concentration in the surrounding solution. Figure 1 below show the results.
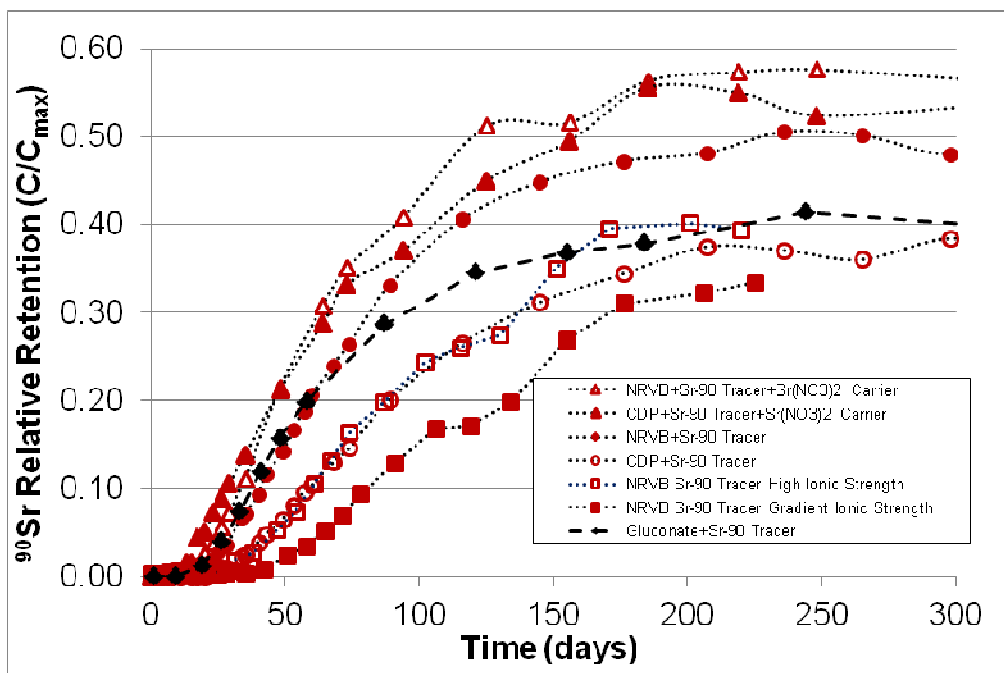

Fig. 1 Results of the ^{90}Sr diffusion experiments

The effect on the migration of ^{90}Sr caused by the presence of CDP is seen to be significant at tracer concentrations where, contrary to expectations, migration was significantly slowed and retention on the NRVB increased. The effects were not evident in the carrier experiments where the Sr concentration was increased with non-active $Sr(NO_3)_2$. The high ionic strength tracer only experiment produced very similar results to the CDP tracer only experiment. The gradient ionic strength experiment produced the slowest initial breakthrough and subsequent diffusion. However the gradient ionic strength results are still increasing and may converge with the high ionic strength experiment.

A tracer only experiment using gluconic acid (in the lactone form, i.e. with no counter ions) as a surrogate for the CDP was also undertaken. The results, shown in black on Figure 1, initially resembled the carrier experiments but upon stabilisation the retention on the NRVB was similar to the high ionic strength and CDP tracer only experiments.

The results show that there is an effect on ^{90}Sr migration at tracer concentrations due to the presence of CDP and/or the increased ionic strength. At this stage there is insufficient evidence to confirm which effect is dominant under any given set of experimental conditions.

The slowing of Sr migration could be due to the formation of a ternary complex between a component of the CDP, the surface of the cement matrix and Sr, or enhanced ion exchange with calcium in the cement phases in the matrix. Increasing electrostatic interaction is believed to be the reason why diffusion is slowed as the ionic strength increases.

^{45}Ca Diffusion

There had been an expectation to observe some mobility of calcium in the cementitious systems being investigated primarily because calcium is present in high concentration in both solid (> 25% w/w) and solution (~800 ppm or ~2×10^{-2} mol·dm^{-3}). The addition of ^{45}Ca was so small in comparison that isotope exchange would be the only effect observed. However, it is not clear how migration would be driven by isotope exchange and the mechanism may simply be slow diffusion across a very small ^{45}Ca concentration gradient.

The short half-live of ^{45}Ca (163 days) could also be an issue if mobility was slow. After one year, and with no breakthrough of ^{45}Ca, one of the NRVB experiments was stopped and the cylinder sectioned for autoradiography. This was done because of the need to establish whether the decay of ^{45}Ca had rendered it difficult to detect on the autoradiography plates. The resulting images are shown below.

Fig. 2 Autoradiograph and intensity plot of NRVB cylinder from the ^{45}Ca diffusion experiments (central core "plugged" to shield highest activity at inner walls).

It is clear that ^{45}Ca has moved into the NRVB matrix from the central core, penetration appears to be several millimetres. The image of the activity in the matrix has been made clearer by screening, with a plastic plug (absorbing the beta radiation from ^{45}Ca decay), the much higher activity present on the surface of the core. The unshielded autoradiograph and intensity plot are shown below.
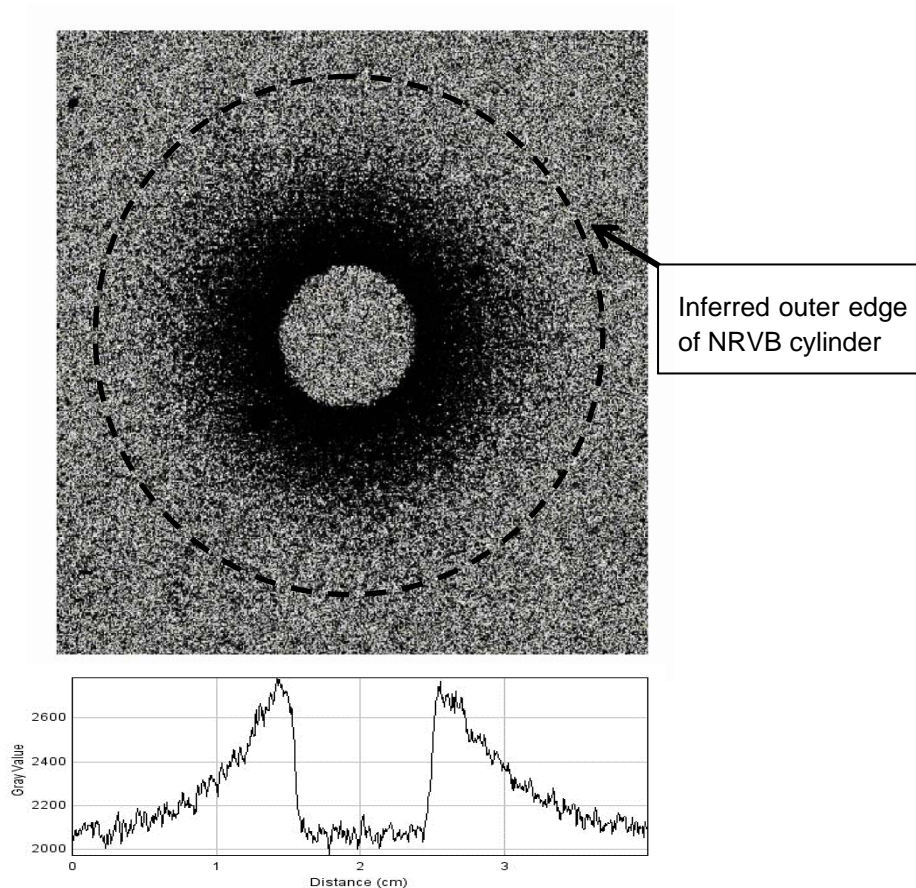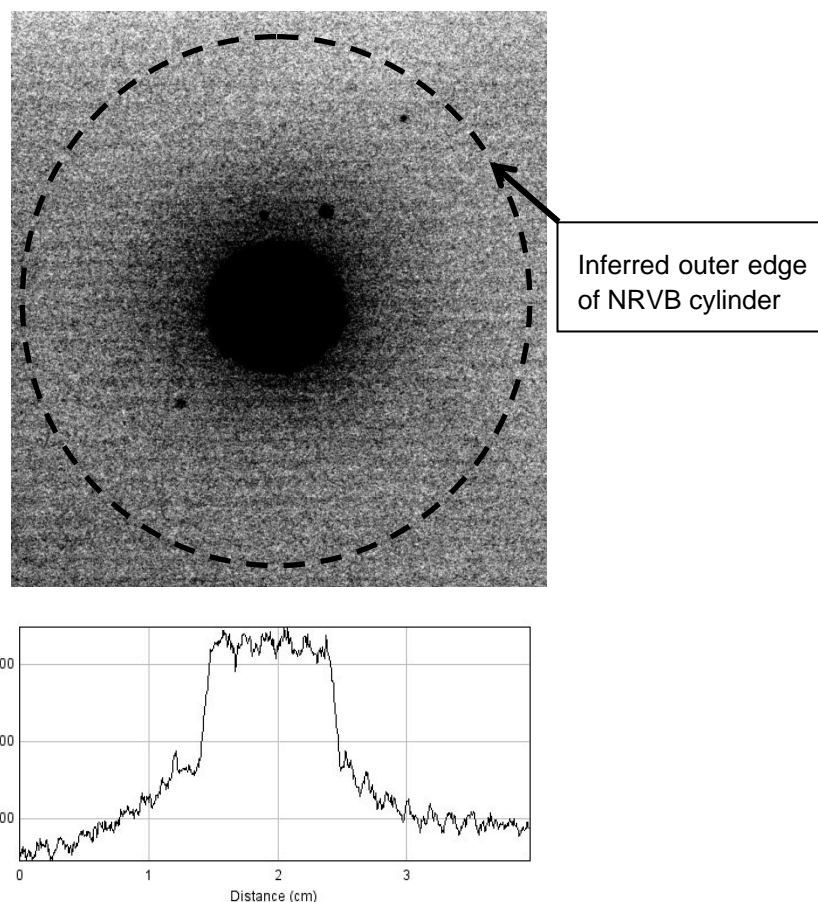
Fig. 3 Autoradiograph and intensity plot of NRVB cylinder from the Ca-45 diffusion experiments (central core "unshielded" to show highest activity at inner walls)

It should be noted that the intensity plots are not calibrated and it is only possible to infer relative concentrations. The unshielded figures demonstrate that a significant proportion of the ^{45}Ca has remained on the inner walls of the central core. Additionally the 2 cm^3 of solution remaining in the core when the experiment was halted, was removed and analysed by liquid scintillation counting and the ^{45}Ca activity concentration was found to be at background.

Advection Experiments

A radial advection apparatus has been designed and manufactured and is now operational. Results for ^{90}Sr and ^{45}Ca in the presence and absence of CDP have been obtained. The photographs below show the main parts dismantled and the completed set up. The apparatus has been manufactured to enable testing of cementitious cylinders with similar dimensions those used in the diffusion experiments. The "eluent" is pushed from the steel reservoir through the cylinder using N$_2$ pressure. The whole system is effectively closed to O$_2$ and CO$_2$ ingress up to the end of the sample collection tube where interaction with the atmosphere is limited by the small internal diameter of the teflon tubing.

Fig. 4 Photographs of the advection apparatus

The ^{90}Sr and ^{45}Ca plots below show that the method works. Flow rate control using N_2 pressure remains an issue as outgassing is visible within the cell at the NRVB surface. The "step" changes and data gaps observed in the results were generally associated with interventions e.g. refilling the reservoir, changing the gas bottle or clearing blocked tubing.

45Ca Advection

Figures 5 and 6 below show the results of the ^{45}Ca advection experiment using NRVB equilibrated water.
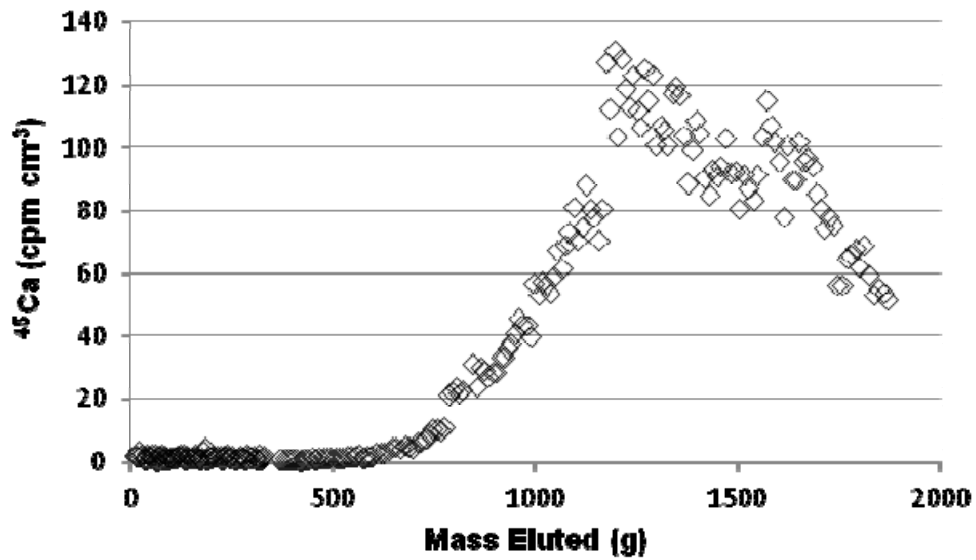

Fig. 5 Graph showing advection of 45Ca through NRVB
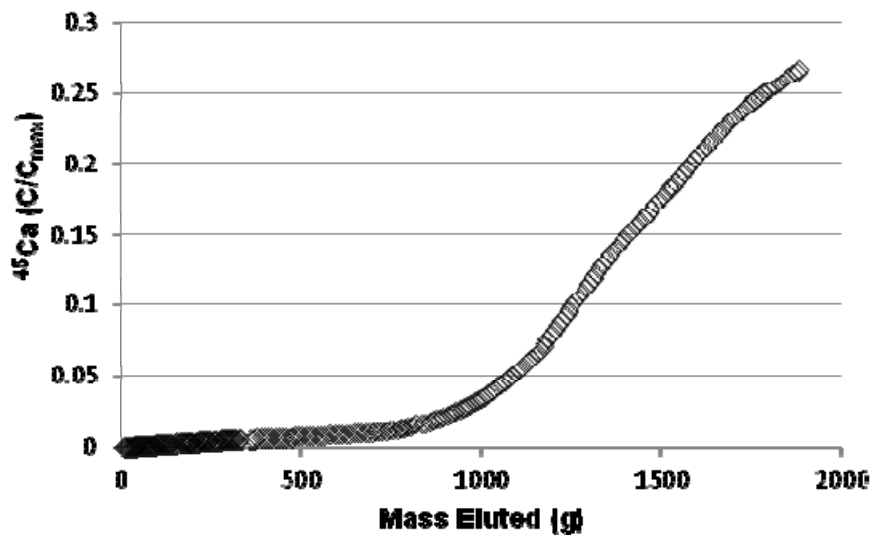
Fig. 6 Graph showing cumulative 45Ca results

The recovery of ^{45}Ca was less than 30% implying that over 70% was retained on the NRVB. A similar experiment which ran for the same total flow was undertaken using a CDP solution and no ^{45}Ca was eluted. The runs were stopped before the elution of ^{45}Ca had ceased so that autoradiographs could be produced, the resulting images are shown as Figures 7 and 8.
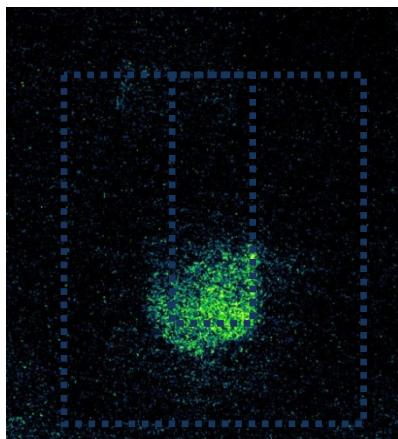
Fig. 7 Autoradiograph of NRVB cylinder showing ^{45}Ca distribution (no CDP present)
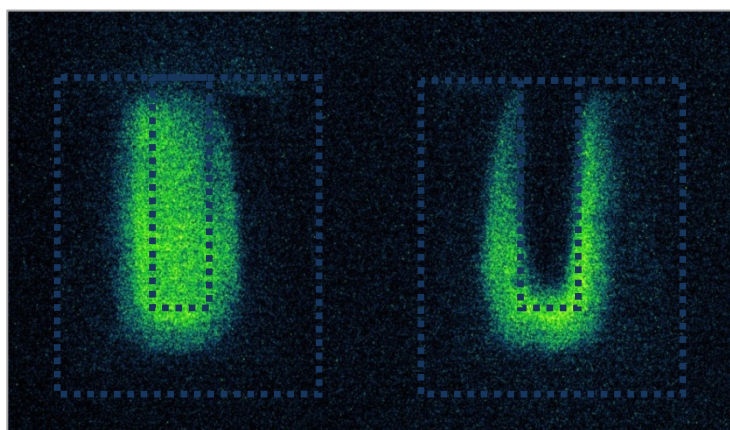
Fig. 8 Autoradiograph of NRVB cylinder showing ^{45}Ca distribution (CDP present)unshielded image on the left, clay shielding placed in central well on right hand image.

The autoradiographs clearly show that ^{45}Ca is retained on the NRVB much more significantly in the presence of CDP. There was a delay after ending the experiment prior to producing the image shown as Figure 7 and further decay of the ^{45}Ca will have occurred. As a consequence the ^{45}Ca intensities shown in Figures 7 and 8 are not directly comparable.

90Sr Advection

Figures 9 and 10 below show the results of the 90Sr advection experiments. Runs in the absence of CDP and in the presence of CDP solution are shown. Figure 10 is a cumulative plot of the data shown in Figure 9. Both runs were stopped before the elution of 90Sr had ceased so that autoradiographs could be produced.
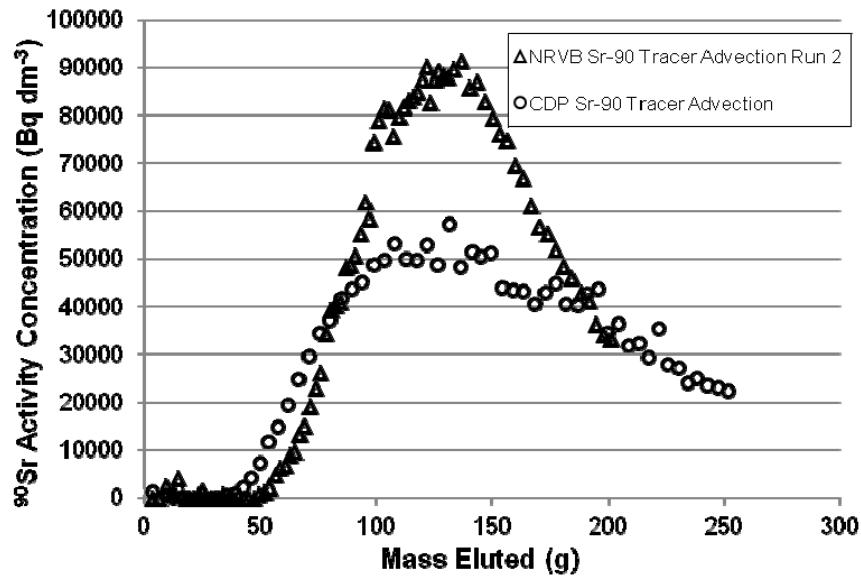
Fig. 9 Graph showing results of the advection of *90*Sr through NRVB in the presence and absence of CDP
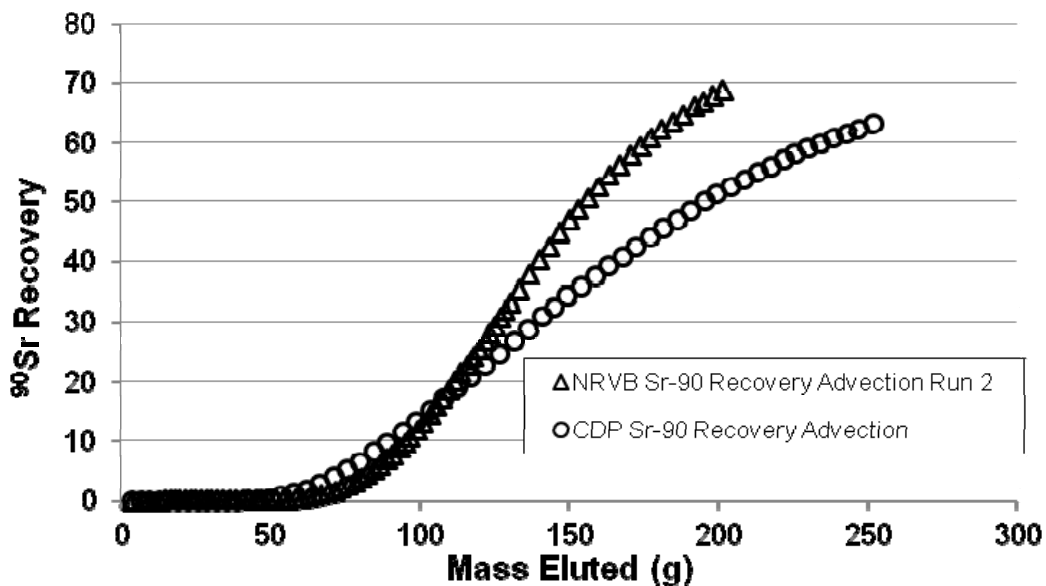
Fig. 10 Graph showing cumulative results of the advection of *90*Sr through NRVB in the presence and absence of CDP

There are clear differences in the elution profiles, the most obvious being the reduced peak height of the CDP experiment. The same mass of tracer was added to each run and there is an indication that more ^{90}Sr is retained in the presence of CDP. However, it is also clear that the CDP profile has a longer tail, implying that all the ^{90}Sr will eventually elute.

The autoradiographs are shown below.
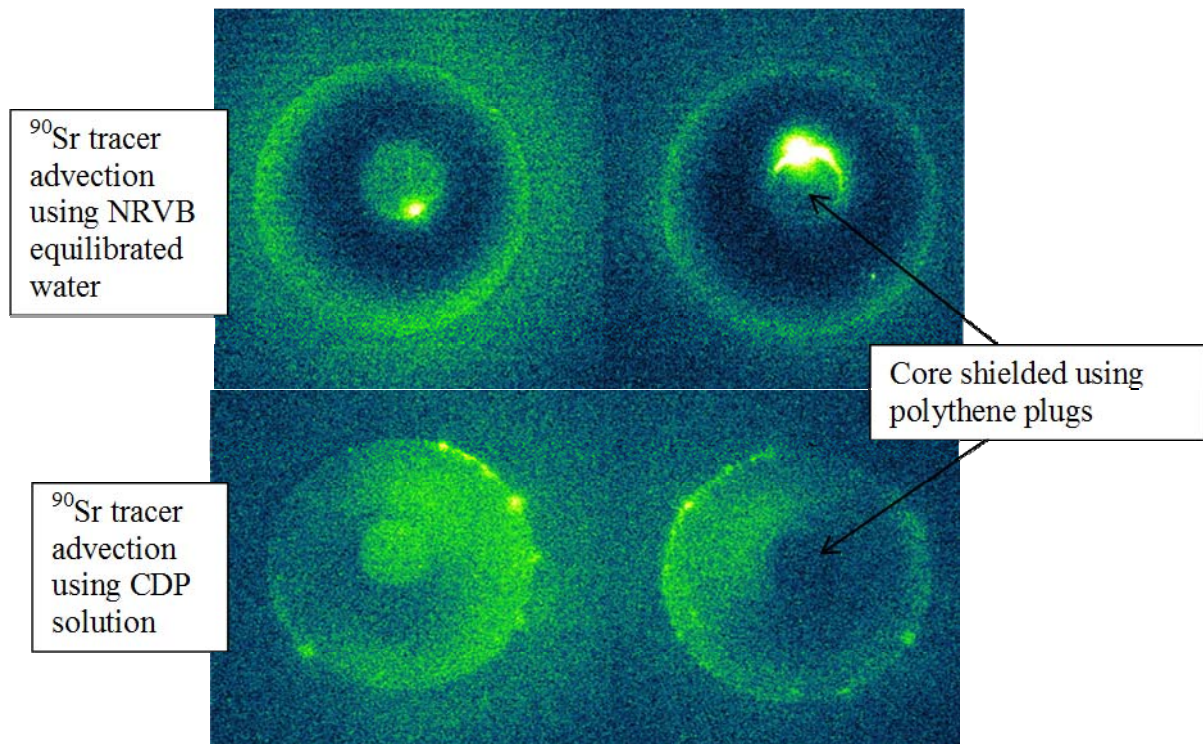
Fig. 11 Autoradiographs from the ^{90}Sr tracer advection experiments

NRVB equilibrated water

- There is a distinct ring of ^{90}Sr tracer activity within the NRVB matrix extending to the outer edge.

- Spots of activity are absent from the outer edge.

- There is a ring of inactivity surrounding the central core.

- The central core has significant residual activity present, this is particularly evident on the upper right image where the intense activity can be clearly seen despite the shielding (Note that this cylinder has had two active runs).

- There is a possibility that the outer ring is Sr and calcite co-precipitation caused by the ingress of atmospheric carbon dioxide similar to that observed in the trial advections.

- The outer ring of activity could also be evidence of the tracer tail being eluted.

CDP solution

- More tracer is present in the NRVB matrix than seen in the NRVB equilibrated water experiment.

- The tracer is more evenly distributed than in the absence of CDP although there are distinct areas where more tracer is present, suggesting preferential flow or an artefact associated with the position of the tracer injection.

- There are spots of tracer activity on the outer edge which appear to be contiguous with the areas of possible preferential flow.

- There is residual tracer activity in the central core but none of the very intense spots seen in the central core of the NRVB equilibrated water experiment.

- The ring of activity around the outer edge is present though not as extensive as in the NRVB equilibrated water experiment.

- There is a possibility that the outer ring is Sr and calcite co-precipitation caused by the ingress of atmospheric carbon dioxide similar to that observed in the trial advections.

Advection – concluding remarks

The advection experiments show that there are clear differences in mobility between the radionuclides tested. The comparison between ^{90}Sr and ^{45}Ca is significant. The ^{45}Ca results indicate a strong interaction with the NRVB which is most likely due to a combination of isotope exchange and solubility limitation. The ^{45}Ca results in the presence of CDP may indicate that precipitation/dissolution of an organic Ca salt is the dominant effect. Additional work will be required to confirm this. The ^{90}Sr results indicate that it is more mobile than ^{45}Ca and has a less significant interaction with the solid matrix.

Acknowledgement

References

Abdullah M. Alshamsi and Hassan D. A. Imran; Development of a permeability apparatus for concrete and mortar. Cement and Concrete Research Volume 32, Issue 6, June 2002, Pages 923-929.

Evans N D M. Binding mechanisms of radionuclides to cement. Cement and Concrete Research Volume 38, Issue 4, April 2008, pages 543-553.

Rowe P W, Barden L; A new consolidation cell. Géotechnique, Vol. 16, No. 2, 1966, pages 116-124.

Francis, A J, Cather, R, and Crossland, I G, Development of the Nirex Reference Vault Backfill; report on current status in 1994, Nirex Science Report S/97/014, UK

Nirex Ltd., Harwell, UK, 1997.

Jakob A, Diffusion of tritiated water (HTO) and 22Na+-ions through non-degraded hardened cement pastes – II. Modelling results. PSI-Bericht Nr. 02-21 December 2002.

Markovaara-Koivisto, M., Read, D., Lindberg, A., Siitari-Kauppi, M., Togneri, L., 2009. Geology of the Sievi, Kuru and Askola sites. Uranium mineralogy at Askola. Research Report TKK-GT-A-4, Helsinki University of Tecnology.

Andersson K, Torstenfelt B. Allard B: Sorption and diffusion studies of Cs and I in concrete Department of Nuclear Chemistry Chalmers University of Technology Göteborg, Sweden January 1983

Mibus J, Sachs S, Pfingsten W, Nebelung C, Bernhard G, Migration of uranium(IV)/(VI) in the presence of humic acids in quartz sand: A laboratory column study. Journal of Contaminant Hydrology 89 (2007).

M.M. Askarieh, A.V. Chambers, F.B.D. Daniel, P.L. FitzGerald, G.J. Holtom, N.J. Pilkington, J.H. Rees. The chemical and microbial degradation of cellulose in the near field of a repository for radioactive wastes. Waste Management 20 2000 pp 93-106.

Pala´gyi S, Tamberg K S, Vodickova H; Transport and sorption of Sr-85 and I-125 in crushed crystalline rocks under dynamic flow conitions. Journal of Radioanalytical Nuclear Chemistry 2010 page 283

Tits J, Wieland R, Bradbury M H; The effect of isosaccharinic acid and gluconic acid on the retention of Eu(III), Am(III) and Th(IV) by calcite. Applied Geochemistry 20 November 2005 Volume 20, Issue 11 pages 2082-2096

Chatterji, S., 1994. Transportation of ions through cement based materials. Part 1: Fundamental equations and basic measurement techniques. Cem. Concr. Res. 24, 907-912.

Chatterji, S., 1995. On the applicability of Fick's second law to chloride ion migration through Portland cement concrete. Cem. Concr. Res. 25, 299-303.

Chatterji, S., 1999. Evidence of variable diffusivity of ions in saturated cementitious materials. Cem. Concr. Res. 29, 595-598.

UPTAKE OF RADIUM BY BARITE AT NEAR TO EQUILIBRIUM CONDITIONS

Martina Klinkenberg[1]*, Felix Brandt[1], Uwe Breuer[2], Dirk Bosbach[1]

[1] Forschungszentrum Jülich, Institute of Energy and Climate Research (IEK-6) Nuclear Waste Management and Reactor Safety, (GER)

[2] Forschungszentrum Jülich, Central Institute for Engineering, Electronics and Analytics (ZEA-3) Analytics, (GER)

* Corresponding author: m.klinkenberg@fz-juelich.de

Abstract

A combined macroscopic and microanalytical approach was applied in order to distinguish between two possible scenarios for the uptake of Ra by already existent barite under repository relevant conditions: (1) formation of a $Ba_{1-x}Ra_xSO_4$ solid solution surface layer on the barite or (2) a complete recrystallization, leading to homogenous $Ba_{1-x}Ra_xSO_4$ crystals. It could be clearly shown that all barite particles analyzed within this study contain Ra not only on their surfaces but within the grains. In addition, the role of Ra during the recrystallization of barite was examined via detailed SEM investigations.

In conclusion, the addition of Ra to a barite at close-to-equilibrium conditions has a significant impact on the system leading to a fast re-equilibration to a $Ba_{1-x}Ra_xSO_4$ solid solution and visible effects on the morphology and particle size distribution, even at room temperature.

Introduction

The possible solubility control of Ra by coprecipitation of a $Ba_{1-x}Ra_xSO_4$ solid solution has been demonstrated in several cases e.g. **Doerner & Hoskins, 1925**. However, an open question is whether a Ra containing solution will equilibrate with solid $BaSO_4$ under repository relevant conditions due to barite recrystallization. Here, Ra enters a system in which barite is in equilibrium with the aqueous solution. Previous studies have revealed that uptake of Ra is not limited by pure adsorption at close-to-equilibrium conditions but involves a significant fraction of the bulk solid (**Bosbach et al. 2010, Curti et al. 2010**).

Here we present new experimental results, following a combined macroscopic and microanalytical approach. Batch experiments were carried out in order to analyze the spatial

distribution of Ra within the solid after the recrystallization experiments as well as the effect of the presence of Ra on the particle size distribution (PSD).

Materials and methods

Sample preparation and characterization

For the Ra uptake experiments, a synthetic, high purity barite (XR-HR10) from Sachtleben Chemie® GmbH was used, which was provided by Enzo Curti (Paul Scherrer Institute PSI, Villingen, Switzerland). The same barite was used in the experiments of ***Bosbach et al. (2010)*** and ***Curti et al. (2010)***. The second barite was a commercially available barium sulfate from Aldrich with a purity of 99.998 %.

XRD confirmed that both powders were pure barite within the precision of this method. A coarse fraction of the Sachtleben (SL) and a fine fraction of the Aldrich (AL) barite were separated. The specific surface area of the separated SL fraction was determined via Kr-BET to be $S_{BET} = 0.17$ m²/g, whereas the AL consisted of particles with a specific surface area $S_{BET} = 1.70$ m²/g.

Experimental setup

Batch recrystallization experiments were performed at ambient conditons (23 ± 2) °C. The barites were pre-treated for 4 weeks in 10 mL of 0.2 N NaCl solutions in 25 mL glass bottles. Afterwards, 10 mL of a Ra^{2+} containing solution were added, resulting in a total volume of 20 mL, an ionic strength of 0.1 N NaCl, and a concentration of 5.0×10^{-6} mol/L $^{226}Ra^{2+}$. The ionic strength was chosen to be comparable to granitic ground waters e.g. at the Äspö site in Sweden. Experiments were carried out with a solid/liquid ratio of 5 g/L and 0.5 g/L. In regular time intervals 500 µL of the aqueous solution were taken and then filtered. The liquid was filtered through Advantec ultrafilters (MWCO = 10,000 Da) and then analyzed for the Ra concentration.

Analysis of aqueous solutions and solids

The Ra concentration in solution was examined via Gamma spectrometry using a N_2 cooled high purity (HP) Ge-detector. The barite particles were studied using the environmental scanning electron microscope FEI Quanta 200 F. In order to avoid artifacts due to precipitation of NaCl, $BaSO_4$ or $RaSO_4$, the samples were separated from their solution by two washing steps in iso-propanol. The samples were then prepared as a suspension on a Si wafer and subsequently dried.

From the SEM images, the PSD was determined. For the AL samples, the longest axis of 360 grains of each sample was measured via image analysis of SEM images at 40,000 x and

20,000 x magnifications. Due to the larger grain size of the SL barite and narrow grain size distribution, 150 grains per SL sample were analyzed. Grains, which were grown together, were regarded as single grain. The equivalent mass of each grain was calculated using the measured grain size as the diameter of an equivalent sphere and the density of barite (4.5 g/cm³).

Within this study, a powder method was developed specifically for the analysis of the recrystallized barite and the detection of Ra in the sub-ppm range by time of flight secondary ion mass spectroscopy (TOF-SIMS). The spatial distribution of Ra and Ba within the recrystallized barite powders was analyzed using an ION-TOF instrument. For the mass spectral analysis a pulsed Bi^{3+} beam of 25 keV was used. The raw data were reconstructed and analyzed using the ION-TOF software package.

Results and discussion

Final Ra concentration in aqueous solution

The Ra concentration in solution significantly decreased during 443 days of experiment. The final concentrations are given in Figure 1. The experiments with 5 g/L barite the Ra concentration showed a decrease from 5.0×10^{-6} to the order of 10^{-9} mol/L whereas the Ra concentration in solution of the 0.5 g/L experiments decreased to the order of 10^{-8} mol/L. According to these results, a Ra/Ba ratio of the solid was calculated from mass balance. A Ra/Ba = 2.5×10^{-4} was calculated for the experiments with S/L = 5 g/L barite whereas for S/L = 0.5 g/L the Ra/Ba ratio was calculated to be one order of magnitude higher (Figure 1).
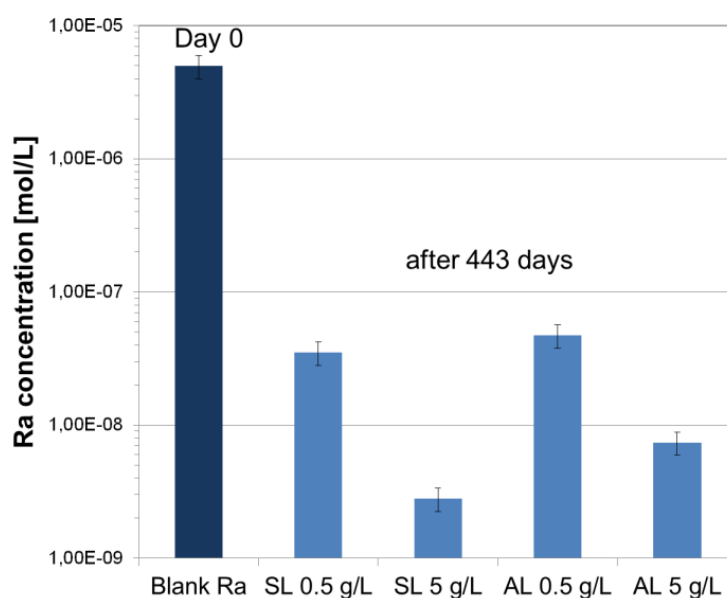
Fig. 1 Final Ra concentrations after 443 days.

TOF-SIMS investigations

Due to the grain size, the SL sample was chosen for a detailed TOF-SIMS investigation of the spatial distribution of Ra and the total Ra/Ba ratio. After these adjustments, individual grains could be identified by comparing a SEM image taken before the measurement (Figure 2 a) with the integrated intensity distribution image of Ba (Figure 2 b) and Ra (Figure 2 c) obtained with TOF-SIMS.
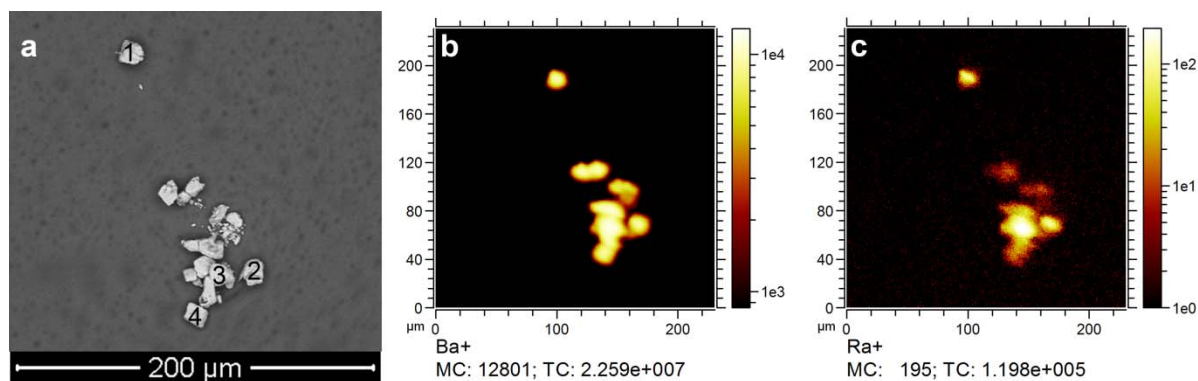
Fig. 2 a) SEM image of SL 0.5 g/L before the TOF-SIMS analysis. Depth profiles of numbered grains (1 - 4) are shown in Figure 3; b) integrated intensity of the Ba signal c) integrated intensity of the Ra signal. MC = Maximum Counts, TC = Total counts.

A comparison of the TOF-SIMS and SEM results shows a good correlation between the areas of high integrated intensities in the TOF-SIMS images and the spatial distribution of the grains in the SEM image. Furthermore, it can be seen in Figure 2 that all grains within this measurement of the recrystallized SL barite contain Ra.

Four grains were identified in the TOF-SIMS and SEM image, grains 1 - 4 in Figure 2 a). For these grains, depth profiles were created using the IONTOF software (Figure 3). The profiles indicate a complete recrystallization of barite to a $Ba_{1-x}Ra_xSO_4$ solid solution on the scale of the TOF-SIMS instrument. All SL grains which were analyzed indicate measurable concentrations of Ra not only on the surface but also within the grains. The total Ra concentration within the grains varies as can be seen by the total counts depicted in Figure 3.
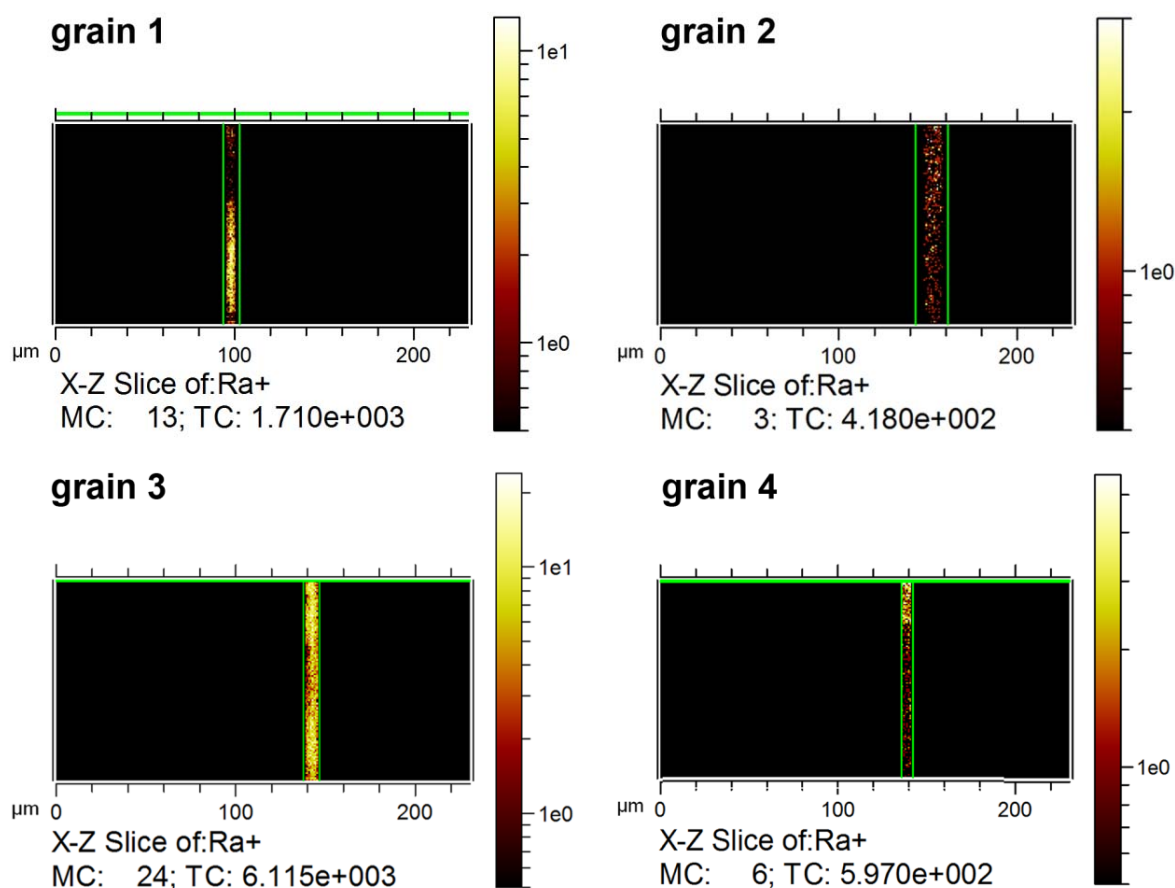
Fig. 3 Depth profiles of the integrated Ra signal (MC = Maximum Counts, TC = Total counts) obtained from the grains depicted in Figure 2.

The Ba/Ra ratio was calculated from several TOF-SIMS measurements, using the integrated elemental signals (Figure 4). Mass balance calculations for the Sachtleben barite suggest a mole fraction ($X_{RaSO4}(s) = (RaSO_4)/(RaSO_4 + BaSO_4)$) of $X_{RaSO4}(s) = 2.3 \times 10^{-3}$, assuming full recrystallization at the end of the experiment. The Ra/Ba intensity distribution of Figure 4 has its maximum between 2 and 4×10^{-3}, corresponding well with the macroscopic results.
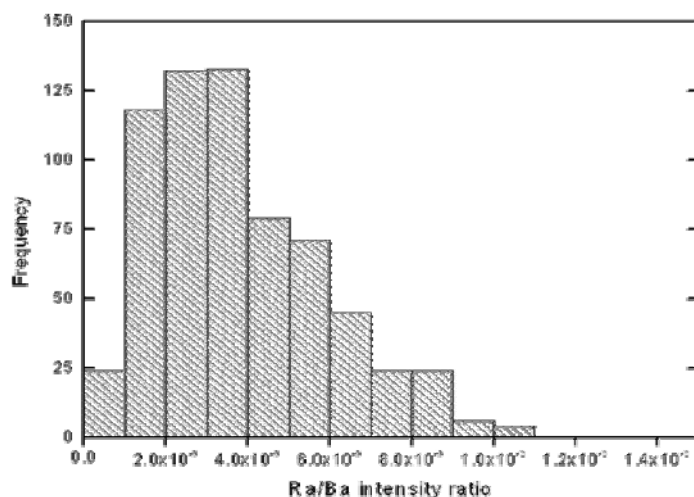
Fig. 4 Evaluation of Ra/Ba intensities as calculated from the TOF-SIMS measurements. The calculated Ra/Ba ratio based on mass balance is 2.3 × 10⁻³.

Evolution of the particle size distribution due to recrystallization in the presence of Ra

Particle size distributions (PSD) were determined to quantify the observations by SEM with more extended statistical information about the ensemble of barite particles. The initial AL type barite is characterized by a wide PSD, covering more than one order of magnitude in the mass based representation (Figure 5, Table 1). A slight shift of the PSD towards higher grain sizes was observed on the AL reference sample which was aged for 443 days. This is more clearly detected in the frequency based PSD. Mainly, the very small grains in the fraction < 500 nm were shifted to the fraction 500 – 1000 nm (Figure 5, left). In the presence of Ra, not only new large grains appeared but also a significant coarsening of the small grains can be deduced from the PSD shown in Figure 5. The most significant effect is visible in the mass based PSD of the 0.5 g/L AL sample where the fraction < 500 nm has almost completely vanished (Figure 5, right).

The original SL barite sample is characterized by a narrow grain size distribution with grain sizes between ~ 6 and 45 µm (Table 1; Figure 6, left). No measurable changes in the PSD could be detected without Ra due to aging. Even in the presence of Ra, the narrow grain size distribution remains mainly unchanged with insignificant differences between minimum and maximum values of the PSD (Figure 6, right; Table 1). Therefore, it can be concluded that a wide PSD is the precondition for a significant PSD coarsening effect. The main coarsening mechanism for the SL barite is the formation of aggregates which might eventually grow together to from large grains. Such effects were also observed by ***Jia & Goa (2008)***, who investigated the growth of well-defined cubic hematite single crystals due to the oriented aggregation of particles and Ostwald ripening (***Ostwald 1896***). Here, particles formed agglomerates which eventually made up single crystals.

Table 1: Overview of grain sizes at the beginning and end of the experiments of SL and AL barite.

	Minimum	Maximum	Mean value	
			Frequency based	Equ. mass based
	[μm]	[μm]	[μm]	[μm]
AL Reference at the beginning	0.19	2.20	0.50	0.69
AL Reference 5 g/L after 443 days	0.19	2.97	0.58	0.82
AL 5 g/L after 443 days	0.28	3.58	0.80	1.15
AL 0.5 g/L after 443 days	0.25	3.59	0.86	1.26
	360 grains per sample analyzed			
	[μm]	[μm]	[μm]	[μm]
SL Reference at the beginning	5.62	44.65	15.00	18.62
SL 5 g/L after 443 days	5.46	38.13	15.28	18.79
SL 0.5 g/L after 443 days	5.91	44.64	14.99	18.33
	150 grains per sample analyzed			
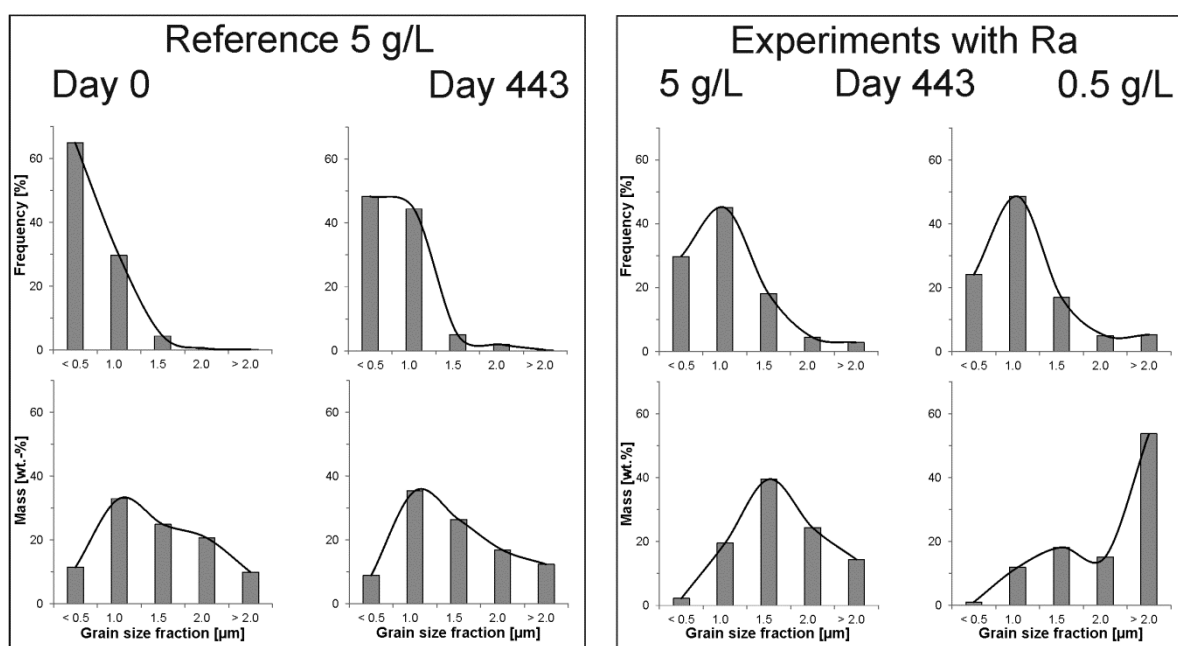
Fig. 5 PSD based on frequency (upper histograms) and equivalent mass (lower histograms) of AL barite. Left: Experiments without Ra (Reference); right: Experiments with Ra.
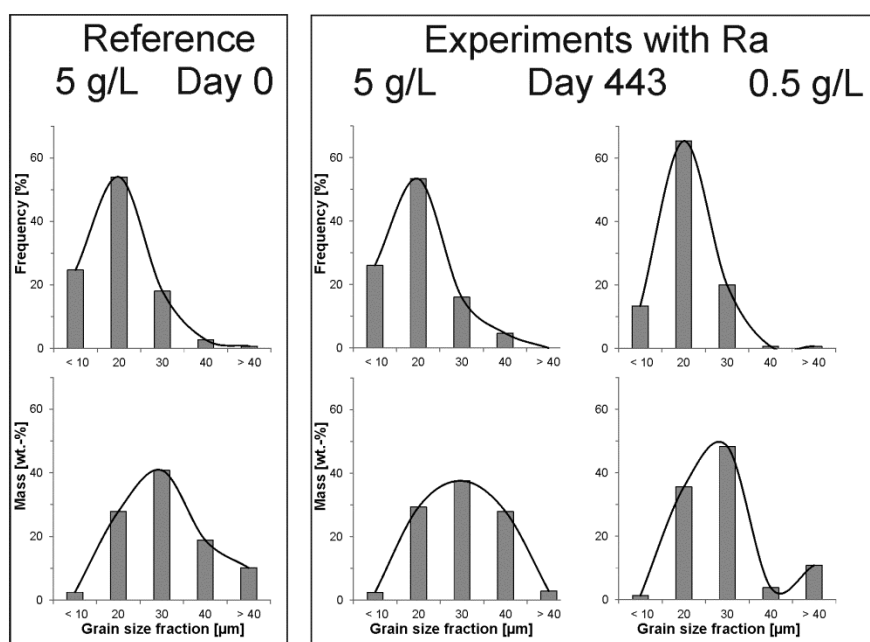
Fig. 6 Comparison of the PSD of SL reference sample without Ra at the beginning of the experiment with the end point of the Ra uptake experiments with 5 g/L and 0.5 g/L barite after 443 days.

Conclusions

ToF-SIMS results clearly show that all barite particles analyzed within this study contain Ra not only on their surfaces but within the grains. For most grains, a homogenous distribution of Ra could be determined. Therefore, a complete recrystallization of barite into a $Ba_{1-x}Ra_xSO_4$ solid solution can be proposed. From the intensities of Ra and Ba obtained during the ToF-SIMS, Ra/Ba intensity ratio distributions were computed. The maximum of the histogram is identical with the expected Ra/Ba ratio calculated from mass balance under the assumption of complete recrystallization.

In summary, two different effects of the presence of Ra can be observed, depending on the original PSD. The wide PSD of AL barite is significantly altered during the recrystallization of barite in the presence of Ra compared to a Ra free reference. On the other hand, the particle size of the SL sample with a narrow PSD remains more or less constant. Here, eventually a coarsening due to the presence of Ra is expected due to the formation of new grains from intergrown agglomerates.

Acknowledgement

References

Bosbach, D.; Böttle, M. & Metz, V. Experimental study on Ra^{2+} uptake by barite ($BaSO_4$), SKB Technical Report TR-10-43 Waste Management, Svensk Kärnbränslehantering AB, 2010

Curti, E.; Fujiwara, K.; Iijima, K.; Tits, J.; Cuesta, C.; Kitamura, A.; Glaus, M. & Müller, W. Radium uptake during barite recrystallization at 23±2°C as a function of solution composition: An experimental 133Ba and 226Ra tracer study Geochimica et Cosmochimica Acta, 2010, 74, 3553-3570

Doerner, H. A. & Hoskins, W. M. Co-precipitation of radium and barium sulfates Journal of the American Chemical Society, 1925, 47, 662-675

Jia, B.; Gao, L., Growth of Well-Defined Cubic Hematite Single Crystals: Oriented Aggregation and Ostwald Ripening. Crystal Growth & Design 2008, 8 (4), 1372-1376.

Ostwald, W. (1896): Lehrbuch der Allgemeinen Chemie, Vol. 2, part 1, Leipzig, Germany

SEQUESTRATION OF EU(III), SE(IV,VI), AND NP(V) BY CALCITE

Frank Heberling*, Sascha Hofmann

Institute for nuclear waste disposal, Karlsruhe Institute of Technology, Germany

* Corresponding author: Frank.Heberling@kit.edu

Introduction

Calcite is the most common polymorph of calcium carbonate and the thermodynamically most stable at standard conditions (room temperature and atmospheric pressure). It is abundant in many environmental settings and plays a key role in controlling the geochemical milieu (pH, alkalinity) of soils and ground water. In the surroundings of potential nuclear waste disposal sites calcite is e.g. present as a mineral constituent in clay formations (up to 20 % in some cases), as fracture filling material in granitic rocks, or as a corrosion product of concrete based materials in the technical barrier. Due to the high reactivity of its surface and its tendency to tolerate considerable variation in its chemical composition, calcite has often been considered as a mineral phase with a high potential for the sequestration of toxic metals.

Selenium and Neptunium are of direct concern for save nuclear waste disposal due to the long half-life of the isotopes [79]Se and [237]Np and the expected high mobility of the corresponding oxidized species. [79]Se is present in nuclear waste as a fission and decay product and [237]Np is a minor actinide, which is produced in nuclear reactors by neutron activation of [235]U or by alpha decay of [241]Am. Europium itself has only little relevance as a fission and decay product. It is studied as a chemical homologue for trivalent minor actinides Pu(III), Am(III), and Cm(III), which dominate the radiotoxicity of nuclear waste on long time scales.

In this report we will focus on new experimental results on Eu(III). Concerning Se(VI), we recently showed that it does neither interact significantly with the calcite surface, nor does it coprecipitate with calcite in significant amounts at surface controlled crystal growth conditions (Heberling et al. (submitted)-a). Only starting from highly supersaturated solutions, Se(VI) coprecipitation with calcite has been reported (***Staudt et al. 1994***). About Se(IV) we reported in the previous annual workshop proceedings (***JUEL-4364, 2013***), and recently submitted a manuscript on an adsorption / entrapment model (***Heberling et al. (submitted)-b***). This model is based on the observations that Se(IV) adsorbs in small but significant amounts at the calcite surface and that this adsorption is equivalent to the formation of a surface monolayer solid solution with a partition coefficient of $D = (0.016 \pm 0.012)$. At elevated supersaturation this surface solid solution can be entrapped by growing calcite, keeping its

composition. However, the precipitated solid solution reflects non-equilibrium conditions. Equilibrium incorporation of Se(IV) into calcite is virtually impossible, $D \approx 10^{-9}$.

Concerning Np(V), we previously showed that upon coprecipitation Np(V) is structurally incorporated into calcite (**Heberling et al. 2008b**), Np(V) adsorbs quite strongly at the calcite surface (**Heberling et al. 2008a**), and the presence of surface adsorbed Np(V) has significant impact on the calcite growth rate (**Heberling et al. 2011**). After the very promising results of aragonite to calcite recrystallization experiments in the presence of Se(IV) (**Heberling et al. (submitted)-b**) and Eu(III) (this work) we launched similar experiments in the presence of Np(V). Experiments aim at Np(V) coprecipitation with calcite at very low supersaturation (SI(calcite) = 0.14) as a function of ionic strength and comparing two different background electrolytes (NaCl and KCl) and correspondingly different cations, which may provide charge compensation upon structural incorporation. However as calcite growth at these experimental conditions is extremely slow, the experiments are still ongoing and conclusive results cannot yet be reported.

Back to Eu(III), we report here aragonite to calcite recrystallization experiments in the presence of 1 µmol/L Eu(III) at two solid to liquid ratios, 20 g/L and 0.2 g/L, and a laser fluorescence spectroscopic investigation of the corresponding reaction products. The results allow us to identify the most relevant substitution mechanism for Eu(III) in calcite and to narrow down the Gibbs free energy of a possible virtual $NaEu(CO_3)_2$ endmember of the dilute $NaEu(CO_3)_2$-calcite solid solution. Interestingly, incorporation species observed in this study agree only partly with those observed before upon Eu coprecipitation with calcite at higher supersaturation (**Marques Fernandes et al. 2008**, **Schmidt et al. 2008**, **Schmidt et al. 2010**), highlighting the importance of experiments at close-to-equilibrium conditions.

Experimental Details

In this study calcite precipitation is induced by aragonite dissolution/recrystallization. This reaction is based on the principle that aragonite is more soluble than calcite at standard conditions, with the solubility products (K_{SP}) being $log10(K_{SP}(aragonite)) = -8.34$ and $log10(K_{SP}(calcite)) = -8.48$, respectively. Therefore, an aragonite equilibrated solution is at standard conditions always supersaturated with respect to calcite with SI(calcite) = 0.14. This gives us the possibility to perform very simple batch type calcite growth experiments at very stable low supersaturation conditions, which are hardly achievable in classical precipitation experiments.

The aragonite we use is synthesized by mixing 0.5 molar Na_2CO_3 solution and 0.5 molar $CaCl_2$ solution at 90 °C. After two to three minutes the precipitated powder is separated from solution by filtration and dried in an oven at 105 °C. The resulting aragonite contains traces of calcite (~ 0.3%) and halite (< 1%). The BET surface area of the aragonite powder is 4 m^2/g.

In a kinetic experiment 1 g of aragonite is brought in contact with 50 mL of 0.1 molar NaCl solution containing 1 μmol/L Eu^{3+} (S/L = 20 g/L), and in a second series of "equilibrium" experiments 0.2 g of aragonite are exposed to 1000 mL of 0.1 molar NaCl solution containing 1 μmol/L Eu^{3+} (S/L = 0.2 g/L). The kinetic experiment is planned as a multisampling experiment, with the aim to monitor the reaction progress, while the "equilibrium" experiments at low S/L ratio are planned as single point measurements, originally aiming at the determination of a Eu-calcite partition coefficient. The kinetic experiment is sampled after: 1, 4, 11, 48, 97, 193, and 420 days. With each sampling the suspension is thoroughly agitated and 5 mL of homogeneous suspension are pipetted directly onto a filter membrane. The separated powder is dried in an oven at 105 °C , and analysed by powder XRD on a Bruker D8 advance powder diffractometer. For the quantitative analysis of the aragonite and calcite content of the powder we use the Topas 4.2 Rietveld refinement software from Bruker AXS. By comparison to a parallel kinetic experiment without Eu^{3+} (**Heberling et al. (submitted)-b**) we can learn about the influence of Eu^{3+} on the recrystallization kinetics.

The "equilibrium" experiments are sampled after 580 days. The dried powders are analysed by powder XRD as described above and the solutions are analysed for Ca^{2+} and Eu^{3+} by ICP-MS.

Samples of the kinetic experiments after one day and after 400 days and one sample of the "equilibrium" experiment are investigated by site selective time resolved laser fluorescence spectroscopy (TRLFS). We perform TRLFS measurements on a Nd-YAG laser pumped optical parametric oscillator (OPO) laser system. The wavelength of the laser light is tuned with a resolution of 0.01 nm. The sample is cooled to 20 K during the measurements. First we record an excitation spectrum by scanning the excitation wavelength from 575 nm to 582 nm and recording the total fluorescence yield. In this excitation spectrum each Eu-species with a distinct chemical environment produces an individual peak at a certain wavelength, which corresponds to the energy level of the species' $^{7}F_0$-$^{5}D_0$ transition. In a second set of measurements we directly excite the $^{7}F_0$-$^{5}D_0$ transitions of the species and record the corresponding fluorescence emission spectra. The ground state splitting of the fluorescence emission allows us to draw conclusions about the symmetry of the coordination environment around a certain species (cf. e.g. (**Schmidt et al. 2008**)) or can be used like a fingerprint to identify similar species in different samples.

Results and Discussion

The results of the powder diffraction analyses concerning the calcite content of the samples taken during the kinetic experiment are summarized in Figure 1. Figure 1 clearly shows that in the kinetic experiment at high S/L ratio the recrystallization rates in absence and presence of Eu^{3+} are very similar, i.e. Eu^{3+} has no significant influence on the recrystallization rate. A decreased reaction rate at the beginning and the end of the experiment is observable. If we assume that the period between 97 and 193 days represents a steady state regime, we can

approximate the reaction rate, R, during this period to be $R = 2 \times 10^{-10}$ mol/(m^2 s), which is indeed very slow compared to other calcite precipitation experiments (**Curti 1999**). This value is only a rough approximate because we do not know exactly, which is the relevant reactive surface area, that should be considered. As a first approximation we use the surface area of the original aragonite in this calculation.
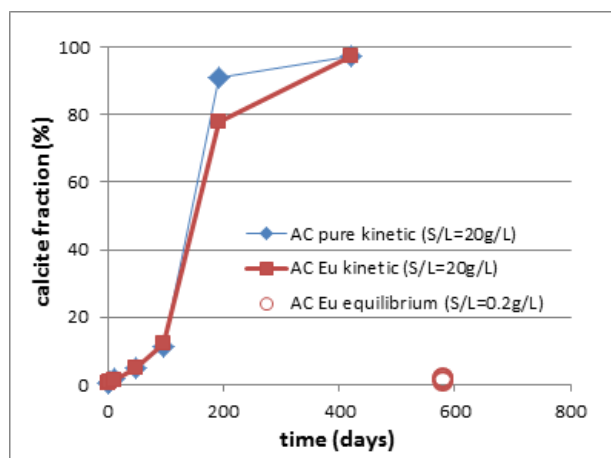
Fig. 1 Calcite content of the samples from kinetic (AC Eu kinetic) and "equilibrium" experiments (AC Eu equilibrium) as obtained from the analysis of powder diffraction data. The kinetic experiment in the presence of Eu^{3+} is compared to data obtained in Eu^{3+}-free experiments (AC pure kinetic) (Heberling et al. (submitted)-b).

The TRLFS spectra of the almost pure Eu doped calcite (97.5 %) after 400 days of the kinetic experiment reveals that the Eu-speciation in this sample is dominated by one species, which is excited at 579.55 nm. Two minor species are excited at 579.65 nm and 579.75 nm, respectively (Figure 2a).
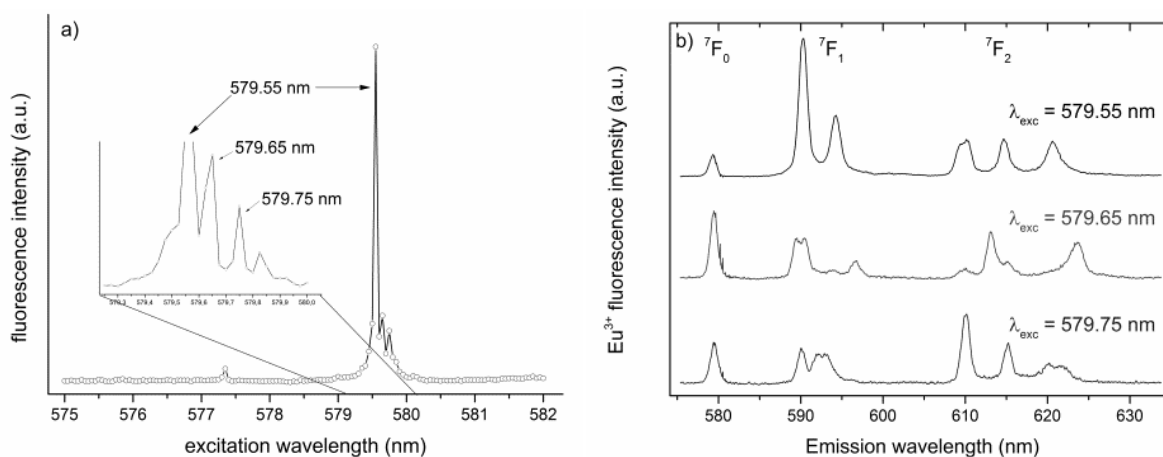
Fig. 2 TRLFS excitation (a) and emission (b) spectra of Eu-doped calcite after 400 days of recrystallization.

Small peaks at 577.80 nm and 579.85 nm are likely not indicative for a particular Eu-species, as no distinct emission spectra were detectable upon excitation into these bands. Emission spectra of the three confirmed Eu-species are shown in Figure 2b. The species at 579.55 nm can be clearly identified as the well-ordered incorporation species reported earlier (**Marques Fernandes et al. 2008**, **Schmidt et al. 2008**). A direct comparison between the emission spectrum recorded in this study and that of the earlier studies is shown in Figure 3. Marques Fernandes et al. and Schmidt et al. showed that there is clear evidence that this species is related to Eu^{3+} incorporated into the calcite structure according to a coupled substitution mechanism, in which two Ca^{2+} are substituted by one Eu^{3+} and one Na^{+}.

Interestingly, in earlier studies, in which calcite was precipitated at higher supersaturation compared to this work, this incorporation species was always accompanied by two further species at 578.1 nm and 578.4 nm, which were interpreted as a surface species and a low symmetry incorporation species (**Marques Fernandes et al. 2008**, **Schmidt et al. 2008**). These species are absent in our present study. The two minor species we observed at wavelengths higher than 579.55 nm have not been reported before.
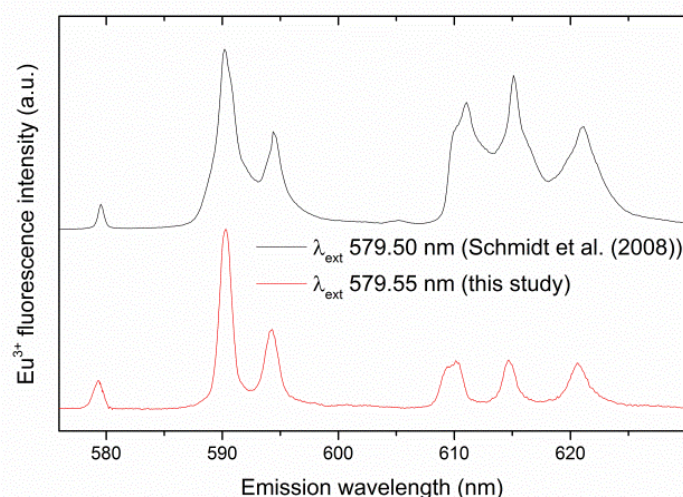
Fig. 3 Comparison of emission spectra of the main species identified in Eu-doped calcite in this study and the well-ordered incorporation species reported earlier (Schmidt et al. 2008).

Due to technical problems we could not perform fluorescence lifetime measurements and prove structural incorporation of the Eu-species during this study, but due to the similarity of the emission spectra (Figure 3) we interpret our main species in analogy to Marques Fernandes et al. (2008) as $NaEu(CO_3)_2$ in calcite. The two minor species at 579.65 nm and 579.75 nm are, due to the strong red shift and the fluorescence emission spectra, likely less ordered incorporation species. The fact that the main species in our experiment can be attributed to a $NaEu(CO_3)_2$ -calcite solid solution, provides us with important information for further quantitative modelling of the incorporation process.

A first surprising result is observed in TRLFS spectra measured on aragonite contacted with Eu^{3+} containing solution for one day during the kinetic experiment (Figure 4). Only one Eu-species can be identified. This species coincides perfectly with a structural incorporation species of Eu^{3+} in aragonite reported earlier (**Schmidt et al. 2009**). The broad shoulder from 578.0 to 579.2 nm is possibly caused by minor Eu^{3+} species, which could not be further resolved and characterized.
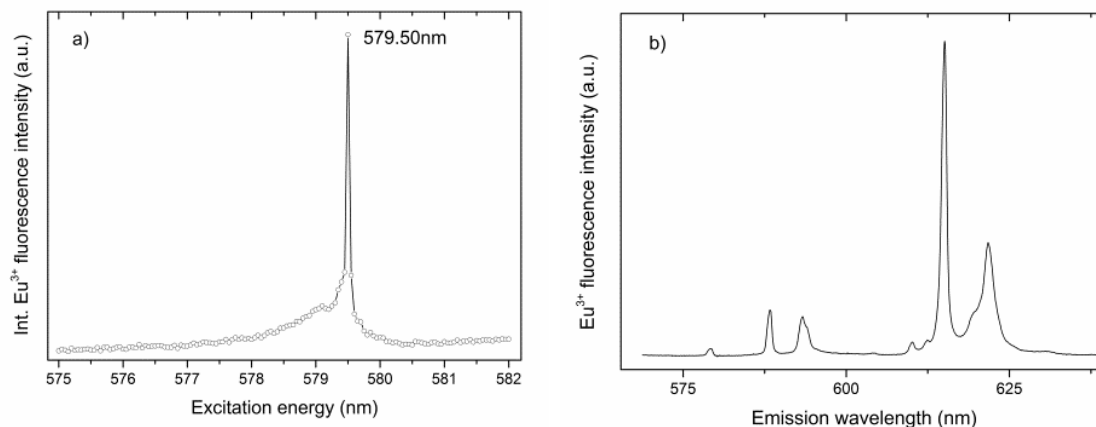
Fig. 4 Excitation and emission spectrum of Eu^{3+} in aragonite.

Accordingly, aragonite does not only dissolve to form calcite, but undergoes as well a surface recrystallization, which leads to Eu^{3+} incorporation into aragonite within 24 h.

The biggest surprise, however, is certainly that in the "equilibrium" experiments at low S/L ratio we observe virtually no formation of calcite. The calcite content of three independent samples increased during the reaction period only from initially 0.3 % to 1.0 % to 1.9 % after 580 days. The TRLFS spectrum of the aragonite after 580 days in the "equilibrium" experiment (not shown here) is quasi identical to the one observed in the kinetic experiment after one day (Figure 4).

ICP-MS measurements revealed that 99.4 % of the Eu^{3+} sorbs at aragonite. As mentioned above, TRLFS identified an incorporation species for Eu^{3+} sorbed at aragonite. If correspondingly we interpret the sorption as a solid solution formation process and assume that, as in calcite, coupled substitution of sodium provides charge balance, the partition coefficient of $NaEu(CO_3)_2$ in aragonite would be D(aragonite) = 1350. If we interpret the sorption as a surface recrystallization reaction and quantify the result in terms of an adsorption K_D, the corresponding value would be K_D = 200 L/m^2, and the observed surface coverage would correspond to about 10% of a monolayer.

The fact that Eu^{3+} sorbs at aragonite offers us the possibility of a tentative explanation, why we observe aragonite dissolution and consecutive formation of calcite only at high solid to liquid ratio. According to spectroscopy results Eu^{3+} incorporation into calcite may be described as a solid solution between $NaEu(CO_3)_2$ and $Ca_2(CO_3)_2$. A phase similar to the

Eu-endmember $NaEu(CO_3)_2 \cdot 6\, H_2O$ has a solubility product of $log10(K_{SP}(NaEu(CO_3)_2 \cdot 6\, H_2O)) = -20.5$ (**Curti et al. 2005**, **Fannin et al. 2002**). Analogously to the approach we applied previously (**Heberling et al. (submitted)-b**) we assume that the dilute solid solution obeys Henry's law and we can describe the Eu^{3+} incorporation into calcite as a virtual pseudo-ideal solid solution between a virtual $NaEu(CO_3)_2$ endmember and $Ca_2(CO_3)_2$. The solubility product of the virtual endmember is defined such that the virtual solid solution is ideal by definition and describes the real behaviour of a $Na_XEu_X,Ca_{(2-2X)}(CO_3)_2$ solid solution in a limited range of $NaEu(CO_3)_2$ content in calcite.

Model calculations show that, if we consider thermodynamics of whole system involved, i.e. the total amount of solid and liquid, the calcite solid-solution is in any case more stable than aragonite, no matter how we choose the solubility of the virtual $NaEu(CO_3)_2$ endmember. Therefore, we may rule out any simple thermodynamic explanation. On the other hand, the kinetic experiment indicates that Eu^{3+} incorporation has no significant impact on the calcite growth or aragonite dissolution rate. This makes a kinetic inhibition effect as an explanation unlikely as well. However, if we assume that in order to grow calcite we need an initial small amount of Na, Eu-calcite solid solution, e.g. a growth nucleus, which is in partial equilibrium with the aqueous solution, it is possible to show that such initial small nuclei become unstable relative to aragonite at low solid to liquid ratio, if $log10(K_{SP}(NaEu(CO_3)_2:virtual)) \leq -21.3$. According to such a scenario the system of a 0.2 g/L aragonite in suspension and 4.8×10^{-9} mol/L Eu^{3+} in solution (after adsorption of 99.4% of the Eu^{3+} at the aragonite surface) remains in a metastable state and calcite cannot form, because any initial calcite nuclei must contain a high amount of Eu^{3+} and this destabilizes them relative to aragonite. This relation is illustrated in Figure 5.

In a similar scenario at higher solid to liquid ratio the Eu^{3+} concentration in solution is much lower because more Eu^{3+} is adsorbed at the aragonite surfaces. A corresponding calculation as depicted in Figure 5 is not shown for this scenario, but the resulting curves look identical only that the whole diagram is shifted to lower solubility products and the change to stable nuclei appears already at smaller nucleus sizes. Correspondingly, a metastable suspension is much less likely. For a precise calculation, the amount of Eu^{3+} sorption at 20 g/L aragonite needs to be known. Depending on the Eu^{3+} sorption mechanism, formation of an aragonite solid solution or adsorption, the estimated Eu^{3+} concentration in solution varies between 10^{-11} mol/L and 10^{-9} mol/L and this uncertainty has a high impact on any model calculation. Nevertheless, due to sorption of Eu^{3+} at aragonite, the Eu^{3+} concentration in solution is always lower at the higher S/L ratio than at lower S/L ratio, and this likely explains the difference between the kinetic and the "equilibrium" experiments (which never reached equilibrium).
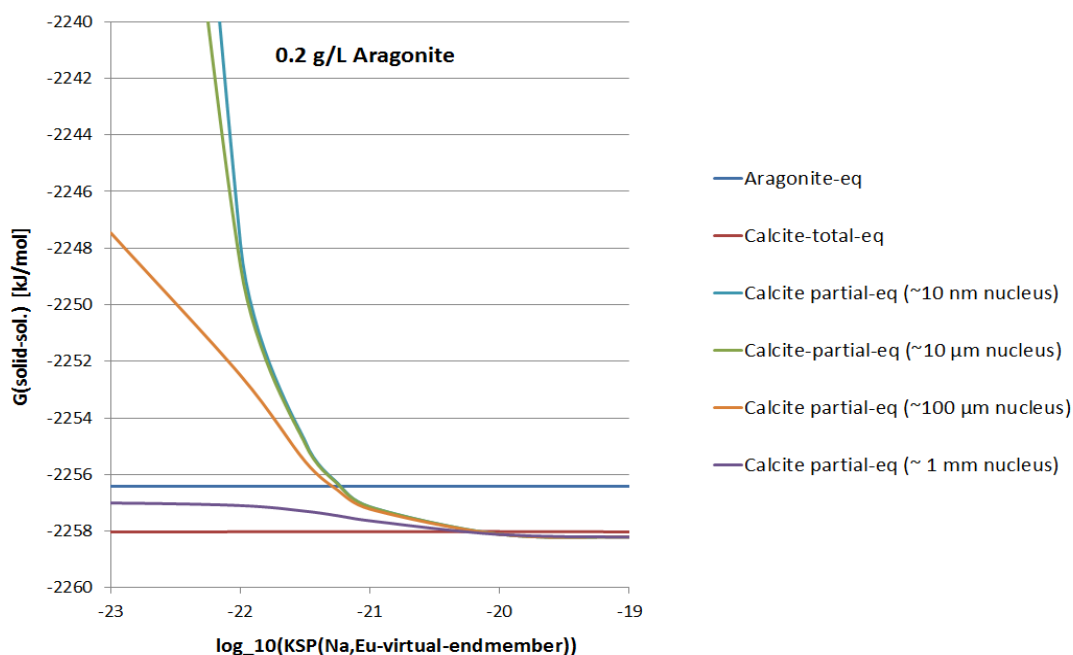
Fig. 5 Gibbs free energy of single Na,Eu-calcite solid solution particles in partial equilibrium with aqueous solution as a function of the solubility product of the virtual NaEu(CO$_3$)$_2$ endmember. Shown are a series of nuclei of various sizes and total calcite and aragonite equilibria for comparison. For $log_{10}(K_{SP}(NaEu(CO_3)_2$:virtual$)) \leq -21.3$ small solid solution nuclei are unstable relative to aragonite. Recrystallization could in such a scenario only occur if large amounts of calcite, corresponding to a ~1 mm nucleus, would form instantaneously. This is extremely unlikely. On the other hand, for $log_{10}(K_{SP}(NaEu(CO_3)_2$:virtual$)) \geq -21.2$ a corresponding metastable situation cannot be achieved at all.

Conclusions and Future work

Experiments confirm the very high affinity of Eu^{3+} towards incorporation into CaCO$_3$ minerals aragonite and calcite.

Sorption at aragonite proceeds, depending which mechanism is assumed, with an adsorption $K_D = 200$ L/m^2 or a solid solution partition coefficient, D = 1350.

On Eu-reacted aragonite only incorporation species are detected by TRLFS.

At high solid to liquid ratio, Eu^{3+} incorporation into calcite has no significant impact on the calcite growth / aragonite dissolution rate.

TRLFS indicates that coupled substitution corresponding to the formation of a Na$_x$Eu$_x$Ca$_{(2-2x)}$(CO$_3$)$_2$ solid solution between a virtual NaEu(CO$_3$)$_2$ and the Ca$_2$(CO$_3$)$_2$ (calcite) endmember, is the most relevant incorporation mechanism for Eu^{3+} in calcite involved in experiments in this study. Comparison to previous studies shows that this is not generally the case. In previous studies (***Curti et al. 2005, Marques Fernandes et al. 2008, Schmidt et al.***

2008) other mechanisms were identified to be most likely, or the Na,Eu incorporation species was accompanied by significant amounts of other species.

At low solid to liquid ratio a meta-stable situation can be achieved and calcite formation is inhibited. This phenomenon may only be explained for a solubility of the virtual $NaEu(CO_3)_2$ endmember of $\log_{10}(K_{SP}(NaEu(CO_3)_2:virtual)) \leq -21.3$.

In a next step we will investigate Eu^{3+} species in calcite and aragonite by EXAFS spectroscopy. Future experiments will aim at the substitution mechanism of Eu^{3+} in aragonite and will test the meta-stability of aragonite suspension at low S/L ratio in the presence of Eu^{3+}.

Acknowledgement

References

Curti, E., 1999. Coprecipitation of radionuclides with calcite: estimation of partition coefficients based on a review of laboratory investigations and geochemical data. Appl Geochem 14, 433-445.

Curti, E., Kulik, D.A., Tits, J., 2005. Solid solutions of trace Eu(III) in calcite: Thermodynamic evaluation of experimental data over a wide range of pH and pCO(2). Geochimica et Cosmochimica Acta 69, 1721-1737.

Fannin, C., Edwards, R., Pearce, J., Kelly, E., 2002. A study on the effects of drying conditions on the stability of $NaNd(CO_3)_2 \cdot 6H_2O$ and $NaEu(CO_3)_2 \cdot 6H_2O$. Appl Geochem 17, 1305-1312.

Heberling, F., Bosbach, D., Eckhardt, J.-D., Fischer, U., Glowacky, J., Haist, M., Kramar, U., Loos, S., Müller, H.S., Neumann, T., Pust, C., Schäfer, T., Stelling, J., Ukrainczyk, M., Vinograd, V., Vučak, M., Winkler, B., (submitted)-a. Reactivity of the calcite-water-interface, from molecular scale processes to industrial applications. Appl Geochem.

Heberling, F., Brendebach, B., Bosbach, D., 2008a. Neptunium(V) adsorption to calcite. J Contam Hydrol 102, 246-252.

Heberling, F., Denecke, M.A., Bosbach, D., 2008b. Neptunium(V) Coprecipitation with Calcite. Environ. Sci. Technol. 42, 471-476.

Heberling, F., Scheinost, A.C., Bosbach, D., 2011. Formation of a ternary neptunyl(V) biscarbonato inner-sphere sorption complex inhibits calcite growth rate. J Contam Hydrol 124, 50-56.

Heberling, F., Vinograd, V.L., Gale, J.D., Heck, S., Rothe, J., Winkler, B., Bosbach, D., Geckeis, H., (submitted)-b. A thermodynamic adsorption/entrapment model for selenium(IV) coprecipitation with calcite. Geochimica et Cosmochimica Acta.

JUEL-4364, 2013. 2nd Annual Workshop Proceedings, 7th EC FP - SKIN, 21th - 22th November 2012 Villigen PSI - Switzerland. Berichte des Forschungszentrums Jülich.

Marques Fernandes, M., Schmidt, M., Stumpf, T., Walter, C., Bosbach, D., Klenze, R., Fanghänel, T., 2008. Site selective time resolved laser fluorescence spectroscopy of Eu3+ in calcite. Journal of Colloid and Interface Science 321, 323-331.

Schmidt, M., Stumpf, T., Fernandes, M.M., Walther, C., Tanghanel, T., 2008. Charge compensation in solid solutions. Angew Chem Int Edit 47, 5846-5850.

Schmidt, M., Stumpf, T., Walther, C., Geckeis, H., Fanghanel, T., 2009. Incorporation versus adsorption: substitution of Ca^{2+} by Eu^{3+} and Cm^{3+} in aragonite and gypsum. Dalton T, 6645-6650.

Schmidt, M., Stumpf, T., Walther, C., Geckeis, H., Fanghanel, T., 2010. Phase transformation in $CaCO_3$ polymorphs: A spectroscopic, microscopic and diffraction study. Journal of Colloid and Interface Science 351, 50-56.

Staudt, W.J., Reeder, R.J., Schoonen, M.A.A., 1994. Surface structural Controls on Compositional Zoning of SO_4^{2-} and SeO_4^{2-} in synthetic Calcite Single-Crystals. Geochimica et Cosmochimica Acta 58, 2087-2098.

DETERMINATION OF DISSOLUTION AND PRECIPITATION RATES OF CLAYEY MATERIALS BY ^{29}SI/^{28}SI ISOTOPIC EXCHANGE. EFFECT OF TEMPERATURE

Tomo Suzuki-Muresan[*], Karine David, Solange Ribet, Katy Perrigaud, Bernd Grambow

SUBATECH, Unité Mixte de Recherche 6457, Ecole des Mines de Nantes, CNRS/IN2P3, Université de Nantes (FR)

* Corresponding author: tomo.suzuki@subatech.in2p3.fr

Abstract

Surface study on illite, illite/smectite and Callovo-Oxfordian argillite clay mineral phases are performed in conditions close to equilibrium for three temperatures (35, 50 and 90 °C) in 0.01 mol/L NaCl solution. Prior the experiments, clays were purified by elutriation to remove a large part of quartz phase. Characterization of the solids was done by SEM, XRD and XPS. Concentrations of Si, Fe and Al were measured in solution by Q-ICP-MS. Maximum concentration of Si values were determined for each solids in contact with the solution and a pseudo-equilibrium is reached after 50 days of contact time. These values ($\sim 10^{-5}$ – $\sim 10^{-4}$ mol/L) under the solubility of quartz values correspond to the solubility values of the clays. Concentration of Fe is 2.5×10^{-6} mol/L and Al is 3×10^{-6} mol/L in solution. After 326 to 483 days of alteration, ^{29}Si spike was added in each system studied. The results obtained for the illite/smectite system indicate that in condition close to equilibrium a dynamic exchange of ^{29}Si and ^{28}Si occurs at the interface solid/solution. The isotopic exchange was performed during 100 days with a dissolution rate of $\sim 7 \times 10^{-15}$ mol Si/m²/s and a precipitation rate of $\sim 4 \times 10^{-15}$ mol Si/m²/s. The XPS and XRD analyses indicate no modification for both initial and altered illite/smectite after 538 days of alteration. XRD analyses for illite and Callovo-Oxfordian argillite showed no structural modifications after 640 days of experiments.

Introduction

According to the French laws for the management of nuclear wastes, high level nuclear glass wastes are planned to be stored in deep geological formation. At 490 m in depth, the Callovo-Oxfordian formation displays interesting properties in terms of high retention coefficients of radionuclides, low permeability of water, large specific surface area, reactivity and

pronounced sorption capacity (***ANDRA 2005, Bergaya et al. 2006***). This geological formation is mainly characterized by the presence of illite, interstratified illite/smectite 40-45%, carbonates 30-40%, tectosilicates 20-30% and pyrite 1-2% (***Gaucher et al. 2004***). Prior the determination and the acceptance by the public of the final site for the geological disposal CIGEO directed by ANDRA, an underground research laboratory has been built in Meuse/Haute-Marne in the Callovo-Oxfordian formation (northeastern, France) to evaluate the feasibility of disposal of radioactive wastes in a deep clay rock formation. After having filled the galleries by the nuclear waste (high level long lived and intermediate level long lived), the disposal locations will be sealed from access tunnels by bentonite plugs. The Callovo-Oxfordian argillite host rock and the bentonite will both become saturated with the groundwater. The increase of temperature caused by the heat-emitting high level waste emplacement may also change the chemical and physical properties of the clay barrier and in particular its dissolution kinetics.

In literature, a number of studies are performed on dissolution of clays minerals focusing on the temperature dependence and pH effects (eg. ***Bauer and Berger 1998, Ganor et al. 1995, Huertas et al. 2001, Köhler et al. 2003, Palandri and Kharaka 2004, Rozalén et al. 2009***). The overall results showed a typical dissolution rates profile with an increasing of rates values in the acid and alkaline pH-range, and a minimum in near neutral pH. However, rare are the studies on understanding of clays surfaces in conditions close to equilibrium. A recent study, with illite and montmorillonite, showed that a dynamic equilibrium is established between the claystone and the porewater and is described as a dissolution/precipitation mechanism (***Suzuki-Muresan et al. 2011***). Current models consider that the frayed edge sites are stable but these recent results with illite coupled to Si/^{32}Si isotopic exchange studies indicate that an ongoing dissolution/precipitation mechanism at solubility equilibrium may be related to a permanent dissolution/reconstruction on frayed edge sites.

Related to the context of nuclear waste disposal in deep geological formation, the high level nuclear waste vitrified by PUREX method will be stored in tunnels and sealed by swelling clays materials as bentonite plugs for the French programme. Considering the resaturation period and the equilibrium time with the bentonite and the Callovo-Oxfordian argillite, the concentration of Si in the porewater in equilibrium with the Callovo-Oxfordian argillite (1.8×10^{-4} mol/L, ***Tournassat et al. 2007***) will increase to the maximum concentration of 2×10^{-3} mol/L in presence of bentonite (***Suzuki-Muresan et al. 2011***). This later is four times higher than the solubility of the nuclear glass waste ([Si] 5×10^{-4} mol/L at 90 °C; ***Daux et al. 1997, De Cannière et al. 1998***) and may control the dissolution of the nuclear glass waste. The contribution of tectosilicates impurities in the Callovo-Oxfordian argillite may also contribute to the inventory of silicium in the porewater and may control the solubility of the clay.

The question raised in this study is how the surface of the Callovo-Oxfordian argillite will behave in presence of a source term in silicon stemming from the radioactive nuclear glass waste. For that, two clay minerals (illite and interstratified illite/smectite) considered as

reference minerals are studied and compared to the Callovo-Oxfordian argillite at different temperatures. The work is focused on the close-to-equilibrium conditions in the experiments. The assessment of the surface reactivity is performed by the $^{29}Si/^{28}Si$ isotopic exchange.

Materials and methods

Solid materials

Natural clayey samples were used for this project: (i) illite/smectite ISCz1 provided by Clay Mineral Society (C.M.S.) (0.5 wt% quartz, 1 wt% kaolinite) and (ii) illite IMT2 from C.M.S. (7.5% quartz, 2% microcline); (iii) Callovo-Oxfordian argillite from the Underground Research Laboratory at Bure (40–45% illite, interstratified illite/smectite, 20-30% quartz, 30-40% carbonate, 1-2% pyrite (**ANDRA 2005b, Gaucher et al. 2004**). Samples contain a fraction of quartz phase for which the proportions could be considered as none neglectable for the experiments. The clayey samples were therefore purified by the method of elutriation defined as *"the process of separating the lighter particles of a powder from the heavier ones by means of an upward directed stream of fluid (gas or liquid)"* (**IUPAC 1997**).

Batch experiments

The experiments were performed in batch systems for three temperatures studied 35, 50 and 90 °C. The solution composition is a solution of NaCl 0.01 mol/L with an initial pH of 5.5. The aqueous solution is then filled into PFA Teflon reactors (Savillex, 250 mL) containing 1 g of solid. One reactor contains only one type of solid. This operation is repeated for each temperature at 35, 50 and 90 °C. For each set of temperature, one reactor containing only a solution of NaCl is prepared as blank experiment (free of solids). A total of 12 reactors were prepared (4 reactors × 3 temperatures) with a solid/solution (m/V) ratio of 6.7 g/L. The temperature of the ovens was controlled by a digital system. Before sampling, the reactors were taken out of the ovens and quenched at room temperature and filtered at 0.45 μm (Q-ICP-MS) or ultrafiltrated at 5 kDa (HR-ICP-MS). Solution aliquots were taken, measured for pH (pHC3006 Ag/AgCl, Radiometer), acidified with HNO$_3$ 2% for ICP-MS analyses.

Initial dissolution rates (expressed as Si release rates in mol Si/m²/s) were calculated from the variation of aqueous silicon concentrations far from the equilibrium at very early time in all systems.

$$R_{dissolution} = \frac{[Si]_t - [Si]_0}{\frac{m}{V} \times SA/m \times t}$$

where $[Si]_t$ and $[Si]_0$ (mol/L) stand for the final and initial silicon concentrations in solution, m/V (g/L) for the ratio of the solid mass onto the solution volume, SA/m (m²/g) for the specific surface area and t (s) for the reaction time.

Isotopic exchange experiments

The stable isotope of silicon ^{29}Si was used to study the isotopic exchange between ^{28}Si and ^{29}Si at the interface solid/solution. The tracer supplied by Euriso-top® as solid SiO_2 form with an enrichment of ^{29}Si up to 99.9% was prepared on the base of the procedure of Van den Boorn et al. (2006). The tracer was prepared gravimetrically and dissolved in $NaOH.H_2O$ (99.99% Suprapur) at 200 °C in a PFA pressure vessel. The working tracer solution was obtained after taking up the residue in Milli-Q water and then adding a 10mol/L HCl solution in order to get a final concentration of silicon equal to (459.2 ± 1.2) µg/g (1 sigma) in 0.25 mol/L NaOH and pH 13.4. The stable tracer was added when the conditions close to equilibrium were reached i.e. after 399 days of contact from the beginning of the experiments for Illite, 483 days for Illite/Smectite and 326 days for Callovo-Oxfordian argillite.

From the mixed isotope ratio determined experimentally by HR-ICP-MS, the percent of Si atom exchanged was calculated from the expression below (***Handler et al. 2009***):

$$\text{percent exchanged} = \frac{\delta_t - \delta_i}{\delta_e - \delta_i} \times 100$$

where the δ_t, δ_i and δ_e are the isotopic composition at time t, the initial isotopic composition of the phase and the equilibrium isotope composition, respectively (***Gorsky et al. 2012***). The later δ_e is calculated from the mass balance-weighted isotopic composition of the two-components system silicon in silicate and silicon in spike:

$$\left(\delta^{29/28}Si_{mix}\right)\left[Si_{silicate} + Si_{sp}\right] = \left(\delta^{29/28}Si_{silicate}\right)\left[Si_{silicate}\right] + \left(\delta^{29/28}Si_{sp}\right)\left[Si_{sp}\right]$$

For instance, considering the illite/smectite clay mineral, the concentration of Si in the mineral phase $[Si]_{silicate}$ was calculated on the base of EDS measurement (20 %at.) and the masse molar (M = 385.143 g/mol (***Gailhanou et al. 2007***), the concentration of spike is given by the measurement from HR-ICP-MS, the isotopic ratio of $\left(\delta^{29/28}Si_{silicate}\right)$ corresponds to the natural ratio in the clay mineral and the isotopic ratio of $\left(\delta^{29/28}Si_{sp}\right)$ is given by the certificate. From this, if we consider that all the exchangeable silicon between solid and solution occurred, the equilibrium isotope composition $\left(\delta^{29/28}Si_{mix}\right) = \delta_e$ gives a value of 0.035 at 35°C with which we can calculate a percent of Si exchanged at a given time t.

Dissolution rates and precipitation rates were calculated after addition of ^{29}Si spike according to the quantity of Si released from illite/smectite, and the precipitation rates have been calculated by considering the quantity of ^{29}Si-spike in solution. The rates values are compared with those calculated at the beginning of the experiments far from equilibrium.

Analytical methods

Determinations of element concentrations in solution were carried out by plasma based techniques, namely Quadrupole Inductively Coupled Plasma Mass Spectrometry (Q-ICP-MS, X Series, Thermo Electron Corporation) and sector field High Resolution Inductively

Coupled Plasma Mass Spectrometry (HR-ICP-MS, Thermo Scientific Element-XR instrument).

Q-ICP-MS. Aliquots sampled during the experiments were prepared for concentration measurements of silicon, iron and aluminum by Q-ICP-MS using external calibration with ^{45}Sc and ^{115}In as internal standards for signal drift correction. The quantification limit calculated as ten times the standard deviation of the blank (i.e. 0.2% HNO_3 solution) is equal to 7×10^{-7} mol/L for silicon, 7×10^{-8} mol/L for iron and 4×10^{-8} mol/L for aluminum. Multi-Element calibration standard and sample solutions for analysis were prepared in 2% HNO_3. The ^{45}Sc-^{115}In mixed internal standard solution at 20ppb was introduced on-line in all solutions. Any residual signal drift was corrected from the measurement of the "quality-check" multi-element standard performed every five samples. All standards used during the course of the study were supplied by Scp Science, ultrapure water was obtained with a Milli-Q water purification system and HNO_3 acid was purified by sub-boiling distillation.

HR-ICP-MS. Si isotope ratios were measured on the SEM in analog mode using a mass resolution of 4000 ($\Delta m = 0.007$ u.m.a. for m = 28, 29, 30) for complete removal of isobaric spectral interferences on ^{28}Si, ^{29}Si and ^{30}Si. The use of a free-Si liquid sample introduction device with PFA Teflon nebulizer and spray chamber but also an injector torch made of platinum as well as purified reagents will greatly improve the silicon instrumental background and as a consequence the accuracy and reproducibility of Si isotopic ratios after ^{29}Si tracer addition. The instrument sensitivity is around 20000 cps/ppb and the detection limit for silicon is equal to 1.3×10^{-7} mol/L - 6×10^{-8} mol/L. Working matrix-matched standard solutions of silicon were prepared in 0.01 mol/L HCl using 1000 mg/l silicon and sodium stock solutions purchased by SCP Science and Alfa Aesar, respectively. All samples and standards were diluted to a final Si concentration ranging from 100 ppb to 500 ppb. During the analysis session, five samples are bracketed by a silicon working solution and a 0.01 N HCl blank solution in order to correct raw isotope data from blank (blank/sample ratio less than 15%) and mass bias using the mass fractionation exponential law. Every sample and standard measurements are followed by a 5 min wash of the complete sample introduction system using 0.01 N HCl. The acquisition procedure allows the collection of one hundred measurements of each silicon isotope ratios in 3min20s with in-run precision around 0.1-0.2% ($1\sigma/\sqrt{10}$) for $^{29}Si/^{28}Si$.

Characterization methods

BET. The surface area of illite, interstratified illite/smectite and Callovo-Oxfordian argilite samples were determined from N_2 adsorption isotherms at 77 K experiments and obtained with a Micromeritics ASAP 2010 M. Prior to analyses, the samples were outgassed in vacuum overnight. Surface area of illite is 50.9 m²/g, interstratified illite/smectite 82.3 m²/g and Callovo-Oxfordian argillite 92.8 m²/g.

Granulometry. The particle size was determined by means of the particle sizing system (PSS) from CAD instrumentation. Size distributions (volume based) from 1 to 100 μm diameter

range were determined by single-particle optical sensing using an AccuSizer^{TM} 780 optical PSS.

SEM. Surface morphology were observed by scanning electron microscopy and the chemical composition was determined by energy dispersive spectroscopy (EDS) with a JEOL 5800-LV using a PGT IMIX-PTS (Princeton Gamma-Tech, Energy Dispersive Spectrometer with germanium) probe operating at 15 kV.

XRD. Patterns were collected with a Bruker-AXS D5000 (Bragg-Brentano geometry Advance diffractometer (Bragg$^+$Brentano geometry) equipped with a Cu anticathode under the following experimental conditions: 0.2 mm receiving slits and 1 mm divergence slits for radial divergence, a 16 mm-high receiving slit, and a 2.3° Soller slit. X-ray powder diffraction data were collected with a step size of 0.02° 2θ over the angular range from 10-60° 2θ. MAUD program (**Luterroti 2000**) with the full pattern XRD Rietveld fitting procedure combined with a Fourier analysis were used to describe the broadening of peaks (**McHale et al. 1997**). This method consists in refining the experimental diffractograms from the structural model of the phases.

XPS. The spectra were collected on an XPS apparatus (KRATOS Nova). The source of photons is a monochromatized AlK$_\alpha$ lamp (1486.6 eV) and a FWHM at 0.26 eV. The charge effects were corrected using the 1s line at 284.6 eV (**Moulder et al. 1993**) of the contaminant carbon (C–H species species). The XPS spectra are fitted with the software CasaXPS Version 2.3.16 PR 1.6 program (Copyright © 1999-2011 Casa Software Ltd). The precision on binding energy values is ± 0.2 eV.

Results

Dissolution of clays.

The results of the dissolution of illite/smectite, illite and Callovo-Oxfordian argillite are shown in Figure 1 and present the concentration of Si (mol/L) measured in solution against the contact time (days) at 35, 50 and 90 °C. From a general observation, the concentrations at 35 and 50 °C are very similar and lower to that of at 90 °C. After about 50 days, a maximum of Si-concentration is reached. The concentrations of Si in presence of illite and illite/smectite are higher at 35 and 50 °C by a factor 2 compared to the Callovo-Oxfordian argillite. At 90 °C the concentrations in all the systems are similar. At low temperature, the dissolution of illite and/or illite/smectite seems not to participate to the dissolution of the Callovo-Oxfordian argillite due to the lower concentration of the later. The presence of muscovite and kaolinite in the Callovo-Oxfordian argillite request more investigation to assess the influence of each of the clay mineral phases present. At 90 °C, the results indicate clearly that illite and/or illite/smectite may control the dissolution of the Callovo-Oxfordian argillite. Comparing to the data published in Suzuki et al., the concentrations of Si in solution for the Callovo-Oxfordian argillite sample is lower in this study by a factor 2. This could be explained by the

presence of quartz fraction existing in the study of Suzuki et al. (2011) which has been removed by purification in this study. In this work, we have assessed the maximum concentration values of Si for the Callovo-Oxfordian argillite in conditions close to equilibrium. This implies that the quartz fraction in the geological disposal will be a key fraction and may compete with the dissolution of the nuclear glass waste. All the results indicate that the behavior of the dissolution of the Callovo-Oxfordian is a function of temperature. Illite and illite/smectite may not control the dissolution of the Callovo-Oxfordian argillite at low temperature but may influence at 90 °C. At 35 and 50 °C, other mineral phases such as kaolinite (for e.g.) may expect to be in competition with the two other clays.

Isotopic exchanges.

Experiments of isotopic exchange were performed in all systems in which the stable isotope ^{29}Si was added in solution after 399 days of equilibrium between illite and solution, 483 days for illite/smectite and 326 days for Callovo-Oxfordian argillite. The results obtained for the interaction ^{29}Si with illite/smectite are detailed in this paper. The quantification of the mix isotopic ratio ^{29}Si/^{28}Si was determined in solution by HR-ICP-MS and the results are presented in Figure 2. The limit range of the isotope ratios is 0.05080 for the natural abundance and 2497.5 for the ^{29}Si-spike solution. Experimentally, the range of the mix isotopic ratio was 0.14046 (35 °C), 0.12297 (50 °C) and 0.07684 (90 °C) at the beginning and 0.10048 (35 °C), 0.09203 (50 °C) and 0.06823 (90 °C) after 98 days of isotopic exchange. These values are to be compared with the IUPAC reference value of 0.0508. From this result, we notice that the mix isotopic ratios are close to the IUPAC reference which indicates a low disturbance of the system studied. Moreover, the mix isotopic ratios decrease against the time reaching a stable value higher than the IUPAC reference value. This indicates an exchange of Si between solid and solution. It may also mean that the isotopic ratio ^{29}Si/^{28}Si has reached a new value characteristic of the studied system. If this value came to evolve, it will take a long time to recover the reference value of natural ^{29}Si/^{28}Si isotopic ratio. The quantity of Si exchanged between illite/smectite and solution has been calculated. About 36% (35 and 50 °C) and 20% (90 °C) of Si have been exchanged and half of this quantity has been exchanged after 18 days. The Figure 3 shows the results of the percent of Si exchanged between the cited clayey mineral against the time for the 3 temperatures studied.

In addition to the data collected on the concentration of Si measured in solution, aluminum and iron were measured in solution. The results are given in the 2nd annual workshop proceedings (***Bosbach et al. 2012***).
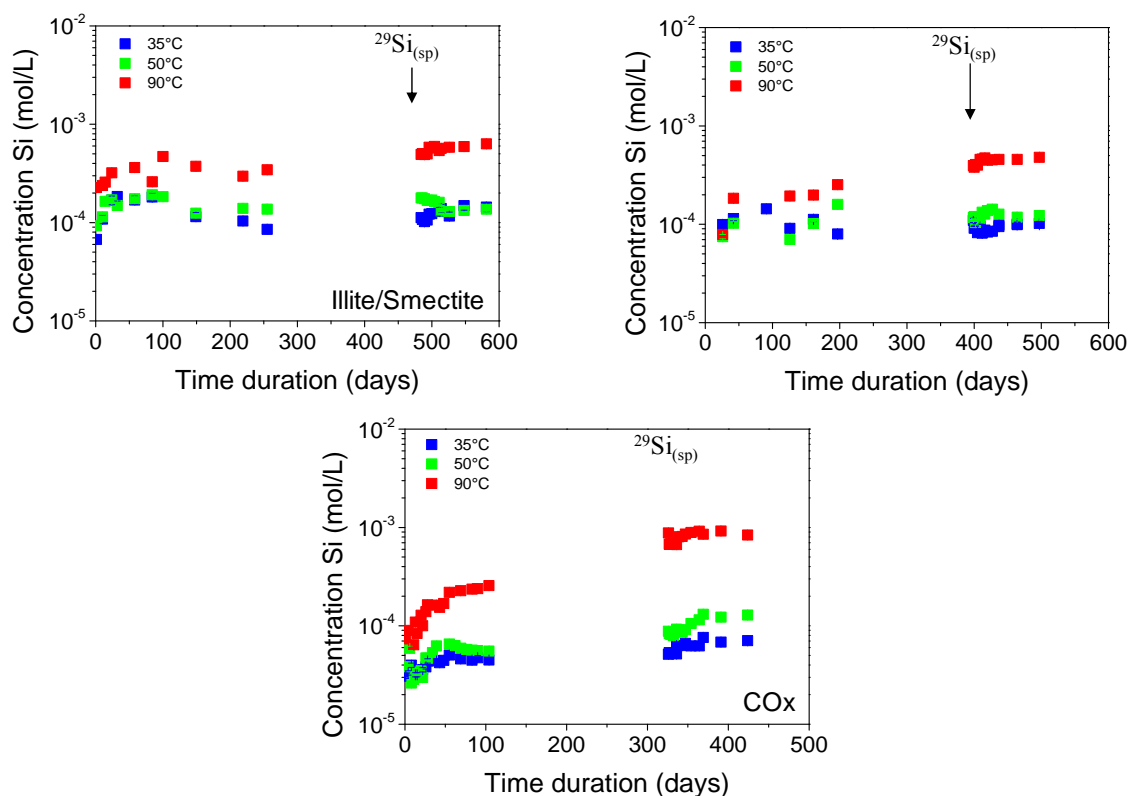
Fig. 1 Evolution of Si-concentration in solution versus time for different temperatures (35, 50, and 90 °C) for illite/smectite: m/V = 6.7 g/L, SA/m = 82.3 m²/g, NaCl 0.01 M, pH 7.7 – 7.5, for illite: m/V = 6.7 g/L, SA/m = 50.9 m²/g, NaCl 0.01 M, pH 7.6 – 8.1, for Callovo-Oxfordian argilite: m/V = 6.7 g/L, SA/m = 92.8 m²/g, NaCl 0.01 M, pH 8.0 – 8.2 .
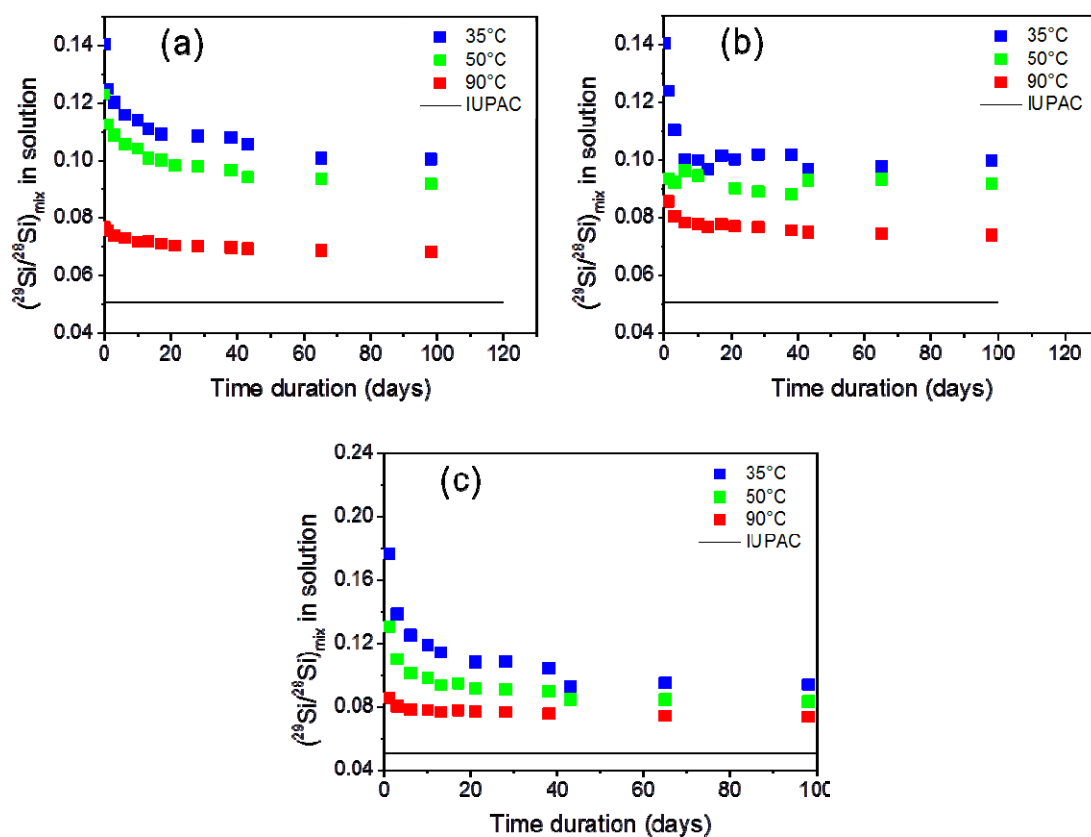
Fig. 2 Evolution of the isotope ratio $^{29}Si/^{28}Si$ in solution versus time for different temperatures (35, 50, and 90 °C) for (a) illite/smectite, (b) illite, (c) Callovo-Oxfordian argilite.
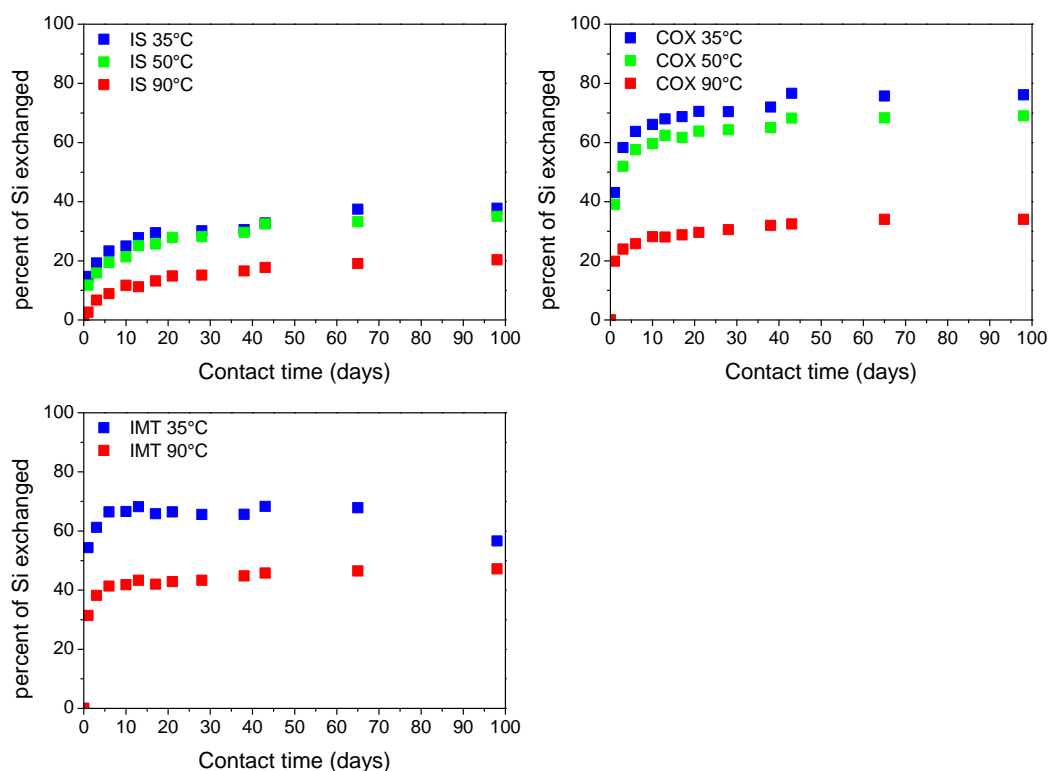
Fig. 3 Evolution of the percent of Si exchanged between solid and solution versus time for different temperatures (35, 50, and 90 °C) for illite/smectite, Callovo-Oxfordian argillite and illte.

Dissolution / Precipitation rates

From these results, the initial dissolution rates R_{diss} (mol Si/m²/s) far from equilibrium were calculated between 0 and 25 days or 0 and 50 days depending on the clayey systems and the temperature. The results are presented in Table 1. The general observations show an increase of the dissolution rates with the temperature and the rate values for the Callovo-Oxfordian argillite are lower than that of illite and illite/smectite by 0.8 to 0.3 orders of magnitude. The dissolution rate values are almost similar between illite and illite/smectite at 35 and 50 °C, while at 90 °C the values are close for the three clayey minerals.

In condition close-to-equilibrium, the addition of ^{29}Si-spike in solution has allowed to assess how the system reacts after the disturbance of the system. Dissolution rates and precipitation rates were calculated on the base of the results given by the isotope ratios measurements. In particular, the dissolution rates have been calculated by taking into account the quantity of Si released from the clayey mineral, and the precipitation rates have been calculated by considering the quantity of ^{29}Si-spike in solution. For instance, for the illite/smectite system, the results give dissolution rates of 7.8×10^{-15} mol Si/m²/s (35 °C), 4.6×10^{-15} mol Si/m²/s (50 °C) and 6.5×10^{-15} mol Si/m²/s (90 °C) and precipitation rates of 3.9×10^{-15} mol Si/m²/s (35 °C), 4.6×10^{-15} mol Si/m²/s (50 °C) and 5.9×10^{-15} mol Si/m²/s (90 °C). The results

indicate that, for the case of illite/smectite, the dissolution rates values are in good agreement with literature data. Dissolution and precipitation rates were calculated for all studied systems and reported in Table 2. The results show that the dissolution rates are higher than 1 order of magnitude compare to the precipitation rates. The main contribution of this increase may come from the pH effect during the addition of the spike. Indeed, the pH of the later is 12 in the stock spike solution and an aliquot has been added in each system which has locally increased the pH by a maximum of 4 orders of magnitude. In literature data, one can notice that the increase of 1 order of magnitude the pH-value results in the increase of 1 order of magnitude the dissolution rates. This is coherent with our experimental results. Thus, precipitation rates calculated in conditions close to equilibrium were compared with the dissolution rates far from equilibrium. Considering the dissolution rates vs. precipitation rates (Figure 4), the experimental results determined in this work are compared with those obtained in a previous work. On the base of the results obtained for the illite/smectite, illite and Callovo-Oxfordian argilite systems, the data indicate that a dynamic equilibrium of dissolution/precipitation exists in the studied system. In this work, we were able to assess the dissolution rate on purified clayey minerals which are consistent with literature data. The addition of ^{29}Si-spike has allowed to assess the precipitation rates in conditions close-to-equilibrium which are similar to the dissolution rates for all type of clayey minerals. Compare to the data from Suzuki et al. (2011), we have shown clearly that the quartz phase contained naturally in the clayey minerals may contribute to the dissolution rates up to 15%. However, in experiments conducted by Neeway et al. by combining different system containing Callovo-Oxfordian argillite and nuclear glass waste (*Neeway et al. 2011*), they shown that for a fixed concentration of Si (equivalent to the concentration in Si in equilibrium with the groundwater in the geological formation) in synthetic groundwater imposed at the inlet of the system (percolation type experiments), the absence or presence of nuclear glass does not change the concentration of Si in the outlet of the experiments. By consequence, they have calculated the normalized dissolution rates of the nuclear glass waste and they showed that the values remain unchanged independently of the presence or absence of Callovo-Oxfordian argillite. Finally, with the method of isotopic exchange we have been able to distinguish the contribution of the clayey minerals and the quartz phase in the dissolution rates calculation.

Table 1: Initial dissolution rates R_{diss} (mol Si/m²/s) of illite/smectite, illite and Callovo-Oxfordian argillite (COx) at 35, 50 and 90 °C in NaCl 0.01M solution.

	Log R_{diss} (mol Si/m²/s)		
	Illite	**Illite/smectite**	**Cox**
35°C	-13.6	-13.4	-14.2
50°C	-13.5	-13.4	-13.7
90°C	-12.7	-13.1	-13.4

Table 2: Dissolution rates R_{diss} and Precipitation rates (mol Si/m²/s) in conditions close-to-equilibrium after the addition of ^{29}Si-spike in illite/smectite, illite and Callovo-Oxfordian argillite (COx) systems at 35, 50 and 90 °C in NaCl 0.01 M. Dissolution and precipitation rates for illite at 50 °C were not determined due to the absence of a kinetic isotopic exchange.

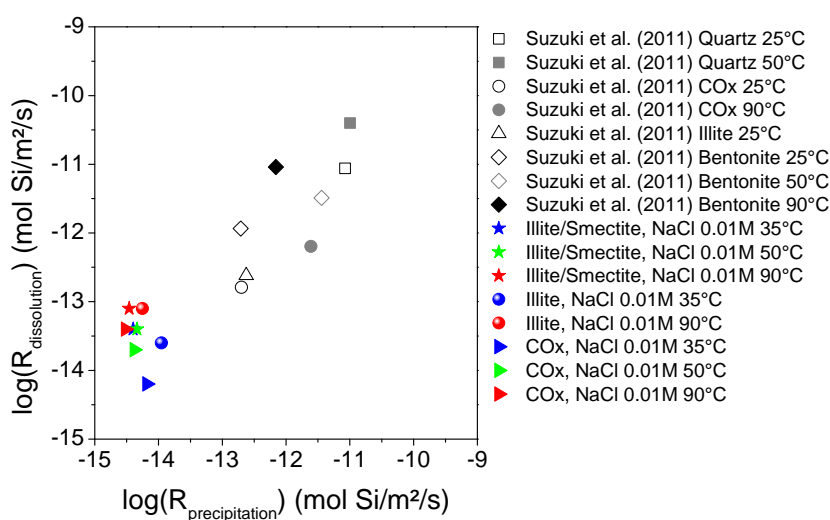|	Log R_{diss} (mol Si/m²/s)		
	Illite	**Illite/smectite**	**Cox**
35 °C	-12.3	-13.1	-12.5
50 °C	-	-13.0	-12.4
90 °C	-12.3	-13.0	-12.1
	Log R_{prec} (mol Si/m²/s)		
	Illite	**Illite/smectite**	**Cox**
35 °C	-14.0	-14.4	-14.2
50 °C	-	-14.3	-14.4
90 °C	-14.3	-14.5	-14.5

Fig. 4 Precipitation rates versus dissolution rates calculated by isotopic exchange of ^{29}Si/^{28}Si. Results compared with the dissolution/precipitation rates calculated by ^{32}Si/Si exchange (Suzuki et al. 2011) for different temperatures for illite/smectite, illite, bentonite, quartz and Callovo-Oxfordian argilite, NaCl 0.01 M.

Characterization of the solids.

The characterizations by X-Ray diffraction of Callovo-Oxfordian argillite and illite were performed before and after purification of the clays, respectively. The method of purification by elutriation has allowed to remove 76% and 63% of quartz fraction from the the Callovo-Oxfordian argillite and illite, respectively. For the illite/smectite, almost 100% of the quartz fraction has been removed. This method has not completely removed all quartz fractions although sonification has been used to separate the secondary mineral phases from the clayey materials. This method has not allowed the complete removal of the quartz phase but it's a compromise between the decrease as much as possible of the quantity of quartz phase and the preservation of the structure of the clays. The granulometry of the clays after purification give a median diameter of particles of (1.0 ± 0.1) µm. The detailed results are showed in the second annual workshop proceedings (***Bosbach et al. 2012***). The XRD-patterns of illite and Callovo-Oxfordian argillite after 559 days of experiments and 643 days of experiments for illite/smectite do not show structural modification compared with the initial solid (Figure 5). Characterizations by scanning electron microscopy were performed for all samples at the end of experiments. Figure 6 shows the SEM pictures after alteration at 35 °C.
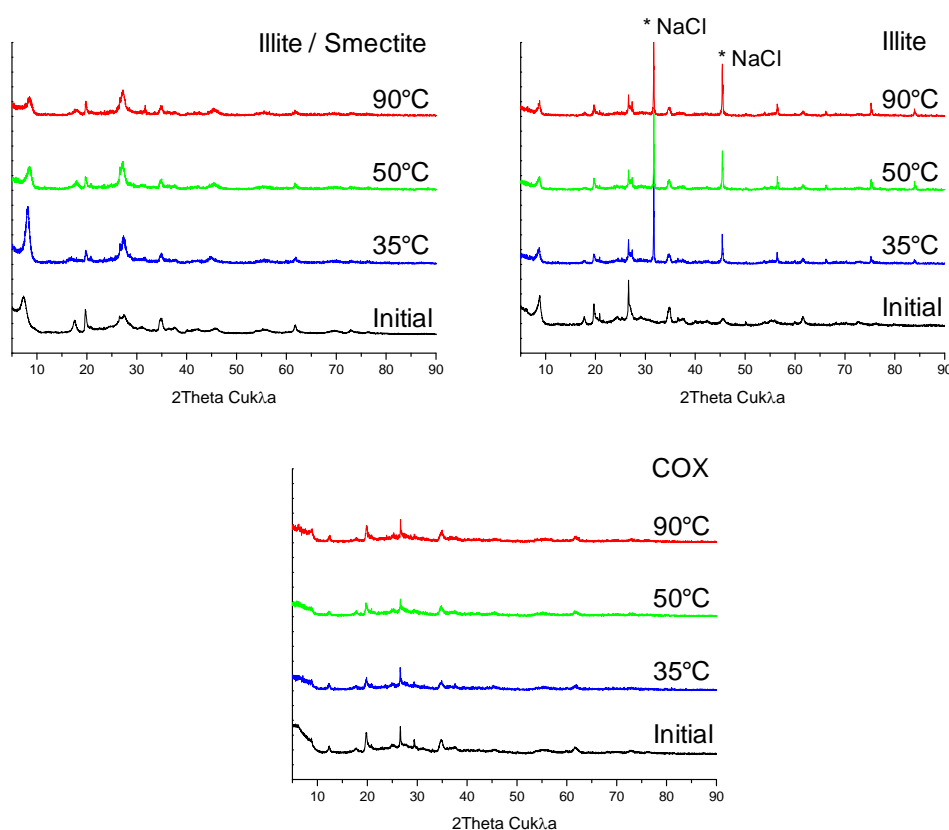
Fig. 5 XRD patterns of illite and Callovo-Oxfordian argillite after 559 days of experiments and 643 days of experiments for illite/smectite at 35, 50 and 90 °C.
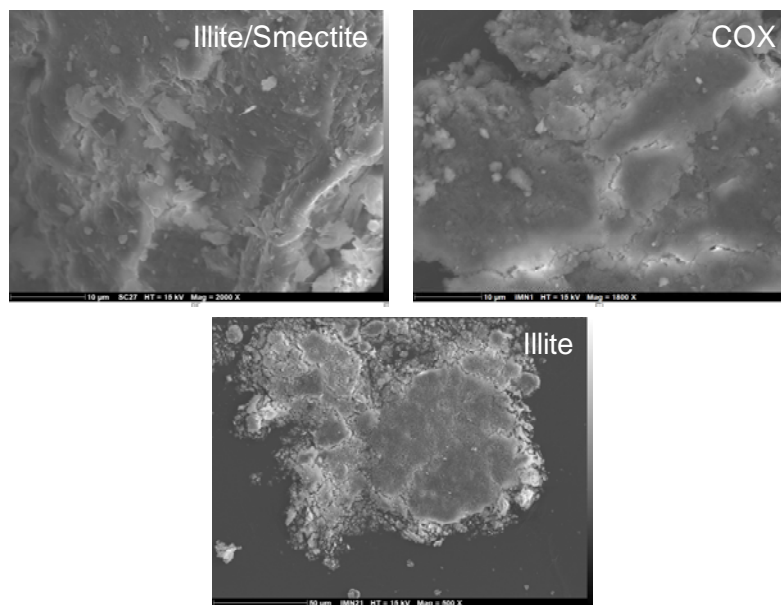
Fig. 6 SEM pictures of illite and Callovo-Oxfordian argillite after 559 days of experiments and 643 days of experiments for illite/smectite at 35 °C.

Characterization by XPS was performed for all the systems studied. The binding energies of A12p (E_b 74.7 (1.7) eV), Si2p (E_b 103.0 (1.7) eV) and Ols (E_b 531.9 (2.1) eV, 536.2 (2.5) eV) peaks were found to be similar for both the initial, altered and ^{29}Si exchanged illite/smectite, suggesting that no significant modification of the chemical environement of Al and Si between the surface and the solution occurred after 538 days of experiments (including 52 days of contact with ^{29}Si tracer) (Figure 7). The binding energy position of the Ols peak was nearly the same in all spectra obtained. The experimental value obtained at 531.9 (2.1) eV is likely due to oxygen ions in the strongly bound water of the interlayer cations (***Moulder et al. 1993***). Finally, the carbon peak, Cls, was due to carbon contamination in XPS measurements and was observed in every spectrum obtained. Ratio of Al/Si was calculated from the quantitative data obtained by XPS. The results give a ratio of 0.36 for both initial and altered illite/smectite at 35, 50 and 90 °C. This value is in good agreement with the literature data (montmorillonite (***He et al. 2007***)) confirming the weak change of the chemical environment of Si and Al against the temperature and the alteration duration.
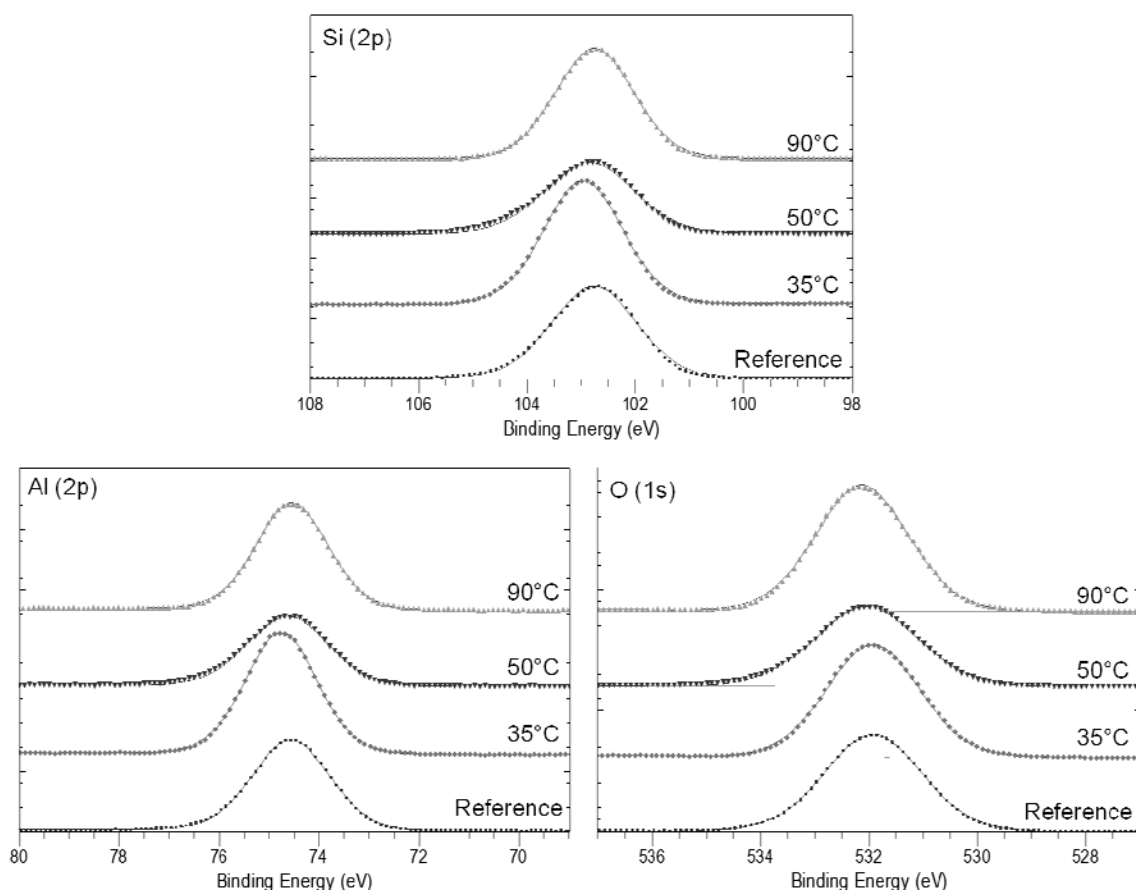
Figure 7: XPS spectra of Si(2p), Al(1s) and O(1s) binding energies of illite/smectite after 643 days at 35, 50 and 90 °C compared to the initial material before alteration (reference).

Conclusions and final work

The dissolution of illite, illite/smectite and Callovo-Oxfordian were perfomed at 35, 50 and 90 °C in NaCl 0.01 mol/L solution in batch system. Concentrations of Si, Fe and Al were measured in solution with a strong influence of temperature on the release rates and the maximum concentration in solution. The dissolution behaviour of the Callovo-Oxfordian argillite could be explained by the dissolution of the various mineral phases existing in argillite. Less than 90 °C, mineral phases such as kaolinite and/or muscovite could influence the dissolution behaviour whereas at temperature higher than 90 °C, illite and/or illite/smectite may control the dissolution of the argillite. The efficiency of the purification of clayey materials allows to consider that the quartz fraction is present in the minerals as impurities. The concentrations of Si measured in the experiments are lower than the solubility of quartz. This indicates that the influence of the quartz fraction contained in the clayey materials is neglectable in this study.

After 3-years project, we have characterized the behavior of clayey minerals (illite/smectite, illite and Callovo-Oxfordian argillite) at 35, 50 and 90 °C in conditions far from equilibrium

(dissolution rates $\sim 4 \times 10^{-14}$ mol Si/m²/s) and close to equilibrium (precipitation rates $\sim 5 \times 10^{-15}$ mol Si/m²/s). By the means of isotopic exchange method $^{29}Si/^{28}Si$, we have assessed the dissolution/precipitation rates and we have confirmed that a dynamic equilibrium between the clay and the solution may occur. However, at this stage we have not distinguished in which proportion the illite and illite/smectite phases contribute in the dissolution/precipitation mechanism in Callovo-Oxfordian argillite.

Acknowledgement

References

ANDRA (2005). Dossier ANDRA argile: Evaluation de la faisabilité du stockage géologique en formation argileuse

Bauer, A. and Berger, G. (1998). Kaolinite and smectite dissolution rate in high molar KOH solutions at 35° and 80°C. Applied Geochemistry, 13, 905–916

Bergaya, F., Theng, B.K.G., Lagaly, G. (2006). Handbook of Clay Science, Developments in Clay Science. Elsevier, Amsterdam

Bosbach D., F. Brandt, L. Duro, B. Grambow, D. Kulik, T. Suzuki-Muresan (2013). 2nd Annual Workshop Proceedings (SKIN project), 7th EC FP - SKIN, 21th - 22th November 2012 Villigen PSI, ed. Institut für Energie- und Klimaforschung, Nukleare Entsorgung und Reaktorsicherheit (IEK-6), July 2013, ISSN 0944-2952.

De Cannière, P., Moors, H., Dierckx, F., Gasiaux, F., Aertsens, M., Put, M., Van Iseghem, P. (1998). Diffusion and Sorption of 32Si-labelled silica in the boom clay. Radiochimica Acta, 82, 191–196

Daux, V., Guy, C., Advocat, T., Crovisier, J.-L., Stille, P. (1997). Kinetic aspects of basaltic glass dissolution at 90°C: role of aqueous silicon and aluminium. Chemical Geology, 142, 109–126

Gailhanou, H., J. C. van Miltenburg, J. Rogez, J. Olives, M. Amouric, E. C. Gaucher and P. Blanc (2007) Thermodynamic properties of anhydrous smectite MX-80, illite IMt-2 and

mixed-layer illite/smectite ISCz-1 as determined by calorimetric methods. Part I: Heat capacities, heat contents and entropies. Geochimica et Cosmochimica Acta 71(22), 5463–5473.

Ganor, J., Mogollón, J.L., Lasaga, A.C. (1995). The effect of pH on kaolinite dissolution rates and on activation energy. Geochimica Cosmochimica Acta, 59, 1037–1052

Gaucher, E., Robelin, C., Matray, J.M., Négrel, G., Gros, Y., Heitz, J.F., Vinsot, A., Rebours, H., Cassagnabère, A., Bouchet, A. (2004). ANDRA underground research laboratory: interpretation of the mineralogical and geochemical data acquired in the Callovian-Oxfordian formation by investigative drilling. Physics and Chemistry of Earth, Parts A/B/C 29, 55–77

Gorski, C.A., Handler, R.M., Beard, B.L., Pasakarnis, T., Johnson, C.M., Scherer, M.M. (2012) Environ. Sci. Technol., 46, 12399−12407

Handler, R.M., Beard, B.L., Johnson, C.M., Scherer, M.M. (2009). Atom exchange between aqueous Fe(II) and goethite: an Fe isotope tracer study. Environ. Sci. Technol., 43, 1102–1107

He, H., Q. Zhou, R. L. Frost, B. J. Wood, L. V. Duong and J. T. Kloprogge (2007). A X-ray photoelectron spectroscopy study of HDTMAB distribution within organoclays Spectrochimica Acta Part A: Molecular and Biomolecular Spectroscopy 66(4-5): 1180-1188.

Huertas, F.J., Caballero, E., Jiménez de Cisneros, C., Huertas, F., Linares, J. (2001). Kinetics of montmorillonite dissolution in granitic solutions. Applied Geochemistry, 16, 397–407

IUPAC (1997). Compendium of Chemical Terminology, 2nd ed. (the "Gold Book"). Compiled by A. D. McNaught and A. Wilkinson. Blackwell Scientific Publications, Oxford

Köhler, S.J., Dufaud, F., Oelkers, E.H. (2003). An experimental study of illite dissolution kinetics as a function of ph from 1.4 to 12.4 and temperature from 5° to 50°C. Geochimica Cosmochimica Acta, 67, 3583–3594

Lutterotti L. (2000). MAUD program, CPD, Newsletter (IUCr) No. 24. 2000, http://www.ing.unitn.it/~maud/.

McHale J.M., Auroux A., Perrotta A.J., Navrotsky A. (1997). Science, 1997, 277, 788.

Moulder, J.F., Stickle, W.F., Sobol, P.E., Bomben, K.D. (1993). in: J. Chastain, R.C. King, Jr. (Eds.), Handbook of X-ray Photoelectron Spectroscopy, Physial Electronics, Inc.

Palandri, J.L. and Kharaka, Y.K. (2004). A compilation of rate parameters of water-mineral interaction kinetics for application to geochemical modelling, US GEOLOGICAL SURVEY

Rozalén, M., Huertas, F.J., Brady, P.V. (2009). Experimental study of the effect of pH and temperature on the kinetics of montmorillonite dissolution. Geochimica Cosmochimica Acta, 73, 3752–3766.

Suzuki-Muresan, T., et al. (2011). Solution controls for dissolved silica at 25°, 50° and 90°C for quartz, Callovo-Oxfordian claystone, illite and MX80 bentonite. Physics and Chemistry of the Earth, Parts A/B/C 36(17-18): 1648-1660

Tan, K.H. (1982). The effect of interaction and adsorption of silica on structural changes in clay minerals. Soil Sci. 136, 300–307.

van den Boorn, S. H. J. M., P. Z. Vroon, C. C. van Belle, B. van der Wagt, J. Schwieters, M. J. van Bergen (2006). Determination of silicon isotope ratios in silicate materials by high-resolution MC-ICP-MS using a sodium hydroxide sample digestion method. Journal of Analytical Atomic Spectrometry, 21(8): 734-742

THORIUM OXIDE SOLUBLITY BEHAVIOR VS. THE SURFACE CRYSTALLINE STATE

Tomo Suzuki-Muresan[*], Johan Vandenborre, Katy Perrigaud, Bernd Grambow

SUBATECH, Unité Mixte de Recherche 6457, Ecole des Mines de Nantes, CNRS/IN2P3, Université de Nantes, 4 rue Alfred Kastler, BP 20722, 44307 Nantes cedex 03, France.

* Corresponding author: tomo.suzuki@subatech.in2p3.fr

Abstract

In literature, huge discrepancies are reported in solubility values and it is now accepted that the surface solid state may have influence on the determination of the solubility values. The aim of the work in SKIN-project was to re-assess the solubility of $ThO_2(s)$ in the pH range 3 to 7 as a function of the surface crystalline state.

Previous studies indicated that thorium oxide solubility is very much dependent on the material at the grain boundary. With the use of powdered material, the cleaning of the surface is expected to be more effective, so that artefacts derived from pre-altered surface phases will be minimised. The attainment of apparent solubility equilibrium was followed by analysing ^{232}Th with time. In condition close to equilibrium, half of the solution was removed and kept for desorption experiment. In the remaining half solution in the experiments, ^{229}Th trace was added to the solution/solid system and the isotopic exchange was monitored by Q-ICP-MS. In all solution analyses, colloids were removed by ultra-filtration at 10kDa but Th analyses of colloidal material were included in the mass balance. Once ^{229}Th uptake on the surface has reached a steady state, desorption experiments was performed putting the solids with a ^{229}Th enriched surface into the previously conserved solution without ^{229}Th. Typical duration of experiments is longer than a year. Different analytical techniques will be used for solution and solid analyses: Q-ICP-MS, SEM, XRD and BET-method.

Synthesis of the solid oxide has been performed with different calcination temperatures (RT, 700, 900 and 1300 °C) in order to obtain 4 crystalline states of thorium oxide with different ratio of grains vs. grain boundaries. In addition, separation of ThO_2 crystallized kernel from the coating layers of HTR of ThO_2 has been conducted. These two methodologies have provided samples of the oxide with different crystallinity, i.e., grain size.

Dissolution, $^{229}Th/^{232}Th$ isotopic exchange and desorption measurements have been conducted in the acidic pH range and the results compared with available data in the

literature. Results show the relationship between the crystalline state of the ThO_2 surface and the relative enrichment in [229Th] at the solid/solution interface.

Introduction

We study Th atom exchange between different thorium oxide surfaces and aqueous solution (0.01 mol.L^{-1} NaCl for pH = 3.2, 5.0, 6.8) to address the Task 3.2. In a previous work (***Vandenborre et al. 2010***), we have determined by the solid-state characterization (XPS, SEM, AFM) that 80 % of the XPS accessible near surface region of sintered thorium oxide is represented by the less reactive $ThO_2(cr)$ grains. The remaining 20 % corresponds to $ThO_x(OH)_y(H_2O)_z$ which is largely associated with grain boundaries. The empirical solubility data does not correspond to thermodynamic bulk phase/solution equilibrium, as measured solution concentrations are controlled by specific site exchange mechanisms at the solid/solution interface. Therefore for sparingly soluble solids, one needs to quantify the specific surface site involved in the attachment and detachment rates if one wants to assess solubility constraints. For this reason, the purpose of our work is to study different crystalline states of thorium oxide surfaces with different grains vs. grain boundaries ratios.

Material and Methods

Samples

In this aim, we synthesized thorium oxides from thorium oxalate $Th(C_2O_4)_2,4·H_2O$ as precursor in order to control the grain size of ThO_2 crystallized with different heating temperatures (T = 700, 900, and 1300 °C) (***Rand et al. 2008, Heisbourg 2003, Oktay and Yayli 2001***). The second solid used in this study is provided by J. Fachinger from Forschungzentrum Jülich (Germany), which are under spherical particles forms and synthesized at a high calcination temperature (1600 °C). A part of the spheres used for solubility experiments are crushed in order to remove all the grain boundaries even into the core of the sphere by the pre-washing experiments. The synthesis method and the physical properties of the solid are described in (***Vandenborre et al. 2010, Müller 2006***), respectively. Table 1 presents the 4 sets of solid sample: (I) Crushed ThO_2 spheres, (II) Initial ThO_2 spheres, (III) ThO_2 powder synthesized at 1300 °C, (IV) ThO_2 powder synthesized at 700 °C.

Table 1: Sets of solid samples.

Samples	Solid description
I	Crushed ThO$_2$ spheres
II	Initial ThO$_2$ spheres
III	ThO$_2$ powder synthesized at 1300 °C
IV	ThO$_2$ powder synthesized at 700 °C

Solid characterization

Solid surface pictures are performed by SEM (scanning electron microscopy, JEOL 5800 SV with a 15 kV voltage). The SEM samples were covered by a Pt layer in order to improve electron conduction and increase the picture resolution. XRD patterns are recorded with the diffractometer BRUKER-AXS D5000 (Bragg-Brentano geometry, copper anticathode Cu at λ = 1.5406 Å). Moreover N$_2$-gas adsorption by B.E.T. method, using a COULTER SA3100 apparatus, is carried out in order to determine the specific surface area for each solid sample, in particular versus the heating temperature during the synthesis process.

Dissolution and ^{229}Th Addition experiments

The pre-washing and dissolution batch experiments were performed exposing 150 mg of solids ThO$_2$(cr) (synthesized powder with different heating temperature, spheres crushed or intact) to an aqueous solution in undersaturated conditions. A HDPE (High Density poly-ethylene) reaction vessel is used, containing 15 mL 0.1 mol·L^{-1} HCl solution under continuous stirring during 15 days.

We have started the dissolution experiments by the contact between each pre-washed solid with the NaCl 0.01 mol·L^{-1} aqueous solution at different pH values (3.2, 5.0, 6.8) under atmospheric conditions. For the experiments at pH = 3.2, solutions were spiked with a ^{229}Th (t$_{1/2}$ = 7340 years) carrier-free solution to achieve a final [^{229}Th]$_{aq}$ = 4.9 × 10^{-10} mol·L^{-1}. The addition date of 200 days corresponds to the time necessary to reach a constant ^{232}Th concentration ("steady state"). Immediately after the addition of the acid ^{229}Th aliquot, the acid perturbation of the solution pH was compensated for by the addition of small aliquots of 0.01 mol·L^{-1} NaOH until the target pH value of 3.2 was reached again. The objective of adding the spike is to test the reversibility and to allow one to follow the potentially ongoing solution/surface isotopic exchange on the ThO$_{2(cr)}$ surface at "steady state". The dissolution process of ^{232}ThO$_{2(cr)}$ and the uptake of ^{229}Th from solution are monitored by sampling aliquots of 0.5 mL over a period of 220 days. After, the solution samples were ultrafiltered, using 1.8 nm cutoff membranes (5 kDa) in order to exclude colloidal particles commonly described in the literature. The ultrafiltered solutions were then acidified with 2% distilled nitric acid and analyzed by inductively coupled plasma mass spectrometry

(THERMOELECTRON) for determination of the $^{232/229}$Th concentrations in solution ($[^{232/229}$Th$]_{aq}$) with an estimated error of 10%.

Desorption experiments

For the last part of the dissolution experiment, we have performed desorption experiment. At 470 days from the initial contact time, solutions are totally removed from each batch sample. Moreover, initial solutions (15 mL NaCl 0.01 mol·L^{-1} with pH = 3.0) are added to each batch sample in order to carry out the desorption experiments. Solutions measurements are performed with the same protocol as the previous dissolution experiments. The total contact time is about 500 days for the experiment.

Normalization of solution concentrations and rate values

The measured solution concentrations in experiments are normalized to solid composition and surface area and expressed as normalized mass loss NL using the equation

$$NL = \frac{[Th] \times MW_{ThO_2}}{S/V}$$
(1)

where [Th] signifies the measured ^{232}Th or ^{229}Th concentrations in mol·m$^{-3}_{H2O}$, MW$_{ThO2}$ is the molecular weight of ThO$_2$ (g·mol^{-1}), S is the surface area (m^2) of the solid, and V the solution volume (m^3). The normalized mass loss rate (in g·m^{-2}·d^{-1}) is then calculated with the following equation:

$$NLR = \frac{\Delta NL}{\Delta t}$$
(2)

where Δt signifies an interval in contact time (d) and ΔNL the variation of normalized mass loss in this interval.

Relative Enrichment in ^{229}Th calculations

The relative enrichment in 229Th is a parameter linked to the solubility of a solid surface and is calculated by the ratio between two ratios of ^{229}Th onto ^{232}Th at the surface and at the solution as described by:

$$RE = \frac{\left(^{229}Th \middle/ ^{232}Th \right)_{surface}}{\left(^{229}Th \middle/ ^{232}Th \right)_{solution}}$$
(3)

Results

Solid characterization

SEM picture of HTR sphere surface shows grains of thorium oxide coated by grain boundaries (Figure 1) which control the solubility without pre-washing. The solids characterization by X-Rays Diffraction is performed onto the ThO_2 spheres in order to check the high crystalline state of this sample. From the results, we confirm the different crystallization states by the decrease of Full Width Half Middle observed onto the XRD peaks when the heating temperature increases (Figure 2). Hence, the ratio between grains and grain boundaries is different for all these samples. The B.E.T. method give us the specific surface area values between 17.8 m^2/g for the lower crystallized sample (synthesized at 700 °C) and 1.9 m^2/g for the higher crystallized (synthesized at 1300 °C) in Table 2. The specific area value for initial ThO_2 sphere can be estimated from the geometric structure at 1.2×10^{-3} m^2/g. However, it seems not realistic because the pre-washing must be implying a non negligible effect onto the surface of the spheres which increase the specific surface area. Moreover, as shown by Figure 1, the specific surface evolves during the different dissolution, isotopic exchange and desorption experiments.
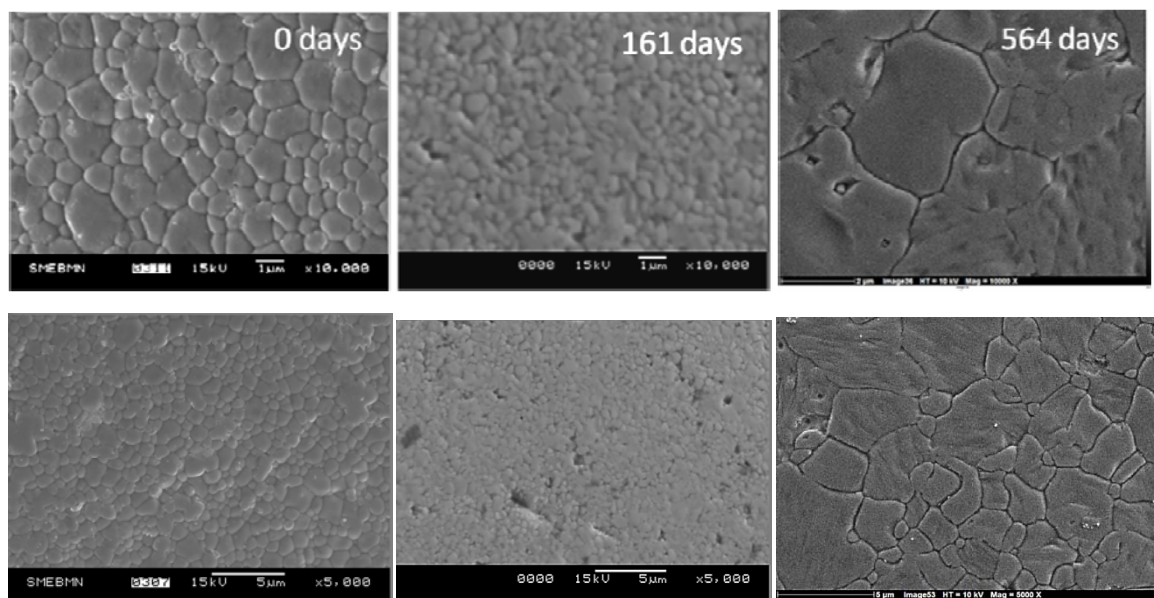
Fig. 1 SEM pictures of ThO2(cr) HTR sphere (sample II) at different contact times with the ×10000 and ×5000 zoom
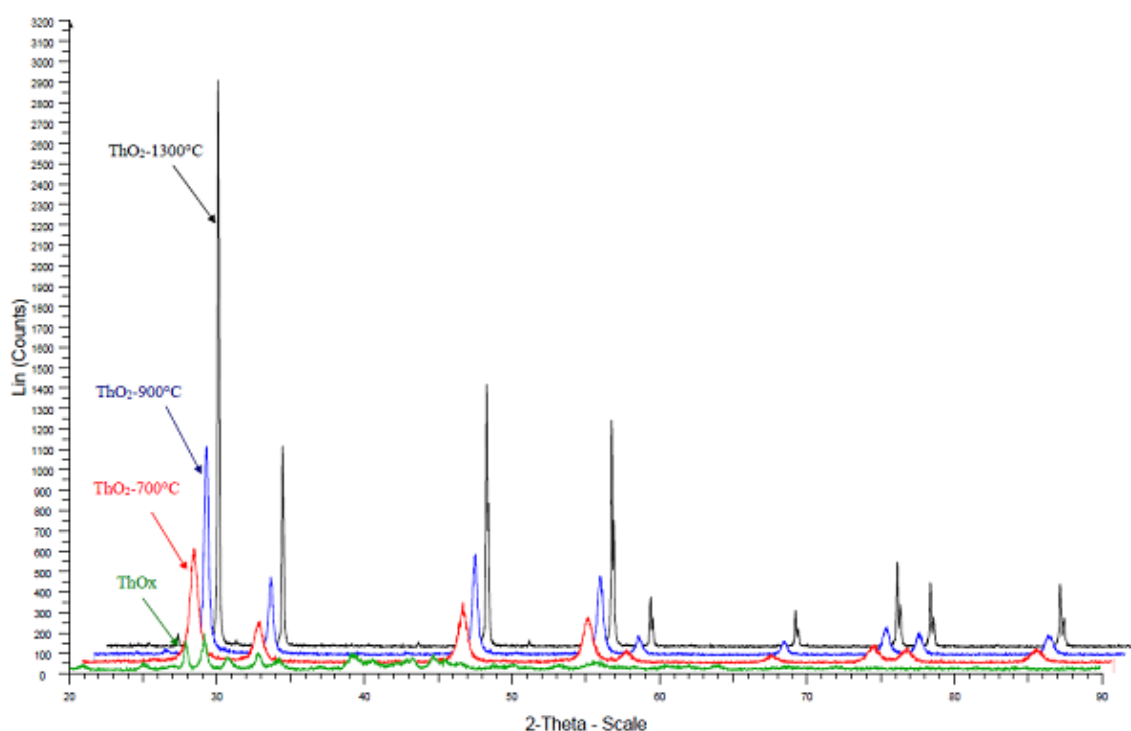
Fig. 2 XRD diagrams of ThO₂ synthesized powder samples crystallized at 700 °C (IV), 900 °C or 1300 °C (III)

Dissolution experiments

The Figure 3 presents the results for a contact time of about 100 days. During the dissolution step corresponding to the period between 0 and 10 days, the slopes are different between the 4 sets of sample: (I), (II), (III), (IV) (cf. Table 1). From the results (Table 2), the slope values, which describe the kinetic state of the system, are higher for the powder samples than for the spheres ones and they are similar between the powder synthesized at 1300 °C (III) and the crushed sphere (I). After about 50 days, the pseudo steady-state equilibrium is reached for all samples with different [Th] measurements presented in Table 2. Again, the values are close between the powder synthesized at 1300 °C and the crushed sphere. It seems that the global and the kinetic dissolution behaviours are similar for these two samples. These results indicate the similar behaviour and the close crystalline degree between the powder synthesized at 1300 °C (III) and the crushed sphere (I). We can notice that the NLR value for the sample (II) has been not calculated depending on the value of the specific surface area which has changed during the Dissolution experiments (cf. SEM pictures in Figure 1).
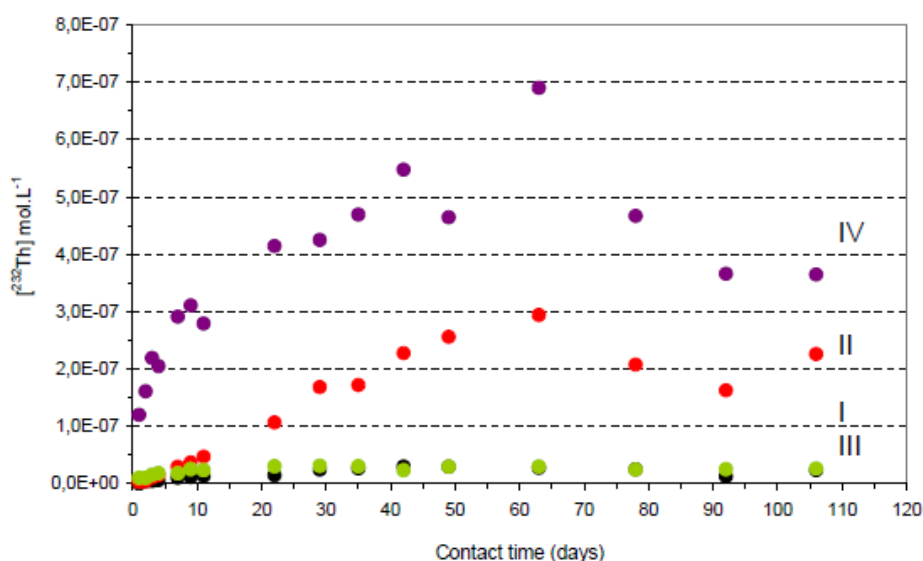
Fig. 3 [^{232}Th] = f(contact time) for each sample at pH = 3.2, monitored by ICP-MS, (I) Crushed ThO$_2$ spheres, (II) Initial ThO$_2$ spheres, (III) ThO$_2$ powder synthesized at 1300 °C, (IV) ThO$_2$ powder synthesized at 700 °C.

Table 2: Experimental data from the dissolution experiments for Samples (I), (II), (III), (IV) with a contact time of 110 days.

Samples	[Th]10d mol/L	Slope (1-10d) mol/L/d	Specific Area m^2/g	NLR(1-10d) g/m^2/d	[Th]50d mol/L
I	1.35×10^{-8}	1.35×10^{-9}	1.9	1.88×10^{-5}	2.95×10^{-8}
II	4.71×10^{-8}	4.38×10^{-9}	?	?	2.56×10^{-7}
III	2.37×10^{-8}	1.33×10^{-9}	1.9	1.85×10^{-5}	2.98×10^{-8}
IV	3.11×10^{-7}	1.91×10^{-8}	17.8	2.83×10^{-5}	4.64×10^{-7}

From the results, we made the evidence that the crystalline state of the samples is involved in the dissolution mechanism during the initial kinetic leaching and the reaching of the pseudo steady-state equilibrium. The normalized mass loss rates (NLR) depending on the specific surface area show again the similar behaviour between the powder synthesized at 1300 °C (III) and the crushed sphere (I).

Finally the same evolution of the ratios grain/grains boundaries and global/kinetic leaching behaviour can be described as following: (IV) > (II) > (I) = (III) with (I) Crushed ThO$_2$ spheres, (II) Initial ThO$_2$ spheres, (III) ThO$_2$ powder synthesized at 1300 °C, (IV) ThO$_2$ powder synthesized at 700 °C.

ThO$_2$ powder synthesized at 700 °C (Sample IV)

The Figure 4 presents the concentrations of [^{232}Th] and [^{229}Th] as a function of the contact time for sample (IV) ThO$_2$ powder synthesized at 700 °C at pH = 3.2 and monitored by ICP-MS for a contact time of 500 days. The Table 3 presents the experimental data from the dissolution experiments of sample (IV). When the NLR is determined as a negative value, we can assume that a precipitation process occurs onto the solid surface after the ^{229}Th spike experiments. Then, after the ^{229}Th addition, a quick precipitation of the ThO$_x$(OH)$_y$(H$_2$O)$_z$ phase occurs at the surface of the ThO$_2$ powder synthesized at 700 °C (I) and the slow leaching of this phase is following by the ^{229}Th and ^{232}Th isotopes measurements. Then, we assume that the Thorium Oxide at the surface is not completely crystallized and/or is nano-crystallized. That is the reason why we propose ThO$_x$(OH)$_y$(H$_2$O)$_z$ as possible phase at the surface as described elsewhere (*Vandenborre et al. 2001*). Moreover we can observe a dynamic exchange between the ^{232}Th onto the surface with the ^{229}Th in the solution. This dynamic exchange process is based on the increasing concentration values of ^{232}Th and on the decreasing concentration values of ^{229}Th. So, we can conclude that the ThO$_x$(OH)$_y$(H$_2$O)$_z$ phase with the low crystallinity of the surface and then the high kinetic of leaching is reactive versus the isotopic Th exchange. During the Desorption experiment, the same behaviour of the surface/solution system is displayed. Then, the dynamic exchange between the surface and the solution is quickly reached, less than one day. So we can conclude that the thermodynamic solubility has been reached for this sample due to the secondary phase ThO$_x$(OH)$_y$(H$_2$O)$_z$ which control the solubility.
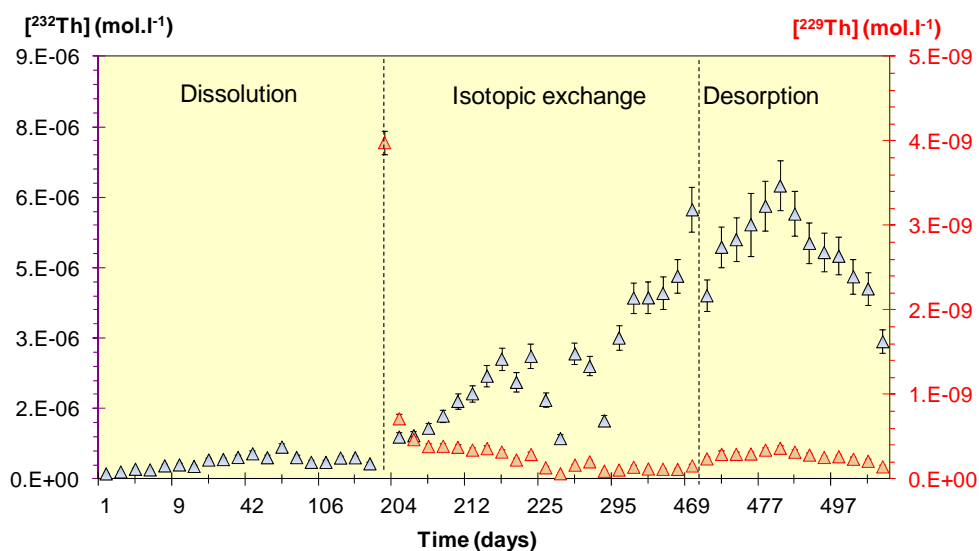

Fig. 4 [^{232}Th] and [^{229}Th] = f(contact time) for Sample (IV) ThO$_2$ powder synthesized at 700 °C at pH = 3.2, monitored by ICP-MS.

Table 3: Experimental data from the Dissolution experiments for Sample (IV) with a contact time of 220 days.

Th isotope	[Th]50d mol/L	Slope (1-10d) mol/L/d	NLR(1-10d) g/m^2/d	Slope (200-220d) mol/L/d	NLR(200-220d) g/m^2/d
^{232}Th	4.64×10^{-7}	1.91×10^{-8}	2.83×10^{-5}	1.01×10^{-7}	1.50×10^{-4}
^{229}Th	×	×	×	-2.86×10^{-11}	-4.25×10^{-8}

Initial ThO$_2$ spheres (Sample II)

The Figure 5 presents the concentrations of [^{232}Th] and [^{229}Th] as a function of the contact time for Sample (II) Initial ThO$_2$ spheres at pH = 3.2 and monitored by ICP-MS for a contact time of 500 days. The Table 4 presents the experimental data from the dissolution experiments of Sample (II). The "×" indicate that ^{229}Th has not been spiked into the solution before a contact time of 200 days. From the results, we can conclude that, in the case of the Initial ThO$_2$ spheres (II), leaching phenomena did not occur after the ^{229}Th addition. However, for this case (at contact time of 160 days) the SEM picture in Figure 1 shows the dissolution process of the grain boundaries. On the contrary, in the first part (between 200 and 225 days), the slow precipitation of one phase mixing ^{229}Th and ^{232}Th is shown with a low kinetic explained by its slow diffusion into the grain boundaries of the solid surface. The second part (between 225 and 470 days) shows a dissolution process of the fresh precipitate phase, maybe the same ThO$_x$(OH)$_y$(H$_2$O)$_z$ phase with the same dynamic exchange observed in the sample IV (see above). In the final range of time (564 days) the SEM picture (Figure 1) displays the reprecipitation process into the grain boundaries (grain size increase). This change of the surface behaviour during the Isotopic Exchange implies a difference in the accessiblity of the grains boundaries for the Th into the solution. The gap displayed at 470 days of contact time makes the evidence that this dissolution mechanism is a kinetic process. In the desorption experiment, the redissolution process of this phase goes on to occur at the solid/solution interface. The thermodynamic solubility of this solid has not been reached in this experiment. Nevertheless, the results, presented here for the Initial ThO$_2$ spheres (II), are not quite determined because the Specific Surface Area can not been measured the classical N$_2$ adsorption method. Moreover, as seen in the SEM pictures (see Figure 1), the specific surface area has changed during the Dissolution, isotopic exchange and desorption experiments with an evolution of the grains vs. grain boundaries ratio. So, we cannot measure or calculate the specific surface area for this solid sample.
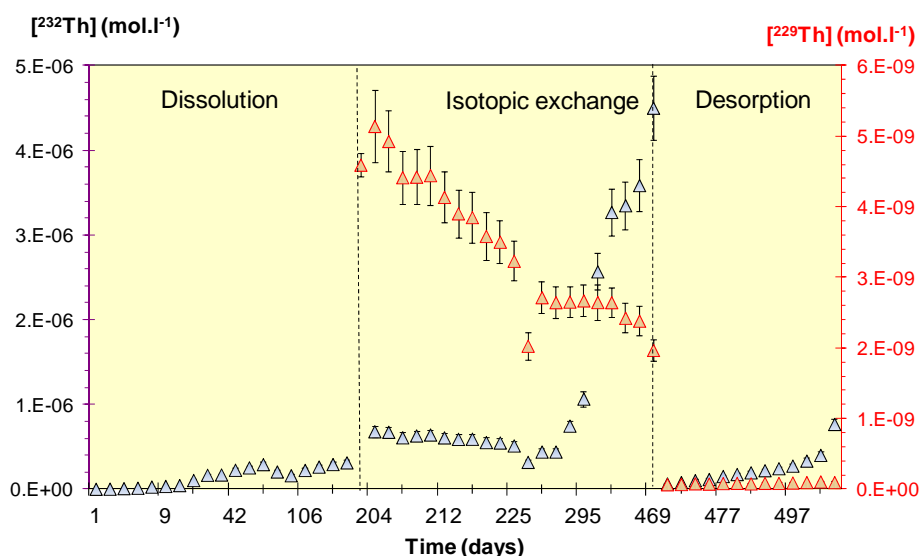
Fig. 5 [^{232}Th] and [^{229}Th] = f(contact time) for Sample (II) Initial ThO$_2$ spheres at pH = 3.2, monitored by ICP-MS.

Table 4: Experimental data from the Dissolution experiments for Sample (II) with a contact time of 220 days.

Th isotope	[Th]50d mol/L	Slope (1-10d) mol/L/d	NLR(1-10d) g/m^2/d	Slope (200-220d) mol/L/d	NLR(200-220d) g/m^2/d
^{232}Th	2.56×10^{-7}	4.38×10^{-9}	?	-7.76×10^{-9}	?
^{229}Th	×	×	×	-9.65×10^{-11}	?

Crushed ThO$_2$ sphere and ThO$_2$ powder synthesized at 1300°C (Samples I and III)

The Figure 6 presents the concentrations of [^{232}Th] and [^{229}Th] as a function of the contact time for sample (I) Crushed ThO$_2$ sphere and sample (III) ThO$_2$ powder synthesized at 1300 °C at pH = 3.2, monitored by ICP-MS for a contact time up to 500 days. The Table 5 presents the experimental data from the dissolution experiments of Samples (I) and (III). The "×" indicate that ^{229}Th has not been spiked into the solution before a contact time of 200 days. As shown in the previous Dissolution experiments, before the ^{229}Th addition, the behavior versus the leaching phenomena of the surface of the Crushed ThO$_2$ spheres (I) and of the ThO$_2$ powder synthesized at 1300 °C (III) is very close. Moreover, the same results are been observed after the ^{229}Th addition: there is no exchange between the two isotopes of the Th (229 and 232) and we observed a slower leaching process of the solid surface. Moreover, we can conclude that the leaching rate values for the samples (I) and (III), respectively

2.22 × 10^{-5} and 1.62 × 10^{-5} g/m^2/d, are lower to its of the ThO$_2$ powder synthesized at 700 °C (I), 2.83 × 10^{-5} g/m^2/d, which has been described as an ThO$_x$(OH)$_y$(H$_2$O)$_z$ phase. Similar as the desorption experiment for the initial ThO$_2$ sphere (sample II), a gap in Th concentrations is measured in solution. However, in this desorption experiment the curve slope calculated (6 × 10^{-10} mol/L/d) is ten-fold lower than the value calculated in the Initial HTR sphere (6.0 × 10^{-9} mol/L/d). We can conclude that there is no ThO$_x$(OH)$_y$(H$_2$O)$_z$ phase precipitation/dissolution in this case and no grain boundaries at the solid surface. Thus, the dissolution mechanism is a kinetic process for this sample and thermodynamic solubility is not yet reached in this experiment and need a longer duration time (more than 500 days in this experiment).
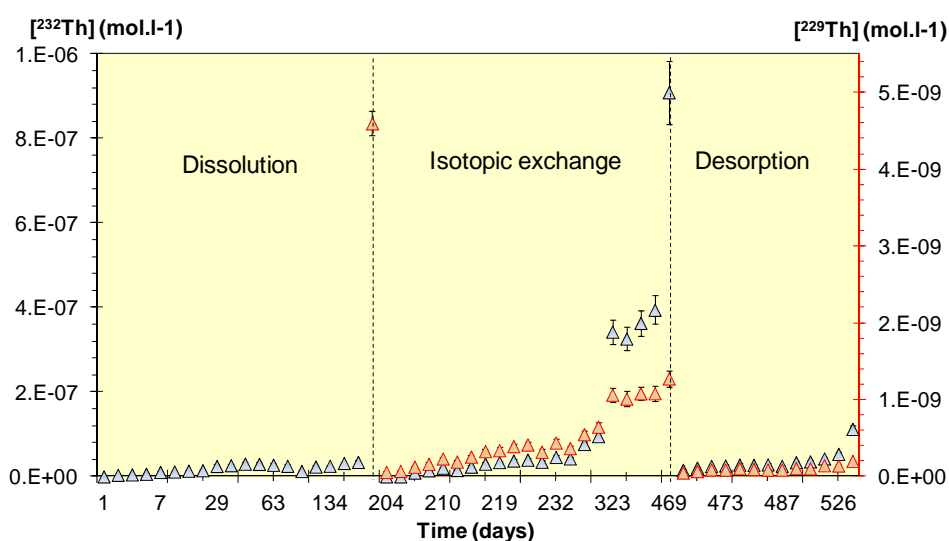
Fig. 6 [^{232}Th] and [^{229}Th] = f(contact time) for Sample (I) Crushed ThO$_2$ sphere and Sample (III) ThO$_2$ powder synthesized at 1300 °C at pH = 3.2, monitored by ICP-MS.

Table 5: Experimental data from the Dissolution experiments for Samples (I) and (III) with a contact time of 220 days.

Th isotope	[Th]50d mol/L	Slope (1-10d) mol/L/d	NLR(1-10d) g/m^2/d	Slope (200-220d) mol/L/d	NLR(200-220d) g/m^2/d
^{232}Th / Ech I	2.95 × 10^{-8}	1.35 × 10^{-9}	1.88 × 10^{-5}	1.60 × 10^{-9}	2.22 × 10^{-5}
^{232}Th / Ech III	2.98 × 10^{-8}	1.33 × 10^{-9}	1.85 × 10^{-5}	1.17 × 10^{-9}	1.62 × 10^{-5}
^{229}Th / Ech I	×	×	×	1.98 × 10^{-11}	2.75 × 10^{-7}
^{229}Th/ Ech III	×	×	×	2.01 × 10^{-11}	2.79 × 10^{-7}

Relative enrichment for the samples I, II, III and IV

Relative enrichment (RE) values in 229Th have been calculated for each sample, as described in experimental section. Results are shown in Figure 7 with logarithmic scale for y-axis. These calculations check that all sample surfaces are more and more rich in ^{229}Th isotope because RE increases with contact time and is high than 1. The RE values of samples IV, 700 °C powder, and II, initial sphere, quickly increase for the first days of contact time after ^{229}Th addition (between 200 and 250 days) which correspond to the precipitation process of the $ThO_x(OH)_y(H_2O)_z$ phase in grain boundaries (GB) for the Initial sphere case. For the second part of contact time (between 300 and 450 days) a steady-state is measured for all the samples with for higher than 10 RE values (samples IV and II with GB) a dynamic isotopic exchange between the surface and the solution; and for the other samples (I and III without GB) with RE values lower than 10 a pseudo equilibrium state with no Th isotopes exchange between the surface and the solution. For the last part (between 450 and 550 days of contact time) no change in RE values occurs for the samples (I and III) without GB because of the slow dissolution process of the ThO_2 crystallized grains ($5 < RE < 10$). Moreover, no change occurs too for the samples IV (700 °C powder) due to the thermodynamic solubility equilibrium reached for this system by the main $ThO_x(OH)_y(H_2O)_z$ phase control with an high RE value ($300 < RE < 400$). However, for the Initial sphere (sample II) the same behaviour than for the first part is observed but it is relied on the redissolution process of the $ThO_x(OH)_y(H_2O)_z$ phase into the GB with RE value close to the sample IV (~100).

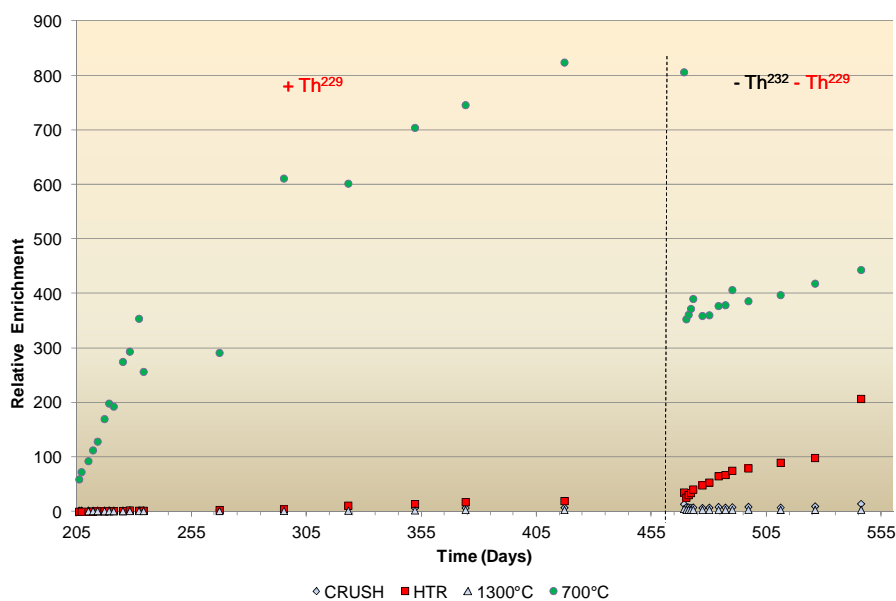**Fig. 7 Relative Enrichment in ^{229}Th in Log scale = f(contact time) for Samples (I) Crushed ThO$_2$ sphere, (II) Initial ThO$_2$ spheres, (III) ThO$_2$ powder synthesized at 1300 °C and (IV) ThO$_2$ powder synthesized at 700 °C at pH = 3.2.**

Conclusions and Future work

We have described the different behaviour of the surfaces of ThO_2 versus the surface crystalline state. The use of the isotopic $^{229}Th/^{232}Th$ exchange assesses the key issue of this Workpackage: the realistic solubility behaviour of the ThO_2 surface. We have classified the 4 sets of solid samples versus the leaching behaviour: (IV) > (II) > (I) = (III) with (I) Crushed ThO_2 spheres, (II) Initial ThO_2 spheres, (III) ThO_2 powder synthesized at 1300 °C, (IV) ThO_2 powder synthesized at 700 °C. Moreover, the behavior of the solid versus the $^{229}Th/^{232}Th$ exchange occurs if the $ThO_x(OH)_y(H_2O)_z$ phase is implied into the solid surface leaching. Moreover, three kinds of surfaces of the ThO_2 have been studied:

1) Powder synthesized at low temperature (700 °C): this surface displays a low crystallinity with a strong control of the thermodynamic solubility by the $ThO_x(OH)_y(H_2O)_z$ phase. The curve of relative enrichment in ^{229}Th isotope vs. the contact time gives the high exchange between the surface and the solution in order to reach this thermodynamic equilibrium.

2) Initial HTR sphere of ThO_2: this surface presents a high crystallinity but with grain boundaries (GB). In this case it is the accessibility of the GB phase, probably the same phase that $ThO_x(OH)_y(H_2O)_z$, which control the dissolution/precipitation/redissolution mechanisms. These processes have been check by SEM analysis where the grains size of ThO_2 clearly evolves during the contact time. The curve of relative enrichment in ^{229}Th isotope vs. the contact time makes the evidence that the high slope value of the RE corresponds to the precipitation process and for the second one to the redissolution process of the GB phase.

3) Powder synthesized at high temperature (1300 °C) and the crushed HTR sphere: these both samples present exactly the same behavior for all the 500 days of solid/solution contact experiment. These surfaces present a high crystallinity without GB. The main process is the slow dissolution of the ThO_2 crystallized grains which is validated by the slow evolution of the RE curve slope. In this case, the thermodynamic solubility cannot be reached before a higher contact time than in our study (500 days).

The future and complementary work which can be performed is the modeling of our experimental data in order to propose dissolution/precipitation mechanisms of the ThO_2 in solution, in particular by taking into account the $ThO_x(OH)_y(H_2O)_z$ phase which can be described as a solution-solid at the solid surface.

Acknowledgement

References

Heisbourg, G., 2003. Synthèse, caractérisation et études cinétique et thermodynamique de la dissolution de ThO_2 et des solutions solides $Th_{1-x}M_xO_2$ (M = U, Pu), Ph.D. Université Paris XI, Orsay.

Müller, A., 2006. Establishment of the technology to manufacture uranium dioxide kernels for PBMR fuel. Proceedings HTR2006 : 3rd International Topical Meeting on High Temperature Reactor Technology B00000070.

Oktay, E., Yayli, A., 2001. Physical properties of thorium oxalate powders and their influence on the thermal decomposition. Journal of Nuclear Materials 288, 76-82.

Rand, M., Fuger, J., Neck, V., Grenthe, I., Rai, D., 2008. Chemical Thermodynamics of Thorium. North Holland Elsevier Science Publishers B. V., Amsterdam, The Netherlands.

Vandenborre, J., Grambow, B., Abdelouas, A., 2010. Discrepancies in Thorium Oxide Solubility Values: Study of Attachment/Detachment Processes at the Solid/Solution Interface. Inorganic Chemistry 49, 8736-8748.

THE EFFECT OF PH AND IONIC STRENGTH ON THE DISSOLUTION OF TCO$_2$ IN HYPERALKALINE ENVIRONMENTS

N.D.M. Evans*

Department of Chemistry, Loughborough University, UK

* Corresponding author: n.d.m.evans@lboro.ac.uk

1.   Introduction

The UK has a relatively high inventory of ^{99}Tc in the wastes to manage. Under the planned cementitious Geological Disposal facility (GDF) conditions of high pH and low Eh most technetium should be immobile as the solid phase TcO$_2$(am). Nevertheless, not much is known about the behaviour of this solid phase. The Loughborough University task within work-package 3 was to investigate the dissolution behaviour of amorphous technetium (IV) oxide containing the isotope ^{99}Tc as a function of various parameters, viz. pH (10.5, 12.5 and 13.3), ionic strength (I = 1 mol dm^{-3} and I = 3 mol dm^{-3}), and the age of the solid phase (1 day to 1 year).

2.   Experimental

To this aim, fully-reduced, high purity ^{99}TcO$_2$(s) was produced electrochemically using the method in Warwick *et al*[1], from ammonium pertechnetate. The ammonium pertechnetate solution (20 mL in a 50 mL centrifuge tube in an anaerobic glove box, concentration 4×10^{-6} mol L^{-1} technetium in each tube) was adjusted to pH 10.5, 12.5 or 13.3 and ionic strength 1.0 mol L^{-1} or 3.0 mol L^{-1} before reduction for 2 hours at 6 V using vitreous carbon cathode and Pt wire anode in the presence of 0.01 mol L^{-1} sodium dithionite as a holding reductant. Five replicates of each system were set-up and kept in an anaerobic glove box for up to 12 months for sampling.

2.1   *Procedure for Liquid Scintillation Counting to measure [^{99}Tc](aq)*

The sample to be counted (2 cm^3) was placed into a 20 cm^3 scintillation vial and pH adjusted to circumneutral using dilute HCl(aq) as appropriate. Gold Star Scintillation cocktail (10 cm^3) was added to the sample and which was then mixed on a Labnet VX100 vortex mixer for approximately 5 seconds. The sample was then placed inside the Packard liquid scintillation analyser TRI-CARB 2750/LL and allowed to light adjust for one hour prior to analysis of the sample. The sample was counted until 10 000 counts were measured, or for one hour, whichever condition was reached first.

3.   Results and Discussion

3.1   pH 10.5, Ionic strength = 1.0 mol L^{-1}

Figure 1 shows the data on the aqueous concentration of technetium collected over a period of 12 months from the solutions at pH 10.5 and an ionic strength of 1.0 mol L^{-1} sodium chloride solution. Steady state was reached after around 24 hours at an aqueous concentration of technetium of (12.8 ± 1.0) nmol L^{-1}. Any perceived fluctuations in the data from the third datum point onwards have been shown to be statistically insignificant using the ANOVA single factor test at both 95% and 99% confidence limits, thus this set of experiments has been terminated.

Fig. 1 Supernatant concentration of ^{99}Tc as a function of time at pH 10.5 ± 0.1 (addition of NaOH) and ionic strength = 1.0 mol L^{-1} (addition of NaCl), 20 mL solution of 4 ⅹ 10^{-6} mol·L^{-1} [Tc] in each tube before reduction, i.e. 8 ⅹ 10^{-6} g ^{99}Tc per tube, 5 replicates of each, error bars ± 1 s.d.

3.2   pH 10.5, Ionic strength = 3.0 mol L^{-1}

Figure 2 shows the data on the aqueous concentration of technetium collected over a period of 12 months from the solutions at pH 10.5 and an ionic strength of 3.0 mol L^{-1} sodium chloride solution. Steady state was reached after around 2 hours at an aqueous concentration of technetium of (17.0 ± 2.1) nmol L^{-1}. No significant change was observed in this concentration over the period of a year, thus this set of experiments has also been terminated.

Fig. 2 Supernatant concentration of ^{99}Tc as a function of time at pH 10.5 ± 0.1 (addition of NaOH) and ionic strength = 3.0 mol L^{-1} (addition of NaCl), 20 mL solution of 4 ✕ 10^{-6} mol L^{-1} [Tc] in each tube before reduction, i.e. 8 ✕ 10^{-6} g ^{99}Tc per tube, 5 replicates of each, error bars ± 1 s.d.

3.3 Effect of ionic strength at pH 10.5

The steady-state aqueous concentration of technetium changed from (12.8 ± 1.0) nmol L^{-1} to (17.0 ± 2.1) nmol L^{-1} as the ionic strength rose from 1.0 to 3.0 mol L^{-1} in the presence of NaCl as a background electrolyte. This change has been investigated using the ANOVA single factor test and is significant at the 99% confidence level. Therefore, it can be said that the change in ionic strength has affected the steady-state aqueous concentration of technetium. Until a new set of experiments has been set-up it is not possible to determine is this is due to changes in the solid phase of chloride complexation or some other factor(s).

3.4 pH 12.5, Ionic strength = 1.0 mol L^{-1}

Figure 3 shows the data on the aqueous concentration of technetium collected over a period of 12 months from the solutions at pH 12.5 and an ionic strength of 1.0 mol L^{-1} sodium chloride solution. Steady state was reached after around 100 hours at an aqueous concentration of technetium of (29.6 ± 3.1) nmol L^{-1}. Any perceived fluctuations in the data from the fourth datum point onwards have been shown to be statistically insignificant using the ANOVA single factor test at both 95% and 99% confidence limits, thus this set of experiments has been terminated.
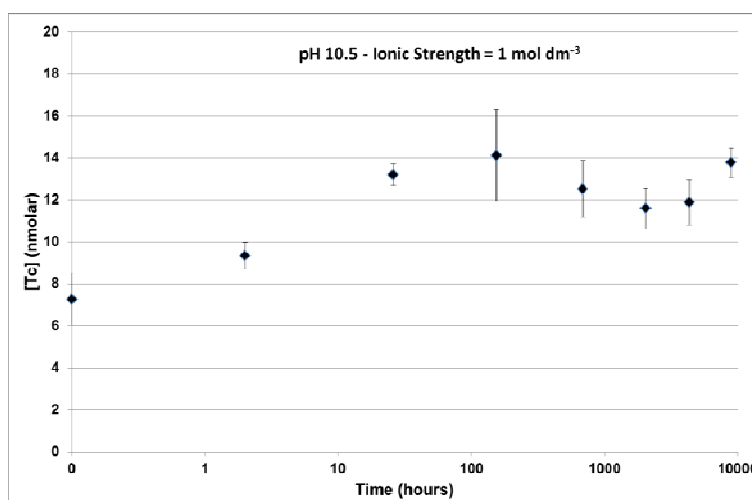
Fig. 3 Supernatant concentration of *99****Tc as a function of time at pH 12.5 ± 0.1 (addition of NaOH) and ionic strength = 1.0 mol·L-1 (addition of NaCl), 20 mL solution of 4 × 10-6 mol L-1 [Tc] in each tube before reduction, i.e. 8 × 10-6 g 99Tc per tube, 5 replicates of each, error bars ± 1 s.d.***

3.5   pH 12.5, Ionic strength = 3.0 mol L-1

Figure 4 shows the data on the aqueous concentration of technetium collected over a period of 12 months from the solutions at pH 12.5 and an ionic strength of 3.0 mol L-1 sodium chloride solution. Steady state was reached before the 689 hours at an aqueous concentration of technetium of (30.3 ± 2.7) nmol L-1. The apparent upward trend of the data points in Figure 4 has been shown not to be statistically significant from the 689 to 8921 hour data points using the ANOVA single factor test at both 95% and 99% confidence limits, thus this set of experiments has also been terminated.

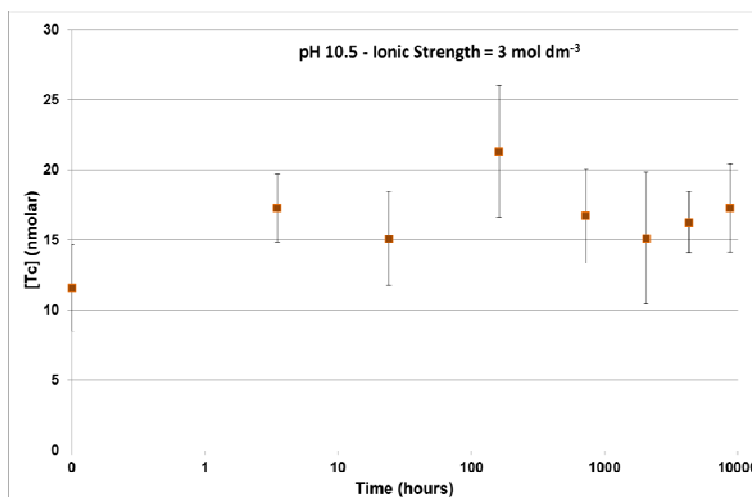**Fig. 4 Supernatant concentration of ^{99}Tc as a function of time at pH 12.5 ± 0.1 (addition of NaOH) and ionic strength = 3.0 mol L^{-1} (addition of NaCl), 20 mL solution of $4 \cdot 10^{-6}$ mol L^{-1} [Tc] in each tube before reduction, i.e. $8 \cdot 10^{-6}$ g ^{99}Tc per tube, 5 replicates of each, error bars ± 1 s.d.**

3.6   Effect of ionic strength at pH 12.5

The data show that there is no effect of changing the ionic strength from 1.0 mol L^{-1} to 3.0 mol L^{-1} at pH 12.5.

3.7   pH 13.3, Ionic strength = 1.0 mol L^{-1}

Figure 5 shows the data on the aqueous concentration of technetium collected over a period of 12 months from the solutions at pH 13.3 and an ionic strength of 1.0 mol L^{-1} sodium chloride solution. Steady state was reached at around 1000 hours at an aqueous concentration of technetium of (175 ± 33) nmol L^{-1}. From that time onwards, no significant change was observed in the data, thus this set of experiments has also been terminated.
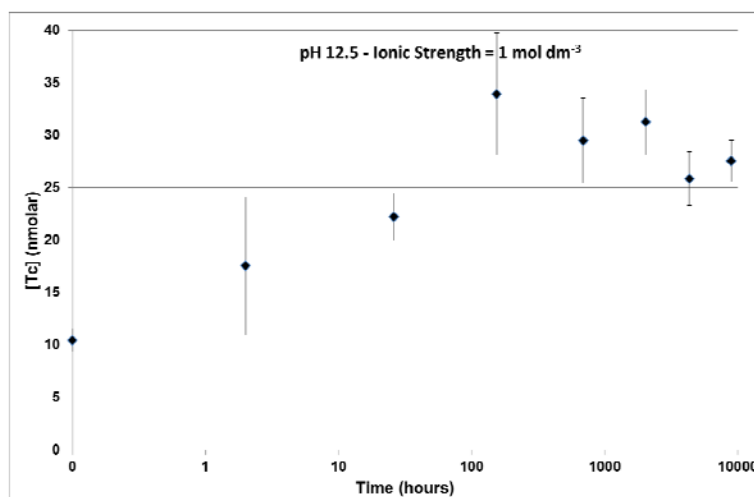
Fig. 5 Supernatant concentration of ^{99}Tc as a function of time at pH 13.3 ± 0.1 (addition of NaOH) and ionic strength = 1.0 mol L^{-1} (addition of NaCl), 20 mL solution of 4×10^{-6} mol L^{-1} [Tc] in each tube before reduction, i.e. 8×10^{-6} g ^{99}Tc per tube, 5 replicates of each, error bars ± 1 s.d.

3.8   pH 13.3, Ionic strength = 3.0 mol L^{-1}

Figure 6 shows the data on the aqueous concentration of technetium collected over a period of 12 months from the solutions at pH 13.3 and an ionic strength of 3.0 mol L^{-1} sodium chloride solution. Steady state has not been reached in this set of experiments. The aqueous concentration of technetium of (356 ± 59) nmol L^{-1}. There is one final set of tubes yet to be sampled. These will be sampled early in 2014 to determine if steady-state has been reached at 18 months.
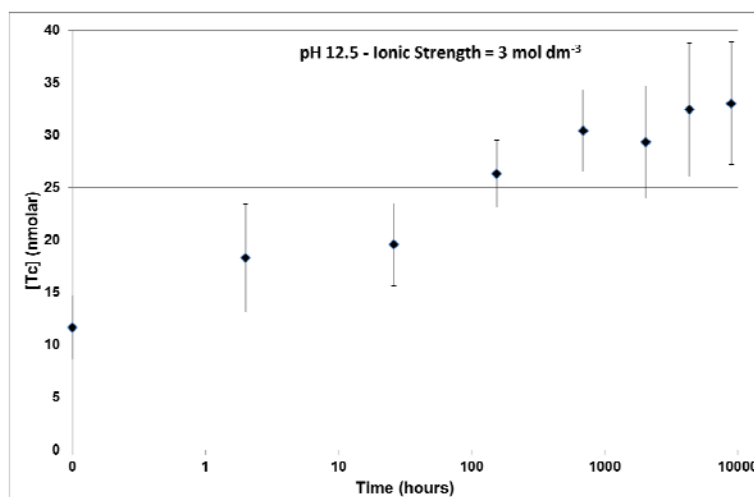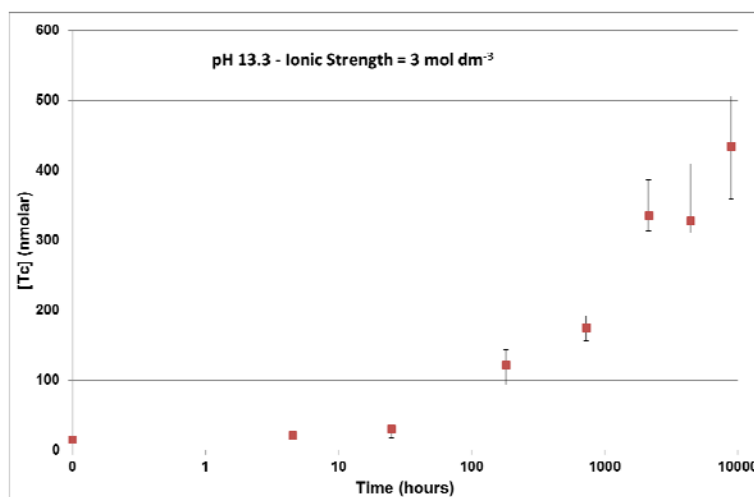
Fig. 6 Supernatant concentration of ^{99}Tc as a function of time at pH 13.3 ± 0.1 (addition of NaOH) and ionic strength = 3.0 mol L^{-1} (addition of NaCl), 20 mL solution of 4⋅10^{-6} mol L^{-1} [Tc] in each tube before reduction, i.e. 8⋅10^{-6} g ^{99}Tc per tube, 5 replicates of each, error bars ± 1 s.d.

3.9   Effect of ionic strength at pH 13.3

The measured aqueous concentration of technetium changed from (175 ± 33) nmol L^{-1} to (356 ± 59) nmol L^{-1} as the ionic strength rose from 1.0 to 3.0 mol L^{-1}. As the pH 13.3, I = 3.0 mol L^{-1} system has not reached steady state, no firm conclusion can be drawn except to say that it appears as though the same ionic-strength-effect as at pH 10.5 is being observed.

3.10   Summary of concentration data

Table 1 summarises the final measured aqueous concentrations of technetium measured.

*Table 1: Steady-state supernatant concentration of ^{99}Tc from pH 10.5 to 13.3 at ionic strengths of 1.0 and 3.0 mol L^{-1}, 5 replicates of each, errors ± 1 s.d. *Not at steady-state after 12 months*

pH	Ionic Strength (mol L^{-1})	Steady state [Tc] (nmol L^{-1})
10.5	1	12.8 ± 1.0
10.5	3	17.0 ± 2.1
12.5	1	29.6 ± 3.1
12.5	3	30.3 ± 2.7
13.3	1	175 ± 33
13.3	3	356 ± 59*

References

[1] The Solubility of Technetium(IV) at High pH, P. Warwick, S. Aldridge, N. Evans and S. Vines, Radiochimica Acta, 2007, 95(12), 709-716

THE EFFECT OF AGE OF SOLID PHASE ON THE DISSOLUTION OF TCO₂ IN HYPERALKALINE ENVIRONMENTS

N.D.M. Evans*

Department of Chemistry, Loughborough University, UK

* Corresponding author: n.d.m.evans@lboro.ac.uk

1. Introduction

The UK has a relatively high inventory of ^{99}Tc in the wastes to manage. Under the planned cementitious Geological Disposal Facility (GDF) conditions of high pH and low Eh most technetium should be immobile as the solid phase TcO_2(am). Nevertheless, not much is known about the behaviour of this solid phase. The Loughborough University task within work-package 3 was to investigate the dissolution behaviour of amorphous technetium (IV) oxide containing the isotope ^{99}Tc as a function of various parameters, viz. pH (10.5, 12.5 and 13.3), ionic strength ($I = 1$ mol dm^{-3} and $I = 3$ mol dm^{-3}), and the age of the solid phase (1 day to 1 year).

2. Experimental

Fully-reduced, high purity $^{99}TcO_2$(s) was produced electrochemically using the method in Warwick *et al*[1], from ammonium pertechnetate. The ammonium pertechnetate solution (20 mL in a 50 mL centrifuge tube, concentration 4×10^{-6} mol L^{-1} technetium in each tube) was adjusted to pH 10.5, 12.5 or 13.3 and ionic strength 1.0 mol L^{-1} or 3.0 mol L^{-1} in a nitrogen atmosphere anaerobic glove box (< 1 ppm O$_2$), before reduction for 2 hours at a potential difference of 6 V using a vitreous carbon cathode and Pt wire anode in the presence of 0.01 mol L^{-1} sodium dithionite as a holding reductant. Three replicates of each system were set-up and kept in an anaerobic glove box for up to 12 months for sampling. To investigate the effect of the age of the solid phase the systems were centrifuged and the supernatant removed to waste. This was replaced by an equal volume of the same solution, i.e. the same pH and ionic strength. The new system was allowed to equilibrate for 24 hours before a sample was taken in triplicate for measurement of the aqueous concentration of technetium.

2.1 Procedure for Liquid Scintillation Counting to measure [^{99}Tc](aq)

The sample to be counted (2 mL) was placed into a 20 cm^3 scintillation vial and pH adjusted to circumneutral using dilute HCl (aq) as appropriate. Gold Star Scintillation cocktail (10 mL)

was added to the sample and which was then mixed on a Labnet VX100 vortex mixer for approximately 5 seconds. The sample was then placed inside the Packard liquid scintillation analyser TRI-CARB 2750/LL and allowed to light adjust for one hour prior to analysis of the sample. The sample was counted until 10 000 counts were measured, or for one hour, whichever condition was reached first.

3. Results and Discussion

3.1 pH 10.5, Ionic strength = 1.0 mol L^{-1}

Figure 1 shows the data on the aqueous concentration of technetium collected over a period of 12 months from the supernatant above different ages of solid phase TcO_2(am) 24 hours after separation and addition of a fresh solution at pH 10.5 and an ionic strength of 1.0 mol L^{-1}. The measured aqueous concentration of technetium in the supernatant after 24 hours was determined to be (22.6 ± 4.7) nmol L^{-1}. The fluctuations in the data have been shown to be not statistically significant using the ANOVA single factor test at a 95% confidence limits, i.e. no correlation was found between the age of the solid phase and the measured aqueous concentration of technetium in the supernatant after 24 hours equilibration in fresh solution. Thus this set of experiments has been terminated.

Fig. 1 Supernatant concentration of ^{99}Tc in fresh solution, equilibrated for 1 day, as a function of aging time at pH 10.5 ± 0.1 (NaOH), I = 1.0 mol L^{-1} (NaCl), 20 mL solution of 4×10^{-6} mol L^{-1} [Tc] in each tube before reduction, i.e. 8×10^{-6} g ^{99}Tc per tube, 3 replicates, error bars ± 1 s.d.

3.2 pH 10.5, Ionic strength = 3.0 mol L^{-1}

Figure 2 shows the data on the aqueous Tc concentration collected over a period of 12 months from the supernatant above different ages of solid phase TcO_2(am), 24 hours after separation

from the original supernatant, with subsequent addition of a fresh solution at pH 10.5 and an ionic strength of 3.0 mol L^{-1}. The measured aqueous concentration of technetium in the supernatant after 24 hours was determined to be (257 ± 63) nmol L^{-1}. No statistically significant correlation was found between the age of the solid phase and the measured aqueous concentration of technetium in the supernatant after 24 hours equilibration in fresh solution. Thus this set of experiments has been terminated.
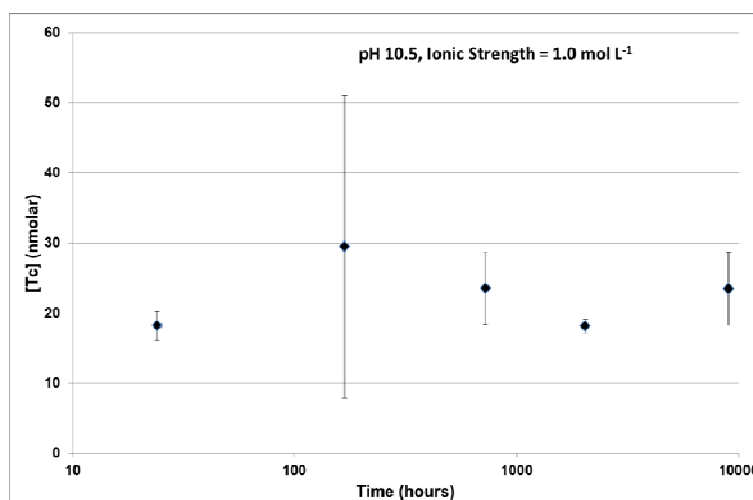

Fig. 2 Supernatant concentration of ^{99}Tc in fresh solution, equilibrated for 1 day, as a function of aging time at pH 10.5 ± 0.1 (NaOH), I = 3.0 mol L^{-1} (NaCl), 20 mL solution of 4✻10^{-6} mol L^{-1} [Tc] in each tube before reduction, i.e. 8✻10^{-6} g ^{99}Tc per tube, 3 replicates, error bars ± 1 s.d.

3.3   Effect of ionic strength at pH 10.5

The steady-state aqueous concentration of technetium changed from (22.6 ± 4.7) nmol L^{-1} to (257 ± 63) nmol L^{-1} as the ionic strength rose from 1.0 to 3.0 mol L^{-1} in the presence of NaCl as a background electrolyte. The change in ionic strength appears to have increased the aqueous concentration of technetium by an order of magnitude.

3.4   pH 12.5, Ionic strength = 1.0 mol L^{-1}

Figure 3 shows the data on the aqueous Tc concentration collected over a period of 12 months from the supernatant above different ages of solid phase TcO$_2$(am), 24 hours after separation from the original supernatant, with subsequent addition of a fresh solution at pH 12.5 and an ionic strength of 1.0 mol L^{-1}. The measured aqueous concentration of technetium in the supernatant after 24 hours was determined to be (32.2 ± 6.3) nmol L^{-1}. No statistically significant correlation was found between the age of the solid phase and the measured aqueous concentration of technetium in the supernatant after 24 hours equilibration in fresh solution. Therefore, this set of experiments has been terminated.

Fig. 3 Supernatant concentration of ^{99}Tc in fresh solution, equilibrated for 1 day, as a function of aging time at pH 12.5 ± 0.1 (NaOH), I = 1.0 mol L^{-1} (NaCl), 20 mL solution of 4 ✻ 10^{-6} mol L^{-1} [Tc] in each tube before reduction, i.e. 8 ✻ 10^{-6} g ^{99}Tc per tube, 3 replicates, error bars ± 1 s.d.

3.5   *pH 12.5, Ionic strength = 3.0 mol L^{-1}*

Figure 4 shows the data on the aqueous Tc concentration collected over a period of 12 months from the supernatant above different ages of solid phase TcO$_2$(am), 24 hours after separation from the original supernatant, with subsequent addition of a fresh solution at pH 12.5 and an ionic strength of 3.0 mol L^{-1}. The measured aqueous concentration of technetium in the supernatant after 24 hours was determined to be (182 ± 50) nmol L^{-1}. No statistically significant correlation was found between the age of the solid phase and the measured aqueous concentration of technetium in the supernatant after 24 hours equilibration in fresh solution. Therefore, this set of experiments has been terminated.
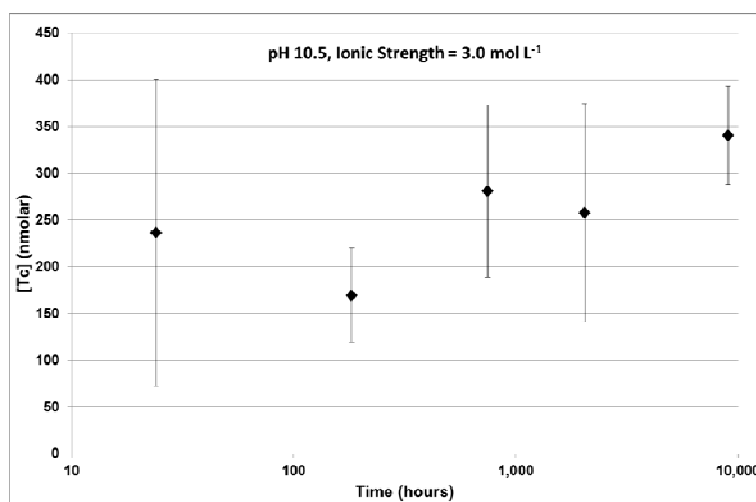
Fig. 4 Supernatant concentration of ^{99}Tc in fresh solution, equilibrated for 1 day, as a function of aging time at pH 12.5 ± 0.1 (NaOH), I = 3.0 mol L^{-1} (NaCl), 20 mL solution of 4 ⅹ 10^{-6} mol L^{-1} [Tc] in each tube before reduction, i.e. 8 ⅹ 10^{-6} g ^{99}Tc per tube, 3 replicates, error bars ± 1 s.d.

3.6   Effect of ionic strength at pH 12.5

The steady-state aqueous concentration of technetium changed from (32.2 ± 6.3) nmol L^{-1} to (182 ± 49.9) nmol L^{-1} as the ionic strength rose from 1.0 to 3.0 mol L^{-1} in the presence of NaCl as a background electrolyte. The change in ionic strength appears to have increased the aqueous concentration of technetium by a factor of around 6.

3.7   pH 13.3, Ionic strength = 1.0 mol L^{-1}

Figure 5 shows the data on the aqueous Tc concentration collected over a period of 12 months from the supernatant above different ages of solid phase TcO_2(am), 24 hours after separation from the original supernatant, with subsequent addition of a fresh solution at pH 13.3 and an ionic strength of 1.0 mol L^{-1}. The measured aqueous concentration of technetium in the supernatant after 24 hours was determined to be (191 ± 62) nmol L^{-1}. No statistically significant correlation was found between the age of the solid phase and the measured aqueous concentration of technetium in the supernatant after 24 hours equilibration in fresh solution. Therefore, this set of experiments has been terminated.
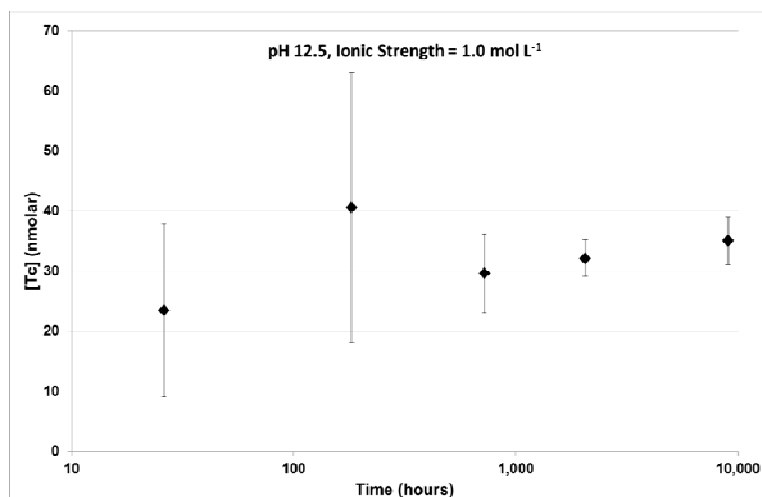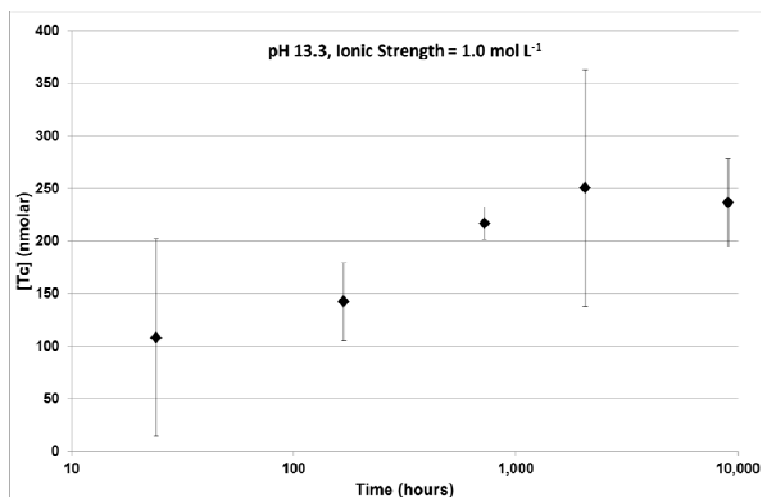
Fig. 5 Supernatant concentration of ^{99}Tc in fresh solution, equilibrated for 1 day, as a function of aging time at pH 13.3 ± 0.1 (NaOH), I = 1.0 mol L^{-1} (NaCl), 20 mL solution of 4 ⋆ 10^{-6} mol L^{-1} [Tc] in each tube before reduction, i.e. 8 ⋆ 10^{-6} g ^{99}Tc per tube, 3 replicates, error bars ± 1 s.d.

3.8   pH 13.3, Ionic strength = 3.0 mol L^{-1}

Figure 6 shows the data on the aqueous Tc concentration collected over a period of 12 months from the supernatant above different ages of solid phase TcO$_2$(am), 24 hours after separation from the original supernatant, with subsequent addition of a fresh solution at pH 13.3 and an ionic strength of 3.0 mol L^{-1}.
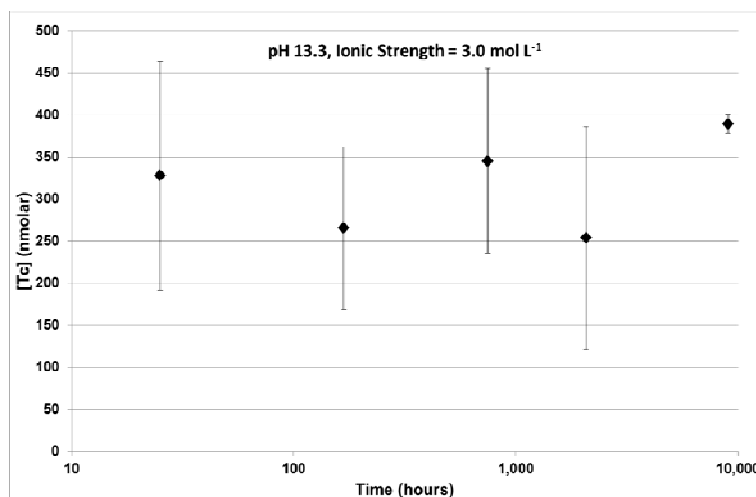
Fig. 6 Supernatant concentration of ^{99}Tc in fresh solution, equilibrated for 1 day, as a function of aging time at pH 13.3 ± 0.1 (NaOH), I = 3.0 mol L^{-1} (NaCl), 20 mL solution of 4✻10[-6] mol L^{-1} [Tc] in each tube before reduction, i.e. 8✻10[-6] g ^{99}Tc per tube, 3 replicates, error bars ± 1 s.d.

The measured aqueous concentration of technetium in the supernatant after 24 hours was determined to be (316 ± 56) nmol L^{-1}. No statistically significant correlation was found between the age of the solid phase and the measured aqueous concentration of technetium in the supernatant after 24 hours equilibration in fresh solution. Therefore, this set of experiments has been terminated.
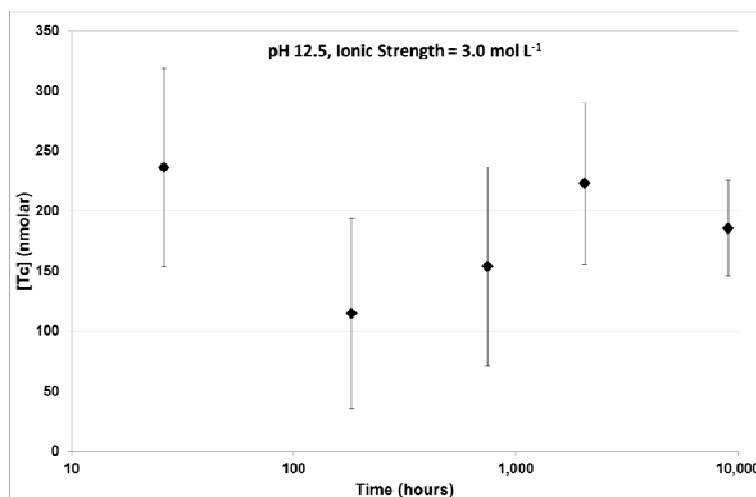
3.9   Effect of ionic strength at pH 13.3

The steady-state aqueous concentration of technetium changed from (191 ± 62) nmol L^{-1} to (316 ± 56) nmol L^{-1} as the ionic strength rose from 1.0 to 3.0 mol L^{-1} in the presence of NaCl as a background electrolyte. The change in ionic strength appears to have increased the aqueous concentration of technetium by a factor of around 1.5 to 2, still a rise but much less significant than at pH 10.5 or 12.5. Clearly with only 3 data points no robust comment can be made about the effect of ionic strength with pH, but the magnitude of the effect seems to decreasing with pH.

3.10   Effect of changes in pH

At an ionic strength of 3.0 mol L^{-1} there was no discernible effect of changing the pH from 10.5 to 13.3. At an ionic strength of 1.0 mol L^{-1} the measured aqueous concentration of technetium was significantly higher at pH 13.3 than at 12.5 or 10.5.

3.11   Summary of 'fresh solution' concentration data

Table 1 summarises the final measured aqueous concentrations of technetium measured.

Table 1: 'Fresh solution' supernatant concentrations of ^{99}Tc from pH 10.5 to 13.3 at ionic strengths of 1.0 and 3.0 mol L^{-1}, 3 replicates of each, errors ± 1 s.d.

Time	[Tc]	[Tc]	[Tc]	[Tc]	[Tc]	[Tc]
(hours)	(nmol L^{-1})	(nmol L^{-1})	(nmol L^{-1})	(nmol L^{-1})	(nmol L^{-1})	(nmol L^{-1})
pH/I (mol L^{-1})	10.5 – 1.0	12.5 - 1.0	13.3 - 1.0	10.5 - 3.0	12.5 - 3.0	13.3 - 3.0
24-26	18.3 ± 2.1	23.5 ± 14	108 ± 93	236 ± 164	236 ± 82	328 ± 136
168-182	29.5 ± 22	40.6 ± 23	142 ± 37	169 ± 51	115 ± 79	266 ± 96.5
722-746	23.6 ± 5.2	29.6 ± 6.6	217 ± 16	281 ± 92	154 ± 83	345 ± 110
2040-2056	18.2 ± 1.0	32.1 ± 3.0	250 ± 113	258 ± 117	223 ± 67	254 ± 132
9021	23.5 ± 5.2	35.1 ± 4.0	237 ± 43	340 ± 52	185 ± 40	389 ± 11.2
Mean	22.6 ± 4.7	32.2 ± 6.3	191 ± 62	257 ± 63	182 ± 50	316 ± 56

3.12   Comparison of 'fresh solution' concentration data with 'steady-state' data

For the six different systems investigated a comparison is shown in Table 2 between the 'steady-state' and 'fresh solution' measured aqueous concentrations of technetium. In 3 cases there is a statistically significant difference, at pH 10.5 – I = 1.0 mol L^{-1}, at pH 10.5 – I = 3.0 mol L^{-1} and at pH 12.5 – I = 3.0 mol L^{-1}. In each case the measured 'fresh solution' concentration of technetium was significantly the higher.

Table 2: Comparison of 'Fresh Solution' and 'Steady-State' supernatant concentrations of ^{99}Tc from pH 10.5 to 13.3 at ionic strengths of 1.0 and 3.0 mol L^{-1}, errors ± 1 s.d.

pH	Ionic Strength (mol L^{-1})	"Steady-State" [Tc] (nmol L^{-1})	"Fresh Solution" [Tc] (nmol L^{-1})	Difference significant at 95%?
10.5	1.0	12.8 ± 1.0	22.6 ± 4.7	Yes
10.5	3.0	17.0 ± 2.1	257 ± 63	Yes
12.5	1.0	29.6 ± 3.1	32.2 ± 6.3	No
12.5	3.0	30.3 ± 2.7	182 ± 50	Yes
13.3	1.0	175 ± 33	191 ± 62	No
13.3	3.0	356 ± 59*	316 ± 56	No

References

[1] The Solubility of Technetium(IV) at High pH, P. Warwick, S. Aldridge, N. Evans and S. Vines, Radiochimica Acta, 2007, 95(12), 709-716

INTERACTION BETWEEN URANIUM AND IRON (III) OXIDES

Mireia Grivé[*], Elisenda Colàs, Lara Duro

Amphos 21 (SPAIN)

* Corresponding author: mireia.grive@amphos21.com

Introduction

The interaction between uranium and iron solid phases is very relevant for the near and the far-field of a deep nuclear waste repository. Iron(III) solid oxides are not only important by their presence as corrosion products in the steel-based containers, but also because of their ubiquity in the geosphere.

The retention of radionuclides, U(VI) among them, by these Fe(III) solid phases is then relevant for the safety evaluation of the repository. The long time frames of interest for the safety assessment and the massive occurrence of iron compounds in the repository highlight the possibility of interactions between U(VI) and iron solid phases in the form of coprecipitates, that might be subjected to changes as the evolution of U(VI)/Fe(III) solids with time.

Among the iron oxides resulting from the steel corrosion processes of the canister and present in some of the engineered and geological barriers, amorphous ferrihydrite is one of the most widespread iron solids. The ageing and transformation process of ferrihydrite will affect the solubility and the retention/release process of uranium from the coprecipitates (**Bruno et al. 1995**). EXAFS analyses using the U L_{III}-edge signal and µ-XRF analyses were performed in Fe(III)-U(VI) coprecipitate samples aged from 1 day to more than 10 years to investigate this influence (**Grivé et al. 2012**) . The analyses showed that the retention of U(VI) within the ferrihydrite structure remains effective after 5 weeks of suspension and after 11 years of a dry-stored sample. Uranium is affected by the ageing process, and the results suggest a re-arranging of the uranium content towards a schoepite-like structure.

Carbonate, which has a high affinity towards both, Fe and U is also expected to influence significantly the overall process. Thus, the study of the effect of carbonate system on the kinetics of iron and uranium oxides dissolution is needed to understand the processes responsible for the contaminant (uranium) concentrations released in natural environments.

The objective of present work is to deepen in the understanding of bounding processes between uranium and iron oxides at long time frames by taking into account the influence of

carbonate on them. To reach this objective, the effect of pCO_2 on the dissolution rate of the different solids (Fe(III)-U(VI) coprecipitates and the corresponding two end-members of the system, ferrihydrite and schoepite) was studied.

Experimental

Ferrihydrite was prepared according to the methods described in ***Schwertmann and Cornell (1991)***. 40 g of $Fe(NO_3)_3 \cdot 9H_2O$ were dissolved in 500 ml of ultra-pure water and KOH was added to bring the pH of the solution to 7-8. The system was vigorously stirred, centrifuged and dialysed rapidly until free from electrolytes. The solid was then freeze dried and stored as a solid.

The solid phase meta-schoepite was synthesised by following a methodology similar to the one reported in ***Bruno and Sandino (1989)***. A 0.04 M U(VI) solution was prepared by dissolving a weighted amount of $UO_2(NO_3)_2 \cdot 6H_2O$ in ultrapure water. A carbonate-free sodium hydroxide solution was drop-wise added to the uranyl solution until pH = 7 to avoid local super-saturation effects. The experiment was kept under nitrogen atmosphere for 1 month; afterwards the solid was filtered, thoroughly washed with ultrapure water and dried under nitrogen atmosphere.

Fe(III)-U(VI) coprecipitates were prepared from $Fe(NO_3)_3 \cdot 9H_2O$ and $UO_2(NO_3)_2 \cdot 6H_2O$ solutions. Initial concentrations were $[Fe] \approx 0.01$ M and $[U(VI)] \approx 10^{-4}$ M at pH = 5.5, that is, initial uranium concentrations were below theoretical schoepite solubility limit. The analysis of the solutions indicated that the uranium content in the coprecipitates was $\approx$ 1-2%.

All the synthesis were carried out at room temperature; thermal transformations are not expected to occur. Different spectroscopic techniques (X-ray diffraction, Extended X-Ray Absorption Fine Structure and Micro X-ray fluorescence) were used in order to characterize the solids obtained.

The effect of carbonate on the dissolution kinetics of iron and uranium oxides was studied in terms of the variation of bicarbonate concentration of the system. The reactor used during the kinetic experiments was a cylindrical chromatographic column; high quality CO_2/N_2 gas mixtures of known composition were used to control the amount of bicarbonate in the system. The dependence of the kinetics of dissolution on the bicarbonate concentrations in the contacting aqueous solution at constant partial pressure of $CO_2(g)$ was measured in 0.5 M $NaClO_4$ medium at 25 ºC for the three solids.

Results

Effect of carbonate on the dissolution kinetics of iron and uranium oxides

The effect of pCO_2 on the dissolution rate of the different solids (Fe(III)-U(VI) coprecipitates and the two end-members of the system, ferrihydrite and schoepite) was studied. The

variation of the dissolution rate was studied in terms of variation of bicarbonate concentration of the system, keeping the reaction far from equilibrium. Flow-through experiments were conducted with column devices. The dissolution rate value was obtained from the difference between the outflow and inflow concentrations once the steady state was reached.

Ferrihydrite

The kinetic data obtained for ferrihydrite at different $CO_2(g)$ partial pressures are shown in Figure 1. As can be seen the rate of dissolution of ferrihydrite is enhanced by bicarbonate. The dissolution rates have a linear dependence with the logarithm of bicarbonate concentration when total carbonate concentrations are higher than $10^{-2.0}$ M.

The rate equation for the dissolution of ferrihydrite normalized to the specific surface area of the solid can be expressed as Eq. (1). The reaction order was estimated as the slope of a linear regression through the experimental points. The fractional order (0.26) suggests a surface control of the dissolution rate.

$$\text{Eq. (1)} \qquad \text{ferrihydrite} \qquad \text{rate}_{Fe} \ (mol \cdot m^{-2} \cdot h^{-1}) = 10^{-9.19} \ [HCO_3^-]^{0.26}$$

Fig. 1 Rates of ferrihydrite dissolution at different $CO_2(g)$ partial pressures, as a function of bicarbonate concentrations in solution.

Schoepite

The dependence of the kinetics of dissolution of meta-schoepite on bicarbonate concentration at constant partial pressure of $CO_2(g)$ (0.01 and 0.30 atm) at 25 ºC was also measured. The dissolution rates (Figure 2) have a linear dependence with the logarithm of bicarbonate concentration. The rate of dissolution of meta-schoepite is enhanced by bicarbonate when total carbonate concentrations are higher than $10^{-1.5}$ M.

Fig. 2 Rates of schoepite dissolution at different $CO_2(g)$ partial pressures, as a function of bicarbonate concentrations in solution.

The rate equation for the meta-schoepite dissolution normalized to the specific surface area of the solid on bicarbonate solutions is shown in Eq. (2).

$$\text{Eq. (2)} \qquad \text{schoepite} \qquad \text{rateU (mol·m}^{-2}\text{·h}^{-1}) = 10^{-4.26} \, [HCO_3^-]^{0.41}$$

The dependence of the dissolution rate on the concentration of bicarbonate in solution indicates a bicarbonate promoted dissolution of the meta-schoepite solid. As in the case of ferrihydrite, the fractional order suggests surface control of the rate of dissolution.

The remaining solid after the dissolution kinetics study of schoepite was characterized by means of XRD measurements. The remaining solid after dissolution of meta-schoepite under the $pCO_2(g)$ studied was identified as metaschoepite, with a lower crystallinity degree than the one observed for the initial solid. No alteration to other uranium containing solids (i.e. rutherfordine) was detected.

Coprecipitate

The rate of dissolution of the co-precipitate is shown in Figue 3 and in Eq. (3). The rate is enhanced by bicarbonate when total carbonate concentrations are higher than $10^{-1.5}$ M.

$$\text{Eq. (3)} \qquad \text{coprecipitate} \qquad \text{rateU (mol·m}^{-2}\text{·h}^{-1}) = 10^{-7.68} \, [HCO_3^-]^{0.74}$$

The rate of dissolution is expressed in terms of uranium, as dissolved iron concentrations were below the detection limit of the analytical technique used (spectrophotometric determination using the Ferrozine method). The fact that the measurement of iron concentrations was possible in the case of ferrihydrite dissolution (see above) while they were under the detection

limit in the co-precipitate case points out that uranium in the coprecipitate is primarily trapping the carbonate of the media. Then, the dissolution process of the coprecipitate by effect of the carbonate ligand appears to be a non-congruent dissolution process, where uranium dissolves preferentially than iron.

Furthermore, the schoepite dissolution rate (see above) is around three magnitude orders higher than the uranium dissolution rate in the co-precipitate sample. This fact would indicate that the co-precipitate process would be playing a retarding role on uranium dissolution.
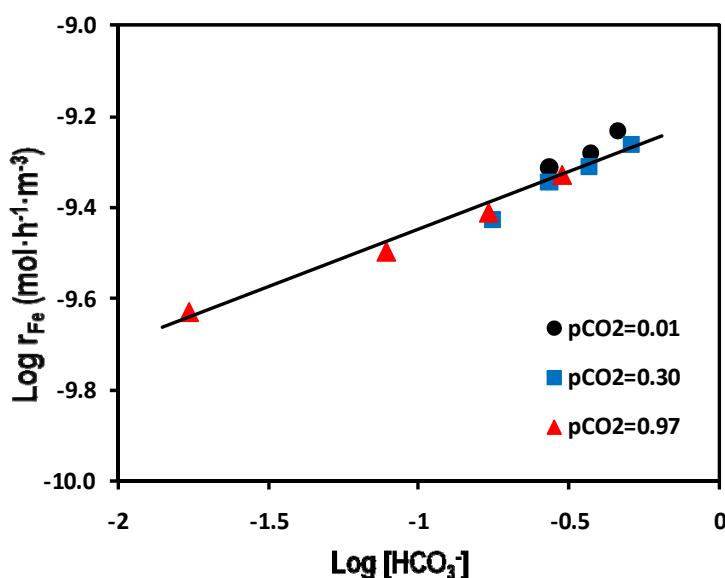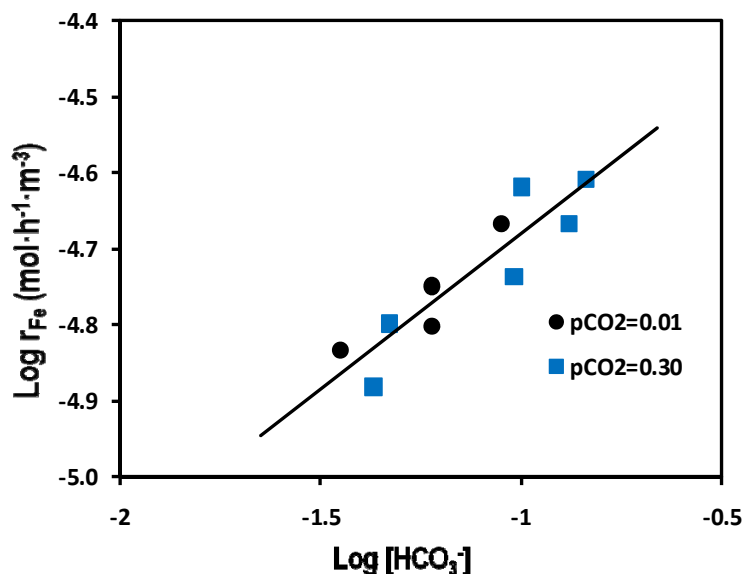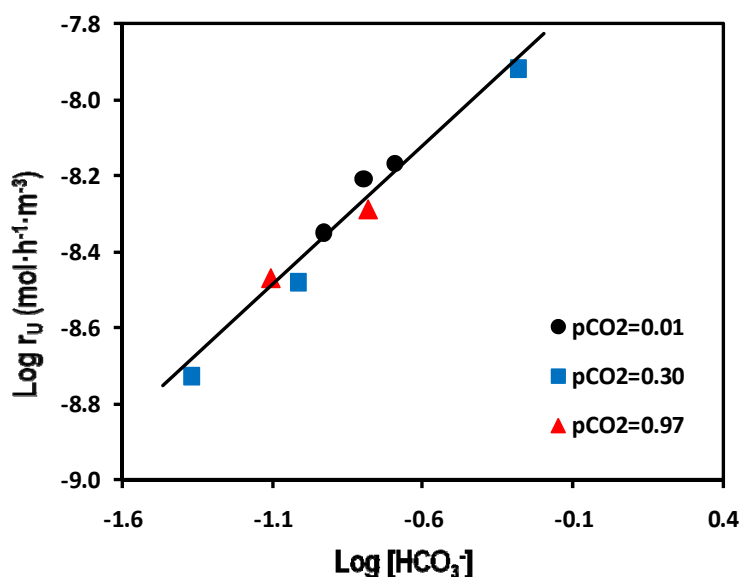

Fig. 3 Rates of coprecipitate dissolution at different $CO_2(g)$ partial pressures, as a function of bicarbonate concentrations in solution.

The overall dissolution process of a mineral phase (such as the ones used in present work) can be explained by using the concept of surface complexation; that is, the dissolution process can be seen as a change in the coordination environment of a specific surface species. The retarding phenomena on the uranium dissolution exerted by the co-precipitate with respect to the schoepite might be explained in terms of the relative strength of the surface complex formed. In the case of the coprecipiate, the surface complex responsible of the solid dissolution would probably involve iron, in addition to uranium and carbonate. However, the surface complex formed in the dissolution process of schoepite would only involve uranium and carbonate. The relative strength of the surface complexation constants seems to be related with the presence or absence of iron within the solid, with a higher affinity of the carbonate to the surface of the solid when it is a pure U(VI) oxide than in a mixed Fe(III)-U(VI) oxihydroxide.

Taking into account this discussion, the surface species controlling the co-precipitate dissolution could be a carbonated surface complex similar to $> FeO_2UO_2HCO_3^-$.

Conclusions and Future work

The dissolution process of ferrihydrite, schoepite and the Fe(III)-U(VI) coprecipitate is affected by carbonate; the results obtained point out a bicarbonate promoted dissolution of the three solids. The dissolution rates have a linear dependence with the logarithm of bicarbonate concentration, and the rate equations for the dissolution of each solid on bicarbonate solutions were determined.

At this stage, a mechanism of the bicarbonate-promoted dissolution of the different studied solids (ferrihydrite, Fe(III)-U(VI) coprecipitate and schoepite) is under development. The surface complexation constants on ferrihydrite

Preliminary results show that the dissolution process of the coprecipitate by effect of the carbonate ligand appears to be a non-congruent dissolution process, where uranium dissolves preferentially than iron. The surface species controlling the co-precipitate dissolution could be a carbonated surface complex similar to $> FeO_2UO_2HCO_3^-$.

Acknowledgement

References

Bruno J., DePablo J., Duro L., Figuerola E. (1995). Experimental study and modeling of the U(VI)-Fe(OH)3 surface precipitation/coprecipitation equilibria. Geochimica et Cosmochimica Acta, 59(20):4113–4123.

Bruno, J. and Sandino, A. (1989). The solubility of amorphous and crystalline schoepite in neutral to alkaline aqueous solutions. Mat. Res. Symp. Proc. Vol. 1989, 127, 871-877

Bruno J., Wersin P., Stumm W. (1992). On the influence of carbonate in mineral dissolution:II. The solubility of FeCO3(s) at 25ºC and 1 atm total pressure. Geochimica et Cosmochimica Acta 56, 1149-1155.

Grivé, M., Colàs, E., Valls, A., Duro, L. (2012) Interaction between uranium and iron (III) oxides. 2nd Annual Workshop Proceedings 7th EC FP – SKIN, 21th – 22th November 2012, Villigen PSI – Switzerland.

Schwertmann, U. I Cornell, R.M. (1991). Iron oxides in the laboratory. VCH, Weinheim, 137pp.

THE INFLUENCE OF CLAY SLURRY INVASION ON THE DISSOLUTION OF SPENT NUCLEAR FUEL UNDER REPOSITORY ENVIRONMENTS

Daqing Cui[1,2*], Kastriot Spahiu[3]

[1]Stockholm University (SE)

[2]Studsvik Nuclear AB(SE)

[3]SKB (SE)

* Corresponding author, studsvik929@yahoo.se

Abstract

In order to evaluate the potential changes on spent nuclear fuel (SNF) dissolution caused by a bentonite slurry during a glacial period, batch experiments were conducted by dissolving crystalized ThO_2 particles (as a simulator of SNF UO_2 matrix) under anoxic conditions, with or without the presence of a synthesised clay (montmorillonite). The results show that, in a neutral pH and CO_2-free water solution, Th concentration reached around ppt level in two months, and increases with decreasing pH and increasing carbonate content. Th(IV) in solution can be sorbed by synthetic montmorillonite. Given that the Th(IV) sorption process is much faster than the ThO_2 dissolution, the Th(IV) concentrations in batch experiments with ThO_2 and clay are much lower than the solubility level of ThO_2. Therefore the quantity of Th(IV) sorbed on the clay in the presence of ThO_2 is much less than the calculated value using K_d value for Th(IV) on montmorillonite and the solubility of Th(IV)oxide.

Introduction

In the KBS-3 repository concept, spent fuel will be encapsulated in copper-cast iron canisters embedded in bentonite clay placed in deep granite bedrock. During a glacial period it has been shown that dilute glacial water may cause erosion of the bentonite clay, followed by severe bentonite losses. When the anoxic glacial melt water reaches the repository, the buffer may be partially or completely eroded, leaving a cavity filled with a slurry of colloidal clay particles. These colloidal clay particles are produced through the erosion of the clay in the tunnel backfill. For a canister breached under such circumstances, the clay particles are not expected to affect the fuel oxidative dissolution rate. Dissolved U(IV) would, however, be expected to be sorbed strongly to the clay particles and the amounts of U(IV) sorbed are

expected to be proportional to its concentration in solution, that is determined by the solubility of $UO_2(s)$ in case solubility equilibrium is attained. In case the dissolution rate of $UO_2(s)$ is very low, solubility equilibrium will not be attained during the residence time of the clay particles in the canister and the amount adsorbed and transported away will be lower.

Erosion of bentonite in tunnel poses fuel in contact with clay slurry. The amount of uranium transported by bentonite particles is described by equation (1):

$$R_U = [U]_{sol} \cdot q \cdot (1 + C_{Clay} \cdot K_d) \tag{1}$$

where: q is the flow rate, C_{clay}- clay concentration and $[U]_{sol}$-solubility of U(IV).

A basic assumption of Equation (1) is U dissolution rate from SNF is not so much slower than U sorption on clay, $[U] \approx [U]sol$, the amount U dissolved from SNF and transport via clay slurry should be much faster than the conditions without clay slurry.

If UO_2 dissolution rate is much lower the U(IV)sorption rate, $[U] << [U]_{sol}$ the amount U dissolved from SNF and transport via clay slurry should be much smaller than that at the conditions with near constant solubility level, as assumed in Equation (1).

The transport rate of clay slurry is another important factor. The high clay transport rate may result in the increase of the amount of U sorbed on the clay and that dissolved from SNF.

Because of the difficulties in avoiding oxidation while working with $UO_2(s)$, crystalline $ThO_2(cr)$ was used to simulate the fuel $UO_2(s)$ matrix.

The major objective of this work is to investigated in how much degree the presence of clay slurry can affect the Th(IV) concentration in ThO_2 leaching experiment. This information is useful to predict the migration of radionuclides from SNF repository.

Experimental

Methods and materials

There are several difficulties that need to be overcome:

Very low solubility of ThO$_2$(cr)

To get enough Th concentration in solution to study ThO_2 dissolution and Th sorption on clay, we conducted experiments at lower pH conditions, pH 5.5 and pH 3.3. ThO_2 dissolution in solutions with normal groundwater pH (8.2) with and without 2 mM $NaHCO_3$ was also investigated.

How to separate clay suspending particles from ThO$_2$ particles?

Molecular sieve, i.e. "membrane bag" with pore size 1000-10000 dalton was used to separate clay slurry and ThO_2 particles and water solution.

Naturally existing clay contains significant Th.

The content of Th in bentonite is ppm level and can disturb Th(IV) sorption experiment. Instead of using naturally existing clay, a synthetic clay, montmorillonite, was manufactured. This clay predominates the BET specific surface areas in bentonite and contains much less Th than the naturally existing bentonite.

Arrangement

The experimental arrangement with two batches is shown in Figure 1. To get rid of suspending ThO_2 particles, all solution samples were high-speed-centrifuged. Thorium concentrations in all samples were analysed by ICP-MS. The detection limit of ICP-MS for Th is about 0.5-1 ppt (10^{-12}).
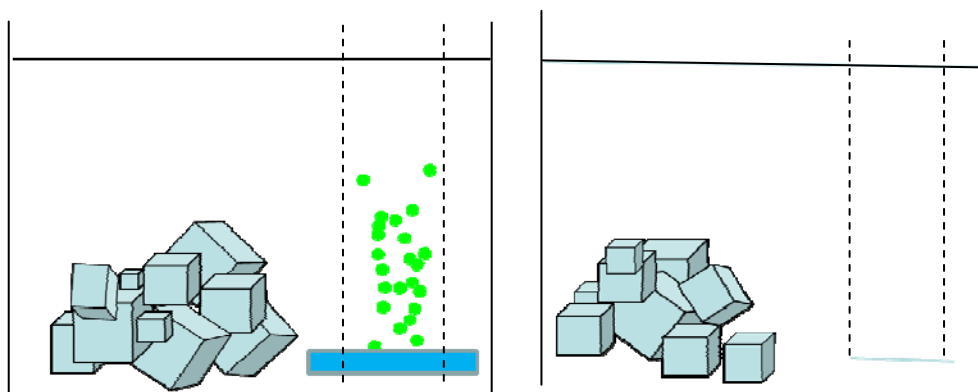
Fig. 1 The arrangement of batch experiments with or without presence of synthesised montmorillonite. (0.25 g) in Membrane bag (1000-10000 Dalton). 0.75g ThO₂ (prewashed 3 times with using ultrasonic bath, till clean solution, 430 ml water solution.

ThO_2 fragments used in the experiment was 0.1 mm sized crystalized ThO_2, pre-rinsed in pH 2.5 solution with using ultrasonic bath and the suspending fine particles were removed. SEM Images of ThO_2 fragments used in the experiments are shown in Figure 2.

The red marks on the top of Figure 3 are the XRD pattern of reference ThO_2. The result of XRD analysis shows the ThO_2 used in this work is a perfectly crystalized ThO_2.

Result and discussion

ThO_2 dissolution and Th(IV) sorption on the clay

The result of experiment at initial pH 3.3 was shown in Figure 4.
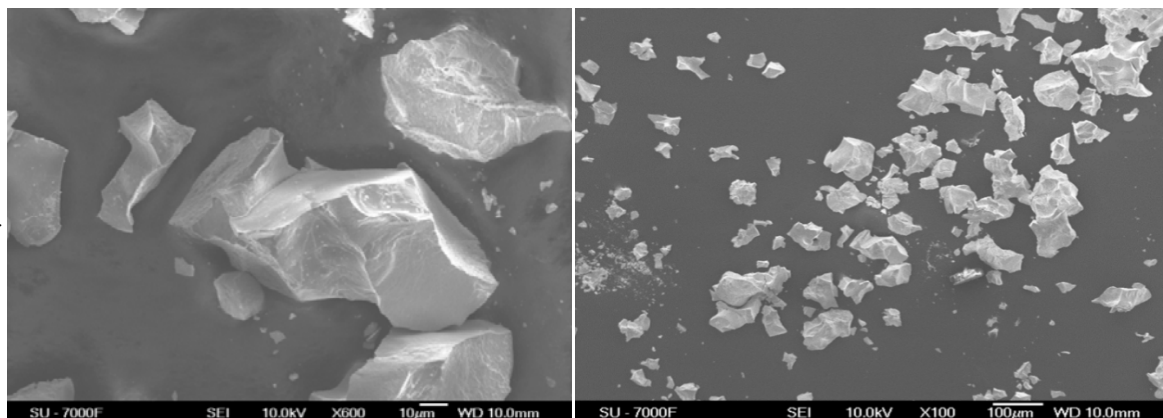
Fig. 2 SEM of ThO$_2$ fragments used in the experiments.
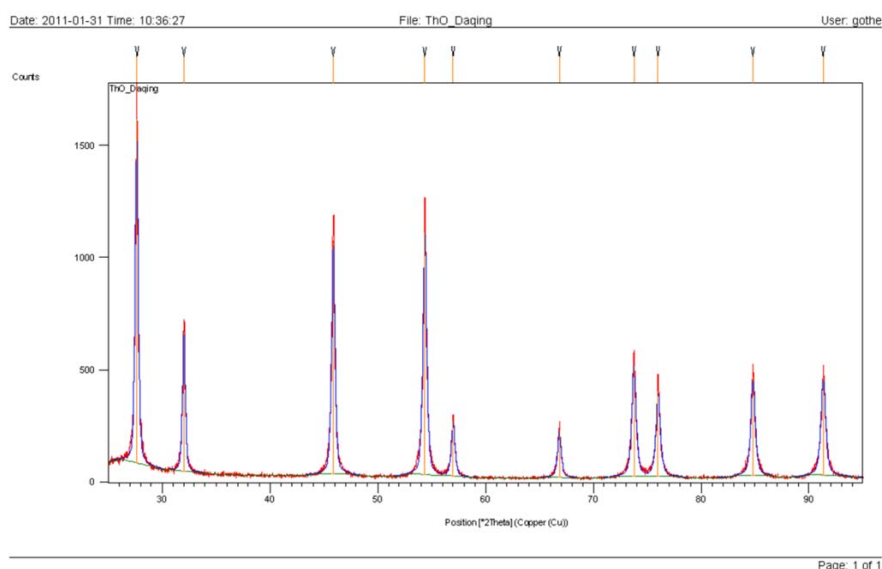
Fig. 3 XRD of ThO$_2$ fragments used in the experiments.

The results are summarized below:

1. The experiment was conducted for three months at pH 8.5 without carbonate. The result is not plotted in figure. In the batch a) with presence of clay, Th(IV) concentration is below to the detection limit 0.5 ppt, 0.02 nM and in the batch b) without clay, Th concentration reached 2 ppt after 3 months interaction. This concentration is much much lower than the solubility of ThO$_2$(cr) at neutral pH that previously reported, 1-10 nM [1]. One reason may be that in the present experiment, all ThO$_2$ fragments are well crystalized and washed in acidic solution.

2. In the experiment with pH 3.5, free from clay and carbonate, ThO$_2$ concentration was approaching its solubility level 35 ppt, 0.15 nM, as shown in Figure 4. The present

work suggests that the dissolution of ThO_2 is a slow process, the concentration of Th(IV) reached a stable level 35 ppt after one month. In the batch experiment with the presence of clay, Th concentration the Th(IV) is lower than that without clay, due to that the Th(IV) sorption process on clay is much faster process than ThO_2 dissolution fromThO$_2$. The sorbed Th(IV) on clay at the end of the experiment: dissolving the clay mineral (0.25 g) with 19 mL acidic solution, 0.5 ml 65% HNO_3, after shaking for one week, Th concentration in solution is 7 ppt. This result indicates that even at acidic solution (1.5% HNO_3),the Th(IV) dissolved from clay at acidic solution is only 15% of that sorbed on clay during 220 days experiment. 19 ml × 7 ppt / (430 ml × 20 ppt) = 15% it means that the most part of Th(IV) sorbed on the clay cannot be easily desorbed.
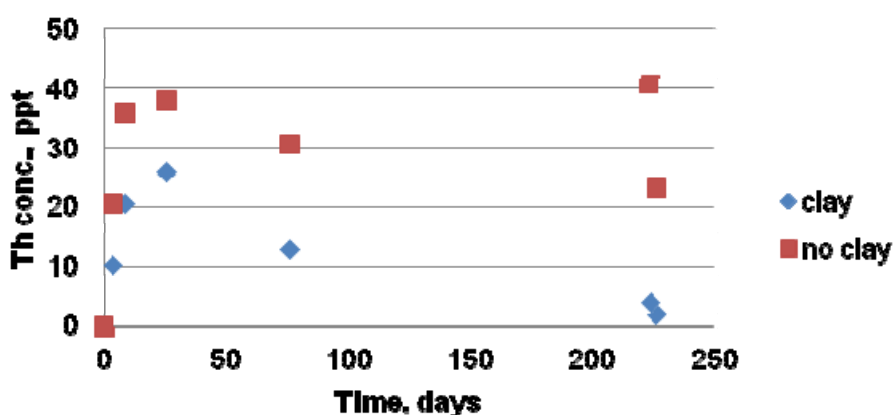
Fig. 4 Th concentrations in batch experiments with or without clay, initial pH 3.3.
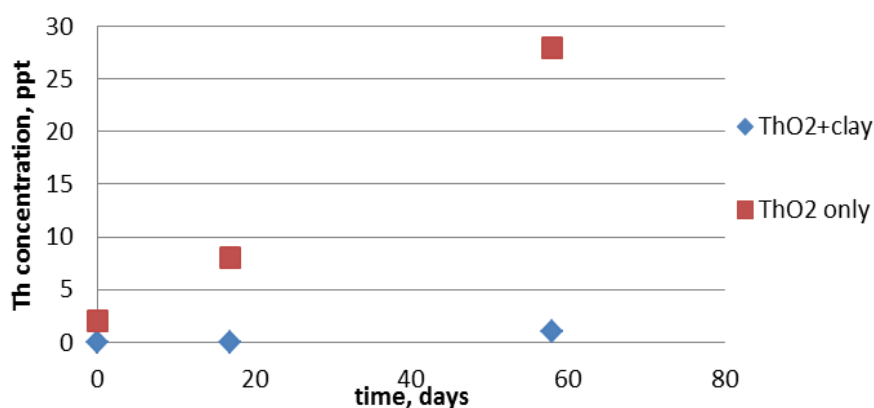
Fig. 5 Th concentrations in batch experiments with or without clay, initial pH 5.5. The two batch experiments contain the same amount of ThO$_2$.

3. At pH 5.5, the sorption of Th(VI) on the clay is much stronger than that at pH 5.5. ThO$_2$ dissolution is a slow process, Th(IV) concentration increases with reaction time. It was previously reported that the Th(aq) concentrations for pH > 5 after 10 days of leaching obtained with high fired ThO$_2$(cr) reach 0.22 nM [2], The result of the present experiment is rather close to this reported data.
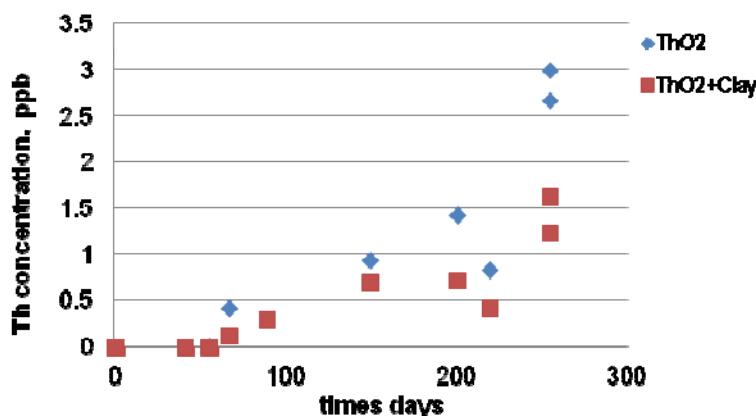
Fig. 6 ThO$_2$ dissolution in 10 mM NaCl and 2 mM NaHCO$_3$ solution, pH 8.2.

4. In the batch experiment with solution of 10 mM NaCl and 2 mM NaHCO$_3$, Th(IV) concentration is three orders of magnitudes higher than that conducted with carbonate free solution, reached 3 ppb. 1.3×10^{-8} M, which is similar with the reported value in the carbonate containing solution 9.7×10^{-9} M up to 6.5×10^{-7} M. It should be noted that in the batch experiment, NaHCO$_3$ concentration is similar to that in normal hard rock groundwater, 2 mM. The carbonate content in snow is 43 ppm.

Conclusions

From the result discussed above based on the experiments using ThO$_2$ to simulate UO$_2$, it can summarized that UO$_2$(s) dissolution rate can be sufficiently low, so that U(IV) solubility, in the canister void, can not be satisfied during the time of the residence of the clay slurry in the void. In this case, the amount of U(IV) sorbed on clay particles (proportional to sorption coefficient (K$_d$) and concentration of U(IV) in solution) will be lower than that in a solution with the U(IV) concentration at UO$_2$ solubility level.

This is clearly seen from the experimental data, where [Th]$_{(ThO2+clay)}$ < [Th]$_{(only\ THO2)}$. Therefore it can be expected that [U](t) should be lower or much lower than [U]$_{(solubility\ of\ UO2)}$ in a very long period of time, even longer than the time of clay staying in SNF canister void. Therefore, we can conclude that the invasion of clay slurry to canister void during the glacial period can enhance the radionuclide migration, but not so much as that conservatively assumed before (Equation 1, SKBTR-11-01), because the U concentration in the canister void is lower than that in clay slurry free conditions.

Therefore, we can say that it is not fair to calculate the amount of transported U(IV) by Equation (1) given in the introduction part. This information is useful for the safety assessment.

Future work

The batch experiment with 2 mM carbonate will be continued until the Th(IV) reach a stable level. Another new batch experiment under relevant conditions will be conducted to prove the observation made in this work. Under SKB's coordination and support, we will conduct similar experiments in a rather long period of time, to better demonstrate the finding in this work.

Acknowledgement

References

J. Vandenborre, A. Abdelouas, B. Grambow, Radiochimica Acta (Impact Factor: 1.37). 01/2008; 96:515-520.

A. Seibert, S. Stumpf, D. Schild, T. Gouder, D. Bosbach, Forschungszentrum Karlsruhe FZKA 7489 (2009).

SKB, Long-term safety for the final repository for spent nuclear fuel at Forsmark, Main report on the SR-Site project, (Vol. III, p. 664). SKB TR-11-01

ADDING UPTAKE KINETICS AND SURFACE ENTRAPMENT TO GEOCHEMICAL MODELS: SELENIUM UPTAKE IN CALCITE

Bruno M.J. Thien[*], Dmitrii A. Kulik, Enzo Curti

Paul Scherrer Institut (Switzerland)

* Corresponding author: bruno.thien@psi.ch

Abstract

The Unified Uptake Kinetics Model *(Thien et al., 2013; WP4.1 Mid-Term Report)*, as implemented in the GEM-Selektor v.3.3 code package for geochemical modelling *(Deliverable 4.2 Report)* has been tested against experimental data for selenite incorporation during coprecipitation with calcite. The model was able to satisfactorily predict these data, which represent an extreme case of entrapment far from thermodynamic equilibrium.

Introduction

The objective of Task 4.1 was to develop a new approach to model the uptake of trace elements in the lattice of host minerals, including radionuclides relevant to radioactive waste disposal sites. Irreversible trace element uptake in growing minerals cannot be accurately predicted using an equilibrium aqueous solid-solution thermodynamic model alone because high precipitation rates and related kinetic effects may lead to (irreversible) non-equilibrium partitioning. A realistic model has to account for such deviations from thermodynamic equilibrium.

In our previous work devoted to Task 4.1, two uptake kinetic models from the literature were merged into a single analytical expression under certain assumptions *(Thien et al. 2014)*. This Unified Uptake Kinetics Model (UUCM), implemented in the GEM Selektor v.3.3 package prototype (*Kulik et al. 2013, Wagner et al. 2012,* http://gems.web.psi.ch*)*, was tested against published partitioning data. It was shown to be capable of reproducing the non-equilibrium partitioning of some relevant cations in growing calcite in complex geochemical systems *(Thien et al. 2014)*, including changes in aqueous chemistry and depletion effects. In this contribution, we applied the UUCM to describe the uptake of selenite anions (SeO_3^{2-}) into growing calcite.

Methods and models

The distribution of a trace element *Tr* between the aqueous solution (or melt) and the mineral (solid solution) relative to the host component *Hc* is usually described by the fractionation coefficient $\Delta_{Tr,Hc}$. Considering selenite SeO_3^{2-} incorporation in calcite, it takes the form:

$$\Delta_{Se,C} = \frac{\left(\dfrac{x(Se)}{x(C)}\right)_{mineral}}{\left(\dfrac{[SeO_3^{2-}]}{[CO_3^{2-}]}\right)_{aqueous}} \qquad (1)$$

where [ ] and $x(\ )$ stand for the aqueous concentrations and the mole fractions, respectively.

The final UUCM equation provides the value of the (non-equilibrium) fractionation coefficient as a function of equilibrium partitioning at the surface and in the bulk of the mineral, and of other parameters originating from the source models:

$$\Delta_{Tr,Hc} = \frac{F \cdot \Delta_{Tr,Hc,eq}}{1 + \dfrac{\left(\dfrac{D_s}{ml}\right)}{\left(\dfrac{D_s}{ml}\right) + R_L}(F-1)} \qquad (2)$$

$$F = \left(\frac{Se}{C}\right)_{surface} \Bigg/ \left(\frac{Se}{C}\right)_{bulk} = \frac{\Delta_{Tr,Hc,sorp}}{\Delta_{Tr,Hc,eq}} \qquad (3)$$

where *F* is the surface enrichment factor, $\Delta_{Tr,Hc,sorp}$ is the fractionation coefficient considered in a case in which only adsorption occurs (at zero growth rate), $\Delta_{Tr,Hc,eq}$ is the equilibrium fractionation coefficient for lattice incorporation at infinitesimally low growth rate, D_s is the surface diffusivity R_L is the linear growth rate (in nm s^{-1}), *l* is the half-thickness of the enriched/ depleted surface layer*,* and *m* is the multiplier linking *l* to the maximal thickness of the diffusivity region.

The UUCP model has been implemented in the GEM-Selektor code. R_L is calculated iteratively at each time step using a calcite growth rate equation from ***Wolthers et al. (2012)***. More details are given in ***Thien et al. (*2014*)***; ***Kulik and Thien (next chapter)***.

Modelling trace selenite uptake in growing calcite

Atomistic calculations by the single-defect method (***Heberling et al. (2013)***) predict that substitution of CO_3^{2-} by SeO_3^{2-} in calcite should be negligible, which leads to extremely low aqueous-solid solution equilibrium fractionation coefficient $\Delta_{Se,C,eq} = 1 \times 10^{-9}$.

However, calcite - selenite mixed-flow co-precipitation experiments by ***Heberling et al. (2013)*** show significant incorporation with effective $\Delta_{Se,C} = 0.04^2\ 0.03$. Selenite sorption

experiments on calcite surfaces yield similar fractionation coefficient values for (ad)sorption. These data allow us to calculate a surface enrichment factor of $F = 4 \times 10^7$, which is very high compared to the usual values obtained for cations (F between 0.1 and 6). In other words, the surface layer must contain 4×10^7 times more selenite than the bulk calcite in equilibrium with the same aqueous solution.

In our GEMS calculations for the calcite – $CaSeO_3$ ideal solid solution – aqueous solution system, we tried to describe mixed-flow reactor coprecipitation experiments of **Heberling et al. (2013)** using the UUCM with F fixed at 4×10^7 and other model parameters as shown in Table 1. Solubility of $CaSeO_3$ phase from the literature (Table 2) is too low to reproduce the equilibrium fractionation coefficient derived by **Heberling et al. (2013)**. Therefore, we adjusted the solubility in order to obtain a correct value of fractionation coefficient.

Table 1: Parameters used with the UUCM.

Parameter	Value
$\Delta_{Se,C,eq}$	1×10^{-9}
F	4×10^7
D_s (nm^2 s^{-1})	1×10^{-11}
Dl (nm^2 s^{-1})	1×10^{-16}
l (nm)	0.5
m	6

Table 2: Solubilities considered for the reaction $Ca^{2+}+SeO_3^{2-} \rightarrow CaSeO_3$ at 25 °C. All other thermodynamic parameters from all other phases and aqueous species come from Nagra-PSI database (Hummel et al. (2002)). The Debye-Hückel equation was used for aqueous activities calculations.

Phase	$log_{10}K_R$	Reference
$CaSeO_3$ crystalline	-6.84	**Baur & Johnson (2003)**
$CaSeO_3$ end-member	0.52	This work

In the process simulator of GEM-Selektor, input flow rates of supersaturated solution (Table 3) were considered by its constant addition at each time step, whereas the output flow rates were accounted for by taking the bulk solid composition from the previous time step and by subtracting amounts of dissolved species accordingly to the output rates at each time step.

Table 3: Initial recipe of the chemical system used for the Process simulation. Input solution has the same composition. Flow rates were from 5 × 10^-4 to 0.02 mL/min.

Name	Quantity	Units
Aqua (H_2O)	80	g
$CaCl_2$	0.006	mol/L
$NaHCO_3$	0.003	mol/L
NaCl	0.01	mol/L
Na_2SeO_3	2.7×10^{-6} to 2.5×10^{-4}	mol/L
H_2SeO_3	1×10^{-10}	mol/L
O_2	1×10^{-9}	mol/L
CO_2	1×10^{-9}	mol/L
H_2	1×10^{-9}	mol/L

As seen in Figure 1, the model reproduces the experimental data reasonably well. It requires a sub-surface diffusivity $D_s = 1 \times 10^{-11}$ nm^2/s for SeO_3^{2-} in calcite, which is extremely low if compared with that for divalent cations in calcite (D_s between 0.01 and 0.1 nm^2/s). This extreme case of entrapment is consistent with the assumption that oxoanions cause a lot of strain and are more difficult to transport than cations in the calcite structure. Some support in this direction is provided by an observation that the unit cell volume of calcite increases with the $Se(IV)O_3^{2-}$ content in the structure *(Aurelio et al. 2010)*.

Unfortunately, the available experiments *(Heberling et al. 2013)* have been performed at about the same calcite precipitation rates ($R_L \approx 2 \times 10^{-4}$ nm s^{-1}). It is necessary to do similar experiments at significantly lower growth rates in order to verify the predicted model trend. It is worth to note that the equilibrium fractionation coefficient of selenite in calcite cannot be measured because this would need growth rates that are infinitesimally low.

Experiments of *Heberling et al. (2013)* have been conducted under several different Se solution concentrations (from 1.7×10^{-13} to 2.5×10^{-4} M). In order to verify whether the dissolved selenite inhibits calcite growth, the experimentally measured growth rates were compared to the modeled growth rates (Fig.2). One can suspect inhibition effects at highest (Se) concentrations because experimental growth rates are up to two times lower than modelled growth rates, but the size of error bars are too large to validate such a conclusion.
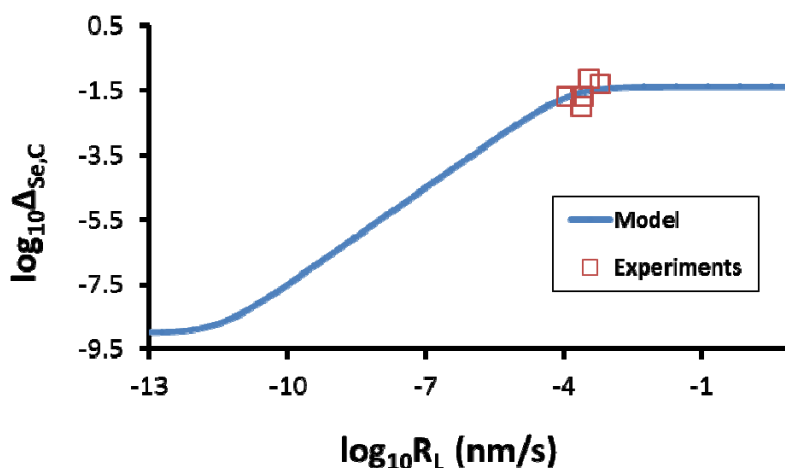
Fig. 1 Predicted Se/C fractionation coefficient as a function of calcite growth rate.
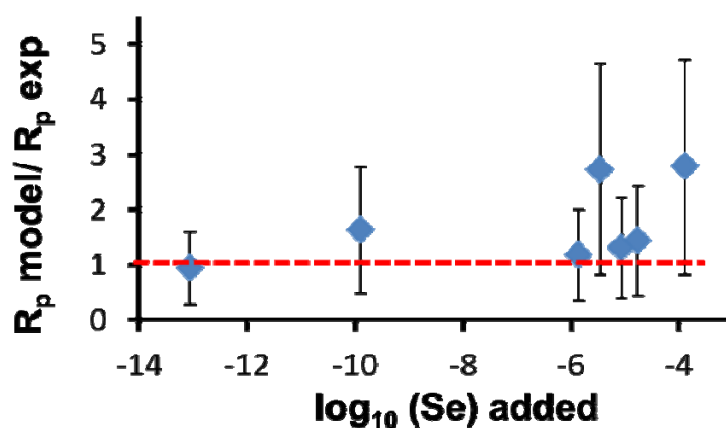
Fig. 2 Comparison between the experimental (diamonds) and the modelled (red line) calcite growth rates, for different total dissolved Se concentrations.

Conclusion

Significant incorporation of selenite ($Se(IV)O_3^{2-}$) in calcite has been found to occur in co-precipitation experiments, albeit the solid solution thermodynamics predicts that no measurable Se incorporation should be observed. Using the UUKM, this discrepancy can be explained as an extreme case of surface entrapment, but a very high surface enrichment factor and a very low sub-surface diffusivity must be taken into the model. Although more experimental data at lower calcite growth rates are required to confirm this finding, our results are encouraging to show that non-equilibrium trace element uptake can be successfully predicted by combining GEM calculations of partial equilibria with mineral-water reaction kinetics and trace element uptake kinetics models.

Acknowledgement

References

Aurelio, G., Fernandez-Martinez, A., Cuello, G. J., Roman-Ross, G., Alliot, I., Charlet, L. (2010). Structural study of selenium(IV) substitutions in calcite. Geochimica et Cosmochimica Acta 270, 249-256.

Baur, I. and Johnson, C.A. (2003). Sorption of selenite and selenate to cement minerals. Environmental Science & Technology 37, 3442-3447.

Heberling F., Vinograd V.L., Polly R., Heck S., Rothe J., Gale J.D., Bosbach D., Geckeis H. and Winkler B. (2013). A thermodynamic entrapment model for the quantitative description of Selenium (IV) incorporation into calcite. Geochimica et Cosmochimica Acta, submitted.

Hummel , W., Berner, U., Curti, E., Pearson, F.J., and Thoenen, T. (2002). Nagra/PSI Chemical Thermodynamic Data Base 01/01. Universal Publishers, Parkland, Florida.

Kulik D.A., Wagner T., Dmytrieva S.V., Kosakowski G., Hingerl F.F., Chudnenko K.V., and Berner U. (2013). GEM-Selektor geochemical modeling package: revised algorithm and GEMS3K numerical kernel for coupled simulation codes. Computational Geosciences 17, 1-24.

Thien B.M.J, Kulik D.A, and Curti E. (2014). A unified approach to model uptake kinetics of trace elements in complex aqueous - solid solution systems. Applied Geochemistry 41, 135-150.

Wagner T., Kulik D.A., Hingerl F.F., and Dmytrieva S.V. (2012). GEM-Selektor geochemical modeling package: TSolMod library and data interface for multicomponent phase models. Canadian Mineralogist 50, 1173-1195.

Wolthers M., Nehrke G., Gustafsson J. P., and Van Cappellen, P. (2012). Calcite growth kinetics: Modeling the effect of solution stoichiometry. Geochimica et Cosmochimica Acta 77, 121-134.

ADDING UPTAKE KINETICS AND SURFACE ENTRAPMENT TO GEOCHEMICAL MODELS: CODE EXTENSIONS AND TEST RESULTS

Dmitrii A. Kulik[*], Bruno M.J. Thien

Paul Scherrer Institut, Laboratory for Waste Management (LES), 5232 Villigen PSI (CH)

* Corresponding author: dmitrii.kulik@psi.ch

Summary

Our work was aimed at the development of a new partial equilibrium approach to geochemical modeling of the slow uptake of radionuclides in host mineral solid solutions, verified against the literature experimental data. In this work, the extensions of the TKinMet code library of the GEM-Selektor package, necessary for the simulation of kinetically-controlled mineral-water interactions, have been implemented. This is a pre-requisite for using kinetic models efficiently in reactive transport codes coupled with the Gibbs Energy Minimization software (GEMS). In the framework of SKIN project, a comparative study of available models of trace element uptake kinetics upon host mineral precipitation has been performed. The resulting "unified uptake kinetics model" (UUKM) for trace element incorporation upon the host mineral growth *(Thien, Kulik and Curti, 2014)*, initially tested using GEMS process simulator scripts, has also been implemented in TKinMet library of the GEM-Selektor code package (http://gems.web.psi.ch). The extended code has been tested using the literature data for the rate-dependent uptake of trace elements upon calcite growth.

The first part of this report provides a description of theory and principles used in modelling code extensions, leaving most technical details to the runtime GEM-Selektor help database as part of the GEM-Selektor v.3.3 code prototype. The second part of the report shows how the software extensions have been tested, firstly on two examples of precipitation kinetics of portlandite and calcite, and secondly, against some experimental data for Sr and Cd uptake kinetics in calcite. Geochemically important effects such as the depletion in a closed system and the arbitrarily changing composition of the open system, as reproduced by the implemented kinetic and uptake models, are illustrated by simulations of (hypothetical) variations of Sr uptake in calcite precipitating from seawater. The tests show that the TKinMet code library extensions for mineral-water reaction kinetics and trace element uptake

into solid solutions in aqueous systems within the GEM-Selektor code comprise an efficient modelling tool of potentially wide applicability in aquatic chemistry, chemical engineering, and (nuclear) waste geochemistry.

Introduction

Aquatic chemical systems at Earth surface conditions rarely achieve the truly reversible equilibrium state. No mineral solid precipitates or dissolves instantly; at room temperature T and pressure P, some coarse-crystalline phases are almost unreactive; others (e.g. clays) dissolve relatively fast, but do not precipitate. Particulate solid nanophases with large specific surface areas are metastable with respect to their bulk counterparts due to the positive surface free energy contribution *(Wu and Nancollas 1999, Navrotsky 2011)*. Hence, the phase metastability and solid-aqueous reaction kinetics must be accounted for in any realistic chemical thermodynamic model of a complex aquatic system. This becomes critical when chemical thermodynamic models are embedded in reactive transport simulations, performed using the coupled codes such as PHAST *(Parkhurst et al. 2010)* or OpenGeoSys-GEM *(Shao et al. 2009)* that combine a fluid transport model with the chemical speciation solver, using a discretization of the system in space (many small enough control volumes) and in time (many small enough time steps Δt). In such simulations, based on the *principles of local and partial equilibrium,* the missing or incorrect account for mineral-aqueous reaction kinetics may often lead to intractably small time steps and/or to completely unrealistic predictions.

Methods of GEM simulations of mineral-aqueous reaction kinetics

Local and partial equilibrium

The *local equilibrium* is assumed to take place in each control volume, according to the assigned bulk system composition and the thermodynamic parameters of state (pressure P, temperature T, surface area A of phases). The *partial equilibrium* occurs if some components in some phases cannot reach their equilibrium amounts because of the *additional metastability restrictions* (AMR). All phases and components without AMR take part in the achievement of the partial equilibrium state under the mass balance common to the whole system.

If a chemical speciation solver can handle AMRs, such as the GEM-Selektor *(Karpov et al. 2001, Kulik et al. 2013, Wagner et al. 2012)*, it can be directly employed for simulating the kinetics of a time-dependent chemical process by setting each AMR as a function of the time step duration Δt, the time variable t, the surface area $A_{k,t}$ of k-th solid phase, and the net molar kinetic rate $R_{n,k,t}$ (details are given below). In principle, AMRs may also depend on a linkage of the specific surface of one phase (e.g. an overgrowth, adsorbed layer) to the volume or

surface area of another, "seed", "substrate" or "adsorbent" phase, which may even be inert, or may have its own kinetics.

In a stepwise simulation, the mole amount $n_{k,t+\Delta t}$ of the solid at time $t+\Delta t$ is set by the upper AMR $\bar{n}_{k,t+\Delta t}$ for precipitation or by the lower AMR $\underline{n}_{k,t+\Delta t}$ for dissolution:

$$\bar{n}_{k,t+\Delta t} = n_{k,t} + A_{k,t} R_{n,k,t} \Delta t \quad \text{if} \quad \log_{10} \Omega_k > \varepsilon$$
$$\underline{n}_{k,t+\Delta t} = n_{k,t} - A_{k,t} R_{n,k,t} \Delta t \quad \text{if} \quad \log_{10} \Omega_k < -\varepsilon$$

(1)

where $0 < \varepsilon < 10^{-5}$ is a numerical tolerance. The direction of change depends on the sign of the logarithmic phase stability index $\log_{10} \Omega_k$ (explained below). The surface area of the k-th solid phase is obtained as $A_{k,t} = A_{S,k} M_{M,k} n_{k,t}$, where $A_{S,k}$ is the specific surface area (m^2 kg^{-1}); $M_{M,k}$ is the molar mass (kg mol^{-1}), and $n_{k,t}$ is the current amount (mol) of the k-th phase.

The implementation of metastability and kinetics differs from code to code; so far, there is no conventional data structure for kinetic parameters. Large literature exists on experimental data and kinetic rate laws and parameters of mineral-aqueous reactions *(e.g. Teng et al. 2000, Schott et al. 2009, 2012)*, with a generally better understanding of dissolution compared to that for precipitation and nucleation. Because the experimental rate constants are typically normalized per unit area, they must be scaled by the current reactive surface area of the mineral, which depends on many factors, some of them are external to the chemical system, and some related to the particle/pore morphology, initial size distributions, and surface roughness. At present, the determination of reactive surface areas is perhaps the most important knowledge gap *(Marini et al. 2000, Mironenko and Zolotov 2012, Scislewski and Zuddas 2010)*, related in reactive transport modeling to the impact of porosity changes on transport and kinetic parameters. Many kinetic rate laws contain the activity product term related to a particular reaction mechanism, catalysis, inhibition, etc. *(Schott et al. 2012, Palandri and Kharaka 2004)*. Kinetic rates also depend on the *affinity term* based on the *phase saturation index* Ω_k; particular forms of this term reflect different nucleation, growth or dissolution mechanisms.

Gibbs energy minimization (GEM) method

The GEM IPM (interior points method) algorithm *(Kulik et al. 2013)*, implemented in the GEM Software (GEMS), has a great potential for thermodynamic modeling of mineral-water reaction kinetics because it can directly handle the metastability restrictions. In the GEM IPM, the chemical system is defined by a bulk composition vector, $n^{(b)}$, specifying the input amounts of chemical elements and charge; the standard molar Gibbs energies of all dependent components (species), g^o, at T, P of interest; the parameters of (non)ideal models of mixing in

solution phases *(Wagner et al. 2012)*, needed to calculate activity coefficients λ_j of species indexed with j; and the optional AMRs. After each run, the GEM *primal* (speciation vector $\hat{n}^{(x)}$) and the *dual* (vector $\hat{u}^{(b)}$ of chemical potentials of chemical elements and charge) results provide concentrations and activities of all aqueous species, as well as activities and amounts of all components in all other phases. The stability index Ω_k of any phase, even of that absent from the mass balance, is found as a *dual-thermodynamic* estimate of the sum of (anticipated) mole fractions $\hat{x}_j$ of all phase components:

$$\Omega_k = \sum_j \hat{x}_j = \sum_j \exp\left(\hat{\eta}_j - \frac{g_j^o}{RT} - \ln \lambda_j - \Xi_k \right) \tag{2}$$

where the index j runs over all components in the phase; R is the universal gas constant; Ξ_k is a term for converting species concentration into the common mole fraction scale (e.g. $\ln P$ for gases; $\ln 55.5085$ for aqueous species); and $\hat{\eta}_j$ stands for the *dual-solution chemical potential*

$$\hat{\eta}_j = \sum_i a_{ij} \hat{u}_i^{(b)} \tag{3}$$

where index i runs over all chemical elements and charge, and a_{ij} is the formula stoichiometry coefficient of i-th element in j-th species (e.g. 2 for O in SiO_2).

In the GEM IPM algorithm, the Ω_k index (eq. (2)) is used as a *criterion of stability* for any phase. If, numerically, $-0.01 < \log_{10}\Omega_k < 0.01$ then the positive or zero amount of this phase is in equilibrium with the rest of the system. If $\log_{10}\Omega_k < -0.01$ then the phase is unstable (the rest of the system is under-saturated to this phase), but may be kept in a positive amount in the mass balance by the lower AMR(s) $\underline{n}_j$ set on some or all of its components. If $\log_{10}\Omega_k > 0.01$ then the phase is over-stable (the rest of the system is oversaturated to this phase) because the positive or zero upper AMR(s) $\overline{n}_j$ were set on some of its components from above.

Taken together, the GEM IPM output phase stability index Ω_k together with the input lower-$\underline{n}_j$ and upper $\overline{n}_j$ AMRs make the GEM-Selektor code a versatile tool for modelling various kinds of kinetics and metastability, represented as the sequences of partial (restricted) equilibrium states. Thus, lower-AMRs allow stepwise simulation of *dissolution* of a mineral as long as its stability index $\Omega_k < 1$; upper-AMRs allow stepwise simulation of mineral *precipitation* as long as $\Omega_k > 1$. Setting AMRs as a function of time according to the chosen kinetic rate law allows the GEM software to simulate the kinetics of mineral-aqueous reactions and trace element uptake. The more ample information about the mineral-aqueous reaction is available from the experiment the more accurate and specific form of the rate equation can be applied to the system of interest.

The TKinMet library of models of mineral-aqueous reaction kinetics

Some kinetic rate equations for dissolution, precipitation, and trace element uptake in solid solutions have been implemented in the TKinMet code library used in GEM-Selektor and GEMS3K codes. Eventually, with this library, GEMS will become a general and flexible software tool, extending and superseding the existing (geo)chemical models and codes capable of kinetic simulations *(Parkhurst and Appelo 1999, Made et al. 1994, Fritz et al, 2009, Mironenko and Zolotov 2012)*. In the TKinMet library, mineral-water interaction kinetic rate laws are considered in a traditional form derived from *(Lasaga 1998, Palandri and Kharaka 2004, Schott et al. 2012)*:

$$\frac{dn_k}{dt} = A_{k,t}R_{n,k,t} = -A_{k,t}\sum_{r}^{N(r)_k}\left\{\theta_{k,r,t}f(\kappa,E)_{k,r}f(\Pi a)_{k,r,t}f(\Omega)_{k,r,t}\right\} \tag{4}$$

where k is the index of solid phase of interest (pure solid or solid solution); n_k is the mole amount of k-th phase at time t; $A_{k,t}$ is the current surface area of the phase in m^2; $R_{n,k,t}$ is the total precipitation or dissolution rate (in $mol\ m^{-2}s^{-1}$); $N(r)_k$ is the number of parallel reactions or pathways that affect the amount of k-th phase; r is the index of a reaction or a pathway (dissolution, nucleation, and precipitation can be treated as different parallel reactions); $\theta_{k,r,t}$ is the effective fraction of surface area of k-th phase assigned to the r-th parallel reaction. Time-dependent parameters $A_{k,t}$ and $\theta_{k,r,t}$ may either depend on a built-in model of particle size/area evolution or be externally controlled from the mass transport code. In eq. (4),

$$f(\kappa,E) = \kappa_{k,r}^{o}\Lambda_{k,r}e^{\frac{-E_{k,r}}{RT}} \tag{5}$$

is the *reaction rate constant term* including the temperature correction, where: $\kappa_{k,r}^{o}$ is the rate constant at reference temperature (25 ºC) in $mol\ m^{-2}s^{-1}$ or other appropriate units; the sign convention of $\kappa_{k,r}^{o}$ is: positive sign for dissolution and negative for precipitation; T is the temperature in K; $\Lambda_{k,r}$ is the Arrhenius factor (1 by default); R is the universal gas constant (8.31451 $J\ K^{-1}\ mol^{-1}$); and $E_{k,r}$ is the activation energy ($J\ mol^{-1}$) of r-th «parallel reaction». The expression $e^{\frac{-E_{k,r}}{RT}}$ in eq. (5) is sometimes represented in another form $e^{\frac{-E_{k,r}^{*}}{R}\left(\frac{1}{T}-\frac{1}{298.15}\right)}$ involving the reference temperature 298.15 K *(Palandri and Kharaka 2004)*. Both are connected as:

$$\Lambda_{k,r}\cdot e^{-\frac{E_{k,r}}{RT}} = \Lambda_{k,r}^{*}\cdot e^{\frac{-E_{k,r}^{*}}{R}\left(\frac{1}{T}-\frac{1}{298.15}\right)} \text{ or } \Lambda_{k,r} = \Lambda_{k,r}^{*}\cdot e^{\frac{-E_{k,r}^{*}}{R\cdot298.15}} \tag{6}$$

under the assumption that $E_{k,r}^{*} = E_{k,r}$.

In eq. (4),

$$f(\Pi a)_{k,r} = I^{b_{I,k,r}} \mathrm{pH}^{b_{\mathrm{pH},k,r}} \mathrm{pe}^{b_{\mathrm{pe},k,r}} \mathrm{Eh}^{b_{\mathrm{Eh},k,r}} \left(\prod_{j}^{n(j)_{k,r}} a_{j,k,r}^{b_{j,k,r}} \right)^{p_{k,r}} \tag{7}$$

is the current (at time t) *activity product term*, combined to accommodate most of the literature rate laws, where: I is the (effective molal) ionic strength; $b_{I,k,r}$ is the related empirical parameter; $b_{\mathrm{pH},k,r}$ is the empirical parameter related to pH; $b_{\mathrm{pe},k,r}$ is the parameter related to pe; $b_{\mathrm{Eh},k,r}$ is the parameter related to Eh, V; $p_{k,r}$ is the «reaction order» parameter; $n(j)_{k,r}$ is the number of (aqueous or gaseous or surface) species from other reacting phases involved; $a_{j,k,r}$ is the activity (fugacity) of j-th species ($a_{\mathrm{H+}} = 10^{-\mathrm{pH}}$, $a_e = 10^{-\mathrm{pe}}$); $b_{j,k,r}$ is the (reaction stoichiometry coefficient) parameter. Note that in eq. (6), any term can be disabled if the respective power coefficient is set to the default value of zero.

Finally, in eq. (4), $f(\Omega)_{k,r}$ is the affinity term for r-th reaction, which can take several different forms, all using the current (at time t) k-th phase stability index Ω_k (eq. (2)). Different forms of the affinity term (see section 1.7) reflect different crystal growth or dissolution mechanisms. The classic affinity term is taken in the form $(1 + u_{k,r} - \Omega_k^{q_{k,r}})^{m_{k,r}}$ where $q_{k,r}$ and $m_{k,r}$ are the reaction order parameters (default value 1; $m_{k,r} = 0$ disables the affinity term); and $u_{k,r}$ is the empirical parameter (default value 0).

In eq. (4), the net rate $R_{n,k,t}$ is taken in mol·m^{-2}s^{-1} by default. However, in modern models of mineral dissolution or growth *(e.g. Wolthers 2012, Nielsen et al. 2013)*, the mean orthogonal *velocity of surface propagation* $R_{L,k,t}$ in m·s^{-1} is considered. $R_{L,k,t}$ relates to $R_{n,k,t}$ as

$$R_{L,k,t} = V_{M,k} R_{n,k,t} = \frac{M_{M,k}}{\rho_k} R_{n,k,t} \tag{8}$$

where $V_{M,k}$ is the mineral molar volume in m^3·mol^{-1}; $M_{M,k}$ is the molar mass of the phase in kg·mol^{-1}; and ρ_k is the phase density in kg·m^{-3}.

Specific surface area of the mineral is defined as $A_{S,k} = A_k / m_k$ (in m^2·kg^{-1}) or $A_{V,k} = A_k / V_k$ (in m^{-1}). Upon growth or dissolution, both $A_{S,k}$ and $A_{V,k}$ values vary with time because of changing particle size, shape, and surface roughness. Hence, in kinetic simulations, reactive surface areas must be corrected after each time step, either internally in TKinMet library functions, or externally controlled by the reactive transport model. In the simplest case, currently implemented in the TKinMet library, for particles of similar size and shape, assuming no density change of the mineral upon growth and no other second-order effects,

$$A_{V,k,t} = A_{V,k,t-\Delta t} \frac{\psi_{k,t-\Delta t}}{\psi_{k,t}} \frac{d_{VS,k,t-\Delta t}}{d_{VS,k,t-\Delta t} + 2R_{L,k,t}\Delta t} \tag{9}$$

where $A_{V,k,t}$ is the current specific surface area; $d_{VS,k}$ is the mean particle volume-surface diameter; and $R_{L,k}$ is the current linear rate from eq. (8). As a shape factor, we use the *sphericity* coefficient $0 < \psi_k \leq 1$ *(Wadell, 1935)*, defined as:

$$\psi_k = \pi^{1/3} \frac{\left(6V_p\right)^{2/3}}{A_p} = \frac{6V_p}{d_p A_p} \tag{10}$$

where $d_p = d_{VS,k} = \dfrac{6}{\psi_k A_{V,k}}$ is the *estimated particle size*; $V_p = \frac{1}{6}\pi d_p^3$ is the *mean particle volume*; and $A_p = A_k \dfrac{V_p}{V_k}$ is the *mean particle surface area*. Sphericity (eq. (10)) is the external parameter of the kinetics model; the initial ψ_o value must be defined together with other initial parameters at the beginning of simulations. From simple geometric considerations, perfect mineral crystals must have sphericity about 0.8 ± 0.1; values below 0.7 apply to thin platelets or to rough surfaces of aggregate particles.

In eq. (9), the evolution of sphericity describes the impact of changing morphology and surface roughness on the variation of (reactive) specific surface area and thus onto dissolution or precipitation rates of the solid. Again, this evolution can be controlled externally (from the mass transport model), or represented as a function of some system parameters, for instance

$$\psi_k(t) = \psi_{0,k} + \psi_{1,k}u + \psi_{2,k}u^2 + \dots \tag{11}$$

where $\psi_{0,k}$, $\psi_{1,k}$, $\psi_{2,k}$, … are the empirical coefficients, and the u variable can be e.g. the phase stability index $u = \log_{10}\Omega_{k,t}$, the relative change of phase amount $u = \left(n_{k,t} - n_{k,0}\right)/n_{k,0}$, or the function of growth rate $R_{L,k,t}$, of temperature T, or of other system variables.

At the same stoichiometry and chemical potential, the activity of any *j*-th component and the stability index of the whole phase Ω_k will depend on the value(s) of its standard-state per-mole Gibbs energy g^o_j (see eq. (2)). In fact, the g^o_j parameter can also reflect the differences in stability for polymorphic modifications of the same compound (e.g. amorphous calcium carbonate, vaterite, aragonite, calcite), as well as the impact of surface free energy (or interface tension) γ, or other energy factors. Therefore, we consider the g^o_j term with its possible modifications and extensions as a main spot to connect thermodynamic models, kinetic rates, and crystallization pathways, in addition to the $\psi_{k,t} = f(t,n,\Omega,\dots)$ function and $\theta_{k,r,t}$ parameters for parallel reactions.

In the TKinMet library, some parameters, e.g. the dissolution rate constant, the activation energy, the reaction type and order constants for parallel reactions, are considered as

chemical properties of the solid phase, kept in the respective phase definition record in GEMS project database. Other parameters, such as the shape factor function $\psi_{k,t} = f(t, n, \Omega, ...)$ and reactive fraction $\theta_{k,r}$ of surface area assigned to r-th parallel reaction, are related to evolving particle or pore size and shape distributions. Such parameters can be set externally, e.g. on the basis of assumptions of the reactive-transport or the crystallization pathway model. These parameters with their variation should generally come into TKinMet calculations from the process simulator or from the transport part of the coupled reactive transport code.

Aqueous - solid solution systems

For solid solutions, in the next partial equilibrium state at time $t+\Delta t$, the TKinMet code will split the new AMRs for the total amount of phase $\overline{n}_{k,t+\Delta t}$ into AMRs to the end members $\overline{n}^{(x)}_{j,t+\Delta t}$ (the symbols here refer to both upper- and lower AMR cases in eqs. (1)). There are several ways of such splitting, depending on a particular dissolution, precipitation, or nucleation process (this part of TKinMet code is still under development). For example, the dissolution of a sparingly-soluble solid solution usually occurs stoichiometrically *(Glynn and Reardon 1990)*, which can be represented by changing AMRs for end members proportional to their mole fractions:

$$\underline{n}_{k,t+\Delta t} = n_{k,t} + A_{k,t} R_{n,k,t} \Delta t \quad \text{if} \quad \log_{10} \Omega_k < -\varepsilon$$
$$\underline{n}^{(x)}_{j,t+\Delta t} = n^{(x)}_{j,t} + x_{j,t} (\underline{n}_{k,t+\Delta t} - n_{k,t})$$

(12)

Here, $x_{j,t}$ is the current mole fraction of *j*-th end member, and the index *j* runs over all end members in the solid solution phase. The impact of another (secondary) phase precipitation on the dissolution rate $R_{n,k,t}$ is accounted for by changes in the saturation index $\Omega_{k,t}$ or explicitly by augmenting the shape factor $\psi_{k,t}$ or the reactive area fractions $\theta_{k,r,t}$. For nucleation and growth, such relationships become complex *(Prieto 2009)* because such processes depend on the contribution of surface free energies that, in turn, depends on particle size and curvature.

In the present contribution, the case of uptake of a trace element (*Tr*) into a binary solid solution with the host element (*Hc*) is presented, as this case was considered in the SKIN project. Here, the rate law for the host mineral is applied to the whole solid solution phase, and used as the basis for the uptake kinetics model discussed previously in the WP4 Task 1 mid-term report, see also *(Thien et al. 2014)*.

The distribution of *Tr* between the aqueous and the solid solution relative to *Hc* is described by the fractionation coefficient $\Delta_{Tr,Hc}$, which is the ratio of two distribution ratios R_d:

$$\Delta_{Tr,Hc} = \frac{R_d(Tr)}{R_d(Hc)}$$

(13)

The distribution ratio is defined as the ratio of component concentration in the solid to that in the aqueous phase. Taking mole fraction x for the solid and total dissolved molality [] for the aqueous part as concentrations:

$$\Delta_{Tr,Hc} = \left(\frac{x_{Tr}}{[Tr]}\right) \Big/ \left(\frac{x_{Hc}}{[Hc]}\right) \text{ or } \Delta_{Tr,Hc} = \frac{x_{Tr}}{x_{Hc}} \cdot \frac{[Hc]}{[Tr]} \tag{14}$$

From the known fractionation coefficient $\Delta_{Tr,Hc}$ and the mole fraction x_{Hc} of Hc end member (usually unity or close to a constant if there are two or more major end members), the mole fraction of Tr end member can be estimated as

$$x_{Tr} = \Delta_{Tr,Hc} x_{Hc} \frac{[Tr]}{[Hc]} \tag{15}$$

At every time step, the correction of upper and lower metastability constraints for the host Hc and trace Tr end members is done using the previous amount $n^{(x)}$ of the respective end member and an increment, which is calculated according to kinetic rates, Hc mole fraction, and the Tr mole fraction obtained from the corrected (eq. (15)) Tr fractionation coefficient:

$$\overline{n}^{(x)}_{Hc,t+\Delta t} = n^{(x)}_{Hc,t} + A_{k,t} R_{n,k,t} \Delta t \cdot x_{Hc,t} \tag{16}$$

$$\underline{\overline{n}}^{(x)}_{Tr,t+\Delta t} = n^{(x)}_{Tr,t} + A_{k,t} R_{n,k,t} \Delta t \cdot x_{Tr,t} \quad \text{where } x_{Tr,t} = \Delta_{TrHc,t} \frac{[Tr]_t}{[Hc]_t} \quad \text{and } x_{Hc,t} = 1 - x_{Tr,t} \tag{17}$$

Equations as (14) and (15) apply to several Hc and Tr end members in the solid solution phase, if x_{Hc} and $[Hc]$ in eqs. (13), (14), (15) and (17) are re-defined as the sums of Hc components.

The unified uptake kinetics model (UUKM)

As we have shown previously *(Thien et al. 2014)*, the common outcome from the surface entrapment model (SEMO, *Watson 2004*) and the surface reaction kinetics model (SRKM, *DePaolo 2011*) is that the fractionation coefficient $\Delta_{Tr,Hc}$ varies between two limits, $\Delta_{Tr,Hc,eq}$ and $\Delta_{Tr,Hc,ads} = F_{Tr} \cdot \Delta_{Tr,Hc,eq}$. The former limit is related to the (hypothetical) aqueous – solid solution equilibrium; the latter limit corresponds to the distribution of adsorbed Hc and Tr components in equilibrium with the same aqueous solution of constant composition. F_{Tr} is the so-called trace element enrichment/depletion factor.

These limits suggest that SRKM might be considered as an integrated and simplified form of SEMO, which assumes that the progressing precipitation tends to "entrap" the adsorbed layer composition, whereas the sub-surface layer dynamics (diffusivity) drives its composition to become closer to that in the assumed aqueous- solid solution equilibrium. Since the mineral continues to grow, the uptake of trace elements in 'older' layers is, in principle, metastable. This irreversible process of enrichment or depletion of the solid with trace element relative to the expected aqueous- solid equilibrium concentration is called *surface entrapment*.

Relatively fast precipitation augments the composition of the newly-grown layer (i.e. buried adsorbed layer) with the *Tr* content greater than expected from $\Delta_{Tr,Hc,eq}$ if *Tr* is hardly compatible with the host mineral structure ($F_{Tr} > 1$), and less than that if *Tr* is favoured by the bulk mineral lattice ($F_{Tr} < 1$). This enrichment or depletion can be counterbalanced by a concurrent partial release of the entrapped *Tr* back to aqueous solution.

Thus, one can assume that the apparent *Tr* sub-surface diffusivity D_s parameter in SEMO is related to the *Tr* backward rate parameter R_b in SRKM, defined by $v_b R_k = v_k R_b$. This assumption leads to the equality $v_k ml = D_s$ and further to the UUKM equation that predicts the effective fractionation coefficient $\Delta^*_{Tr,Hc}$:

$$\Delta^*_{Tr,Hc} = \Delta_{Tr,Hc,eq} \frac{D_s + R_{L,k}ml}{D_s + \dfrac{R_{L,k}ml}{F_{Tr}}}$$

(18)

where the mineral growth rate $R_{L,k}$ (eq. (8)) is taken in nm·s^{-1}. The enrichment parameter F_{Tr} can be, in principle, evaluated if both the *Hc-Tr* solid solution thermodynamic model and the surface complexation model for *Hc* and *Tr* components on the *Hc* surface is available. The D_s parameter is related to surface dynamics, roughness, and reactivity, and can only be assessed in the inverse modelling.

Uptake in seed-overgrowth solid solution phases

The setup of aqueous – solid solution uptake kinetics upon the host mineral growth, described in Sections *1.4* and *1.5*, has a shortcoming that the composition of the overgrowth is mixed or homogenized with that of the initial seed crystals phase (Figure 1,A); it also cannot describe various cases of the (epitaxial) growth on surface of a mineral with other structure.

Therefore, it is desirable to have an option to link the specific surface and the kinetic rates for one "overgrowth" phase to the amount or surface of another "seed" or "substrate" phase; the latter may even be inert, or may have its own slow kinetics. This can be achieved with a *phase linkage*, in which the surface area of one "overgrowth" phase k is determined by the surface area of another ("substrate") phase s (Figure 1,B). If the linkage occurs via the surface area, the relationships between the surface area $A_{k,t}$ and the specific surface area $A_{S,k,t}$ become different from the usual ones as e.g. for the "substrate" phase where

$$A_{k,t} = A_{S,k,t} M_{M,k} n_{k,t}$$

(19)
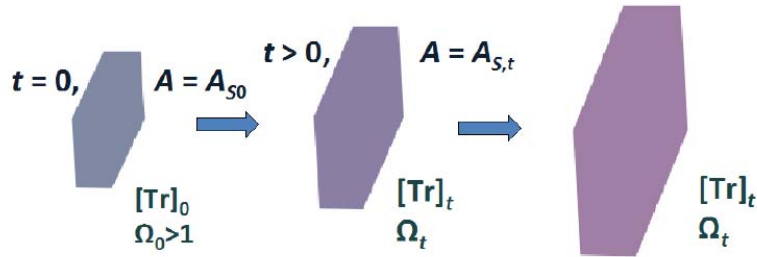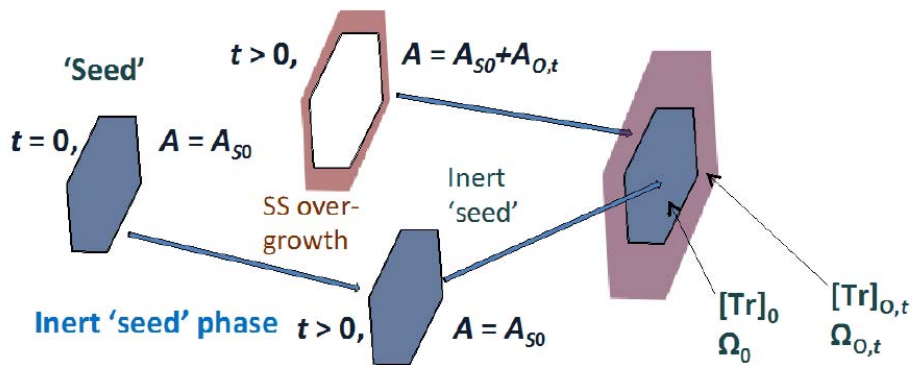
Fig. 1 Schematic representation of two cases of aqueous- solid solution (Aq-SS) uptake: A – single solid solution phase; B – "overgrowth" phase on the surface of "seed" phase, to follow the overgrowth composition independently of the "seed" phase composition.

However, in the case B (Figure 1), this relationship holds constant for the "seed" phase:

$$A_s = A_{S,s} M_{M,s} n_s \tag{20}$$

For the "overgrowth" phase,

$$A_{k,t} = A_{S,k,t} (M_{M,k} n_{k,t} + M_{M,s} n_s) . \tag{21}$$

In this case, in the specific surface correction (eq. (9)), the composite particle size, volume and mass are defined as

$$d_p = \frac{6(V_k + V_s)}{\psi_k A_k} ; \; V_p = \tfrac{1}{6} \pi d_p^3 ; \text{ and}$$

$$A_p = A_k \frac{V_p}{(V_k + V_s)} , \tag{22}$$

respectively.

A similar concept of the *metastability chain* can be further used in thermodynamic modeling of adsorption and ion exchange. In this case, the adsorbed layer (solution) must be linked to the surface of the sorbent similar to the case (Figure 1,B), but it has a limited thickness (total density). So, instead of growth or condensation, there will be a competition between surface species, described by the Langmuir or another adsorption isotherm.

Implementation of co-precipitation uptake kinetics in GEMS

Calculations of kinetic rates of mineral-aqueous reactions according to eq. (4) have been implemented in the TKinMet class, an extension of the GEMS3K code *(Kulik et al. 2013)*, together with the necessary input parameters (Table 1). GEMS3K can be coupled with mass transport simulation codes to perform reactive transport modelling in an "operator-splitting" fashion *(Shao et al. 2009)*.

For each mineral under kinetic rate control, GEMS3K code reads one or more parameter sets for parallel reactions (Table 1) from the GEM IPM input file, and stores them in a TSolMod class instance. If a positive time step is given, the TSolMod functions are automatically executed after the GEM run, resulting in modified AMRs for the respective mineral phase and its component(s), as given by eqs. (1). This process is schematically shown in a flow chart on Figure 2.

In this chart, the function KM_Create(k) creates a TKinMet instance for *k*-th phase. **GEM IPM**(step) run computes a (partial) equilibrium state in the system at the process step. KM_ParPT(k) makes corrections of kinetic and uptake parameters for current *T,P*. KM_InitTime(k) initializes time-dependent values in TkinMet instance; KM_UpdateTime(k) updates them for the current time step. KM_UpdateFSA(k) updates surface areas and other parameters under external control (e.g. in mass transport); KM_ReturnFSA(k) returns such internally changed parameters to external code. KM_InitRates(*k*) initializes kinetic rates and particle/pore properties; KM_CalcRates(*k*) calculates them for the current time step.

KM_SetAMRs(*k*) corrects AMRs for k-th phase using current rates and sets them to be used in the next time iteration. Only in the case of uptake in solid solution, KM_UptakeSS(*ks*) computes new fractionation coefficients and prospective end member mole fractions; then KM_SplitAMRs(*ks*) uses them to split AMRs for the phase into AMRs for its end members.

The necessary affinity terms (Table 2) are invoked by choosing the respective code for each parallel reaction.

Table 1: Input kinetic parameters for r-th parallel reaction.

Index	Comment	Symbol	Default value
0	Standard-temperature net rate constant (mol/m^2/s)	$\kappa_{k,r}^{+}$ or $\kappa_{k,r}^{-}$	0
1	Standard-temperature gross rate constant (mol/m^2/s)	$K_{k,r}^{+}$ or $K_{k,r}^{-}$	0
2	Arrhenius factor	$\Lambda_{k,r}$	1
3	Activation energy (J mol^{-1})	$E_{k,r}$	0
4	Empirical parameter related to I	$b_{I,k,r}$	0
5	Empirical parameter related to pH	$b_{pH,k,r}$	0
6	Empirical parameter related to pe	$b_{pe,k,r}$	0
7	Empirical parameter related to Eh	$b_{Eh,k,r}$	0
8	Reaction order parameter for the activity product term	$p_{k,r}$	1
9	Reaction order parameter in the affinity term	$q_{k,r}$	1
10	Parameter in the affinity term	$m_{k,r}$	0
11	Optional constant in the affinity term	$u_{k,r}$	0
12	«Effective» saturation index for nucleation	$\Omega_{k,eff}$	1
13	Second parameter for nucleation (reserved)		0

Notes to Table 1. If the net rate constant is 0 and gross rate constant is not 0 then the gross rate constant will be used, and vice versa. If both are not 0 then the net rate constant will be used; if both are 0 then this parallel reaction is disabled. The *state of dissolution* of k-th phase is detected when $\Omega_k < 1 - \varepsilon_{kin}$; the *state of precipitation* – when $\Omega_k > 1 + \varepsilon_{kin}$; *equilibrium* – when $1 - \varepsilon_{kin} \leq \Omega_k \leq 1 + \varepsilon_{kin}$ ($10^{-8} \leq \varepsilon_{kin} \leq 10^{-4}$ is the numerical tolerance for kinetic calculations). If the net rate constant is positive ($\kappa_{k,r}^{+}$) and the state is *dissolution* then this parallel reaction will be used, but if the state is precipitation then this parallel reaction will be skipped. If the net rate constant is negative ($\kappa_{k,r}^{-}$) and the state is *precipitation* then this reaction will be used with $|\kappa_{k,r}^{-}|$, but if the state is *dissolution* then this reaction will be skipped. In a single mineral phase definition, via multiple "parallel reactions", these rules allow setup of both dissolution and precipitation kinetics, according to different mechanisms, and/or applicable to several aqueous composition regions at varying temperatures.
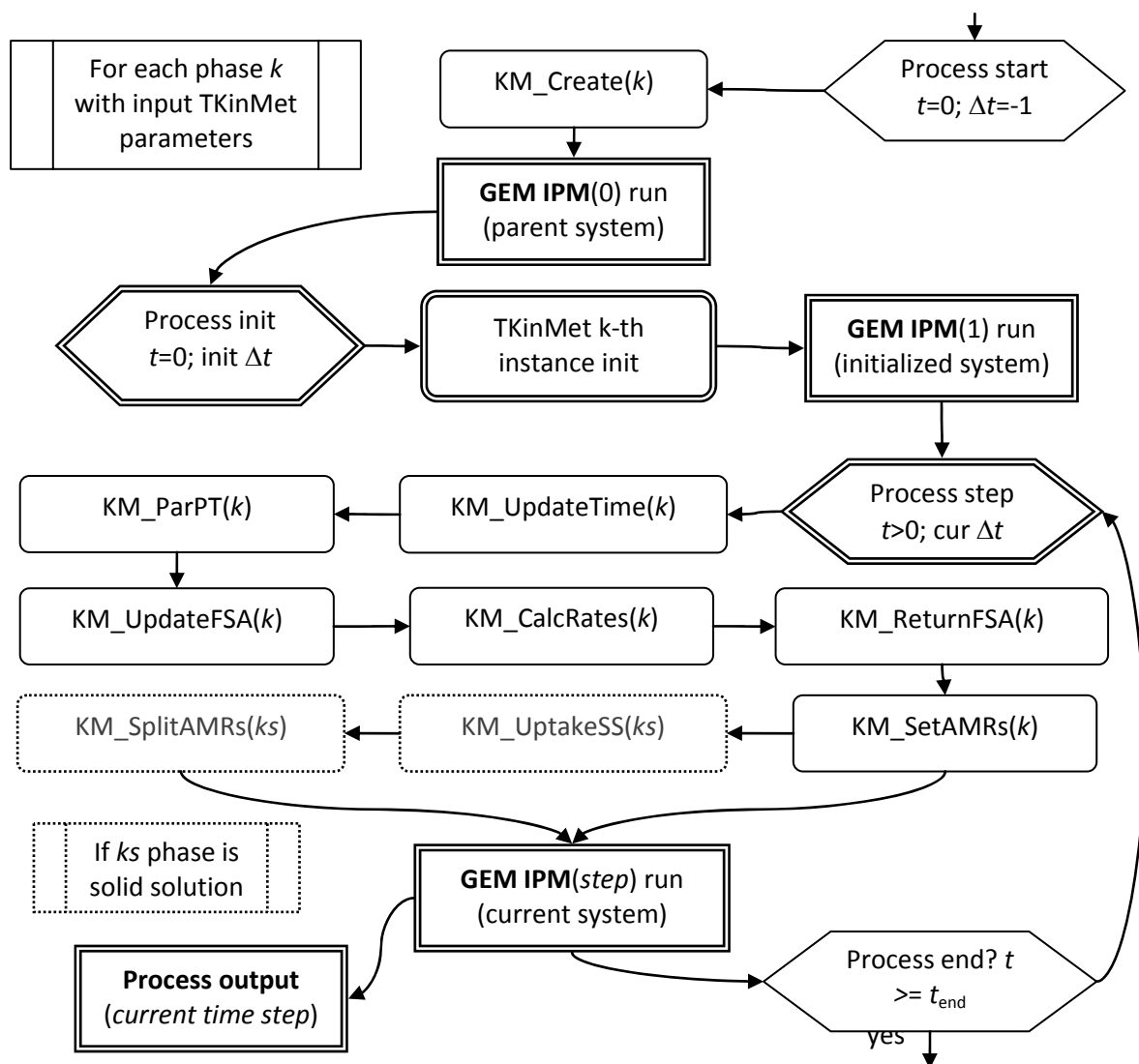
Fig. 2 Flow chart of GEMS process simulation using the TKinMet code library. Three main steps of kinetic simulations are shown: Process start; Process init(ialization); Process run until the end. At each step, TKinMet functions (whose names begin with KM_) are called for each kinetically controlled phase. See text for explanations.

Preparation of kinetic data is convenient to do using the GEM-Selektor v.3.3 code prototype, where such phase definitions with all necessary coefficients can be saved as Phase records in the modeling project database. Selection of aqueous, gaseous, or surface species for the activity product term (eq. (7)) is also stored in the Phase definition as a list of DComp or ReacDC record keys with respective reaction stoichiometry power coefficients $b_{j,k,r}$.

Table 2: Selection of affinity terms currently implemented in the TKinMet library

Code	*Expression*	*Comment, reference*
0	$(1 + u_{k,r} - \Omega_k^{q_{k,r}})^{m_{k,r}}$	Normal (default) affinity term
1	$(\Omega_k^{q_{k,r}} - 1 - u_{k,r})^{m_{k,r}}$	Inverse normal affinity term
2	$e^{-m_{k,r}/\Omega_k}$	(Schott et al. 2012), Fig. 1e
3	$1 - e^{-(q_{k,r} \ln \Omega_k)^{m_{k,r}}}$	(Hellmann and Tisserand, 2006), eq. (9)
4	$m_{k,r}(\Omega_k - 1) \cdot \ln \Omega_k$	(Teng et al. 2000), eq. (13)
5	$\Omega_k^{m_{k,r}}$	Nucleation (Teng et al. 2000), Fig. 6
6	$(\Omega_k - \Omega_{k,eff})^{m_{k,r}}$	Nucleation and growth (Fritz et al. 2009), eq. (6)

Notes to Table 2. $\Omega_{k,eff} \geq 1$ is the effective saturation index (default value 1) at the onset of nucleation. More choices of affinity terms will possibly be added in order to accommodate the rate laws available in literature for mineral-aqueous reactions.

Parameters of the uptake kinetics model described in section 1.5 and listed in Table 3 are supplied only in the solid solution Phase definition record in addition to the parameters for mineral-water reaction kinetics. The value of $\Delta_{Tr,Hc,eq}$ can be found in preliminary GEM calculations of aqueous-solid solution equilibria, or taken from the literature. Other parameters in Table 3 should be estimated as described in WP4 Task 1 mid-term report.

If the metastability linkage between the "overgrowth" solid solution and the "substrate" phase needs to be considered (section 1.6), it has to be provided as a special option in the Phase record for the "overgrowth" phase. There the record key of the "substrate" phase is selected from the modeling project database, along with the type and parameters for the linkage. Currently, the link to the "substrate" phase surface area is implemented, with a parameter being an effective fraction of surface to be used in scaling the amount of overgrowth phase over time steps (default fraction is unity).

Table 3: Uptake model parameters

Index	Comment	Symbol	Default
0	Surface enrichment/depletion factor	F_{Tr}	1
1	*Tr* fractionation coefficient in solid solution in equilibrium with the medium	$\Delta_{Tr,Hc,eq}=\alpha_{eq}$	1
2	*Tr* surface diffusivity, $nm^2 s^{-1}$	D_s	0
3	lattice diffusion coefficient, $nm^2 s^{-1}$	D_l	0
4	half-thickness of surface enriched/depleted layer (nm)	l	0
5	multiplier linking *l* to the maximal thickness of the diffusivity region	m	1

The whole simulation of kinetically-dependent system can be performed in the Process Simulator mode of GEM-Selektor v.3.3 package prototype. The TKinMet calculations are automatically activated when the time iterator of the process is set with the positive time step value and more than one step.

Technical details can be found in Phase and Process create/remake wizards, as well as in the GEM-Selektor runtime help database. Note that in the provided software, the TKinMet library options have been tested only for the methods described above and using only the test systems described in Section 2 below. Before the general use of the software becomes possible, many more extensions, tests and benchmarks need to be performed in on-going and future projects.

Modelling examples and verification

The idea of simulation examples was to test and verify the new functionality implemented in the TKinMet code library of GEMS3K code, as well as Phase and Process simulator modules of GEM-Selektor code. The test example about portlandite shows how the seeded mineral growth is simulated, and why the proper shape factor function for the A_S correction may be needed to fit the experimental data. The example for calcite precipitation verifies the growth rate model *(Wolthers et al. 2012)* against the independent experimental data. This rate model for calcite is used as a background in other test simulations, aimed at showing how the UUKM (eq. (18)) describes the strontium uptake upon calcite growth, with important effects such as the impact of growth-rate variation and/or solution depletion.

Seeded growth of portlandite

This example shows a simulation of seeded precipitation of portlandite $Ca(OH)_2$ from aqueous solution at room temperature, with kinetic rate constant and shape factor function parameterized against the experimental data *(Tadros et al. 1976)*. In these experiments, the

supersaturated solutions were prepared by mixing equal volumes of 0.07 M $CaCl_2$ and 0.14 M NaOH stock solutions under CO_2-free conditions. In one series of experiments, the crystallization of portlandite was initiated by adding 10 mg of seed crystals with specific surface area $A_S = 2.1$ $m^2 \cdot g^{-1}$ to 300 ml of the supersaturated solution. The time variation of the conductance was followed until constant readings achieved in about 90 min. Plots of log(conductance at t – conductance at equilibrium) were assumed proportional to log($[Ca]_{aq,t}$ – $[Ca]_{aq,eq}$), provided that the Cl^- and Na^+ concentrations remain constant during growth. Using this assumption, initial $[Ca]_{aq} = 0.0351$ m, and equilibrium $[Ca]_{aq,eq} = 0.0231$ m (Table 4), we have converted in a spreadsheet the conductance data (Figure 2 in *Tadros et al. 1976*) into total dissolved $[Ca]_{aq}$ values, with the estimated uncertainty less than 0.3×10^{-3} m.

Table 4: Initial recipe of the chemical system "PortlKinExp" for the Process simulation.

Property	Name	Quantity	Units	Comment
xa_	Aqua (H_2O)	299.26	g	Addition of 300 ml water H_2O at 1 bar, 25 °C
xa_	CaCl2	0.0105	mol	Addition of 0.0105 moles of $CaCl_2$ (in 150 ml of 0.07 M $CaCl_2$ solution)
xa_	NaOH	0.021	mol	Addition of 0.021 moles of NaOH (in 150 ml of 0.14 M NaOH solution)
xd_	Portlandite	0.01	g	Addition of 10 mg $Ca(OH)_2$ "seed" crystals
bi_	Nit	0.0016	mol	Addition of atmospheric nitrogen
bi_	O	0.0004	mol	Addition of oxygen (to form a CO_2-free atmosphere)
dul_	Portlandite	0.000135	mol	Upper AMR for 10 mg of "seed" portlandite

"Property" identifies an entry in the GEM-Selektor Recipe dialog.

Model calculations have been performed using the GEM-Selektor v.3.3 code prototype, in the "Kinetics" test modeling project, at $P = 1$ bar, $T = 25$ ºC. The initial system recipe was set as given in Table 4; the Davies equation was used for computing aqueous activity coefficients. The input thermodynamic data were taken from GEMS version of the PSI-Nagra database 01/07 (*Thoenen, 2012;* http://gems.web.psi.ch/TDB). The GEM-calculated initial saturation index of portlandite was 2.836, the total dissolved $[Ca]_{aq} = 0.0351$ m. In a separate GEM calculation of equilibrium in the same system without the upper AMR for portlandite, $[Ca]_{aq,eq}$ was found to be equal to 0.0231 m.

Kinetic parameters of the Portlandite phase were set according to a simple rate equation $R_{Port} = \kappa^-_{Port}(1 - \Omega_{Port})$. The rate constant value κ^-_{Port} together with the dependence of the sphericity factor ψ_{Port} on saturation index given as $\psi_{Portl}(t) = \psi_0 + \psi_1 u$ where $u = \log_{10} \Omega_{Port,t}$,

were adjusted in trial-and-error process simulations using the CEM-Selektor Process module with Graphics dialog.

The time interval was [0; 6000] s with time step Δt of 15 or 30 s; no visible differences on the model curves were found with these Δt values. Excellent fit to the experimental conductivity data (Figure 3) was obtained with parameters given in Table 5.

Table 5: Parameters of the kinetic model for portlandite seeded growth.

Parameter	Value	Comment
Net rate constant at 25 C κ^-_{Port} (mol·m⁻²·s⁻¹)	-3.23 × 10⁻⁵	Fit to data
Arrhenius factor Λ_{Port}	1.0	Default
Activation energy E_{Port}	0	Default
Reactive surface area fraction θ_{Port}	1.0	Default
Sphericity factor dependence $\psi_0 + \psi_1 u : \psi_0$	0.83	Geometry;
ψ_1	-1.6	fit to data
Initial specific surface area $A_{S,Port,0}$ (m²·g⁻¹)	2.1	experiment
Initial portlandite "seed" mass m_{Port} (g)	0.01	experiment

For comparison, Figure 3 shows curves simulated with the same parameters, but without the correction of shape factor (sphericity), kept constant at its "equilibrium" value of 0.83. This shows that a significant change in morphology of portlandite particles must take place during the early stages of growth. This is indirectly corroborated by ***(Tomazic et al. 1986)*** who provide the evidence of morphology changes upon portlandite precipitation.

Some other model sensitivity cases are given in Figure 4, on the left-hand side of which the "best" fit at constant ψ_{Port} = 1.0 and κ^-_{Port} = -2.1 mol·m⁻²s⁻¹ shows that the absence of shape factor correction results in a wrong shape of the model curve that cannot be fixed by adjusting the rate constant. The right-hand side shows the impact of too large time step duration Δt. To find the optimal time stepping is a non-trivial issue, which requires more investigation. Presently, the practical rule would be to demonstrate that the same model curve is produced with two different (small enough) time step length values.
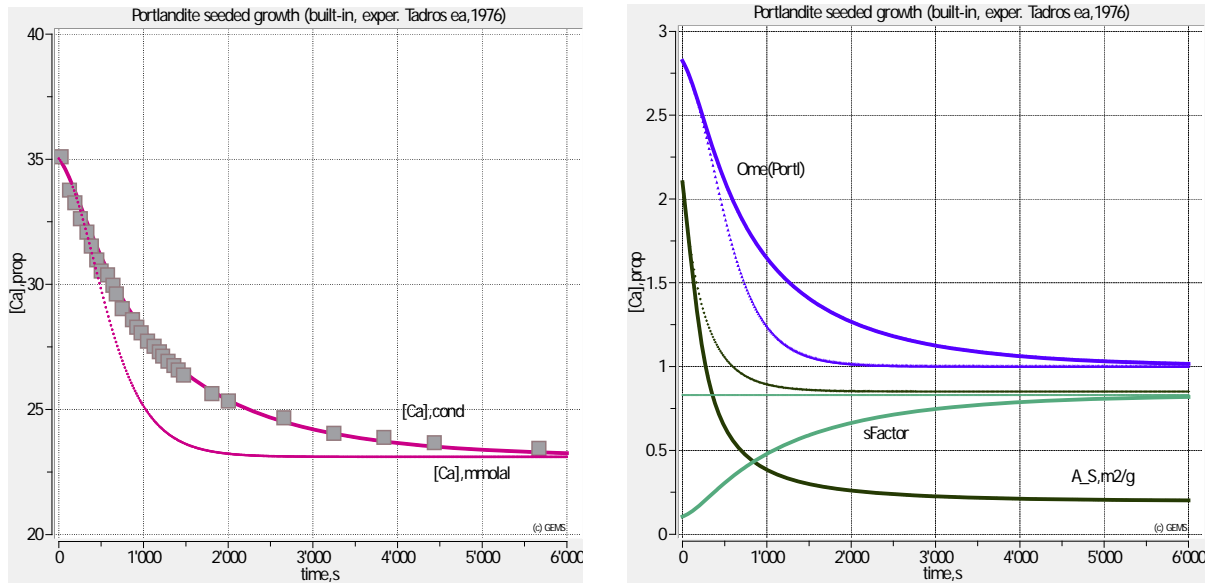
Fig. 3 Simulation of seeded growth of portlandite (dense curves) in comparison with experimental data from (Tadros et al. 1976) (squares) and another simulation with constant sFactor (sphericity factor) ψ_{Port} = 0.83 (thin dotted curves). Ome(Portl) denotes $\Omega_{Port,t}$.
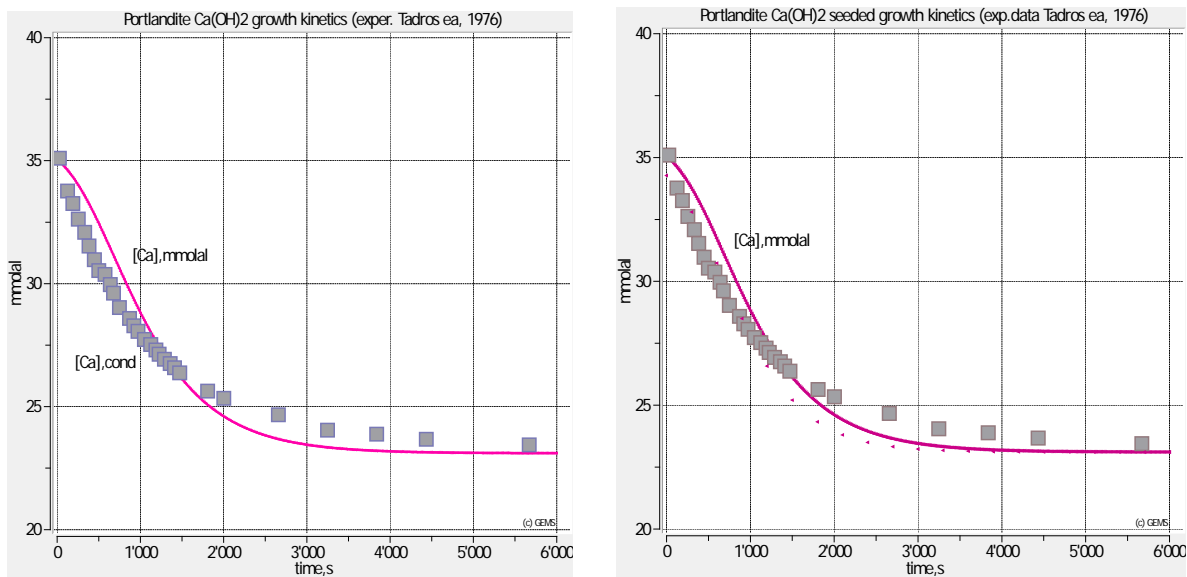
Fig. 4 Sensitivity of kinetic simulations of seeded growth of portlandite. Left-hand side: "best fit" with ψ_{Port} = 1.0, κ^-_{Port} = -2.1 mol·m^{-2}·s^{-1}, and Δt = 15 or 30 s. Right-hand side: the same model run compared with the one at time stepping of Δt = 300 s (dots).

Calcite precipitation

For modelling kinetics of trace element uptake in calcite, eq. (18) must be combined with the calcite precipitation rate law. We used the rate law (at $T = 20$ °C) from *(Wolthers et al. 2012)*:

$$R_{L,Cal} = I^{-0.004} pH^{-10.71} \cdot \left(\frac{a_{Ca^{2+}}}{a_{CO_3^{2-}}} \right)^{-0.35} \cdot (\Omega^{0.5} - 1)^2 \tag{23}$$

where $R_{L,Cal}$ is the mean orthogonal surface propagation velocity (in m·s^{-1}). It can be converted using eq. (8) into the net precipitation rate R_{Cal} (in mol·m^{-2}·s^{-1}):

$$R_{Cal} = 10^6 \frac{R_{L,Cal}}{V_{M,Cal}} = 27075.3 \cdot R_{L,Cal} \tag{24}$$

where $V_{M,cal} = 36.934$ cm^3·mol^{-1} is the calcite molar volume. For seawater (diluted and undiluted), *Wolthers et al. (2012)* proposed a slightly different rate law to account for the inhibition effects of Mg^{2+} and other ions:

$$R_{L,Cal,SW} = I^{0.36} pH^{-10.99} \cdot \left(\frac{a_{Ca^{2+}}}{a_{CO_3^{2-}}} \right)^{-0.71} \cdot (\Omega^{0.5} - 2)^2 \tag{25}$$

The activation energy of calcite is 48.1 kJ·mol^{-1} at $T = 25$ °C *(Inkseep and Bloom, 1985)*. Using eq. (6) yields the Arrhenius constant $\Lambda_{k,r} = 1 \cdot \exp[-E_{k,r}^* / (R \cdot 298.15)] = 2.6706 \cdot 10^8$ leading to the correction factor from 298 to 293 K equal to 0.7163; the coefficient -27075.3/ 0.7163 = -37800 was put in place of the rate constant κ_{Cal}^- used in eq. (4).

Let us check the rate eq. (23) on an example for seeded precipitation of calcite CaCO$_3$ from aqueous solution at $T = 10$ °C, compared with the experimental data *(Dreybrodt et al. 1997)*. These authors prepared supersaturated solutions by dissolving CaCO$_3$ powder and CO$_2$ in deionized water. Immediately after filling the vessel with the supersaturated solution (4×10^{-3} M [Ca^{2+}]), 3×16 mmol of calcite seed (with $A_{S,0} = 0.184$ m^2·g^{-1}) was introduced. Because of calcite precipitation, [Ca^{2+}]$_t$ (monitored by conductance measurements) decreased with time tending toward the equilibrium [Ca^{2+}]$_{eq}$ value of 2.8×10^{-3} M.

Simulations at 1 bar, 10 °C were performed in the "Kinetics" test modeling project using the GEM-Selektor v.3.3 prototype, using the Davies equation for aqueous activity coefficients. Thermodynamic data were taken from the GEMS version of the PSI-Nagra database 01/07 (*Thoenen, 2012*; http://gems.web.psi.ch/TDB). Initial system recipe is given in Table 6.

Table 6: Initial recipe of the chemical system "Calcite" for the GEM process simulation

Property	Name	Quantity	Units	Comment
xa_	Aqua	262	g	Addition of 262 ml water H_2O at 1 bar, 10 °C
xa_	$CaCO_3$	0.00435	mol	Addition of 0.00435 moles of $CaCO_3$ for both the solution and the seed calcite.
xa_	CO_2	0.0011	mol	Addition of 0.011 moles of CO_2 to obtain $pCO_2 = 1 \times 10^{-3}$ bar (adjusted by trial-end-error)
xa_	O_2	1×10^{-6}	mol	Addition of O_2 to stabilize redox state
dll_	Calcite	0.00316	mol	Lower AMR for 0.00316 mol of "seed" calcite
dul_	Calcite	0.00316	mol	Upper AMR for 0.00316 mol of "seed" calcite

Table 7: Parameters of the kinetic rate model for calcite precipitation

Comment	Value	Reference
Net rate constant at 25 °C κ_{Cal}^- (mol·m^{-2}·s^{-1})	-37800	See text
Arrhenius factor Λ_{Cal}	2.671×10^8	See text
Activation energy E_{Cal} (kJ·mol^{-1})	48.1	***(Inkseep and Bloom 1985)***
Reactive surface fraction θ_{Cal}	1.0	Default
Sphericity factor ψ_{Cal}	0.8	Geometry (as for cube)
Initial specific surface area $A_{S,Cal,0}$ (m^2·g^{-1})	0.184	Experiment
Initial calcite "seed" mass (g)	0.316	Experiment

The GEM calculation for this system yields the initial saturation index of calcite ($\log_{10}\Omega_{Cal}$ = 2.53). Note that this system is extremely sensitive to the addition of CO_2 to bulk composition. The value in Table 6 was found by trial-and-error to set calculated pCO_2 = 0.001 bar, as mentioned by ***Dreybrodt et al. (1997)***.

Kinetic parameters in the Calcite phase record were set according to Table 7. The sphericity factor of calcite was set constant at ψ_{Cal} = 0.8. Process simulations were performed in the time interval [0; 44000] s with the time step Δt = 10 s (Figue 5).

The model reproduces well the measured [Ca^{2+}] at times longer than 8000 s. Some deviation at shorter times may be due the "seed" sample heterogeneity or variation in particle morphology upon growth, both not accounted for in the present model.

In general, a good fit to the experimental data without any parameter adjustment confirms the validity of calcite growth kinetic rate equation *(Wolthers et al. 2012)*, especially at close-to-equilibrium conditions and slow rates.
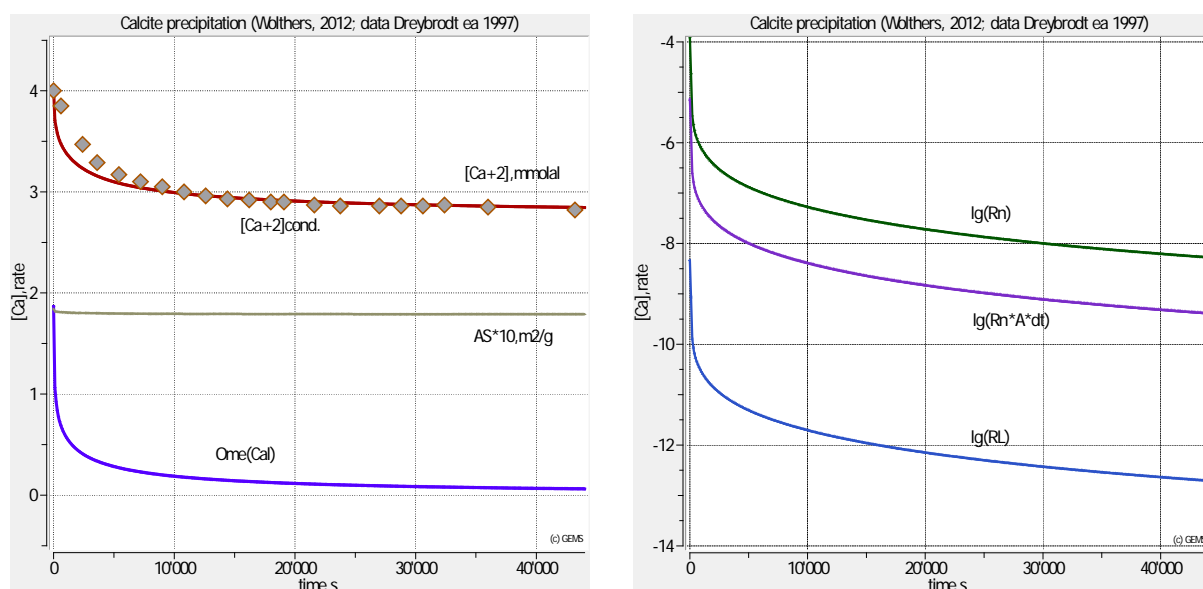
Fig. 5 Simulations of calcite precipitation with kinetic parameters from Table 7. Calcite specific surface area AS*10 is $10 \cdot A_{S,cal}$ in $m^2 \cdot g^{-1}$. Ome(Cal) is the current stability index Ω_{Cal} of calcite. Decimal logarithmic rates (right-hand side) are shown in $mol \cdot m^{-2} \cdot s^{-1}$ (Rn); in moles per time step (Rn*A*dt); and in $m \cdot s^{-1}$ (RL).

Simulations of Sr and Cd uptake kinetics in calcite

In this example for seeded co-precipitation of the "incompatible" cation Sr^{2+} in calcite $CaCO_3$ from aqueous solution, the uptake kinetics model has been parameterized against the experimental data by *(Lorens 1981)*. In this experiment, the precipitation of calcite was triggered by a constant addition of Na_2CO_3 stock solution with a rate 2.16×10^{-8} mol$\cdot$s^{-1} to the initial solution, which induced an average calcite growth rate of 2.94×10^{-6} mol$\cdot$m$^{-2} \cdot$s^{-1}.

Simulations have been performed using the GEM-Selektor v.3.3 code prototype, in the "LorensSrCa" test-modeling project, at 1 bar, 25 °C. The initial system recipe is given in Table 8; the Extended Debye-Hückel equation was used for aqueous activity coefficients. The input thermodynamic data were taken from the GEMS version of PSI-Nagra database 01/07.

Table 8: Recipe of initial chemical system "SrCaLorens7" for the Process simulation.

Property	Name	Quantity	Units	Comment
xa_	Aqua	150	g	Addition of 150 ml water H_2O at 1 bar, 25 °C
xa_	NaCl	0.1035	mol	Addition of 0.1035 moles of NaCl
xd_	NaHCO$_3$	0.00145	mol	Addition of 0.00145 moles of $NaHCO_3$
xa_	CaCl$_2$	0.0015	mol	Addition of 0.0015 moles of $CaCl_2$
xa_	Na$_2$CO$_3$	1×10^{-7}	mol	Addition of 1×10^{-7} moles of Na_2CO_3
xa_	CaCO$_3$	9.2×10^{-5}	mol	Addition of 9.2×10^{-5} moles of $CaCO_3$ for seed
xd_	Sr+2	4.59×10^{-8}	mol	Addition of 4.59×10^{-8} moles of $SrCl_2$
xd_	Cl-	9.18×10^{-8}	mol	Addition of 4.59×10^{-8} moles of $SrCl_2$
xa_	CO$_2$	0.055	g	Addition of CO_2 to equilibrate the solution
xa_	O$_2$	0.1	g	Addition of O_2 to set redox state
xa_	N$_2$	3	g	Addition of N_2 to equilibrate the solution
dll_	Cal_seed	9.2×10^{-5}	mol	Lower AMR set for "seed" calcite
dul_	Cal_seed	9.2×10^{-5}	mol	Upper AMR set for "seed" calcite

Process simulation: titration by adding Na_2CO_3 with a rate 2.16×10^{-8} mol·s^{-1}.

A solid-solution phase Calcite-Sr_ovg consisted of two end-members, Cal (calcite) and SrCO3-cal (SrCO$_3$ with calcite structure), and a regular parameter W_G = 4.4 kJ·mol^{-1} *(Kulik et al. 2010)*. This phase was initially used without AMRs to calculate the equilibrium fractionation coefficient $\Delta_{Sr,Ca,eq}$ = 0.021. The recipe of the initial system is provided in Table 8. Kinetic rate parameters for the Calcite-Sr_ovg phase were taken the same as in Table 7; the UUKM parameters were set according to Table 9. The Calcite-Sr_ovg phase was linked to the surface area of the Calcite_seed pure phase, with the initial $A_{S,Cal}$ = 0.8 m^2·g^{-1}.

Table 9: Parameters of the uptake kinetic model for Sr in calcite.

| Comment	Value	Reference
Initial specific surface area $A_{S,0}$ (m^2·g^{-1})	0.8	experiment
Initial calcite "seed" mass (g)	9.2×10^{-3}	experiment
Surface enrichment factor F_{Sr}	6.2	*(Thien et al. 2013)*
Equilibrium fractionation coefficient $\Delta_{Sr,Ca,eq}$	0.021	*(Kulik et al. 2010)*
Sr sub-surface diffusivity $D_{s,Sr}$ (nm^2·s^{-1})	0.02	*(Thien et al. 2013)*
Sr lattice diffusivity in calcite $D_{l,Sr}$ (nm^2·s^{-1})	1×10^{-16}	the same
Length l at which DS applies in the subsurface layer (nm)	0.5	the same
Length multiplicator m	6	the same
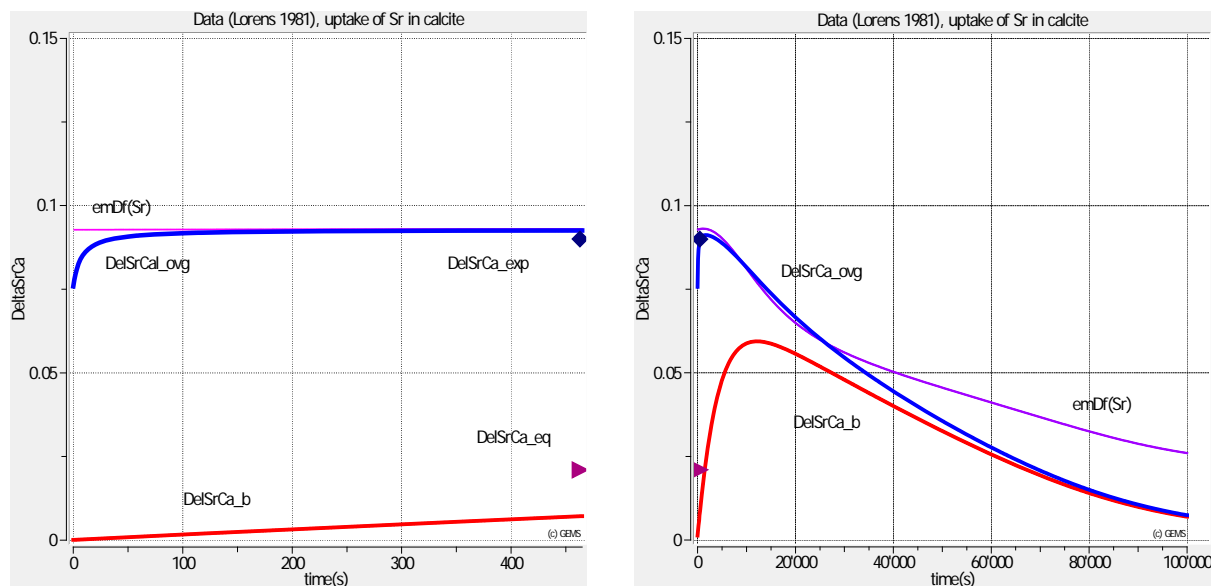
Fig. 6 Simulations of time-dependent uptake of Sr in calcite (different time scales on left- and right-hand sides). DelSrCa_exp: experimental $\Delta_{Sr,Ca}$; DelSrCa_eq: aqueous – solid solution equilibrium $\Delta_{Sr,Ca,eq}$; emDf(Sr): effective $\Delta_{Sr,Ca}$ (eq. (18)); DelSrCa_ovg: average $\Delta_{Sr,Ca}$ in the overgrowth phase; DelSrCa_b: bulk $\Delta_{Sr,Ca,eq}$ in the seed + overgrowth phase.

A first Process simulation has been run within the time interval [0; 540] s (actual duration of the experiment) with time step of 1 s. To explore the potential depletion effects, the second simulation has been performed within a hypothetical longer time interval [0; 10000] s. The results are shown in Figure 6. They indicate a similar enrichment of Sr in over-grown calcite as in the experiments ***(Lorens, 1981)***, whereas at long reaction time, the aqueous solution depletion effect drives the effective Sr fractionation coefficient back to its aqueous-solid solution equilibrium value (0.021) and then to much lower values.

In another example, the seeded precipitation of "compatible element" cadmium with calcite at 1 bar, 25 °C has been simulated and compared with the experimental data ***(Lorens, 1981)***. As in the previous example, the process is driven by constant addition of Na_2CO_3 at the rate 8.37×10^{-9} mol·s^{-1} that induces the initial growth rate of calcite $R_{n,Cal} = 2.975 \times 10^{-6}$ mol·m^{-2}·s^{-1}.

Simulations have been performed in the "CdCalcite" test modeling project. The initial system recipe was set as given in Table 10; the Extended Debye-Hückel equation was used for computing aqueous activity coefficients. The input thermodynamic data were from the GEMS version of the PSI-Nagra database 01/07; those for otavite $CdCO_3$ - from ***(Gamsjäger et al. 1999)***; and for Cd aqueous species – from the SUPCRT database (built-in in GEM-Selektor).

A solid-solution Calcite-Ota_ovg consists of two end-members, Cal (calcite) and Otavite (CdCO$_3$), with the regular interaction parameter W_G = 2.975 kJ mol^{-1} *(Tesoriero and Pankow 1996)*. This phase was initially used without AMRs to calculate the equilibrium fractionation coefficient $\Delta_{Cd,Ca,eq}$= 33.0; the recipe of the initial system is provided in Table 10.

Table 10: Recipe of initial chemical system "CdCaLorens2" for the Process simulation.

Property	Name	Quantity	Units	Comment
xa_	Aqua	150	g	Addition of 150 ml water H$_2$O at 1 bar, 25 °C
xa_	NaCl	0.1035	mol	Addition of 0.1035 moles of NaCl
xd_	NaHCO$_3$	0.0017	mol	Addition of 0.0017 moles of NaHCO$_3$
xa_	CaCl$_2$	0.0015	mol	Addition of 0.0015 moles of CaCl$_2$
xa_	CaCO$_3$	3.1×10^{-5}	mol	Addition of 3.1×10^{-5} moles of CaCO$_3$ for seed
xd_	Cd+2	1×10^{-6}	mol	Addition of 1×10^{-6} moles of CdCl$_2$
xd_	Cl-	2×10^{-6}	mol	Addition of 1×10^{-6} moles of CdCl$_2$
xa_	CO$_2$	0.043	g	Addition of CO$_2$ to equilibrate the solution
xa_	O$_2$	0.1	g	Addition of O$_2$ to equilibrate the solution
xa_	N$_2$	2	g	Addition of N$_2$ to equilibrate the solution
dll_	Cal_Seed	3.1×10^{-5}	mol	Lower AMR for 3.1×10^{-3} g of "seed" calcite
dul_	Cal_Seed	3.1×10^{-5}	mol	Upper AMR for 3.1×10^{-3} g of "seed" calcite
dul_	Cal	1×10^{-10}	mol	Upper AMR for 1×10^{-10} mol of calcite end member
dul_	Otavite	1×10^{-12}	mol	Upper AMR for 1×10^{-12} mol of otavite end member

Table 11: Parameters of the uptake kinetic model for Cd in calcite.

| Comment	Value	Reference
Initial specific surface area $A_{S,0}$ (m$^2 \cdot$g^{-1})	0.8	experiment
Initial calcite "seed" mass (g)	3.1×10^{-3}	experiment
Surface enrichment factor F_{Cd}	0.3	*(Thien et al. 2013)*
Equilibrium fractionation coefficient $\Delta_{Cd,Ca,eq}$	33.0	*(Tesoriero and Pankow 1996)*
Cd sub-surface diffusivity $D_{s,Cd}$ (nm$^2 \cdot$s^{-1})	0.02	*(Thien et al. 2013)*
Cd lattice diffusivity in calcite $D_{l,Cd}$ (nm$^2 \cdot$s^{-1})	1×10^{-16}	the same
Length l at which D_S applies in the subsurface layer (nm)	0.5	the same
Length multiplicator m	6	the same
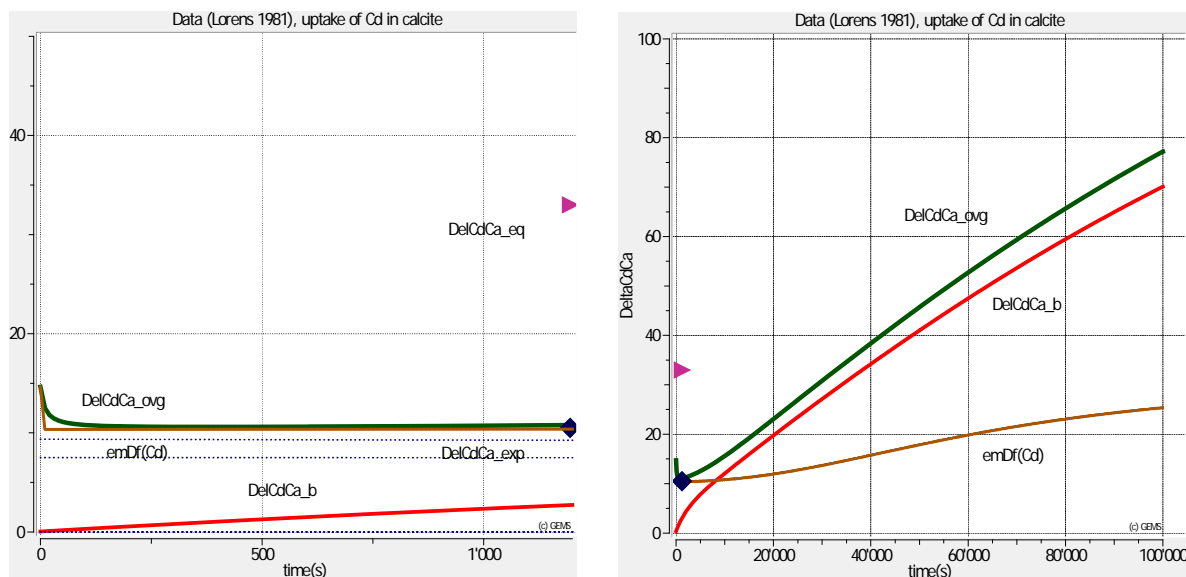
Fig. 7 Simulations of time-dependent uptake of Cd in calcite (different time scales on left- and right-hand sides). DelCdCa_exp: experimental $\Delta_{Cd,Ca}$; DelCdCa_eq: aqueous – solid solution equilibrium $\Delta_{Cd,Ca,eq}$; emDf(Cd): effective $\Delta_{Cd,Ca}$ (eq. (18)); DelCdCa_ovg: average $\Delta_{Cd,Ca}$ in the overgrowth phase; DelCdCa_b: bulk $\Delta_{Sr,Ca,eq}$ in the seed + overgrowth phase.

Kinetic rate parameters for the Calcite-Ota_ovg phase were taken the same as in Table 7; the UUKM parameters were set according to Table 11. The Calcite-Ota_ovg phase was linked to the surface area of the Calcite_seed pure phase, with initial $A_{S,Cal}$ = 0.8 m^2·g^{-1}.

The first Process simulation has been run in the time interval [0; 1200] s (actual duration of the experiment) with time step of 10 s. To explore the potential aqueous solution depletion effects, the second simulation has been run within a longer time interval [0; 100000] s with time step of 100 s. The results are shown in Figure 7. They indicate the same depletion of Cd in over-grown calcite as observed in the experiments *(Lorens, 1981)*, whereas at long reaction times, the aqueous solution depletion effect would drive the effective Cd fractionation coefficient up to its aqueous-solid solution equilibrium value.

Simulation of Sr uptake in calcite from the seawater –air system

The idea of this example was to demonstrate the potentially complex uptake processes on the background of temperature, composition change, and depletion effects in aqueous- solid solution systems that can be modeled with the new TKinMet code functionality. The obtained predictions may comprise a challenge for future experimental verifications. We also compare both one- and two- solid solution cases as outlined in Figure 1.

One solid solution case. The initial chemical system "Sr-calcite" was set in the "CarbSea" test modeling project, using the recipe in Table 8 and the Extended Debye-Hückel equation with the common size parameter for aqueous activity coefficients. The input thermodynamic data was taken from the GEMS version of the PSI-Nagra database 01/07.

The solid-solution phase Calcite-Sr_ovg with two end-members, Cal (calcite) and SrCO3-cal ($SrCO_3$ with calcite structure), and a regular parameter $W_G = 4.4$ kJ·mol⁻¹ was included into the system definition. This phase model is the same as that considered in Section 2.3 above.

Table 12: Recipe of initial chemical system "SrCalcite" for the Process simulation.

Property	Name	Quantity	Units	Comment
xa_	Aqua	965	g	Addition of H_2O to produce 1 kg of seawater
xa_	AtmAirNit	10	kg	Atmosphere (pCO_2 = 36 Pa)
xa_	$CaCO_3$	1.0×10^{-4}	mol	Addition of 0.1 mmoles of $CaCO_3$ for seed
xd_	SeaSalt	35	g	Addition of 35 g normative sea salt
dul_	Cal	1.001×10^{-4}	mol	Upper AMR set for 10 mg·kgw⁻¹ "seed" calcite
dul_	SrCO3-cal	1.8×10^{-10}	mol	Upper AMR set for trace Sr content in"seed" calcite

Process simulation: titration by adding Na_2CO_3 with a rate of 0.05 mmol per hour; time interval: [0; 200] h; time step Δt = 1 h. Normative sea salt composition (in mmol·kgw⁻¹, without H_2O):

C	1.93895	Mg	54.9493
Ca	10.6366	Na	484.336
Cl	565.497	O	123.597
H	2.339	S	29.1959
K	10.5568	Sr	0.09308

Kinetic rate parameters for the Calcite-Sr_ovg phase were taken the same as in Table 7; the UUKM parameters were set as in Table 12, except that initial $A_{S,0}$ set equal to 0.09 m²·g⁻¹. In Figure 8, the results of simulations at P = 1 bar, T = 25 °C and 15 °C are presented.

The linked two-solid-solutions case. The initial chemical system "Sr-calc-ovg" was set in the "CarbSea" test modeling project, using the recipe in Table 8 and other features similar to the previous case. Two solid solution phases were included. The "seed" ArgStr phase with end members Arg (aragonite) and Str (strontianite) had the properties from *(Kulik et al. 2010)*.
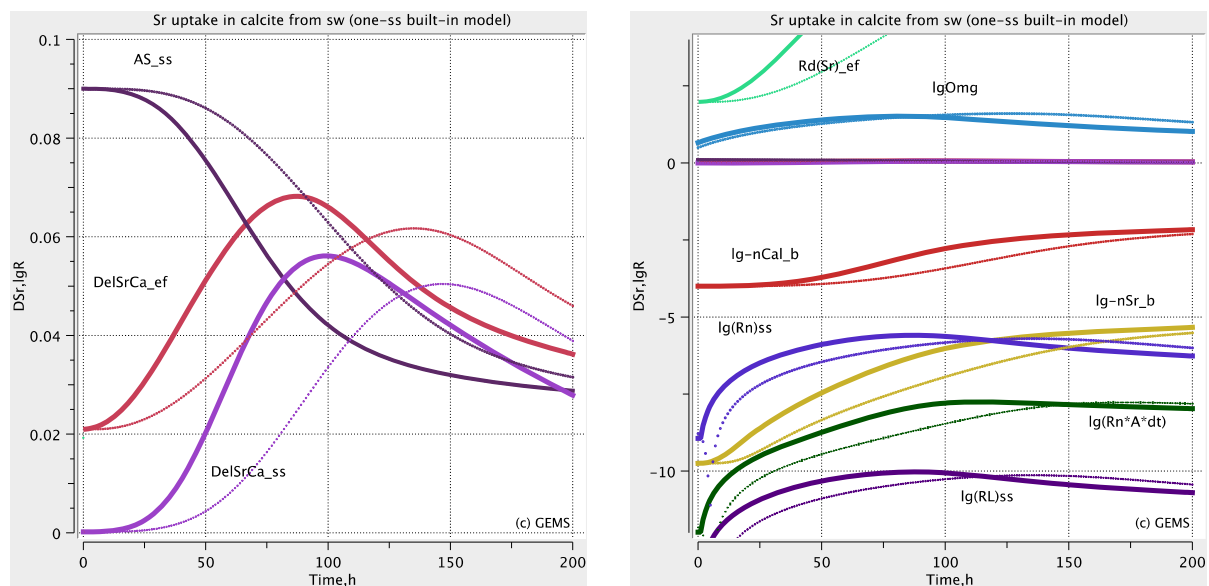
Fig. 8 Simulation runs for one-phase case of Sr uptake in calcite from seawater, showing the effects of temperature (thick curves: T=25 °C, thin dotted curves: T=15 °C), varying precipitation rate, and seawater depletion. DelSrCa_ef: effective $\Delta_{Sr,Ca}$ (eq. (18)); DelSrCa_ss: bulk $\Delta_{Sr,Ca}$ in solid solution phase; AS_ss: specific surface area; lgOmg: saturation index; nCal_b and nSr_b: amounts of end members; Rn, RL and Rn*A*dt: precipitation rates in mol·m^{-2}·s^{-1}, m·s^{-1}, and mol per time step, respectively.

The amount of Arg was fixed by lower and upper AMRs at 0.0001 mol, and the amount of Str end member fixed at 10^{-9} mol; the initial specific surface area was $A_{S,0} = 0.09$ m^2·g^{-1}. The "overgrowth" solid-solution phase Calcite-Sr_ovg with end-members, Cal (calcite) and SrCO3-cal (SrCO$_3$ with calcite structure) was the same as in the previous case, except that it was linked to the surface of the "seed" phase. The time step and interval were the same as before.

The simulation results for this case are shown in Figure 9, where the variation of the amount and composition of the "overgrowth" phase can now be followed separately from the "seed" phase. Variation of the "bulk solid" Sr fractionation coefficient is clearly the same as in the single phase case at the same temperature: it increases by factor 3 or more at maximum calcite growth rate, then decreases due to depletion of the aqueous solution.

The variation of composition of the "overgrowth" phase is confined between the curve for the effective fractionation coefficient predicted by the UUKM (upper curve) and the "bulk" coefficient at relatively high mass of the overgrowth at longer times. The specific surface area of the overgrowth phase evolves exactly as that in the single-phase case because it is related to layered aggregate particles made of the "seed" in the core and "overgrowth" outside.
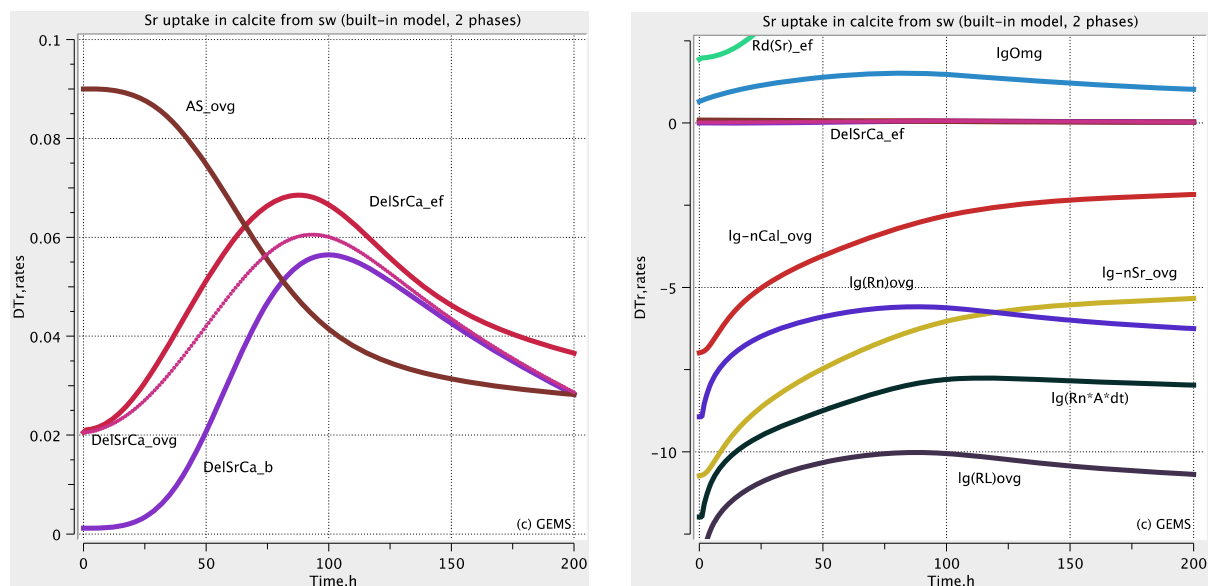
Fig. 9 Simulation runs for the linked two-phase case of Sr uptake in calcite from seawater at P =1 bar, T =25 °C, showing the effects of varying precipitation rate and seawater depletion. DelSrCa_ef: effective $\Delta_{Sr,Ca}$ (eq. (18)); DelSrCa_ovg: $\Delta_{Sr,Ca}$ in"overgrowth" solid solution phase; DelSrCa_b: bulk $\Delta_{Sr,Ca}$ in the solid; AS_ovg: specific surface area of the "overgrowth"; lgOmg: saturation index; nCal_ovg and nSr_ovg: amounts of end members of the "overgrowth" phase; Rn, RL and Rn*A*dt: precipitation rates.

Conclusions and Future Work

This report summarizes the development of a new to geochemical modeling of mineral-water reaction kinetics and related uptake of radionuclides in host mineral solid solutions, verified by modeling of the experimental literature data.

Mineral precipitation with trace element incorporation is the chemical process that usually deviates from "true" aqueous-solid equilibrium. This can be modeled beyond the "complete equilibrium" concept, by invoking the principles of local- and partial equilibrium. The changes in amount and composition of an *overgrowth* phase (solid solution, surface solution, adsorbed layer) can be linked to the surface area or to volume of another, *substrate* phase (seed, sorbent), which can be itself stable or metastable with respect to aqueous solution. In the latter case, kinetic rates should be scaled by the outer surface area of the *layered composite* solid (particles).

As an extension of the GEMS3K and GEM-Selektor codes for chemical thermodynamic modelling *(Kulik et al. 2013)*, some mineral reaction kinetic rate laws and uptake models for separate or metastablilty-linked (layered) solution phases have been implemented in the GEM-Selektor TKinMet C++ code library. In particular, the "unified uptake kinetics model"

(UUKM) for trace element incorporation upon the host mineral growth *(Thien, Kulik and Curti 2013, 2014)* was implemented.

The TKinMet library is designed similar to the TSolMod C++ code library for models of (non-ideal) mixing in phases-solutions *(Wagner et al. 2012)* with the goal of keeping the GEM IPM algorithm independent of specific physicochemical features of phases and their components, while collecting all these specific parameters in Phase definition records kept in GEM-Selektor project databases. Thus, the TKinMet and the TSolMod libraries in the GEMS3K code make the application of advanced kinetic and uptake models in reactive transport simulations of complex aqueous – solid solution systems possible in repository safety scenarios.

In GEM-Selektor v.3.3 process simulations described in this report, with systems including the precipitation kinetics of portlandite and calcite, as well as the Sr and Cd uptake kinetics in calcite, some geochemically important effects are clearly demonstrated. These effects include the change of trace element uptake upon variation of precipitation rates, different temperatures, and depletion in closed- and semi-open systems. Capability of modelling such effects goes far beyond the strict limitations (e.g. constant aqueous solution composition, constant growth rate) of previously published uptake kinetics models *(Watson 2004, DePaolo 2011)*. The test examples also show that shifts from equilibrium in the partitioning of trace elements induced by the host mineral growth are significant and extend to very slow processes at near-equilibrium conditions. In turn, this makes the GEMS codes enhanced with the TKinMet library an efficient and versatile modelling tool of potentially wide applicability in aquatic chemistry, chemical engineering, and (nuclear) waste geochemistry.

The future work should concentrate on further testing and verification of the TKinMet functionality for experimental systems that include re-crystallization of sulphates and uptake of radionuclides in them; on surface precipitation of solid solutions on goethite or other environmentally relevant substrates; on the impact of nucleation on trace element partitioning upon growth; and on studies of back-coupling and time-stepping effects and artefacts in kinetic- and reactive transport simulations.

Acknowledgement

References

DePaolo D. J. (2011). Surface kinetic model for isotopic and trace element fractionation during precipitation of calcite from aqueous solutions. Geochimica et Cosmochimica Acta 75, 1039-1056.

Dreybrodt W., Eisenlohr L., Madry B., and Ringer S. (1997). Precipitation kinetics of calcite in the system CaCO3-H2O-CO2: The conversion to CO2 by the slow process H++HCO3- -> CO2+H2O as a rate limiting step. Geochimica et Cosmochimica Acta 49, 2165-2180.

Fritz B., Clement A., Amal Y., and Noguera C. (2009). Simulation of the nucleation and growth of simple clay minerals in weathering processes: The NANOKIN code. Geochimica et Cosmochimica Acta 73, 1340-1358.

Gamsjäger H., Preis W., Königsberger E., Magalhaes M. C. and Brandao P. (1999). Solid-solute phase equilibria in aqueous solution. XI. Aqueous solubility and standard Gibbs energy of cadmium carbonate. Journal of Solution Chemistry 28, 711-720.

Glynn P. and Reardon E.J. (1990). Solid-solution aqueous-solution equilibria: Thermodynamic theory and representation. American Journal of Science 290, 164-201.

Hellmann R. and Tisserand D. (2006). Dissolution kinetics as a function of the Gibbs free energy of reaction: An experimental study based on albite feldspar. Geochimica et Cosmochimica Acta 70, 364-383.

Inskeep W.P. and Bloom P.R. (1985). An evaluation of rate equations for calcite precipitation kinetics at PCO2 less than 0.01 atm and pH greater than 8. Geochimica et Cosmochimica Acta 49, 2165-2180.

Karpov I.K., Chudnenko K.V., Kulik D.A., Avchenko O.V., and Bychinskii, V.A. (2001). Minimization of Gibbs free energy in geochemical systems by convex programming. Geochemistry International 39, 1108-1119.

Kulik D.A., Wagner T., Dmytrieva S.V., Kosakowski G., Hingerl F.F., Chudnenko K.V., and Berner U. (2013). GEM-Selektor geochemical modeling package: revised algorithm and GEMS3K numerical kernel for coupled simulation codes. Computational Geosciences 17, 1-24.

Kulik D. A., Vinograd V. L., Paulsen N., and Winkler, B. (2010). (Ca,Sr)CO3 aqueous-solid solution systems: From atomistic simulations to thermodynamic modelling. Physics and Chemistry of the Earth 35, 217-232.

Lasaga A.C. (1998). Kinetic theory in the Earth sciences. Princeton University Press, Princeton NJ.

Lorens R. B. (1981). Sr, Cd, Mn and Co distribution coefficients in calcite as a function of calcite precipitation rate. Geochimica et Cosmochimica Acta 45, 553-561.

Madé B., Clement A., and Fritz B. (1994). Modeling mineral/ solution interactions: The thermodynamic and kinetic code KINDISP. Computers and Geosciences 20, 1347-1363.

Marini L., Ottonello G., Canepa M., and Cipolli F. (2000). Water-rock interaction in the Bisagno valley (Genoa, Italy): Application of an inverse approach to model spring water chemistry. Geochimica et Cosmochimica Acta 64, 2617-2635.

Mironenko M.V. and Zolotov M.Yu. (2012). Equilibrium–kinetic model of water–rock interaction. Geochemistry International 50, 1-7.

Navrotsky A. (2011). Nanoscale effects on thermodynamics and phase equilibria in oxide systems. ChemPhysChem 12, 2207 – 2215.

Nielsen L.C., De Yoreo J.J., and DePaolo D.J. (2013). General model for calcite growth kinetics in the presence of impurity ions. Geochimica et Cosmochimica Acta 115, 100-114.

Palandri J. and Kharaka Y. (2004). A compilation of rate parameters of water-mineral interaction kinetics for application to geochemical modelling. U.S.G.S.Open File Report 2004-1068, Menlo Park CA, 70 p.

Parkhurst D.L. and Appelo C.A.J. (1999). User's guide to PHREEQC (Version 2): U.S.G.S. WRIR 99–4259, 312 p.

Parkhurst D.L., Kipp K.L., and Charlton S.R. (2010). PHAST Version 2. U.S.G.S. Techn. Methods 6–A35, 235 p.

Schott J., Oelkers E.H., Bénézeth P. Goddéris, Y., and François, L. (2012). Can accurate kinetic laws be created to describe chemical weathering? Comptes Rendus Geoscience 344, 568-585.

Schott J., Pokrovsky O. S., and Oelkers E. H. (2009). The link between mineral dissolution/ precipitation kinetics and solution chemistry. Chapter 6 in RiMG 70, 207-258.

Scislewski A. and Zuddas P. (2010). Estimation of reactive mineral surface area during water-rock interaction using fluid chemical data. Geochimica et Cosmochimica Acta 74, 6996–7007.

Shao H., Dmytrieva S.V., Kolditz O., Kulik D.A., Pfingsten W., and Kosakowski G. (2009). Modeling reactive transport in non-ideal aqueous–solid solution system. Applied Geochemistry 24, 1287-1300.

Tadros M.E., Skalny J., and Kalyoncu, R.S. (1976). Kinetics of calcium hydroxide crystal growth from solution. J. Colloid Interface Science 55, 20-24.

Teng H.H., Dove P.M., and De Yoreo, J.J. (2000). Kinetics of calcite growth: Surface processes and relationships to macroscopic rate laws. Geochimica et Cosmochimica Acta 64, 2255-2266.

Tesoriero A. J. and Pankow J. F. (1996). Solid solution partitioning of Sr2+, Ba2+, and Cd2+ to calcite. Geochimica et Cosmochimica Acta 60, 1053-1063.

Thien B.M.J., Kulik D.A., and Curti E. (2013). Modeling trace element uptake kinetics in secondary minerals. Procedia Earth and Planetary Science 7, 838-841.

Thien B.M.J., Kulik D.A, and Curti E. (2014). A unified approach to model uptake kinetics of trace elements in complex aqueous - solid solution systems. Applied Geochemistry 41, 135-150.

Thoenen T. (2012). The PSI/Nagra Chemical Thermodynamic Database 12/07: Compilation of updated and new data with respect to the Nagra/PSI Chemical Thermodynamic Data Base 01/01. PSI Internal Report TM-44-12-06, Paul Scherrer Institut, Villigen, Switzerland.

Tomazic B., Mohanty R., Tadros M, and Estrin J. (1986). Crystallization of calcium hydroxide from aqueous solution. II. Observations of growth, morphology and secondary nucleation. Journal of Crystal Growth 75, 339-347.

Wadell H. (1935). Volume, shape and roundness of quartz particles. Journal of Geology 43, 250–280.

Wagner T., Kulik D.A., Hingerl F.F., and Dmytrieva S.V. (2012). GEM-Selektor geochemical modeling package: TSolMod C++ class library and data interface for multicomponent phase models. Canadian Mineralogist 50, 1173-1195.

Watson, E. B. (2004). A conceptual model for near-surface kinetic controls on the trace-element and stable isotope composition of abiogenic calcite crystals. Geochimica et Cosmochimica Acta 68, 1473-1488.

Wolthers M., Nehrke G., Gustafsson J. P., and Van Cappellen P. (2012). Calcite growth kinetics: Modeling the effect of solution stoichiometry. Geochimica et Cosmochimica Acta 77, 121-134.

Wu W. and Nancollas G.H. (1999). Determination of interfacial tension from crystallization and dissolution data: a comparison with other methods. Advances in Colloid and Interface Science 79, 229-279.

KINETIC AND THERMODYNAMIC MODELLING OF RADIUM UPTAKE BY BARITE DURING RECRYSTALLIZATION EXPERIMENTS AT ROOM TEMPERATURE

Enzo Curti[*]

Paul Scherrer Institut, Laboratory for Waste Management, 5232 Villigen PSI (CH)

* Corresponding author: enzo.curti@psi.ch

Abstract

The kinetic/thermodynamic modelling of experimental data produced at FZJ on Ra uptake during the recrystallization of two commercial barites (Sachtleben and Aldrich) was updated and now includes results extending to 658 days reaction time. After a first slow kinetic step (120-180 days), recrystallization rates were found to suddenly increase up to 400 μmol m^{-2}d^{-1}, suggesting fast nucleation from supersaturation of a new $(Ba,Ra)SO_4$ phase with ideal or even negative interaction parameter ($a_0 \leq 0$). After this fast nucleation step, Ra concentrations in the aqueous solution slowly increased, approaching the equilibrium line of a regular $(Ba,Ra)SO_4$ solid solution with interaction parameter $a_0 = 1.0$, in agreement with theoretical predictions based on atomistic simulations. Therefore, these data suggest non-equilibrium Ra entrapment during the mentioned fast precipitation event, followed by slow recrystallization towards true thermodynamic solid solution equilibrium.

The Ra uptake experiments carried out at CHALMERS and KIT-INE involved lower total Ra concentrations compared to the FZJ experiments. Moreover, ^{133}Ba tracer addition allowed the independent determination of $(Ra,Ba)SO_4$ recrystallization rates. The kinetic data from CHALMERS could be interpreted using classical recrystallization models. These models failed when applied to the results of the KIT-INE experiments. A new model, requiring repeated dissolution-precipitation of previously formed Ra-barite was developed, which successfully describes these experiments.

Thermodynamic modelling of the CHALMERS data indicates formation of regular $(Ra,Ba)SO_4$ solid solutions with moderately positive interaction parameters ($a_0 = 0.7$-1.2), whereas the KIT-INE data point to the formation of solid solutions close to ideality. One of the most important results drawn from the three experimental studies is that the interaction parameter a_0 for the formation of the binary $(Ba,Ra)SO_4$ solid solution is comprised between

0.0 and ~ 1.0. The latter value seems to reflect long-term thermodynamic equilibrium, in agreement with theoretical predictions from atomistic simulations and part of the previously published data. This finding has direct relevance for the safety assessment of radioactive waste repository sites, since it allows constraining the solubility and thus the mobility of radium in such environments.

Introduction

It is well-known that the equilibrium aqueous concentration of a given element is lower if it precipitates as dilute solid solution than if the same element precipitates as a pure solid. This "dilution" effect is particularly beneficial for safety-relevant radionuclides released from radioactive waste in a geological disposal site. The solubility of a radionuclide trapped as minor element in a solid solution is strongly reduced compared to solubility control by pure solids. In the case of radium, formation of solid solutions with barite, $(Ba, Ra)SO_4$, by reaction of sulphate-rich ground waters with Ba isotopes released from the waste is considered to be likely. This process would reduce the concentration of dissolved radium by orders of magnitude compared to a system in which the solubility is controlled by pure radium sulphate. Eventually, the mobility of ^{226}Ra and its contribution to radiological doses would decrease to levels largely below those predicted assuming that a pure solid (e.g. $RaSO_4$) controls Ra solubility.

A thorough understanding of the mechanisms leading to Ra-barite formation and the careful quantification of relevant thermodynamic data (non-ideality parameters, end-member solubility products) is a prerequisite to reliably predict the contribution of ^{226}Ra to radiological doses in safety assessments calculations.

Recrystallization models

Classical models

In a recrystallization (replacement) process, a newly formed *secondary* phase grows at the expense of a dissolving *primary* phase **(Putnis 2009)**. In this study, the primary phase is pure barite, whereas the secondary phase is Ra-barite solid solution. Barite recrystallization rates can be determined by adding the radiotracer ^{133}Ba to a barite suspension and then monitoring the gamma activity of the aqueous solution over time. The ^{133}Ba removed from solution is incorporated in the secondary phase and is thus an indicator of the amount of newly precipitated barite solid solution. The rate of tracer removal is therefore proportional to the growth rate of the secondary barite, which is defined here with the term "recrystallization rate".

Recrystallization rates derived by isotope tracer methods in batch experiments are forcedly model-dependent since they are associated to conceptual ideas of the recrystallization mechanism at the microscopic scale. So far, two such idealized mechanisms have been tested (**Curti et al. 2010**): the so-called *homogeneous* and *heterogeneous* incorporation models as described by **Doerner and Hoskins (1925)** and **McIntire (1963)**. These models describe trace element uptake during coprecipitation with a solid separating from oversaturated solutions. During homogeneous incorporation, the *total amount* of recrystallized (i.e. newly precipitated) solid is at all times in equilibrium with the solution, so that the trace element is distributed homogeneously within the growing solid. The trace element concentration in the solid changes with time, but there is no internal concentration gradient.

In the case of heterogeneous incorporation, equilibrium between growing solid and aqueous solution is limited to a thin surface layer, ideally a few atomic monolayers thick. As recrystallization proceeds, this surface layer is covered by newly precipitated material and becomes isolated from exchange with the aqueous solution. In such systems, no full thermodynamic equilibrium is reached, only partial equilibrium between solution and mineral surface layer. Consequently, there is no internal equilibration of the growing crystals and the trace element distribution within the solid will be in general heterogeneous, giving rise to characteristic concentric zoning patterns frequently observed in natural crystals.

The mathematical development of the ^{133}Ba tracer method applied to the aforementioned models is described in **Curti et al. (2010).**

The "continuous recrystallization" model

In the classical recrystallization models, it is implicitly assumed that dissolution-repreipitation is a "one way" process, i.e. the primary phase dissolves and a new more phase is produced in a single step. Here, we describe a new model (denoted "continuous recrystallization model") in which it is assumed that each infinitesimal layer of newly formed solid undergoes repeated recrystallization cycles during the course of the process. This model was developed after realizing that the data obtained at KIT-INE cannot be explained by the classical models (see later).

The continuous recrystallization model assumes monolayer by monolayer recrystallization from outside towards the internal part of the primary crystals, i.e. it follows the pseudomorphic replacement model described by **Putnis (2009)**. A monolayer is a single atomic layer (thickness $d = 3.5 \times 10^{-10}$ m for barite). After the first monolayer of the primary pure mineral is dissolved, it reprecipitates in situ as more stable phase, for instance as Ra-barite solid solution. The solution then reacts with the next monolayer of primary solid and the same recrystallization step takes place, and so on (Figure 1).

The basic idea is that, before a given monolayer of the primary solid is dissolved and re-precipitated, all the previously formed secondary solid must recrystallize again in order to

adjust to the new solution composition. This means that all monolayers (except the most internal one) will have to recrystallize repeatedly. In other words, the total amount of recrystallized mineral (the integral) is at any time larger than the net amount of recrystallized solid.
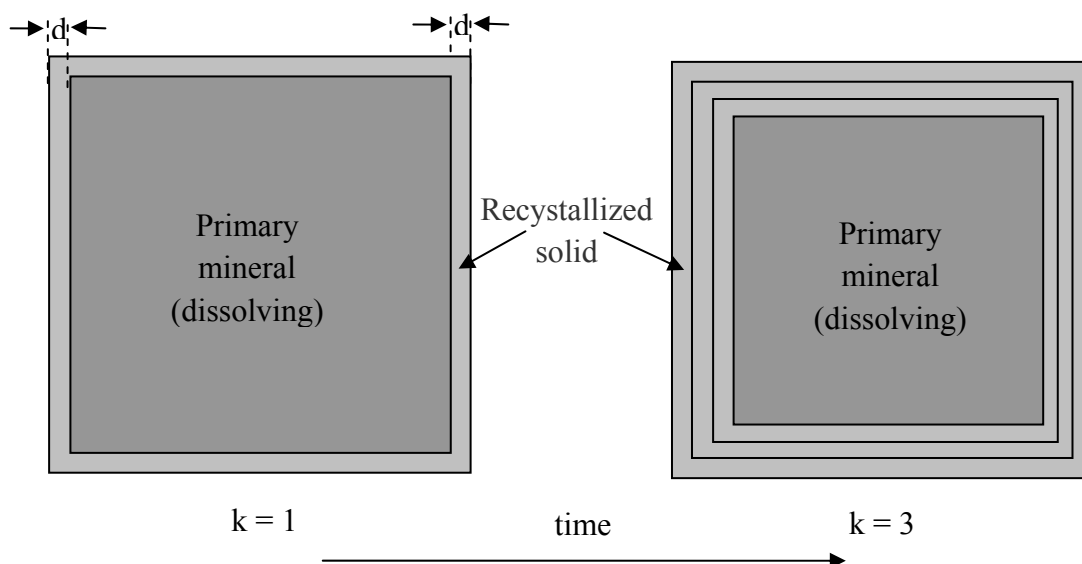

Fig. 1 Sketch of the proposed recrystallization model, showing the state of a particle after recrystallization of 1 and 3 monolayers

Modelling of FZJ data

Experimental

Extensive Ra uptake experiments were carried out at FZJ. In these experiments, conducted at room temperature (RT) and 90 °C, two commercial barite powders, Sachtleben® (SL) and Aldrich® (AL) were aged in 0.1 M NaCl + 5 μM RaBr$_2$ solutions during up to 658 days. The Ra concentration in solution was measured by gamma spectrometry at regular intervals. Here, we present modelling work performed on the data delivered until October 31, 2013.

Kinetic model

Because no [133]Ba exchange experiments were carried out at FZJ, an identification of the recrystallization mechanisms based on the models described in the previous chapter is not possible. However, it is possible to infer recrystallization rates for homogeneous recrystallization by the fitting procedure described below.

The recrystallization time t(s) may be expressed through eq. (1) as a function of the amount of newly formed barite solid solution n (mol), the specific surface area σ (m^2/g), the solution

volume V (l), the particle concentration S/L (g/l) and a surface-normalized recrystallization rate R (mol m^{-2} d^{-1}):

$$t = \frac{n}{\sigma V (S/L) R}$$
(1)

In the equation above, σ is a constant equated to σ_0, the initial mineral surface area. New particle size distribution data, based on SEM images, showed however that the specific surface area of AL barite had decreased by about a factor of two after 443 days aging in the presence of Ra-bearing solution. A much smaller decrease (less than 10%) was observed for SL barite under the same conditions. In order to evaluate the effect of variations in mineral surface area, the simple growth kinetics model described by eq. 1 has been extended to account for variations in surface area between the initial value σ_0 and a final value σ_f. It was simply assumed that the surface area varies linearly with the amount of recrystallized barite, n [mol]. The values of n are calculated separately via the GEM-Selektor code (*Kulik et al. 2013, Wagner et al. 2012*) for a given solid solution model, characterized by the mixing parameter a_0.

The Ra concentration data were then fitted using the following two-step procedure:

(a) Calculation of a series of equilibrium states as a function of the increasing amount (n) of (Ra,Ba)SO$_4$ with the GEM-Selektor (GEMS) code. This yields the equilibrium Ra concentrations as a function of n up to the total amount of barite used in the experiments and for the selected solid solution model (ideal or non-ideal).

(b) Determination of the reaction time $t(n)$ via an updated form eq. (1) (σ variation)

For each value of n calculated with GEMS, a reaction time $t(n)$ can then be determined by eq. (1). Because the GEMS calculations include the concentrations of Ra at equilibrium with the selected solid solution, each $t(n)$ value can be readily associated to the corresponding equilibrium Ra concentration, [Ra](n). Since there is no independent determination of the recrystallization rate in these experiments, R was used as adjustable parameter to fit the Ra concentration data.

RT experiments at 0.5 g/l

The data of the two experiments carried out at RT with SL and AL barites at 0.5 g/l are shown in Figure 2a and 2b in comparison with model curves derived from eq. (1). Blue curves are predictions for ideal (Ba,Ra)SO$_4$ solid solutions whereas red curves apply to regular solid solution with interaction parameter $a_0 = 1$. The latter value corresponds to the theoretical equilibrium a_0 recently determined via atomistic simulations by the double defect method (*Vinograd et al. 2013*). Continuous lines correspond to the usual model with constant specific surface area fixed at the initial value, whereas the blue stippled line in Figure 2b was calculated assuming a linear reduction of σ to half the initial value (from 1.7 to 0.85 m^2/g).

In both experiments, the initial slow decrease in the aqueous Ra concentration, simulated through a constant recrystallization rate R_1, is followed by a sudden decrease by 1-2 orders of magnitude after about 100 days (SL) or 180 days (AL) reaction time. This second kinetic step required much higher rates than the initial stage ($R_2 \gg R_1$). Whereas the growth rates inferred for the first kinetic stage are in the order of magnitude of recrystallization rates determined through [133]Ba exchange in previous Ra-barite uptake experiments (**Curti et al. 2010, Bosbach et al. 2010**) R_2 values are, at least for the tests with SL barite, unusually high, probably indicating sudden nucleation of a new Ra-barite phase. During this step, the Ra concentration in the aqueous phase decreases below the ideal solid solution equilibrium line, indicating negative values of the mixing parameter a_0. After reaching a minimum at 200 days (SL) or 350 days (AL) the aqueous Ra concentration slowly increases, approaching in both cases the $a_0 = 1.0$ equilibrium line. At the time of this reporting, no steady state was attained yet, but the observed behaviour strongly suggests that after the fast nucleation step the Ra-barite slowly recrystallizes towards an equilibrium state close to the theoretically predicted a_0 value of 1.0 (**Vinograd et al. 2013**). Therefore, the sudden Ra decrease at 100/180 days probably represents non-equilibrium entrapment, not a thermodynamic equilibrium state.
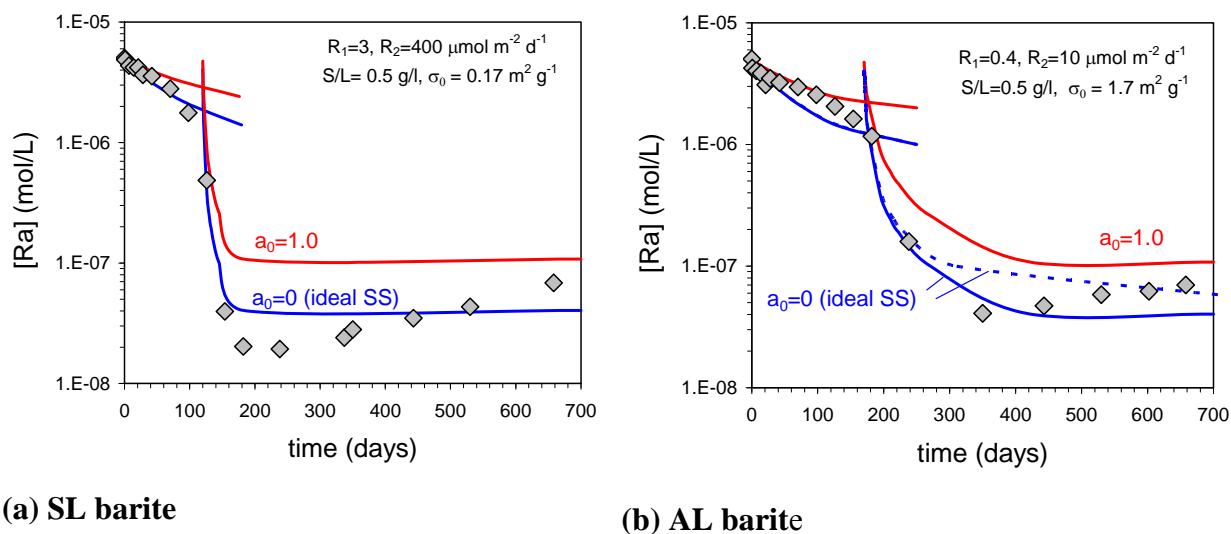

(a) SL barite

(b) AL barite

Fig. 2 Experimental data of FZJ Ra-barite recrystallization experiments carried out at room temperature and S/L= 0.5 g/l, compared with model calculations (see text for explanations).

Figure 2b also shows the effect of decreasing surface area (blue stippled line). As expected, reducing the available surface area leads to a delay in attaining equilibrium conditions (the horizontal, constant Ra concentration line). It is quite evident that the predicted effect is opposite to the observed slight increase in Ra concentrations observed at long reaction times.

This observation and the unusually high inferred recrystallization rates (up to 400 μm m^{-2} d^{-1}) suggest that normalization to the initial bulk mineral surface is inappropriate. This view is corroborated by the fact that SL barite appears to be more reactive than AL barite, although the latter has a 10 times larger specific surface area than SL barite (1.7 m^{2}g^{-1} vs. 0.17 m^{2}g^{-1}).

RT experiments at 5 g/l

The larger reactivity of SL barite towards Ra is even better visible in the experiments conducted at 5 g/l (Figure 3a). In general, the second (fast) kinetic stage of Ra precipitation occurs earlier or is even absent at 5 g/l and lower Ra concentrations are reached with SL barite despite the smaller bulk specific surface area. These phenomena can only be explained assuming homogeneous nucleation (which is independent of the total mineral surface). Moreover, Figure 3b shows that the onset of fast Ra uptake occurs at different, unpredictable times in SL barite suspensions, which also calls for a nucleation process.
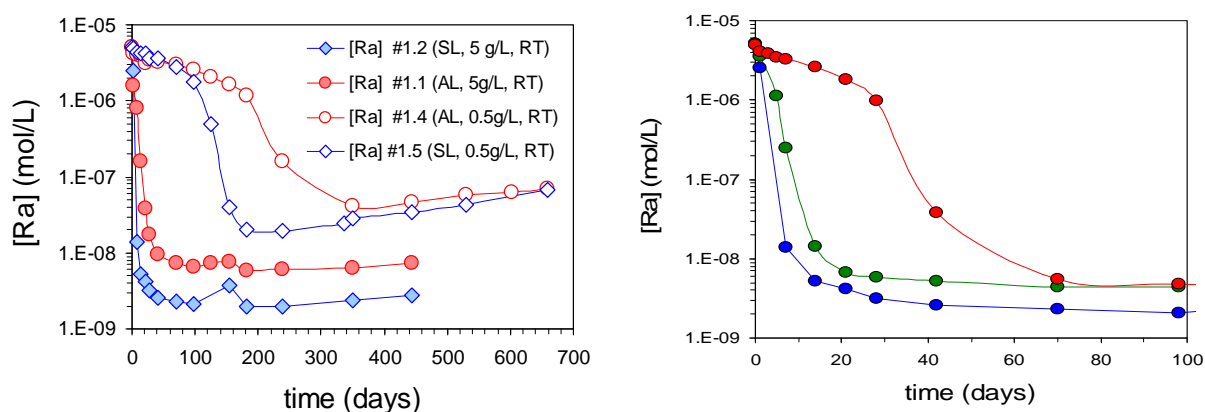

Fig. 3 (a) Comparison of Ra-barite uptake experiments carried out at FZJ with 0.5 g/l (open symbols) and 5 g/l S/L ratio (full symbols). (b) Three different 5 g/l experiments carried out with SL barite showing different onset times of fast Ra precipitation.

Modelling of KIT-INE data

Experimental

Recrystallization experiments at room temperature have been carried out with 0.1 g/l SL barite suspensions in 0.1 M NaCl solutions spiked with ^{133}Ba and ^{226}Ra. The SL barite had been previously aged in the same aqueous solution during 7 months. The simultaneous use of ^{133}Ba and ^{226}Ra tracers allowed a direct determination of the recrystallization rate without the need of fitting procedures and also eliminating the risk of biased results intrinsic in separate ^{226}Ra and ^{133}Ba experiments (see discussion in ***Curti et al. 2010***). Four experiments were performed, as summarized in Table 1, with Ra concentrations (0.5-12 nM) comparable to those used in the experiments of ***Curti et al. (2010)*** and ***Bosbach et al. (2010)*** and much lower than in those performed at FZJ (5 μM).

Table 1: Summary of barite recrystallization experiments carried out at KIT-INE in the framework of the SKIN project.

	$[^{133}Ba]_{total}$ (mol/l)	$[^{226}Ra]_{total}$ (mol/l)	pH
A	2.7×10^{-10}	0	5
B	2.7×10^{-10}	4.7×10^{-10}	3.55
C	2.8×10^{-10}	1.1×10^{-9}	3.15
D	2.7×10^{-10}	1.2×10^{-8}	4.17

Recrystallization Kinetics

It was previously anticipated that it was not possible to reproduce the ^{133}Ba exchange data obtained at KIT-INE using the equations developed for the *homogeneous* and *heterogeneous* incorporation models. This led to the development of a new model, the *continuous recrystallization* model described above, which is based on the assumption of permanent recrystallization of the newly formed secondary barite. Figure 4 shows the modelling results for experiments C and D conducted at KIT-INE. On the left side, best fit curves are shown for the three discussed recrystallization models, in a plot where the aqueous ^{133}Ba activity A_L (normalized to the total ^{133}Ba activity, A_S) is represented as a function of reaction time.

The red curves correspond to the heterogeneous incorporation model, the green curves to the homogeneous incorporation model and finally blue curves depict the behaviour expected if the continuous recrystallization model applies. Experiments C and D are well reproduced only through the continuous recrystallization model. There is no way to reproduce the data with

either heterogeneous or homogeneous incorporation model assuming a constant recrystallization rate. These models predict a much faster decrease in ^{133}Ba aqueous activity than observed in the experiments. Similar, though less unequivocal results are obtained for experiments A and B (not shown).

The right side of Figure 4 shows the *effective* and *bulk* growth rates (R_e and R_b, respectively) corresponding to the continuous recrystallization curve on the left side (i.e. the blue curve). R_e is the rate at which secondary barite is formed at the microscopic scale, assumed to be constant. R_b is the net (macroscopic) growth rate of secondary barite. Because it is assumed that each layer of the barite crystal is being replaced repeatedly, R_b is in general much smaller than the effective rate of mineral replacement, R_e. While the effective rate is constant and very high ($10 < R_e < 173$ µmol m^{-2} d^{-1}) the bulk rate decreases rapidly to values comprised between 1 and 10 µmol m^{-2} d^{-1}, which are quite comparable to the recrystallization rates determined in earlier published experiments.
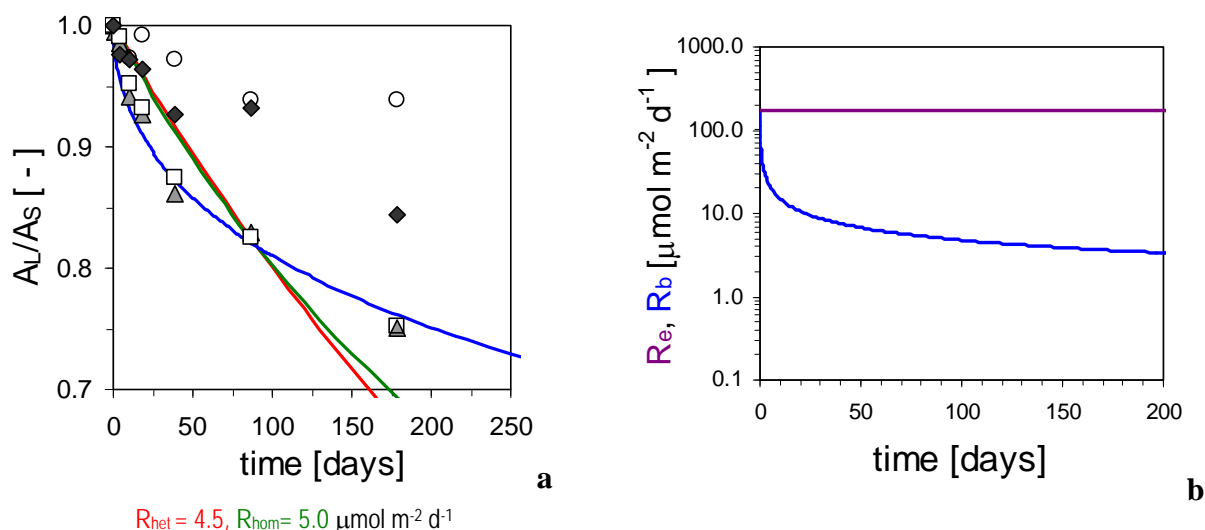

R_{het} = 4.5, R_{hom}= 5.0 µmol m^{-2} d^{-1}

Fig. 4 (a) ^{133}Ba activity data (A_L) normalized to total added activity (A_S) for experiments A (circles), B(rhombs), C(squares) and D (triangles). Model curves show the best fits for experiments C and D.(b) Effective and bulk recrystallization rates corresponding to the blue curve on the left side.

In summary, these modelling results clearly indicate that the "continuous recrystallization" mechanism is more appropriate than the classical recrystallization models to explain the results obtained at KIT-INE. There is no doubt that another mechanism is operating in this case, although the reasons are not understood at the moment. The only systematic difference

between these experiments and those carried out by ***Curti et al. (2010)*** and ***Bosbach et al. (2010)*** seems to be the different aging time of the initial barite. The SL barite used in the KIT-INE experiments was equilibrated during seven months, whereas ageing time in the previous studies were in the range of hours to weeks. A further indication that aging could play a role in affecting the mechanisms of recrystallization is the fact that the surface area of SL barite decrease from about 0.4 to 0.15 $m^2\,g^{-1}$ during the aging (Heberling, pers. comm.).

Thermodynamic Modelling

We used the combined ^{133}Ba and ^{226}Ra data to model the formation of secondary $(Ra,Ba)SO_4$ for experiments B, C and D with the help of GEM-Selektor code (http://gems.web.psi.ch). Values of $[n]$ were calculated directly from experimental ^{133}Ba(solution)/^{133}Ba(total) ratios (A_L/A_S) assuming formation of a homogeneous solid solution.

Figure 5 summarizes the results of thermodynamic calculations in a single plot showing the measured aqueous Ra concentrations as a function of the amount of recrystallized barite.
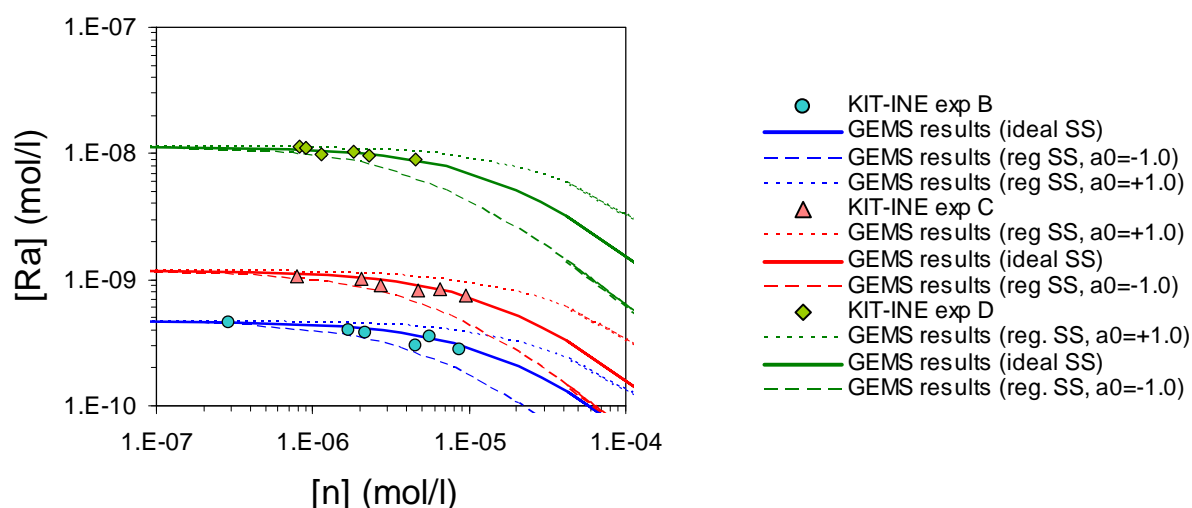

Fig. 5 Experimental data from Ra-barite interaction experiments carried out at KIT-INE compared to predicted Ra equilibrium concentrations for ideal and regular solid solution models as a function of the amount of recrystallized barite.

The data are compared to GEMS calculations for ideal (thick continuous curves) or regular solid solutions with interaction parameters $a_0 = +1.0$ (dotted curves) and $a_0 = -1.0$ (broken curves). The experimental results point to formation of $(Ra,Ba)SO_4$ solid solutions close to ideality in all three experiments, independently of the added Ra concentrations. This result

contrasts with the updated results from the FZJ experiments, which indicate regular solutions with moderately positive interaction parameter in the long-term ($a_0 \rightarrow 1$ for $t > 200$ days). Note, however, that the modelled KIT-INE experiments lasted for only 179 days.

Modelling of CHALMERS data

Experimental

Ra uptake experiments on barite synthesized in-house were carried out at room temperature with simultaneous addition of ^{223}Ra and ^{133}Ba tracers to monitor the recrystallization kinetics. Three solutions (System 1, 2, 3) containing 100 ml of 0.01 M Na_2SO_4 and 0.05 g of $BaSO_4$ were prepared in 250 ml plastic bottles and pre-equilibrated during 10 days. Thereafter, the ^{223}Ra and ^{133}Ba spikes were added. In System 3, only ^{133}Ba was added (Ra-free experiment). The pH of the final suspensions was 5.4. Blank tests without addition of barite showed that no tracer adsorption on the walls of the vessels took place.

Recrystallization Kinetics

Surface normalized rates based on ^{133}Ba data could not be modeled precisely because the specific surface area of the solid was not determined experimentally. Based on the information that the synthesized $BaSO_4$ was passed through 0.5-1.0 mm sieves and assuming a "roughness factor" of two, we estimated a value of $\sigma_0 = 0.0036$ m^2 g^{-1}. The "roughness factor" was determined from available surface area and particle size data of other barite powders.

Figure 6 shows the best fits of the normalized ^{133}Ba aqueous activity data for two experiments against the predictions of the classical homogeneous and heterogeneous recrystallization models, obtained using the aforementioned σ_0 value. The continuous recrystallization model (not shown) was found to be inappropriate. System 1 data refer to a test with simultaneous addition of both ^{133}Ba and ^{223}Ra tracers, whereas in System 3 only ^{133}Ba was added.

In spite of the large uncertainties of recrystallization rates introduced by the approximate value of the barite specific surface area, the current modeling results can be used to identify the appropriate recrystallization mechanism. The data obtained from the System 1 experiment are well reproduced by the homogeneous recrystallization model. It is not possible to obtain a satisfactory fit with the heterogeneous model, which requires an exponential decrease of the ^{133}Ba activity in solution (*i.e.* a linear decrease in the semi-logarithmic plots of Figure 6). In contrast, the data of system 3 define a linear trend, following the heterogeneous recrystallization model, and cannot be explained through homogeneous recrystallization.

We have currently no explanation why in the two experiments two different recrystallization mechanisms should operate; we can only suggest that this difference may be related to the

presence (System 1) or absence (System 3) of radium in solution. Note that the estimated recrystallization rates of 60 μmol m^{-2} d^{-1} and 15 μmol m^{-2} d^{-1} derived from the best fits of System 1 and System 3 data, respectively, are close to the upper limit of values derived for the experiments of *Curti et al. (2010)* and *Bosbach et al. (2010)*.
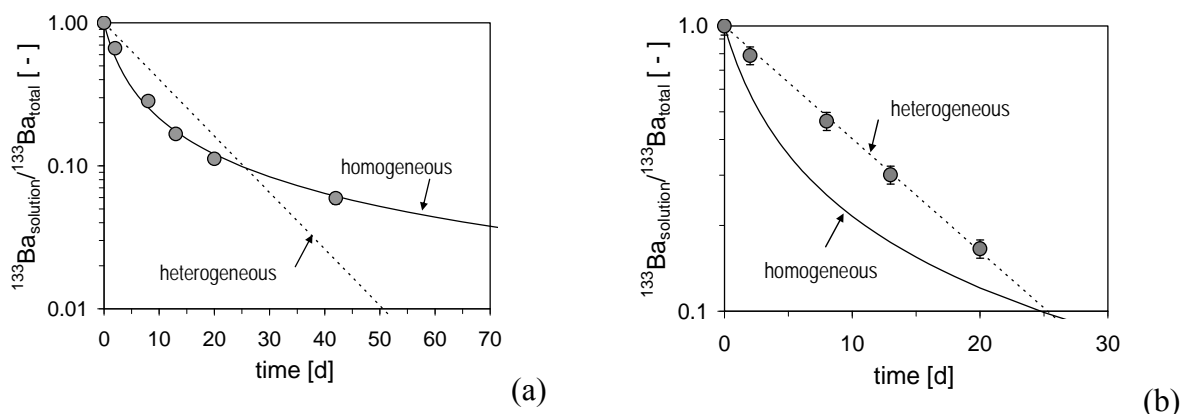

Fig. 6 Best fits of ^{133}Ba data from two BaSO$_4$-tracers interaction experiments in 0.01 M Na$_2$SO$_4$: (a) System 1 = test with simultaneous addition of ^{223}Ra and ^{133}Ba tracers (only data before addition of a second ^{223}Ra aliquot are considered); (b) System 3 = Ra-free test with addition of ^{133}Ba only.

System 1 was a double spiking test, *i.e.* a second aliquot of ^{223}Ra was added after 42 days since the start of the experiment. By that time more than 90% of the initial ^{223}Ra had already decayed. Figure 7 shows simultaneously the ^{133}Ba and ^{223}Ra aqueous concentration data for this experiment. After the addition of the second ^{223}Ra spike at 42 days, a brief transient increase in ^{133}Ba was observed, although no second aliquot of ^{133}Ba spike had been added. The close-up of the 40 - 60 days interval (Figure 7b) shows clearly that ^{133}Ba starts to increase exactly at the time of the second ^{223}Ra addition ($t = 42$ days) before it decreases again after 45 days reaction time.
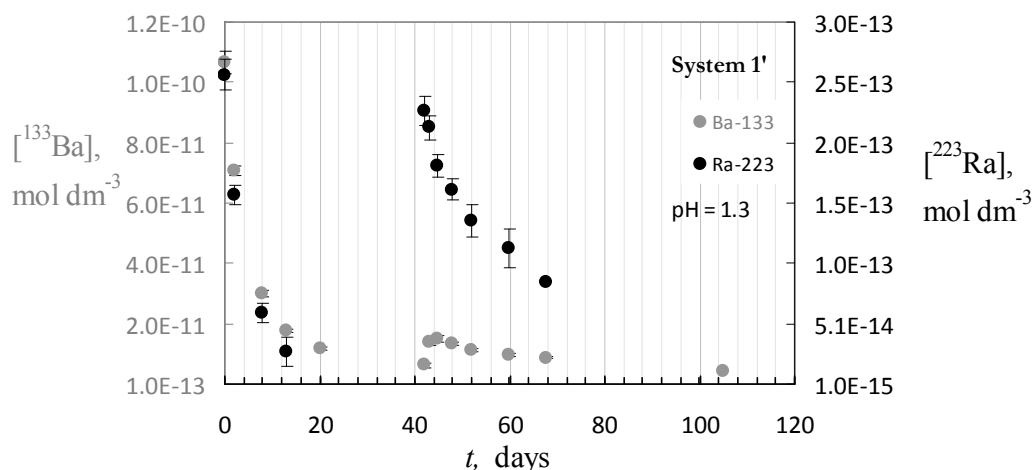
a
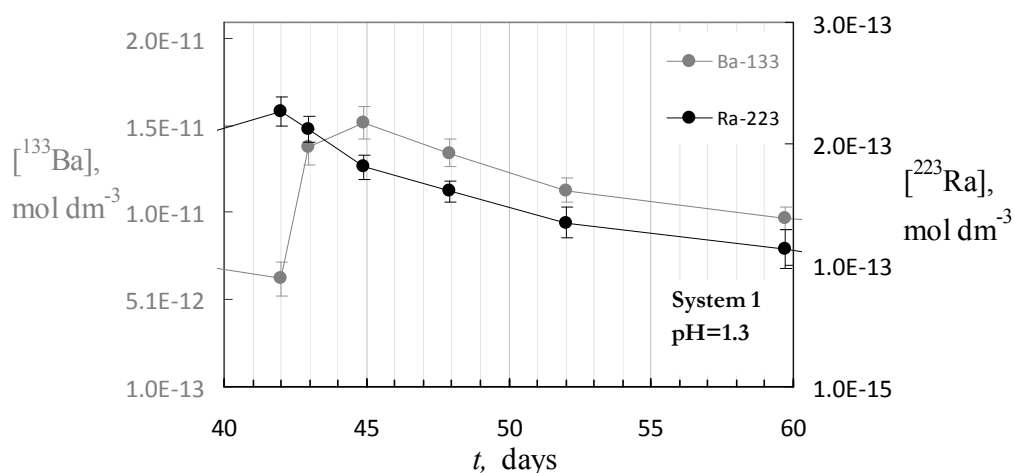
b

Fig. 7 *^{133}Ba and ^{223}Ra concentrations as a function of reaction time for System 1 experiment: (a) entire experiment; (b) close-up of the time interval shortly before and after the second ^{223}Ra spike addition at t = 42 days.*

This short-term, transitory increase in ^{133}Ba is a clear indication that the Ra-barite formed after the first tracer addition partially dissolved soon after addition of the second ^{223}Ra aliquot. Because most of the ^{223}Ra from the first spike had already decayed at that time (and therefore the secondary Ra-barite had "reverted" to almost pure BaSO$_4$) the addition of the second radium aliquot must have caused a destabilization and thus dissolution of the first (almost radium free, but ^{133}Ba bearing) solid, causing a net release of ^{133}Ba to the aqueous phase. The decrease in ^{223}Ra concentration between 42 and 45 d indicates simultaneous growth of a new

secondary Ra-barite. The fact that we observe a transitory increase in ^{133}Ba implies that the net rate of ^{133}Ba release from the first secondary barite exceeded the rate of ^{133}Ba uptake by the new solid, a quite fortuitous and lucky circumstance revealing the details of the growth and dissolution reactions taking place in this system.

Thermodynamic Modelling

The data obtained at CHALMERS for the System 1 experiment could not be modelled in the same way as the KIT-INE data since the Ra uptake was monitored using the short-lived ^{223}Ra tracer ($t_{1/2}$ = 11.3 days) instead of the long-lived ^{226}Ra ($t_{1/2}$ = 1600 years). Using ^{223}Ra has the advantage of decreasing the detection limit far below the picomolar level and avoids generating long-lived radioactive waste. The cost, however, is that solid solution equilibria may rapidly shift during the laboratory experiments because of the fast decay of ^{223}Ra, which is at a comparable timescale as barite growth rates. Because ^{223}Ra decays completely to ^{207}Pb within a few months, the Ra concentrations in a $(Ra,Ba)SO_4$ solid solution will decrease significantly during experiments with duration of up to 60 days.

Therefore, GEMS calculations were not carried out with the usual iterative "process", which produces model curves for a given constant total Ra concentration (Figure 5). A "point by point" strategy was used, by which a separate calculation was carried out for each single data point, taking into account the decay of ^{223}Ra at each sampling time. Moreover, because, after addition of the a second ^{223}Ra aliquot it is no longer possible to determine [*n*] quantitatively, solid solution thermodynamic calculations had to be restricted to the data before 42 days. This limits our modelling capability to the three data points of System 1 at *t* = 2, 8 and 13 days.

A short account of the essential results of the GEMS calculations is given in Table 2. They indicate consistently positive interaction parameters close to the theoretical a_0 (+1.0) calculated by *Vinograd et al. (2013)* and to the long-term values approached in the FZJ experiments. They are also close to the lower limit of the a_0-range inferred in the experiments of *Curti et al. (2010)* (1.5-2.5) but differ from the KIT-INE results, which point to solid solutions close to ideality.

Table 2: Main results of the three GEMS calculations carried out to model $(Ra,Ba)SO_4$ solid solution formation during System 1 experiment. Each row corresponds to a single experimental point (sampling times at 2, 8 and 13 days).

GEMS-ID	$[n]_{out}$	[Ra]	X(Ra)	a_0
	mol/kgw	mol/kgw	[-]	[-]
CHALM-1-2d	1.50×10^{-7}	1.58×10^{-13}	4.67×10^{-7}	0.71
CHALM-1-8d	7.44×10^{-7}	5.96×10^{-14}	1.32×10^{-7}	1.14
CHALM-1-13d	1.47×10^{-6}	2.78×10^{-14}	6.05×10^{-8}	1.21

Acknowledgement

References

Bosbach D., Boettle M. and Metz V. (2010) Experimental study on Ra^{2+} uptake by barite $BaSO_4$. Kinetics of solid solution formation via $BaSO_4$ dissolution and $Ra_xBa_{1-x}SO_4$ (re) precipitation. Technical Report TR-10-4. Svensk Kårnbrånslehantering AB. Swedish Nuclear Fuel and Waste Management Company, Stockholm, Sweden.

Curti, E., Fujiwara K., Iijima K., Tits J. Cuesta C., Kitamura A., Glaus M.A. and Müller W. (2010). Radium uptake during barite recrystallization as a function of solution composition at $23 \pm {}^oC$: An experimental ^{133}Ba and ^{226}Ra tracer study. Geochim. Cosmochim. Acta **74,** 3553-3570.

Doerner, H.A. and W.M. Hoskins (1925) Co-precipitation of radium and barium sulfates. Journal of the American Chemical Society **47**, 662-675.

Kulik D.A., Wagner T., Dmytrieva S.V., Kosakowski G., Hingerl F.F., Chudnenko K.V., and Berner U. (2013). GEM-Selektor geochemical modeling package: revised algorithm and GEMS3K numerical kernel for coupled simulation codes. Computational Geosciences **17**, 1-24.

McIntire W. L. (1963) Trace element partition coefficients - A review and application to geology. Geochim. Cosmochim. Acta **27**, 1209-1264.

Putnis, A. (2009) Mineral Replacement Reactions. In: Reviews in Mineralogy & Geochemistry, Vol. **70**, pp. 87-124, Mineralogical Society of America.

Vinograd V.L., Brandt F., Rozov K., Klinkenberg M., Refson K., Winkler B. and Bosbach D. (2013) Solid–aqueous equilibrium in the $BaSO_4$-$RaSO_4$-H_2O system: First-principles calculations and a thermodynamic assessment. Geochim. Cosmochim. Acta **122,** 398–417.Wagner T., Kulik D.A., Hingerl F.F., and Dmytrieva S.V. (2012). GEM-Selektor geochemical modeling package: TSolMod library and data interface for multicomponent phase models. Canadian Mineralogist **50**, 1173-1195.

THEORY ON THE AFFINITY LAW

Solange Ribet, Bernd Grambow

SUBATECH, Unité Mixte de Recherche 6457, Ecole des Mines de Nantes, CNRS/IN2P3, Université de Nantes (FR)

* Corresponding author: solange.ribet@subatech.in2p3.fr

Abstract

A review of literature data concerning the kinetic properties of some minerals in function of the deviation from equilibrium was carried out in this study. Reported studies combined the Transition State Theory and the Surface Complexation Modeling concept for expressing a rate law in function of solution composition and chemical affinity. It was shown that different classes of rate models are available and no generalized rate equation can be used to model mineral dissolution over the full range of geochemical conditions. It is premature to test affinity law on several minerals at equilibrium due to the lack of coherent and precise data in this range.

Introduction

The present task concerns the theory of the chemical affinity law for dissolution or precipitation of minerals. Numerous experimental observations note that the rate decreases when solution reaches a composition close to the saturation of the mineral. Investigators have also attempted to extrapolate far-from-equilibrium data to near-equilibrium conditions, to predict natural processes like weathering, sometimes with poor results because of the lack of understanding of the dependence of dissolution rate on the Gibbs free energy of the reaction. This study aimed to understand the deviations observed and the roles of surface charge, compositions, surface defect, selective dissolution, etc. on the rate parameters.

Definitions and theoretical background

Several terms had been defined in order to estimate the distance from equilibrium. We can use either the saturation ratio (Ω) which is the quotient between the ion-activity-product (Q) and

the thermodynamic equilibrium constant (K) (eq. (1)) or the chemical affinity which is related to the saturation ratio by its logarithm value (eq. (2)).

$$\Omega = \frac{Q}{K} = \exp\left(\frac{\Delta G}{RT}\right)$$

(1)

$$A = -\Delta G = -RT \ln\left(\frac{Q}{K}\right)$$

(2)

ΔG, the Gibbs free energy of the reaction, is the energy driving the reaction towards its products. For an affinity value $A > 0$, the solution is undersaturated and dissolution of mineral is observed. For an affinity value $A < 0$, the solution is oversaturated and there is precipitation of mineral. For $A = 0$, the net rate is zero, there is equilibrium.

The models attempted to describe kinetic of minerals are mostly based upon the Transition State Theory (TST) which defines an intermediate species between reactant and product as an activated complex. Both the forward rate and the backward rate are function of the concentration of this activated complex in solution, which is also considered in equilibrium with a precursor complex. The net rate is the difference between the two processes. The hypothesis of the Transition State Theory is that the activated complex is the same in the two ways (called the principle of detailed balancing), and that there is only one limiting step or one elementary reaction to control the kinetics. This assumption of microscopic reversibility leads to a connection between kinetics and thermodynamics because ratio of forward rate and reverse rate equals the thermodynamic constant K when reversibility holds *(Rimstidt and Barnes 1980, Dove and Crerar 1990)*. This assumption also maintains that processes which increase the rate of a forward reaction can be expected to also increase the rate of the reverse reaction, provided that dissolution and precipitation mechanisms are identical *(Lasaga 1984)*. In that case only, the net rate can be expressed with eq. (3) *(Lasaga 1998)*:

$$r_{net} = r_+ - r_- = r_+\left(1 - \frac{r_-}{r_+}\right) = k_+ \cdot \prod a_i^{n_i} \times \left(1 - \exp\left(-\frac{A^*}{\sigma RT}\right)\right)$$

(3)

where σ is a stoichiometric coefficient inserted to take into account the difference between the composition of the activated complex and the true mineral, defined as the number of moles of precursor complex that can be formed from one mole of mineral. Identically, it is also defined as the ratio of the rate of destruction of the activated complex relative to the overall reaction *(Lasaga et al. 1994)*. In the mineral precipitation literature, it is rather related to the precipitation mechanism *(Teng et al. 2000)*.

A^* is the affinity of the reaction involving the activated complex. Generally, A^* refers to the composition of surface layer, which could be different than the bulk mineral composition

(Daux et al. 1997). A solution can attain equilibrium with the leached surface distinct from that it could attain from the original solid.

The affinity term shows how the overall rate slows down as the driving force ΔG decreases. When a mineral approaches equilibrium, the dissolution rate no longer simply reflects forward dissolution, but is also influenced by the reverse reaction, in which case the rate of dissolution may decrease *(Wimpenny et al. 2010)*. As $\exp(x) \xrightarrow[x=0]{} 1 + x$, the chemical affinity law states that close to equilibrium, the rate will vary linearly with affinity.

The forward rate r_+ can be expressed as $r_+ = k_+ \prod a_i^{n_i}$, a product of a forward rate constant (k_+) and a function of elemental activity of reactant or product, that could catalyze or inhibit the reaction in the near-to-equilibrium region. r_+ corresponds generally to the expression of rate far from equilibrium, at undersaturation conditions.

The sign of the rate (for example positive for dissolution, negative for precipitation) is only a matter of convention.

TST is strictly considered appropriate for an elementary reaction, and one controlling-rate process. This is difficult to assess for minerals with complex structure and several different structural units. However, in the case of multi-step dissolution mechanism, the rate would be controlled by the slowest step. Therefore, if the mechanism of this slowest step is rate limited by an elementary reaction, then TST may be applied to the overall reaction *(Lasaga (1984))* and eq. 3 can be fitted over the data.

The main difficulty in the study of mineral dissolution (or precipitation) and application of eq. 3 comes from the necessary knowledge (or assumption) of the rate limiting steps in the reaction mechanism and/or the precursor complexes compositions and formation reactions *(Pokrovsky and Schott 2001)*.

Unfortunately, it arrives that above conditions (of single limiting mechanism) are not satisfied, and studies of dissolution behavior versus large range of chemical affinity led the investigators *(Nagy et al. 1991, Burch et al. 1993)* to propose a so-called non linear rate law according to eq. (4a) or (4b) or even a combination of eq. (4) and eq. (3):

$$r_{net} = r_+ \left(1 - \exp\left(-n \left(\frac{\left| A^* \right|}{RT} \right)^m \right) \right) \tag{4a}$$

$$r_{net} = r_+ \left(1 - \exp\left(-n \left(\frac{\left| A^* \right|}{RT} \right) \right) \right)^m \tag{4b}$$

This alternative expression induces a sigmoidal behavior of the rate versus chemical affinity. *n* and *m* are fitted parameters. In that case, investigators generally tried to link the expression with a critical *ΔG* value, corresponding to a switch of reaction mechanism, and involving the formation of crystal defects such as etch pits *(Arvidson and Lüttge 2010)*, which are active sites for undersaturated solutions. At near equilibrium conditions, the difference of free energy is insufficient to open etch pits at screw dislocations. Therefore these pits do not form and cannot contribute to the overall dissolution rate *(Cama et al. 2000, Brantley 2008, Lüttge and Arvidson, 2008)*.

However, as both the chemical affinity term and the forward rate (r_+) term may depend on the concentration of reactant and products, it also could happen that a sigmoidal behavior could be represented by an adequate expression of eq. (3).

Rate expressions could then be not unique and that shows the complexity to propose correct mechanism. In a recent study, *Schott et al. (2012)* tried to reconcile the microscopic observation of surface state and the macroscopic measurement of rate dependence. They proposed that non-linear behavior comes from the low availability of active sites for minerals with low surface area, and that the rate dependence on chemical affinity could be function of the history of treatment before reaction *(Lüttge 2006, Arvidson 2010)*. On the other hand, minerals with high specific surface area have sufficient reactive sites at the surface, and the reaction could proceed via direct attachment/detachment of reactant, leading to a linear behavior.

Evaluation of literature data

Literature data on the effect of approaching equilibrium on the kinetic of mineral dissolution had been widely studied by Schott and coworkers *(Schott et al. 2009)* and references therein or *Brantley et al. (2008)*.

Simple oxides or hydroxides, aluminosilicate minerals and glasses, or carbonates have been studied for many years, with respect to their dissolution (or precipitation) behavior as a function of the deviation from equilibrium in solution, at variable conditions of temperature, pH or solution composition. Batch reactor experiments are a simple way to obtain the equilibrium conditions, but in that case, concentration of products and reactants change continually with time and *ΔG* value is not constant with time over an experiment. Also, interpretation of the rate data may be affected by the precipitation (backward) process. Mixed Flow Reactor experiments are largely preferred to study the variation of rate with chemical affinity, as uniform fluid compositions are easily reached, and reaction rates are straightforwardly deduced from steady state conditions. Moreover this technique avoids diffusion-limited conditions and minimizes accumulation of residual or incongruent product

on the surface *(Dove 1990)*. A wide range of departure from equilibrium can be attained by simply changing the input solution composition and/or flow rate.

The concept of surface speciation (surface complexation modeling) has been combined with TST to understand mineral dissolution rates far from equilibrium *(Brady and Walther 1990, Schott 2009)* for oxides, hydroxides or aluminosilicates. Accordingly, the rate law is linked with the formation of leached surface layers on the mineral surface, due to successive breaking of several metal-oxygen bonds upon the proton attack, until no further viable structure remains. This constitutes the rate-controlling precursor complex. The dissolution proceeds by successive removal of metal from the fastest to the slowest breaking bond. The rate limiting step is the destruction of the slowest breaking M-O bond essential for maintaining the mineral structure. In case of aluminosilicates, depending on the pH, this slowest step could be the breaking of Si-O bond (acid pH) or octahedral Al-O bond (basic pH). The leaching of alkali-or alkaline-earth or other cations leaves Si tetrahedra that are still connected to the lattice by bridging oxygen *(Brantley 2008)*. In the case of simple oxide or hydroxide, only one type of bond is involved in the mechanism.

Figure 1 (From *(Oelkers 2001)*) illustrates these successive steps and order of importance for several aluminosilicates and basaltic glass at acid pH.

	Reaction	Alkali-Feldspar	Kaolinite	Muscovite	Enstatite	Basaltic Glass
	Formula (example)	$KAlSi_3O_8$	$Al_2Si_2O_5(OH)_4$	$KAl_3Si_3O_{10}(OH)_2$	$MgSiO_3$	
	Alkali Metal – H	Step 1		Step 1		Step 1
	Ca – H					Step 2
	Mg – H [(1)]				Step 1	Step 3
	Al(tetrahedral) – H	Step 2		Step 2		Step 4
	Al(octahedral) – H [(1)]		Step 1	Step 3		
	Breaking Si – O bonds	Mineral destroyed	Mineral destroyed	Mineral destroyed	Mineral destroyed	Solid destroyed

(Left side labels: "Decreasing M – O breaking Rate" with downward arrow; "Exchange reactions")

(1) Mg – H and Al(octahedral) – H exchange is slower than Si – O bond breaking at **basic** conditions

Fig. 1 Illustration of the dissolution mechanisms of some minerals at acid pH. The slowest rate before the mineral destruction is the rate limiting step (From (Oelkers 2001))

For the simple oxide, the dissolution mechanism proceeds by the formation of a leached layer by proton exchange before its final irreversible destruction. This case is illustrated for minerals brucite, boehmite, or quartz.

Brucite Mg(OH)$_2$

Breaking of one type of bond (Mg–O) is assumed. Accordingly, the rate expression that fitted the data of **Pokrovsky and Schott (2004)** for dissolution of Mg(OH)$_2$ (0.2 m^2/g) at 25 °C and basic pH (Figure 2) is expressed as eq. (5):

$$R_{diss} = k_{MgOH\,2+} \cdot \{\equiv MgOH_2^+\}^2 \times \left(1 - \exp\left(\frac{-A}{0.5RT}\right)\right) \qquad (5)$$

In this case, extrapolation of the data and TST appear effective to describe mineral dissolution close to equilibrium.
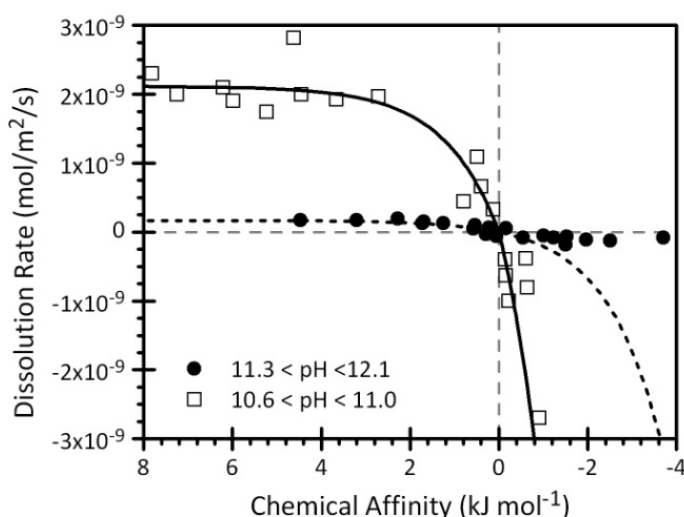

Fig. 2 Application of chemical affinity law on Brucite (Mg(OH)$_2$) dissolution and precipitation at 25 °C and basic pH, using eq. 5 (From (Pokrovsky and Schott 2004))

Boehmite AlOOH

Dissolution and precipitation rates have been expressed as functions of surface speciation ($\equiv AlOH_2^+$, $\equiv AlOH$ or $\equiv AlO^-$ concentration) far from equilibrium and extrapolated to near-equilibrium *(Schott 2009)*. For example, in neutral to basic solution, the principle of detailed balancing yields the following expression for the overall rate (eq. (6)):

$$R = k_{OH} \cdot \{OH^-\}\{\equiv AlO^-\} \times \left(1 - \exp\left(\frac{-A}{RT}\right)\right) \qquad (6)$$

This equation is illustrated in Figure 3A for the ratio of boehmite (1.65 m^2/g) dissolution (precipitation) rate at 100 °C in neutral to basic solution and OH$^-$ concentration as function of the degree of saturation (From **(Bénézeth et al. 2008)**)
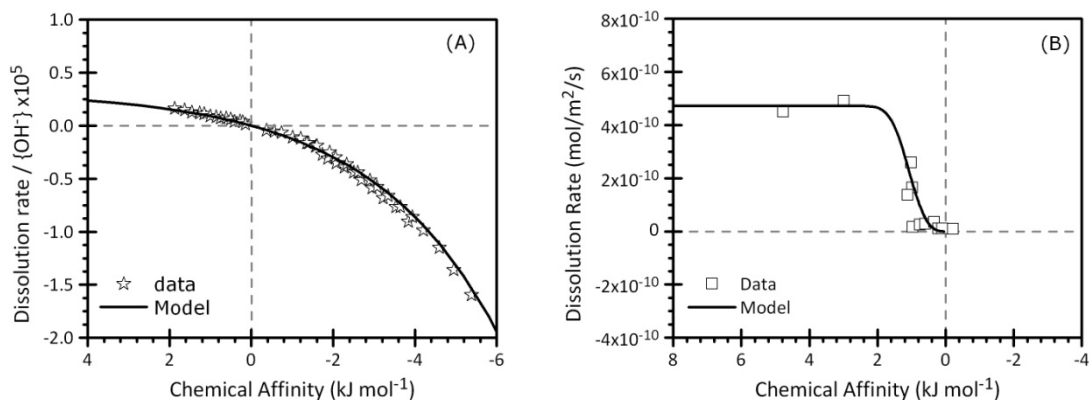

Fig. 3 A) Boehmite dissolution and precipitation rates as function of chemical affinity at 100 °C and neutral to basic pH solution (From (Bénézeth 2008)) B) Gibbsite dissolution rate at 80 °C and pH 3 (From (Nagy and Lasaga 1992))

Gibbsite Al(OH)$_3$

Nagy and Lasaga (1992), reported a different behavior for gibbsite dissolution at 80 °C in acid solution, with a highly non-linear relation of the rate with chemical affinity (Figure 3B), and a precipitation rate expression which differ from the dissolution rate expression. According to these authors, gibbsite (Al(OH)$_3$) dissolution at 80 °C and pH 3 is fitted over the whole range of saturation states studied according to:

$$R_{diss} = k_H \times \left(1 - \exp\left(-8.12 \left(\frac{|A|}{RT} \right)^{3.01} \right) \right)$$
(7a)

However, from their data, it is difficult to evaluate the separate effects of pH, aluminum concentration in solution (as catalyst or inhibitor), and chemical affinity in solution near equilibrium. Moreover, the data near equilibrium exhibits large uncertainties.

When estimating rate equation on a narrow range of saturation state (-0.83 to +0.83 kJ/mol), it could appear that rate becomes linear when approaching equilibrium according to:
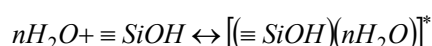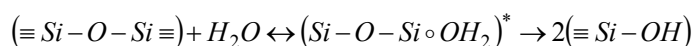
$$R_{diss} = k_H \times \left(\frac{|A|}{RT} \right)^{1.06}$$
(7b)

This relationship is consistent with TST, and implies that the same reaction mechanism may control both dissolution and precipitation in the close-to-equilibrium area.

Quartz SiO$_2$

Quartz is one of the most studied minerals with respect to dissolution-precipitation mechanism. However, there are still some discrepancies between the data, and no generalized rate law is available.

For example, at neutral pH, between 200 °C and 300 °C *(Berger et al. 1994)*, the rate-controlling precursor complex is formed by adsorption of H$_2$O molecules on quartz surface and hydrolysis of Si-O-Si structural unit *(Brady 1990, Schott and Oelkers 1995)*.

$$(\equiv Si-O-Si \equiv) + H_2O \leftrightarrow (Si-O-Si \circ OH_2)^* \rightarrow 2(\equiv Si-OH)$$

$$nH_2O + \equiv SiOH \leftrightarrow [(\equiv SiOH)(nH_2O)]^*$$

4 Si-O-Si needs to be successively broken, but breaking the first Si-O-Si bond is probably the most energetic step, and the dissolution process is limited by the progress of this intermediate reaction *(Dove 1990)*.

Dissolution kinetic of quartz has been combined with surface complexation calculations (involving different surface species like $\equiv SiOH_2^+$, $\equiv SiOH$ or $\equiv SiO^-$) to yield an equation of dissolution rate as function of departure from equilibrium *(Schott 2009)*. In deionized water only, the rate could be expressed as:

$$R = k_{H2O}\{\equiv SiOH\} \times \left(1 - \exp\left(\frac{-A}{RT}\right)\right) \tag{8a}$$

Eq. (8a) is consistent with eq. (3) and shows a linear dependence on chemical affinity.

This case is illustrated in Figure 4A.

In the presence of electrolyte like (NaNO$_3$, Pb(NO$_3$)$_2$, NaCl) the observed behavior changed: the rates are no longer linear functions of the solution saturation state. A sigmoidal behavior is then observed (Figure 4B). Electrolytes may accelerate the dissolution rate by increasing the accessibility of water molecules to the siloxane bonds *(Dove 1990)*. *Davis et al. (2011)* observed also a rate dependence not linear with respect to chemical affinity in the near equilibrium region (Figure 4C). However, they were able to fit the data with two separate linear regions (both consistent with eq. (8a) that are attributed to two parallel processes of dissolution mechanisms.
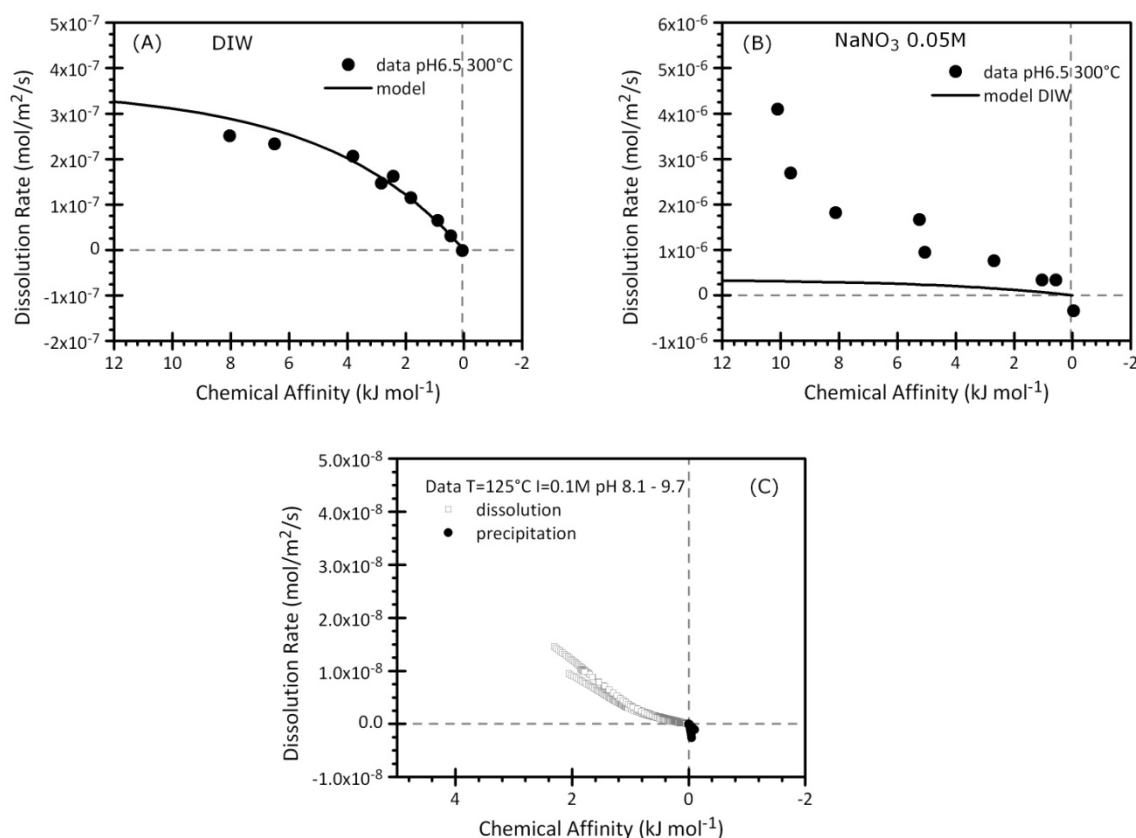
Fig. 4 A) Application of chemical affinity law on Quartz (SiO₂ 0.31m²/g) dissolution in deionized water at 300 °C and neutral pH, using eq. (8a) (From (Schott 2009) and (Berger 1994)) B) in presence of NaNO₃ and pH 6.5 (Refitted from (Berger 1994) with A = -RT ln([H₄SiO₄]/10⁻²)) C) Close to equilibrium data for dissolution and precipitation of quartz (0.26 m²/g) at 125 °C and pH 8.2-9.6 (From (Davis 2011)) as function of A.

In NaCl electrolyte solution, ***Dove and Crerar (1990)*** suggest the following rate law for quartz dissolution between 100 and 300 °C:

$$R = \left(k_+ + k_{ad} \frac{K_{Na^+}\left[Na^+\right]}{1 + K_{Na^+}\left[Na^+\right]} \right) \times \left(1 - \exp\left(\frac{-A}{RT} \right) \right) \tag{8b}$$

Ganor et al. (2005) studied precipitation of quartz (0.06 m²/g) at 180 °C and pH 4 in a batch reactor experiment ***(Ganor et al. 2005)***. Data agree with the principle of detailed balancing, and the rate equation consistent with TST is applied satisfactorily. However, the authors state that their data are not sufficient to retrieve a function that uniquely describes precipitation rate dependence on deviation from equilibrium nor to propose a mechanism for the precipitation of quartz.

Aluminosilicates

The successive breaking of metal (alkali-, alkaline-earth, aluminum and silicon)–oxygen bonds results in a partially Al-depleted Si-rich surface layer, which could be considered as the precursor complex.

Schott and Oelkers *(Oelkers 2001, Schott 2009)* have generalized a dissolution rate law by incorporating a specific effect for Al inhibition at acidic conditions into the forward rate expression. Inhibitory effect of Al^{3+} could be attributed to a back-reaction of specific precursor surface sites *(Brantley 2008)*. According to the aluminum coordination in the structure (tetrahedral sites or octahedral sites), the dissolution behavior could depend on the pH conditions. For example, on minerals which contain only tetrahedral Al (Albite, K-Feldspar), the precursor complex is formed by reversible $Al^{3+}/3H^+$ exchange reversible whatever the pH (acid or alkaline) *(Schott 1995)*. In case of minerals like kaolinite or smectite, with some octahedral Al in their structure, the same exchange reaction forms the precursor complex only at acid to neutral pH. At basic conditions, its formation depends both on aqueous Al and SiO_2. Accordingly, the rate expression may be written as eq. (9a) and (9b).

$$R = k_+ \cdot \left(K^* \cdot \left(\frac{\{H^+\}^3}{\{Al^{3+}\}} \right)^n \middle/ \left(1 + K^* \cdot \left(\frac{\{H^+\}^3}{\{Al^{3+}\}} \right)^n \right) \right) \times \left(1 - \exp\left(\frac{-A}{\sigma RT} \right) \right) \tag{9a}$$

$$R = k_+ \cdot K^* \cdot \left(\frac{\{H^+\}^3}{\{Al^{3+}\}} \right)^n \cdot \left(\frac{1}{\{SiO_2\}} \right) \times \left(1 - \exp\left(\frac{-A}{\sigma RT} \right) \right) \tag{9b}$$

K^* is the equilibrium constant for the Al proton exchange reaction and *n* is a stoichiometric coefficient for the precursor complex.

This Al inhibition can have an important impact on the dependence of kinetics on chemical affinity, resulting in a sigmoidal behavior analogous to that attributed to the etch pits dislocation control of dissolution.

Equation 9a has been applied on chlorite ($Mg_{2.76}Fe^{2+}_{1.90}Fe^{3+}_{0.07}Al_{0.97}Si_{2.48}Al_{1.52}O_{10}(OH)_8$; 1.41 m^2/g) with $n = 0.27$ *(Lowson et al. 2005)*, and on muscovite (mica family $KAl_3Si_3O_{10}(OH)_2$) with $n = 0.5$ *(Oelkers et al. 2008)* both far from equilibrium.

Aluminum speciation in solution has been taken into account to express the rate equation for dissolution of K-Feldspar ($K_{0.81}Na_{0.15}Ba_{0.03}Al_{1.05}Si_{2.96}O_8$) at pH 9 and T = 150 °C with a modification of eq. (9a) according to (eq. (9c)):

$$R = 1.7 \cdot 10^{-13} \cdot \left(\frac{1}{\{Al(OH)_4^-\}^{1/3} \cdot \{H^+\}^{1/3}} \right) \times \left(1 - \exp\left(\frac{-A}{3RT} \right) \right) \tag{9c}$$

with k_+ in mol.m^{-2}s^{-1} *(Gautier et al. 1994)*. Plot of experimental data is presented on Figure 5 in function of chemical affinity.

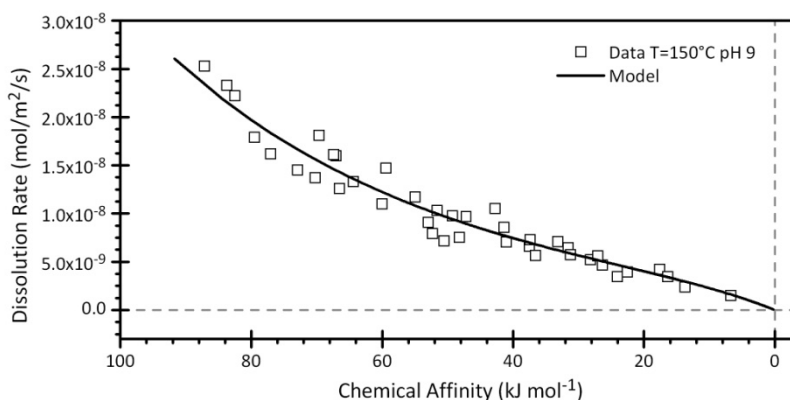***Fig. 5 Application of chemical affinity law on K-Feldspar ($K_{0.81}Na_{0.15}Ba_{0.03}Al_{1.05}Si_{2.96}O_8$) dissolution in deionized water at 150 °C and pH 9 (from (Gautier 1994))***

However, Lüttge's critical analysis revealed that the kaolinite rate data from Gautier et al. (1994) cannot be used to distinguish between different kinetics models: a model based on a simple transition state formulation (with various values for σ) for the chemical affinity dependence of the rate or a model based on the statistical theory of crystal defects growth and dissolution *(Lüttge 2006)*.

Kaolinite ($Al_2Si_2O_5(OH)_4$) had been studied at pH 2-3 and 80 °C *(Nagy 1991)* or 150 °C *(Devidal et al. 1997)*. Both studies show a non linear behavior of the rate dependence on chemical affinity (Figure 6). *Nagy et al. (1991)* fitted their data with eq. (10a), but also stated that without acquiring more data near equilibrium it was premature to assess validity of the principle of detailed balancing.

$$R = 1.24 \cdot 10^{-12} \times \left(1 - \exp\left(\frac{-A}{1.17 \cdot RT} \right) \right) \tag{10a}$$
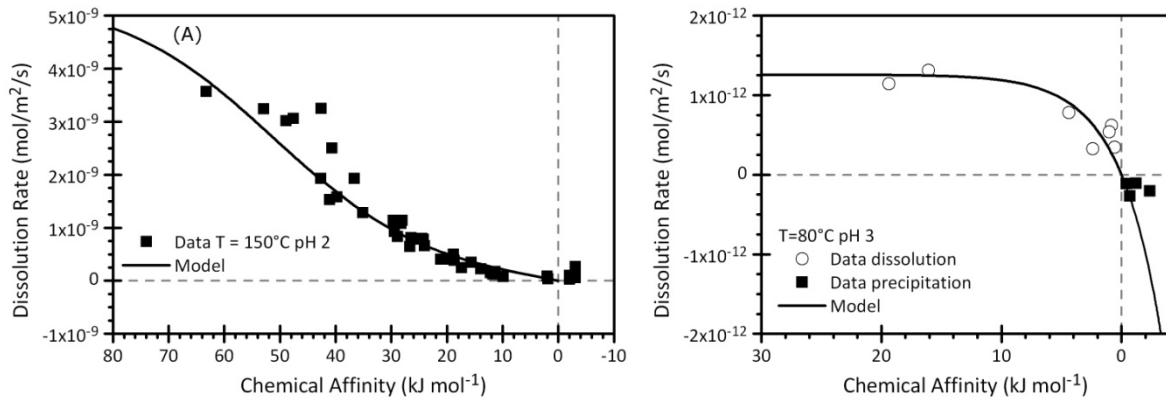
Fig. 6 A) Application of chemical affinity law on Kaolinite (Al₂Si₂O₅(OH)₄) dissolution in deionized water at 150 °C and pH 2 (3.17 m²/g , from (Devidal 1997)) B) at 80 °C and pH 3 (From (Nagy and Lasaga 1990)).

Devidal et al. (1997) tried to improve the rate expression by considering that close to equilibrium, lateral interactions among the precursor complexes on kaolinite in the case of Si-rich or Al-rich solution cannot be neglected. Eq. (9a) then becomes:

$$R = k_+ \cdot \left(K^* \cdot \left(\frac{\{H^+\}^3}{\{Al^{3+}\}} \right) \Big/ \left(1 + K^* \cdot \left(\frac{\{H^+\}^3}{\{Al^{3+}\}} \right) \right) \right) \times \exp\left(\frac{\omega_1}{RT} \frac{K^* \cdot \left(\frac{\{H^+\}^3}{\{Al^{3+}\}} \right) - 1}{K^* \cdot \left(\frac{\{H^+\}^3}{\{Al^{3+}\}} \right) + 1} \right) \times \left(1 - \exp\left(\frac{-A}{2RT} \right) \right) \qquad (10b)$$

with ω_l the interaction energy between two surface species.

Albite (NaAlSi₃O₈) has been studied with respect to chemical affinity at basic pH (8.8-10) and 80 °C ***(Burch 1993)*** or 150 °C ***(Hellmann and Tisserand 2006)***. Both show a sigmoidal behavior non consistent with TST. The rate expression used to represent the data over the full range of chemical affinity reflects the potential presence of two parallel mechanisms, and the presence of a critical *ΔG* value (eq. (11))

$$R = k_1 \left[1 - \exp\left\{ -\left(\frac{n_1 |A|}{RT} \right)^{m_1} \right\} \right] + k_2 \left[1 - \exp\left\{ -\left(\frac{|A|}{RT} \right) \right\} \right]^{m_2} \qquad (11)$$

Generally, values of *n₁, m₁* and *m₂* are correlated, and several mixed expressions can represent the data equally well. Also, the second term is not well enough constrained by the data. ***Burch et al. (1993)*** also stated that the rate dependence on chemical affinity could be considered linear only in a narrow range of chemical affinity (A < 0.9kJ/mol).

Few data are available concerning the dissolution rate of clay minerals as function of saturation state. *Cama et al. (2000)* studied smectite dissolution at pH 8.8 and 80 °C. They show that their data could equally well be fitted with the two following equations (eq. (12a) or eq. (12b))

$$R = 8.1 \cdot 10^{-12} \times \left[1 - \exp\left(-6 \cdot 10^{-10} \times \left(\frac{|A|}{RT} \right)^6 \right) \right]$$ (12a)

$$R = 1 \cdot 10^{-10} \times \left[1 - \exp\left(-9 \cdot 10^{-7} \times \left(\frac{|A|}{RT} \right)^3 \right) \right]$$ (12b)

Figure 7 shows the application of these two equations.
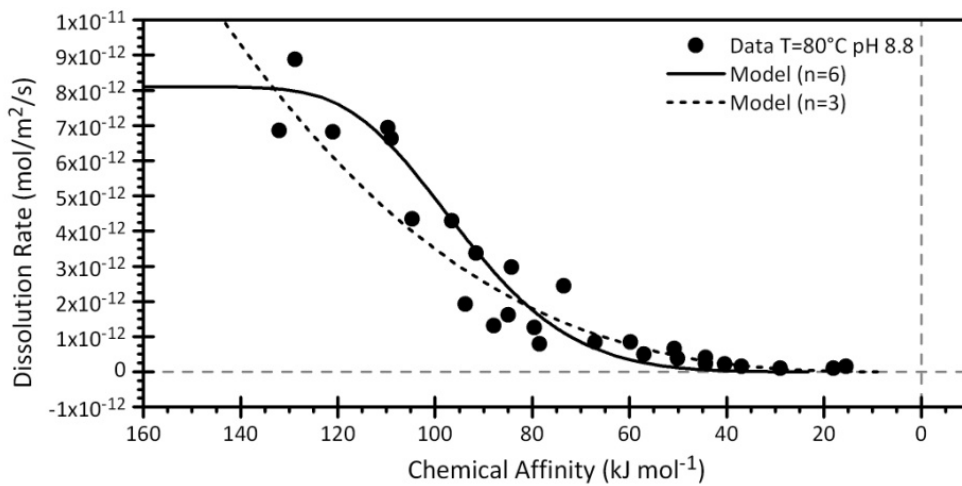

Fig. 7 Application of chemical affinity law on smectite dissolution in deionized water at 80 °C and pH 8.8 (62 m²/g data from (Cama 2000)).

Taking into account the potential inhibitory effect of silicon, they also proposed eq.(12c) applicable at least far from equilibrium:

$$R = k_+ \times \left[\frac{K^* \{OH^-\}}{1 + K^* \{OH^-\} + K' \{H_4SiO_4\}} \right]$$ (12c)

Including an affinity term *(1-exp(-A/R/T))* in equation 12c makes no great difference on the fitting of the curve, showing that there is not enough data close to equilibrium to constrain the model.

Illite du Puy dissolution experiments have been carried out by **Köhler et al. (2003)** between 5 °C and 50 °C and pH ranging from 2 to 12 in batch reactors. Their data is not enough detailed to calculate affinity of the reaction and dissolution rate dependence.

Experiments with clay minerals may appear difficult, as they may not reach a steady state due to a modification of the morphology of clay particles during dissolution **(Köhler et al. 2005)**.

Natural glasses

No thermodynamic equilibrium constant can be defined for glasses since they cannot precipitate from solution. In order to study the approach of equilibrium, affinity term must refer to the leached layer composition. For example, for a basaltic glass, **Daux et al. (1997)** estimated the affinity by:

$$A^* = RT \cdot \ln\left(\frac{\{H_4SiO_4\}\{Al(OH)_4^-\}^{0.36}\{Fe(OH)_3\}^{0.18}\{OH^-\}^{-0.36}}{8.2 \cdot 10^{-5}} \right) \tag{13a}$$

At 90 °C and pH ~8, the data for dissolution rate dependence on chemical affinity show a behavior consistent with TST (Figure 8) and the rate expression is given by eq. (13b) **(Daux 1997)**.

$$R = 3 \cdot 10^{-10} \times \{OH^-\}^{0.39} \times \left(1 - \exp\left(\frac{-A^*}{RT} \right) \right) \tag{13b}$$
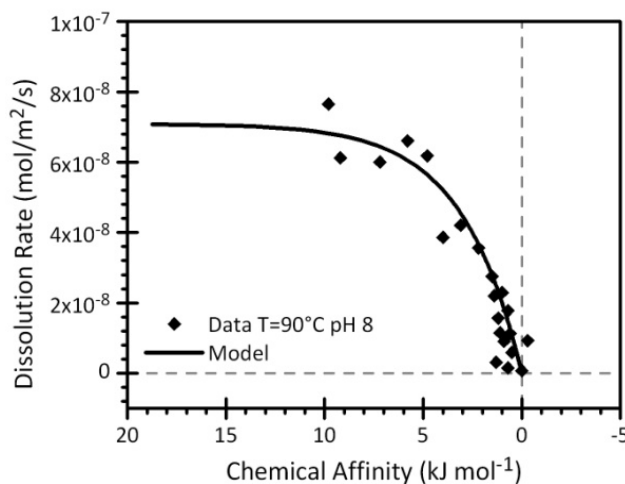

Fig. 8 Application of chemical affinity law for basaltic glass dissolution at 90 °C and pH 8 (from (Daux 1997)).

As for the aluminosilicate minerals, glass dissolution proceeds by a single mechanism at both low and high pH. This mechanism likely consists of the relatively rapid and complete removal of univalent and divalent cations from the near surface layer, then aluminum-releasing exchange reaction between 3 aqueous protons and Al in the basaltic glass structure, followed by the relatively slow detachment of partially liberated silica *(Oelkers and Gislason 2001)*. Far from equilibrium, the data on dissolution of a rhyolitic glass (with low Al content) between 40 °C and 200 °C and pH ranging from 2 to 10 *(Declercq et al. 2013)* are modeled with the following equation eq. (13c) consistent with eq. (9a):

$$R = k_+ \cdot K^* \cdot \left(\frac{\{H^+\}^3}{\{Al^{3+}\}} \right)^{1/11.1} \tag{13c}$$

Carbonates

The surface complexation modeling demonstrated the presence of both carbonate sites and metal cation sites. At neutral pH, the surface sites are all protonated, whereas in alkaline solution, the dissolution is controlled by the hydration of metal cation surface sites *(Oelkers et al. 2009)*. The dissolution rate could then be expressed according to:

$$R = \left[k_{CO3} \{\equiv CO_3 H^+\}^{n_H} + k_{Me} \{\equiv MeOH_2^+\}^{n_{H2O}} \right] \times \left(1 - \exp\left(\frac{-A}{\sigma RT} \right) \right) \tag{14}$$

For example, for calcite ($CaCO_3$), $n_H = 2$ and $n_{H2O} = 1$.

The rate depends on both chemical affinity and the activity of aqueous species that control the concentration of $\equiv MeOH_2^+$ precursor species. At 25 °C for dolomite ($CaMg(CO_3)_2$, 0.105 m^2/g), $n_H = n_{H2O} = 2$ and $\sigma = 0.5$ *(Pokrovsky 2001)*. Above pH 5, dissolution is controlled by the hydration of Mg surface sites and the formation of $\equiv MeOH_2^+$ species. Aqueous calcium and carbonates ions may have an inhibitory effect, resulting in a sigmoidal behavior dependence on chemical affinity (Figure 9).

Saldi et al. (2012) and Shiraki and Brantley (1995) studied precipitation of carbonates (magnesite and calcite). For them, dissolution rate constant and equation cannot be extrapolated to predict precipitation rates *(Shiraki and Brantley 1995, Saldi et al. 2012)*.
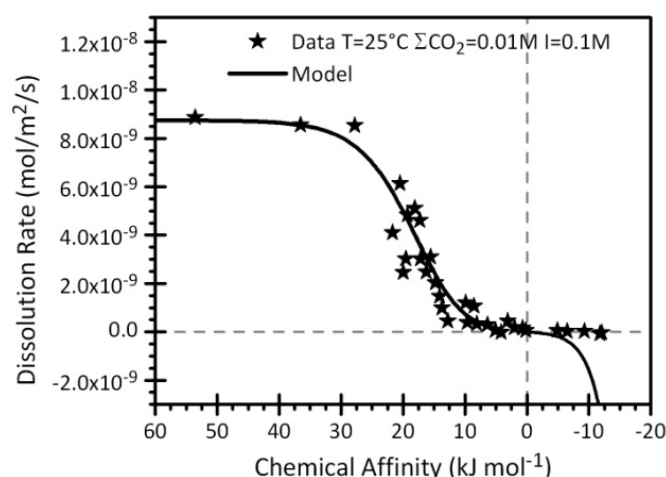
Fig. 9 Dolomite overall reaction rate at 25 °C as a function of chemical affinity at
$\Sigma CO_2 = 0.01 M$ *and* $I = 0.1 M$ *(From (Pokrovsky 2001))*

Experimental means to study very-close-to-equilibrium rates

Review of literature data has shown that affinity-based models may not be useful or sufficient in modeling dissolution and growth rate over the full range of ΔG. Moreover, the current laboratory data for bulk dissolution rates are not precise enough to derive specific dissolution mechanism very close to equilibrium *(Lüttge 2006)*, where a linear dependence could be observed (on a narrow range of affinities). A concept to be defined is "how close is "close-to-equilibrium"?". Usually, this is admitted when $\Delta G << RT$ (i.e. at 25 °C $\Delta G << 2.5$ kJ). Few data are available for this range.

Recent experimental techniques are developed that allow more precise measurement or observation near equilibrium. For example, Atomic Force Microscopy and Vertical Scanning Interferometry show promise towards the development of a fundamental understanding and comprehensive theory of crystal dissolution *(Dove et al. 2005, Lüttge 2006)*.

A Hydrogen-Electrode Concentration Cell has been developed and associated with pH jump relaxation technique and permits measurement of pH in solution with an accuracy of 0.002 pH unit, and then lower uncertainty in calculation of chemical affinity *(Bénézeth 2008, Davis 2011)*.

Isotopic Ratio Measurement: Stable isotopes are powerful environmental tracers that could be used to assess kinetics parameters *(Gee and Bruland 2002)*. Indeed, whereas the total concentration of an element may be affected by secondary phase precipitation (backward reaction), this is not the case with the isotopic composition, assuming that no fractionation occurs. The solution isotopic ratio decreases with the dissolution of a solid with a lower

isotopic ratio. Strontium isotopic composition has been used years ago to calculate the reaction progress of a basaltic glass with an isotopic composition different from the composition of the solution *(Daux et al. 1994, Daux 1997, Valle et al. 2010)*. More recently, solution enriched (spiked) with one less abundant isotope have been used to study atom exchange or dissolution of mineral having a "normal" isotopic composition. For example, ***Gorski et al. (2012)*** studied iron atom exchange between aqueous Fe^{2+} (spiked with ^{57}Fe) and "normal" magnetite in a batch reactor. The same type of study was carried out with goethite (Figure 10) at pH7.5 and 25 °C *(Handler et al. 2009)*.
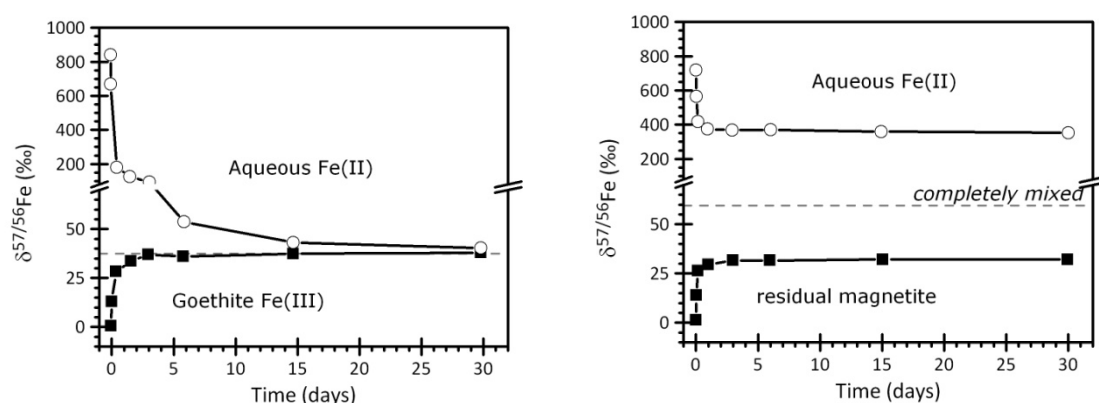

Fig. 10 Illustration of isotopic exchange between spiked ^{57}Fe aqueous solution and iron oxide/hydroxide (goethite or magnetite) (Handler 2009, Gorski 2012)

An approach with the "three-isotopes method" was applied by ***Li et al. (2011))*** to calculate a fractionation factor between an ^{25}Mg enriched solution at equilibrium with epsomite (MgSO$_4$).

Harpaz et al. (2007) and Gruber et al. (2013) have studied dissolution of albite and kaolinite using a mixed flow reactor and an inflow solution enriched with ^{29}Si, at a total silicon concentration of 200 µM and pH ~5, T = 50 °C (far from equilibrium according to PhreeqC calculation). They have shown that calculation of steady state rate with isotopic ratio method is more accurate than the traditional method *(Harpaz et al. 2007, Gruber et al. 2013)*.

The outflow isotopic ratio depends on the ratio and elemental concentration both of the mineral and the input solution, and of the amount of mineral dissolved.

For example, based on these last studies, in the case of using silicon isotopes (^{29}Si spiked inflow solution), the conservation of mass for each isotope, assuming that fractionation is negligible, leads to the following equation for the steady state rate in a mixed flow reactor:

$$Rate = \frac{Q}{A} \times \left[\frac{\left(\frac{29}{28}\right)_{in} - \left(\frac{29}{28}\right)_{out}}{\left(\frac{29}{28}\right)_{out} - \left(\frac{29}{28}\right)_{rock}} \right] \times \frac{Si_{in}}{Si_{rock}} \times \left[\frac{\left(\frac{29}{28}\right)_{rock} + 1.0335}{\left(\frac{29}{28}\right)_{in} + 1.0335} \right] \tag{15}$$

where Q = flow rate (m³/s), A = specific area (m²), Si_{in} = total concentration of Si in the inflow solution (moL/L), Si_{rock} = molar fraction of Si in the dissolving mineral (mol/mol$_{rock}$), $1.0335 = 1 + ({}^{30}Si/{}^{28}Si)$ assumed constant.

Equivalent studies are needed to assess the kinetics of mineral dissolution close to equilibrium and under various solution compositions, where traditional methods lead to large uncertainties.

Conclusions

This study has focused on the literature review for the kinetics of dissolution or precipitation of minerals likes oxides, hydroxides or aluminosilicates, when the evolution with chemical affinity (or saturation state) is available. The knowledge of the exact dependence of rate on chemical affinity is important because in natural systems, reactions occur often close to equilibrium and are strongly influenced by chemical affinity.

Usually, chemical affinity rate law is used as an extrapolation of experiments performed in laboratory to very near equilibrium.

It was shown that, most of the time, a single rate law, based on the Transition State Theory, is poorly or not applicable. It often requires using a succession of different rate laws with parameters with no physical meaning so far. Moreover, experimental data seem to depend on the history of dissolution of the solid, and changes of surface morphology. Different rate laws could equally well fit the data.

Very close to equilibrium, lack of the data and large uncertainties are a real drawback for the study of the impact of saturation state on mineral kinetics. However, new analytical techniques are emerging which would provide precise data in this area, like HECC or isotopic ratio measurements. Recently, isotopic ratio measurements on silicates or iron oxide/hydroxides have been published. More studies of this type need to be compiled in order to refine the effect of approaching equilibrium on the overall reaction rate. Applicability of the principle of detailed balancing to surface reactions consisting of several possible mechanisms on either side of equilibrium is not easy to prove; the data is often non-conclusive. Further work must be carried out to uncover the underlying physical chemistry governing processes the near equilibrium region.

Acknowledgements

References

Arvidson, R.S. and A. Luttge (2010). "Mineral dissolution kinetics as a function of distance from equilibrium - New experimental results." *Chemical Geology* **269**(1-2) 79-88.

Bénézeth, P., D.A. Palmer and D.J. Wesolowski (2008). "Dissolution/precipitation kinetics of boehmite and gibbsite: Application of a pH-relaxation technique to study near-equilibrium rates." *Geochimica et Cosmochimica Acta* **72**(10) 2429-2453.

Berger, G., E. Cadore, J. Schott and P.M. Dove (1994). "Dissolution rate of quartz in lead and sodium electrolyte solutions between 25 and 300°C: Effect of the nature of surface complexes and reaction affinity." *Geochimica et Cosmochimica Acta* **58**(2) 541-551.

Brady, P.V. and J.V. Walther (1990). "Kinetics of quartz dissolution at low temperatures." *Chemical Geology* **82** 253-264.

Brantley, S.L. (2008). Kinetics of Mineral Dissolution. *Kinetics of Water-Rock Interaction*. S. L. Brantley, J. D. Kubicki and A. F. White eds. New-York, NY, Springer**:** 151-210.

Burch, T.E., K.L. Nagy and A.C. Lasaga (1993). "Free energy dependence of albite dissolution kinetics at 80°C and pH 8.8." *Chemical Geology* **105**(1-3) 137-162.

Cama, J., J. Ganor, C. Ayora and C.A. Lasaga (2000). "Smectite dissolution kinetics at 80°C and pH 8.8." *Geochimica et Cosmochimica Acta* **64**(15) 2701-2717.

Daux, V., J.L. Crovisier, C. Hemond and J.C. Petit (1994). "Geochemical evolution of basaltic rocks subjected to weathering: Fate of the major elements, rare earth elements, and thorium." *Geochimica et Cosmochimica Acta* **58**(22) 4941-4954.

Daux, V., C. Guy, T. Advocat, J.-L. Crovisier and P. Stille (1997). "Kinetic aspects of basaltic glass dissolution at 90°C: role of aqueous silicon and aluminium." *Chemical Geology* **142**(1-2) 109-126.

Davis, M.C., D.J. Wesolowski, J. Rosenqvist, S.L. Brantley and K.T. Mueller (2011). "Solubility and near-equilibrium dissolution rates of quartz in dilute NaCl solutions at 398-473 K under alkaline conditions." *Geochimica et Cosmochimica Acta* **75**(2) 401-415.

Declercq, J., T. Diedrich, M. Perrot, S.R. Gislason and E.H. Oelkers (2013). "Experimental determination of rhyolitic glass dissolution rates at 40–200°C and 2<pH<10.1." *Geochimica et Cosmochimica Acta* **100** 251-263.

Devidal, J.-L., J. Schott and J.-L. Dandurand (1997). "An experimental study of kaolinite dissolution and precipitation kinetics as a function of chemical affinity and solution composition at 150°C, 40 bars, and pH 2, 6.8, and 7.8." *Geochimica et Cosmochimica Acta* **61**(24) 5165-5186.

Dove, P.M. and D.A. Crerar (1990). "Kinetics of quartz dissolution in electrolyte solutions using a hydrothermal mixed flow reactor." *Geochimica et Cosmochimica Acta* **54**(4) 955-969.

Dove, P.M., N.Z. Han and J.J. De Yoreo (2005). "Mechanisms of classical crystal growth theory explain quartz and silicate dissolution behavior." *Proceedings of the National Academy of Sciences of the United States of America* **102**(43) 15357-15362.

Ganor, J., T.J. Huston and L.M. Walter (2005). "Quartz precipitation kinetics at 180C in NaCl solutions – Implications for the usability of the principle of detailed balancing." *Geochimica et Cosmochimica Acta* **69**(8) 2043-2056.

Gautier, J.-M., E.H. Oelkers and J. Schott (1994). "Experimental study of K-feldspar dissolution rates as a function of chemical affinity at 150°C and pH 9." *Geochimica et Cosmochimica Acta* **58**(21) 4549-4560.

Gee, A.K. and K.W. Bruland (2002). "Tracing Ni, Cu, and Zn kinetics and equilibrium partitioning between dissolved and particulate phases in South San Francisco Bay, California, using stable isotopes and high-resolution inductively coupled plasma mass spectrometry." *Geochimica et Cosmochimica Acta* **66**(17) 3063-3083.

Gorski, C.A., R.M. Handler, B.L. Beard, T. Pasakarnis, C.M. Johnson and M.M. Scherer (2012). "Fe Atom Exchange between Aqueous Fe^{2+} and Magnetite." *Environmental Science & Technology* **46**(22) 12399-12407.

Gruber, C., L. Harpaz, C. Zhu, T.D. Bullen and J. Ganor (2013). "A new approach for measuring dissolution rates of silicate minerals by using silicon isotopes." *Geochimica et Cosmochimica Acta* **104** 261-280.

Handler, R.M., B.L. Beard, C.M. Johnson and M.M. Scherer (2009). "Atom Exchange between Aqueous Fe(II) and Goethite: An Fe Isotope Tracer Study." *Environmental Science & Technology* **43**(4) 1102-1107.

Harpaz, L., J. Ganor and T.D. Bullen (2007). Developing a new method of measuring dissolution rates of silicate minerals using changes in the isotopic ratio of a spiked solution. *Water-Rock Interaction*. T. D. Bullen and Y. Wang eds. London, Taylor & Francis Ltd. **1&2:** 423-426.

Hellmann, R. and D. Tisserand (2006). "Dissolution kinetics as a function of the Gibbs free energy of reaction: An experimental study based on albite feldspar." *Geochimica et Cosmochimica Acta* **70**(2) 364-383.
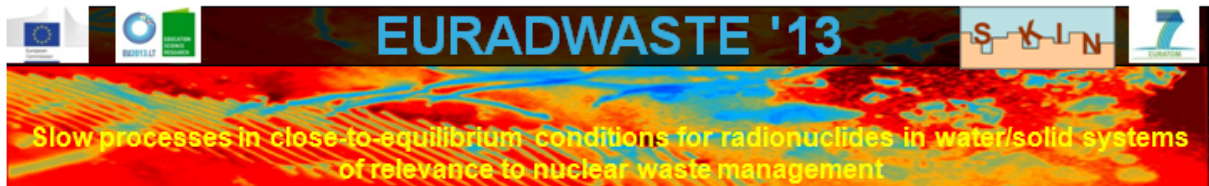
Köhler, S.J., D. Bosbach and E.H. Oelkers (2005). "Do clay mineral dissolution rates reach steady state?" *Geochimica et Cosmochimica Acta* **69**(8) 1997-2006.

Köhler, S.J., F. Dufaud and E.H. Oelkers (2003). "An experimental study of illite dissolution kinetics as a function of pH from 1.4 to 12.4 and temperature from 5 to 50°C." *Geochimica et Cosmochimica Acta* **67**(19) 3583-3594.

Lasaga, A.C. (1984). "Chemical kinetics of water-rock interactions." *Journal of Geophysical Research* **89**(B6) 4009-4025.

Lasaga, A.C. (1998). Kinetic theory in the earth science. Princeton, NJ USA, Princeton University Press.

Lasaga, A.C., J.M. Soler, J. Ganor, T.E. Burch and K.L. Nagy (1994). "Chemical weathering rate laws and global geochemical cycles." *Geochimica et Cosmochimica Acta* **58**(10) 2361-2386.

Li, W., B.L. Beard and C.M. Johnson (2011). "Exchange and fractionation of Mg isotopes between epsomite and saturated $MgSO_4$ solution." *Geochimica et Cosmochimica Acta* **75**(7) 1814-1828.

Lowson, R.T., M.C.J. Comarmond, G. Rajaratnam and P.L. Brown (2005). "The kinetics of the dissolution of chlorite as a function of pH and at 25°C." *Geochimica et Cosmochimica Acta* **69**(7) 1687-1699.

Lüttge, A. (2006). "Crystal dissolution kinetics and Gibbs free energy." *Journal of Electron Spectroscopy and Related Phenomena* **150**(2-3) 248-259.

Lüttge, A. and R.S. Arvidson (2008). The Mineral-Water Interface. *Kinetics of Water-Rock Interaction*. S. L. Brantley, J. D. Kubicki and A. F. White eds. New-York, Springer 73-107.

Nagy, K.L., A.E. Blum and A.C. Lasaga (1991). "Dissolution and precipitation kinetics of kaolinite at 80°C and pH3: The dependence on solution saturation state." *American Journal of Science* **291** 649-686.

Nagy, K.L. and A.C. Lasaga (1990). "The effect of deviation from equilibrium on the kinetics of dissolution and precipitation of kaolinite and gibbsite." *Chemical Geology* **84**(1-4) 283-285.

Nagy, K.L. and A.C. Lasaga (1992). "Dissolution and precipitation kinetics of gibbsite at 80°C and pH 3: The dependence on solution saturation state." *Geochimica et Cosmochimica Acta* **56**(8) 3093-3111.

Oelkers, E.H. (2001). "General kinetic description of multioxide silicate mineral and glass dissolution." *Geochimica et Cosmochimica Acta* **65**(21) 3703-3719.

Oelkers, E.H., P. Bénézeth and O.S. Pokrovsky (2009). Thermodynamic Databases. *Thermodynamics and Kinetics of Water-Rock Interaction*. E. H. Oelkers and J. Schott eds. Chantilly, VA (USA), Mineralogical Society of America. **70:** 1-46.

Oelkers, E.H. and S.R. Gislason (2001). "The mechanism, rates and consequences of basaltic glass dissolution: I. An experimental study of the dissolution rates of basaltic glass as a function of aqueous Al, Si and oxalic acid concentration at 25°C and pH = 3 and 11." *Geochimica et Cosmochimica Acta* **65**(21) 3671-3681.

Oelkers, E.H., J. Schott, J.-M. Gauthier and T. Herrero-Roncal (2008). "An experimental study of the dissolution mechanism and rates of muscovite." *Geochimica et Cosmochimica Acta* **72**(20) 4948-4961.

Pokrovsky, O.S. and J. Schott (2001). "Kinetics and mechanism of dolomite dissolution in neutral to alkaline solutions revisited." *American Journal of Science* **301**(7) 597-626.

Pokrovsky, O.S. and J. Schott (2004). "Experimental study of brucite dissolution and precipitation in aqueous solutions: surface speciation and chemical affinity control." *Geochimica et Cosmochimica Acta* **68**(1) 31-45.

Rimstidt, J.D. and H.L. Barnes (1980). "The kinetics of silica-water reactions." *Geochimica et Cosmochimica Acta* **44**(11) 1683-1699.

Saldi, G.D., J. Schott, O.S. Pokrovsky, Q. Gautier and E.H. Oelkers (2012). "An experimental study of magnesite precipitation rates at neutral to alkaline conditions and 100–200°C as a function of pH, aqueous solution composition and chemical affinity." *Geochimica et Cosmochimica Acta* **83** 93-109.

Schott, J. and E.H. Oelkers (1995). "Dissolution and Crystallization Rates of Silicate Minerals as a Function of Chemical Affinity." *Pure and Applied Chemistry* **67**(6) 903-910.

Schott, J., E.H. Oelkers, P. Bénézeth, Y. Goddéris and L. François (2012). "Can accurate kinetic laws be created to describe chemical weathering?" *Comptes Rendus Geoscience* **344**(11â€"12) 568-585.

Schott, J., O.S. Pokrovsky and E.H. Oelkers (2009). The Link Between Mineral Dissolution/Precipitation Kinetics and Solution Chemistry. *Thermodynamics and Kinetics of Water-Rock Interaction*. E. H. Oelkers and J. Schott eds. Chantilly, VA (USA), Mineralogical Society of America. **70:** 207-258.

Shiraki, R. and S.L. Brantley (1995). "Kinetics of near-equilibrium calcite precipitation at 100°C: An evaluation of elementary reaction-based and affinity-based rate laws." *Geochimica et Cosmochimica Acta* **59**(8) 1457-1471.

Teng, H.H., P.M. Dove and J.J. De Yoreo (2000). "Kinetics of calcite growth: surface processes and relationships to macroscopic rate laws." *Geochimica et Cosmochimica Acta* **64**(13) 2255-2266.

Valle, N., A. Verney-Carron, J. Sterpenich, G. Libourel, E. Deloule and P. Jollivet (2010). "Elemental and isotopic (^{29}Si and ^{18}O) tracing of glass alteration mechanisms." *Geochimica et Cosmochimica Acta* **74**(12) 3412-3431.
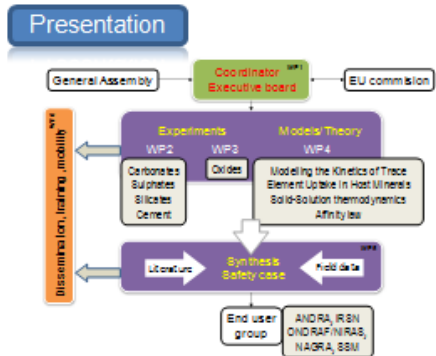
Wimpenny, J., S.R. Gislason, R.H. James, A. Gannoun, P.A.E. Pogge Von Strandmann and K.W. Burton (2010). "The behaviour of Li and Mg isotopes during primary phase dissolution and secondary mineral formation in basalt." *Geochimica et Cosmochimica Acta* **74**(18) 5259-5279.

Poster

EURADWASTE '13

Slow processes in close-to-equilibrium conditions for radionuclides in water/solid systems of relevance to nuclear waste management

A 7th FRAMEWORK PROGRAMME COLLABORATIVE PROJECT (2008-2012)

Bernd Grambow (grambow@subatech.in2p3.fr) and Tomo Suzuki-Muresan (suzuki@subatech.in2p3.fr), Coordinators
SUBATECH, Unité Mixte de Recherche 6457, Ecole des Mines de Nantes, CNRS/IN2P3, Université de Nantes
4 rue Alfred Kastler, BP 20722, 44307 Nantes cedex 03, France

Presentation

SKIN is a 3-years collaborative project focused on the study of very slow processes that can impact on the mobility behaviour of radionuclides from the source term, the near field and the geosphere

Objectives

– **To assess** the use/misuse of solubility data of sparingly soluble tetravalent actinides
– **To understand** the coupling of major and trace element chemistry in RN migration behavior considering the extremely large exchange pool of natural minerals present in the disposal sites
– **To include** irreversibility in models on the mobility of RN in the repository environment
– **To assess**, in PA to what degree the ignorance/non-inclusion of these studied slow processes leads to over-conservative evaluations, or in few cases, even too optimistic evaluations

Partners

End user group : ANDRA, ONDRAF/NIRAS, NAGRA, SSM and IRSN

Compartmental modelling approach

Determining the impact of the studies done in the frame of the SKIN project over the calculations that support safety assessment procedures.

Main results

– **Dynamic exchanges close to solubility equilibrium**
  – *Isotopic exchange:* ThO_2, TcO_2, *silicates*
  – *Bulk phases vs. specific surface sites on solubility control*
– **Incorporation of Tr in host minerals**
  – *Case of Ra in barite: data modelled using the GEMS-Selector code*
  – *Incorporation requires diffusion and/or recrystallisation: very slow processes*
– **Sorption/Desorption processes**
  – *Often reversible but some case irreversible (Cs in illite)*
  – *Ageing can influence the retention and the release of the co-precipitate of U/Fe(III)*
– **Modeling**
  – *SEMO / SRKM : successfully tested*
  – *SEMO + SRKM: implemented in GEMS-Selector geochemical code*
– **Uncertainties in the solubilty and sorption**
  – *Compartmental modelling approach*
  – *Reference case: waste, container, bentonite, granite, sink*

Present status

Start of the project: January 1st, 2011
Kick-Off Meeting: February 1st, 2011, France
1st annual workshop: November 17th-18th, 2011, Barcelona
2nd annual workshop: November 21th-22th, 2012, PSI
3rd annual workshop: November 21st-22th, 2013, Barcelona
1st and 2nd Proceedings: http://www.emn.fr/z-subatech/skin
Publication:
  • Holliday et al., Dalton Trans., 2012, 41, 3642-3647
  • Vinograd et al., GCA, 2013, 22 (1), 398-417
  • Mineralogical Magazine, Goldschmidt conference, 2012
  • Procedia Earth and Planetary Science, 2013, 7, 838–841
  • 25th PSI Waste Management Program Committee Meeting, Villigen, Switzerland, 2013
Conferences:
  • NUWCEM'11
  • Migration'11, '13
  • Goldschmidt'12, '13